Titre: Title:	Ellipsometric characterization of gold/dielectric nanocomposite films
Auteur: Author:	Dan Dalacu
Date:	2000
Type:	Mémoire ou thèse / Dissertation or Thesis
Référence: Citation:	Dalacu, D. (2000). Ellipsometric characterization of gold/dielectric nanocomposite films [Thèse de doctorat, École Polytechnique de Montréal]. PolyPublie. https://publications.polymtl.ca/8849/

UNIVERSITÉ DE MONTRÉAL

Ellipsometric Characterization of Gold/Dielectric Nanocomposite Films

DAN DALACU
DÉPARTEMENT DE GÉNIE PHYSIQUE ET GÉNIE DES MATÉRIAUX
ÉCOLE POLYTECHNIQUE DE MONTRÉAL

THÈSE PRÉSENTÉE EN VUE DE L'OBTENTION
DU DIPLÔME DE PHILOSOPHIÆ DOCTOR (Ph.D.)
(GÉNIE PHYSIQUE)
Décembre 2000

UNIVERSITÉ DE MONTRÉAL

ÉCOLE POLYTECHNIQUE

Cette thèse intitulée:

Ellipsometric Characterization of Gold/Dielectric Nanocomposite Films

présentée par: DALACU Dan

en vue de l'obtention du diplôme de: Philosophiæ Doctor

a été dûment acceptée par le jury d'examen constitué de:

WERTHEIMER, Michael Robert, D.Sc.A., président
MARTINU, Ludvik, Ph.D., membre et directeur de recherche
NAJAFI, Iraj, Ph.D., membre et co-directeur de recherche
ROORDA, Sjoerd, Ph.D., membre
KAY, Eric, Ph.D., membre

À mes chers parents

Acknowlegements

Mes remerciements vont tout d'abord à mon directeur de recherche, le professeur Ludvik Martinu, pour le soutien et la liberté qu'il m'a accordés.

Toute ma profonde gratitude à Mme Jolanta Sapieha dont l'aide ne s'est jamais démentie, même quand elle était trop occupée.

Un grand merci à Gilles Jalbert pour son aide et son silence quand j'ai sali la pompe de diffusion (même la deuxième fois).

Merci également à tout le gang du laboratoire, qui a su entretenir une ambiance bien fun et qui m'a enseigné la langue du labo, le Franglais. Un remerciement tout particulier aux anciens du groupe qui m'ont fait profiter de leur expérience: Daniel Poitras, Oleg Zabeida, Argemiro da Silva, Adam Bergeron, Jiri Cerny, Mohammed Latrèche, et Gregory Czeremuszkin.

Enfin, merci à Marinette, qui, au bout de presque quatre ans, en est arrivée, malgré elle, à en savoir assez long sur ces petites particules métalliques.

Abstract

An optical characterization methodology has been developed to characterize the detailed microstructural characteristics of metal/dielectric nanocomposite thin films. The characterization is based on parametric models of the optical response of the nanocomposite systems applied to spectro-ellipsometric and spectro-photometric optical data. The modeling consists of effective medium approaches in combination with a modified Drude response to describe the metal and a Cauchy/Urbach response to describe the dielectric. The methodology was applied to gold particles in the size range 3 to 30 nm embedded in and deposited on different dielectric materials. The films were fabricated using hybrid approaches consisting of magnetron sputtering of the gold and plasma enhanced chemical vapour deposition (PECVD) of the dielectric, in particular, plasma-polymerized fluorocarbon (PPFC) and hydrogenated amorphous silicon dioxide (SiO_2:H).

Two important factors are critical in regard to the feasibility of such a characterization methodology: (*i*) the sensitivity of the optical constants of nanocomposite materials to the microstructure arising from the excitation of collective conduction electron oscillations, so-called surface plasmons, and (*ii*) the inherent sensitivity of ellipsometric measurements to the optical constants of thin films, combined with the constraints imposed on the optical model by taking spectroscopic measurements at multiple angles of incidence, and by including transmission spectra in the analysis. These two factors make possible the use of fitting procedures to extract either optical or microstructural parameters.

The methodology was utilized in two distinctly different contexts. The first one concerns the characterization of the microstructural dependence of nanocomposite films on the fabrication conditions. This was emphasized in the case of the Au/PPFC system where the dependence of the gold volume fraction on glow discharge parameters and post-deposition thermal treatments was quantified and explained in terms of the ratio of the gold sputtering rate to the plasma polymerization rate and a restructuring of the polymer, respectively.

The second concerns the characterization of the particle size dependence of the optical response of gold. This was emphasized in the case of the Au/SiO_2 system where high temperature post-deposition thermal treatments were used to induce particle growth through diffusion and liquid-like coalescence of smaller particles. In this way, films with particles ranging in size from 4 nm to greater than 20 nm and having the same gold volume fraction could be studied.

Two limiting particle sizes were identified: (*i*) for particles larger than 20 nm phase retardation and scattering become significant, marking the limit of the quasi-static approximation, and (*ii*) for particles less than 10 nm changes in the inter-band optical constants of gold become significant, marking the limit for which the bulk core response is applicable. In between these particle sizes, unprecedented aggreement between the measured spectra and the effective medium model was obtained. This has allowed for two important observations: (*i*) a clear demonstration of dipole-dipole interaction effects seen with increasing particle concentration, and (*ii*) an accurate measure of the width of surface plasmon resonance as a function of particle size.

The changes observed in the core response for particles smaller than 10 nm consist of (*i*) a shift of the inter-band absorption edge to lower energy, (*ii*) a decrease in the slope of the edge, and (*iii*) the broadening of features due to inter-conduction band transitions. These changes were attributed to a combination of surface stress-induced distortion of the atomic structure and the influence of surface atoms which are distinct with respect to the volume atoms by virtue of their decreased coordination.

The finite size-induced changes of the core response of gold were used to account for the observed dependence on particle size of the optical spectra of discontinuous films consisting of substrate supported particles. The 2-D format also allowed for the observation of some additional effects, including (*i*) image charge interaction and its dependence on the matrix/support combination, (*ii*) thermally-induced morphological changes consisting of the assumption of more spherical particle geometries with a smaller size distribution, and (*iii*) metal/matrix interaction, in particular, the transfer of charge at the metal/matrix interface for particles deposited on a conductive support.

The observation and quantification of the various microstructural dependencies was made possible by a combination of (*i*) the careful consideration of the optical response of the constituent materials comprising the effective medium (including both intra- and inter-band absorption in the metal and both dispersion and absorption in the dielectric) and (*ii*) the applicability of the effective medium approach to gold particles embedded in PECVD matrices. The latter criterion concerns the ability to prepare isolated metal particles with a small size distribution in a non-reactive embedding material which serves only as a host for the particles. The corollary of this ability is that these materials are ideally suited for application in such fields as nonlinear optics where the effective medium response is key to device optimization.

Condensé en français

Les propriétés optiques de particules métalliques sont tributaires de l'induction d'une oscillation collective des électrons de conduction, appelée plasmon de surface. Cette induction produit des bandes d'absorption résonantes dans la gamme des longueurs d'onde ultraviolets-visibles, dont l'énergie et la largeur dépendent des caractéristiques morphologiques des particules (taille, forme, concentration, état de coagulation) et des propriétés diélectriques du matériau dans lequel les particules sont intégrées. Cela permet d'utiliser la technique de la spectroscopie optique, méthode sensible et non intrusive de caractérisation des détails microstructurels des matériaux nanocomposites métal/diélectrique.

Les caractéristiques microstructurelles sont extraites en appliquant des modèles optiques à la réponse mesurée. La réponse électrodynamique, qui comprend à la fois l'absorption et la diffusion par une particule de métal de taille arbitraire, est donnée par la théorie de Mie (Éqs. 1.1 à 1.5). L'extinction (c.-à-d. l'absorption et la diffusion) selon la taille découle de la théorie de Mie comme le montre la figure 1.1 et consiste en une série de bandes correspondant à chacun des types d'oscillation des électrons de conduction. L'énergie de résonance des diverses bandes se décale vers le rouge et elles s'élargissent en fonction de la taille des particules à cause, respectivement, du retard de phase et du phénomène de dispersion.

Dans la limite de petites particules et de grandes longueurs d'onde (la limite quasi-statique, LQS), seul le mode dipôle est induit, autrement dit la résonance plasmonique de surface (RPS), et les équations de Mie se réduisent à une expression en fonction de

la taille de la particule qui ne tient compte que de l'absorption (Éq. 1.7). La figure 1.2 montre le spectre d'absorption dans la LQS dans le cas de matériaux intégrés ayant des fonctions diélectriques différentes, ϵ_h. La dépendance de l'énergie de la RPS des propriétés diélectriques du matériau environnant est une conséquence du criblage du champ électromagnétique incident causé par le matériau utilisé.

Dans la LQS, on peut s'appuyer sur la réponse électrostatique prévue par les théories sur le milieu effectif (TME) pour décrire les propriétés optiques d'un ensemble de particules métalliques. Contrairement à la théorie de Mie, qui se révèle exacte dans le cas d'une particule unique, ces théories ne peuvent s'appliquer à une concentration plus forte de particules où l'interaction entre les champs dipôles des particules (effets du champ local) est forte. La TME la plus pertinente aux microstructures consistant en particules isolées est le modèle de Maxwell-Garnett (M-G) (Éq. 1.15). Dans la limite où la fraction volumique du métal (p) est faible, cette théorie se ramène à l'expression de Mie dans la LQS. En augmentant p, la TME de M-G prévoit un élargissement et un décalage vers le rouge de la RPS, comme l'indique la figure 1.4.

Dans la LQS, l'énergie et la largeur de bande de la RPS, selon Mie ou la TME de M-G, ne dépendent que de ϵ_h et de p. Cependant, on peut prévoir d'autres effets, appelés effets de taille limitée, qui découlent de la dépendance de la fonction diélectrique du métal selon la taille des particules. Parmi les effets de taille limitée, notons (i) l'effet quantique (EQ), (ii) le déversement des électrons de conduction, (iii) l'effet d'une couche de surface exempte de toute polarisation du noyau, et (iv), les effets de structure atomique.

L'effet quantique correspond à la discrétisation de la bande de conduction au fur et à mesure de la diminution de la taille des particules et débouche sur l'élargissement de la RPS (Éqs. 1.26 et 1.30) en raison du couplage des plasmons de surface et de l'induction d'électrons entre les divers niveaux discrets (c.-à-d. amortissement de Landau). Ce phénomène de dépendance, caractérisé par un paramètre d'élargissement A, permet de calculer la taille de la particule dans la LQS. Le déversement des électrons

de conduction correspond à la densité non nulle des électrons en dehors du rayon R de la particule définie par le noyau de l'ion (Fig. 1.10) et se traduit par un décalage vers le rouge de la RPS ainsi qu'une diminution de R (Éqs. 1.31 et 1.34).

Les deux autres effets limités sont plus fréquents dans les métaux nobles, contrairement aux métaux alcalins, en raison d'une bande d chargée d'électrons et d'une dépendance concomitante du spectre optique de la réponse du noyau (Fig. 1.3). L'absence de polarisation de la couche de surface s'explique par le fait qu'il n'y a pas de chevauchement des fonctions d'onde des électrons de conduction et de la bande d dans le cas des atomes de surface (Fig. 1.12), ce qui se traduit par un décalage vers le bleu de la RPS avec une diminution de R (Éq. 1.36) en raison de l'augmentation de la proportion des électrons de surface. Par effets de la structure atomique, on entend tant les changements induits par la contrainte de surface de la structure maillée que ceux causés par les atomes de surface, qui diffèrent des atomes internes de la particule parce qu'ils présentent une coordonnation moindre. La dépendance de la réponse optique de la structure atomique découle de son influence sur la réponse du noyau.

Cette étude porte sur la fabrication et la caractérisation microstructurelle des matériaux nanocomposites or/diélectrique sous forme de couche mince. Ces couches ont été fabriquées en appliquant des approches hybrides consistant en pulvérisation magnétron de l'or et en dépôt chimique en phase vapeur activé par plasma du diélectrique. Les systèmes plus particulièrement étudiés sont ceux qui reposent sur des particules d'or intégrées à des matrices, soit de fluoropolymères, soit de SiO_2.

La caractérisation microstructurelle ne reposait que sur des méthodes optiques consistant en l'utilisation de modèles paramétriques pour décrire la réponse optique tant du métal (c.-à-d. Drude, Éq. 1.8) et du diélectrique (c.-à-d. dispersion du Cauchy, Éq. 2.24, et absorption d'Urbach, Éq. 2.25), et de leur réponse comme milieu effectif lorsqu'ils étaient combinés (c.-à-d. Maxwell-Garnett, Éq. 1.25). L'application de ces modèles aux spectres optiques en ajustant les paramètres pertinents est rendue possible par le recours aux données ellipsométriques et photométriques. La sensibi-

lité des mesures ellipsométriques dans le cas des constantes optiques des matériaux, en particulier pour ce qui est d'une couche mince déposée sur un substrat ayant un indice de réfraction similaire, est essentielle pour définir le minimum global lors de la procédure d'ajustement. L'inclusion de données photométriques permet de recueillir toute l'information portée par le faisceau lumineux réfléchi/transmis et se révèle essentielle si l'on veut réduire la corrélation entre les divers paramètres au moment de l'ajustement.

Le premier système que nous avons étudié est un nanocomposite or/fluoropolymère préparé à l'aide de polymérisation par plasma d'un fluorocarbure (octafluorocyclobutane, C_4F_8) et de la pulvérisation simultanée d'or dans un simple réacteur RF à armatures parallèles (Fig. 2.2). Nous avons appliqué le modèle Maxwell-Garnett aux spectres optiques pour déterminer les paramètres microstructurels des couches déposées dans différentes conditions et soumises à divers traitements thermiques après-dépôt.

La concentration volumique d'or variait de 15 à 35%, tout dépendant des paramètres de décharge luminescente (pression du gaz de travail, mélange de gaz, puissance d'entrée) et du recuit après-dépôt. L'influence de p sur les paramètres de décharge (Fig. 3.2) était établie selon le ratio de la dispersion de l'or à la polymérisation du plasma. L'augmentation de p dans un recuit à 160°C (Fig. 3.4) pouvait s'expliquer par une restructuration et la possibilité d'un effet de traitement de la structure réticulée du polymère, qui se traduit par une densification de la couche.

La taille des particules, toutes situées dans la gamme de 4 à 9 nm, était calculée au moyen d'un paramètre d'élargissement $A = 0.25$, déterminé au moyen d'une analyse par microscopie électronique en transmission d'échantillons sélectionnés, et l'on constate qu'elle augmente en fonction de la concentration (Fig. 3.3a). La taille maximale que l'on pouvait obtenir était déterminée par les conditions de fabrication, qui n'offraient pas beaucoup de possibilités de croissance pendant le dépôt, et par la faible température du recuit utilisée, qui ne permettait pas d'obtenir de coalescence

quasi-liquide des particules d'une taille supérieure à $\sim 5\,\text{nm}$ (Fig. 3.6).

Le second système que nous avons étudié était un nanocomposite Au/SiO_2 préparé au moyen d'un dépôt chimique en phase vapeur activé par plasma du SiO_2 grâce à une combinaison des gaz SiH_4 et N_2O et d'une pulvérisation d'or, animée cette fois à l'aide d'une source RF distincte (Fig. 2.3). La matrice SiO_2 diffère du fluoropolymère sous deux aspects principaux : (*i*) elle est plus stable du point de vue thermique et (*ii*) la discontinuité d'absorption a lieu à un niveau d'énergie plus élevé (comparer les Figs. 2.7 et 2.9). Dans le premier cas, les traitements thermiques après-dépôt peuvent être effectués à une température beaucoup plus élevée, de sorte que la coalescence quasi-liquide ne se limite pas aux très petites particules. C'est ainsi que l'on peut observer une croissance des particules et non une coagulation, ce qui permet de préparer des couches à partir de particules de plus de 20 nm.

La couche de grosses particules obtenue lors des traitements thermiques après-dépôt à 900°C permettait de déterminer la limite des grosses particules du modèle de Maxwell-Garnett, c'est-à-dire le début de la dispersion et du retard de phase (Fig. 4.4a et 4.7). L'adhérence du système Au/SiO_2 à la microstructure proposée par la TME de M-G permettait également d'avoir une idée précise de l'influence du champ local (Fig. 4.6) et de l'effet de la taille limitée (Fig. 4.4b) sur l'énergie de la RPS.

L'absence d'absorption de la matrice dans les ultraviolets permettait de faire une analyse détaillée de la réponse du noyau d'or (Fig. 4.8) qui montre une dépendance de la taille des particules consistant en un déplacement de la discontinuité d'absorption interbandes vers une énergie inférieure et une diminution de la pente de la courbe de la discontinuité (Fig. 4.9), ainsi qu'un élargissement des caractéristiques dues à la transition entre les différents niveaux dans la bande de conduction. On a pu montrer que cette dépendance de la taille des particules était un facteur important du déplacement vers le bleu de la RPS à mesure que la taille des particules diminue et l'associer à une augmentation du désordre structurel. L'augmentation du désordre de la structure atomique peut s'expliquer par une augmentation de la déformation

du réseau cristallin induite par la contrainte et une augmentation du pourcentage d'atomes de surface dont la liaison est plus faible et qui ont moins de contrainte dans leurs mouvements thermiques à cause de leur moins grande coordonnation. Cette interprétation est confirmée par la similarité des changements interbandes dépendant de la taille des particules et de ceux qui se produisent lors de la transition à un état liquide (Fig. 5.2).

La taille des particules des nanocomposites Au/SiO_2 était calculée au moyen d'un paramètre d'élargissement $A = 0.15$ déterminé au moyen d'une analyse détaillée par microscopie électronique en transmission (Fig. 6.5, Tableau 6.1) dans des couches bidimensionnelles consistant en particules déposées sur un substrat (Fig. 6.3). Les couches d'or « discontinues » étaient déposées par pulvérisation RF sur des substrats recouverts de matériau de la matrice auxquel s'ajoutait une deuxième couche de $\sim 10\,\text{nm}$ d'épaisseur de ce matériau.

Le format bidimensionnel permettait également de démontrer la dépendance de la RPS (*i*) du matériau de la matrice, (*ii*) de l'interaction de charge virtuelle, (*iii*) de la morphologie de la particule, et (*iv*) du transfert de charge. L'influence de la fonction diélectrique du matériau de la matrice était démontrée au moyen de divers arrangements de structures diélectrique/couche discontinue/diélectrique, à partir des diélectriques SiO_2, TiO_2, et « vide » (Fig. 6.6).

Par interaction de la charge virtuelle, on entend les effets de polarisation du substrat apparaissant à cause de l'interface sous-jacente supportant les particules de la couche bidimensionnelle. Les champs dipôlaires des particules induisent des charges virtuelles dans le substrat qui modifient le champ électrique local (Éqs. 6.3 et 6.4). L'influence de l'interaction de la charge virtuelle est démontrée au moyen d'une matrice TiO_2, en faisant varier la distance entre les couches bidimensionnelles et l'interface TiO_2/substrat (Fig. 6.7).

Les changements morphologiques induits thermiquement, c'est-à-dire l'hypothèse que les particules deviennent plus sphériques (Fig. 1.7), avec une distribution granu-

lométrique étroite, sont mis en évidence en comparant la réponse optique des couches bidimensionnelles initialement déposées et de celles qui ont été recuites pendant cinq heures à une température de 250°C (Fig. 7.1). On a utilisé ces changements morphologiques pour expliquer, selon la taille des particules, la différence de la dépendance de l'énergie de liaison et de la largeur de raie des électrons Au $4f_{7/2}$ (Fig. 7.3) que l'on observe grâce à la spectroscopie des photoélectrons par rayons X (Fig. 7.2).

Enfin, nous avons utilisé des couches bidimensionnelles pour montrer l'effet du transfert d'électron à travers l'interface métal/matrice de la RPS (Fig. 7.1) en déposant ces couches sur des substrats conducteurs (oxyde d'indium-étain). Ce transfert de charge était également nettement apparent dans les spectres de l'Au 4f, qui ne présentait aucun changement de la charge induite au niveau de l'énergie de liaison de l'état $4f_{7/2}$ que l'on pouvait observer dans les couches déposées sur les substrats isolants (Fig. 7.3).

En conclusion, ce travail permettait de démontrer la possibilité de produire des couches minces de nanocomposites présentant une microstructure très semblable à celle prévue par les théories du milieu effectif, à savoir des particules métalliques isolées avec une répartition granulométrique étroite, incorporées dans une matrice diélectrique qui ne sert que de support hôte. Ces couches nanocomposites ont été fabriquées au moyen de matrices déposées chimiquement en phase vapeur activé par plasma (fluorocarbure plasma-polymérisé et SiO_2) dont la structure est amorphe et compacte, en combinaison avec des nanoparticules d'or intégrées, qui sont chimiquement inertes.

Nous avons utilisé la réponse optique des couches nanocomposites pour illustrer deux types de comportements inhérents à ces systèmes : le premier concerne les effets découlant des théories du milieu effectif, à savoir l'influence de l'interaction dipôle-dipôle à une forte concentration des particules, et l'interaction de la charge virtuelle en présence d'une interface substrat/matrice. Il touche également les effets qui ne sont pas prévus par la théorie du milieu effectif, à savoir l'observation du début du retard

de phase et de la dispersion.

Le second partie porte sur la dépendance de la taille des particules des constantes optiques de l'or. La microstructure idéale, combinée à des mesures ellipsométriques précises ainsi qu'à mesures photométriques, a permis d'observer plusieurs effets importants qui apparaissent à mesure que la taille des particules diminue : (*i*) un déplacement de la discontinuité d'absorption interbandes vers les niveaux d'énergie inférieurs, (*ii*) une diminution de la pente de la courbe de discontinuité, (*iii*) un élargissement des caractéristiques dues à la transition entre les différents niveaux dans la bande de conduction et (*iv*) une largeur de la RPS inférieure, pour une particule donnée, à celle qui avait été observée auparavant.

La faible larguer de la RPS est attribuable à une répartition granulométrique étroite des petites particules combinée à une interface métal/diélectrique non réactive. Les essais de quantifier la relation entre la taille des particules et la largeur de la RPS ont abouti à des paramètres d'élargissement de $A = 0.15$ à 0.25, de beaucoup inférieurs à ceux que laissaient présager les modèles classiques et plus semblables, quoique inférieurs, à ceux que prévoyaient les modèles quantiques (Tableau 1.1). La précision de ces valeurs inférieures de A est corroborée par le fait qu'il y a correspondance entre le retard de phase et la dispersion observés et prévus (c.-à-d. à $2R \sim 15 - 20\,\mathrm{nm}$).

Les résultats de cette étude sont pertinents à deux égards : tout d'abord, du point de vue de la caractérisation des effets de taille limitée dans le cas d'une spectroscopie nonintrusive, comparativement à des méthodes plus intrusives, en particulier la microscopie électronique en transmission et la spectroscopie des photoélectrons par rayons X. L'autre aspect est celui des applications actuelles et éventuelles des couches nanocomposites. En ce qui concerne la catalyse hétérogène, la dépendance de la taille des particules et du matériau de support des propriétés électroniques est essentielle pour mieux comprendre l'augmentation de l'activité inhérente aux systèmes de petites particules. Quant aux matériaux nonlinéaires utilisés en télécommunications, la capacité d'intégrer un matériel nanocomposite dans une couche mince qui adhère à

une microstructure, comme le prévoient les modèles du milieu effectif, est essentielle en ce qui concerne l'optimisation du facteur d'amélioration du champ local et, par conséquent, le rendement du dispositif. Pour ce qui est de la nanoélectronique, le fait qu'il y ait un transfert de charge à travers l'interface particule/diélectrique, ainsi que le donnent à penser certaines expériences, laisse entrevoir la possibilité de manipuler la densité des électrons, ce qui est habituellement réservé aux semi-conducteurs, et d'imaginer toute une gamme d'applications éventuelles. Par exemple, on pourrait fort bien imaginer de fabriquer des transistors qui réagissent à la charge d'un seul électron en tablant sur la très faible capacitance de la jonction particule/matrice.

Contents

List of Figures

List of Tables

List of Symbols and Abbreviations

Abbreviations

CBE	Core-level binding energy
C-M	Clausius-Mossotti
CID	Chemical interface damping
DOS	Density of states
EMA	Effective medium approximation
EMT	Effective medium theory
ESCA	Electron spectroscopy for chemical analysis
EXAFS	Extended X-ray fine structure spectroscopy
FC	Fluorocarbon
FWHM	Full-width-half-maximum
HRTEM	High resolution transmission electron microscopy
ITO	Indium tin oxide
K-K	Kramers-Kronig
LDA	Local density approximation
LMFP	Limited mean free path
M-G	Maxwell-Garnett
MS	Magnetron sputtering
MW	Microwave
PECVD	Plasma enhanced chemical vapour deposition

PPFC	Plasma polymerized fluorocarbon
QM	Quasi-melting
QSA	Quasi-static approximation
QSE	Quantum size effect
QSL	Quasi-static limit
RF	Radio frequency
RPA	Random phase approximation
SP	Surface plasmon
SPR	Surface plasmon resonance
S/V	Surface to volume ratio
TDLDA	Time-dependent local density approximation
TEM	Transmission electron microscopy
VASE	Variable-angle spectroscopic ellipsometry
XPS	X-ray photoelectron spectroscopy
XRD	X-ray diffraction

Symbols – Greek

α	Absorption coefficient
$\tilde{\alpha}$	Total extinction coefficient
$\hat{\alpha}$	Polarizability
β_u	Urbach absorption parameter
γ	Ellipsoid axial ratio
γ_u	Urbach absorption parameter
Γ	Effective electron collision frequency
δ	Phase of electromagnetic wave
$\hat{\delta}$	Conduction electron spill-out parameter: spherical geometry
δ_{core}	Deviation in ϵ_{core} form bulk value

Δ	Ellipsometric angle
ϵ	Complex dielectric function or permittivity
$\epsilon_{\perp}$	Complex dielectric function perpendicular to film plane
$\epsilon_{\parallel}$	Complex dielectric function parallel to film plane
ϵ_o	Permittivity of free space
ϵ_{core}	Inter-band contribution to metal dielectric function
$\Re[\epsilon_{core}]$	Real part of ϵ_{core}
$\Im[\epsilon_{core}]$	Imaginary part of ϵ_{core}
ϵ_{Drude}	Intra-band contribution to metal dielectric function
ϵ_{eff}	Effective dielectric function
ϵ_h	Matrix dielectric function
ϵ_m	Metal dielectric function
$\Re[\epsilon_m]$	Real part of ϵ_m
$\Im[\epsilon_m]$	Imaginary part of ϵ_m
ϵ_s	Substrate dielectric function
ζ	Inter-particle spacing
η	Distance between particle dipole moment and its image charge
2θ	Bragg reflection angle
$\hat{\theta}$	Si-O-Si bond angle
κ	Compressibility coefficient
λ	Wavelength
ν_F	Fermi velocity
ρ	Density
$\tilde{\rho}$	Complex amplitude attenuation ratio
σ	Standard deviation
σ_s	Surface tension coefficient
τ_B	Bulk contribution to conduction electron relaxation constant
ϕ_1	Angle of incidence

ϕ_2	Angle of refraction
ϕ_B	Brewster angle
χ_m^3	Third-order non-linear susceptibility of metal
χ_{eff}^3	Effective third-order non-linear susceptibility
Ψ	Ellipsometric angle
ω	Radial frequency
ω_o	Inter-band onset frequency
ω_M	Mie frequency
ω_p	Plasma frequency
ω_{sp}	Surface plasmon resonance frequency
$\sum$	Self-energy

Symbols – Roman (Lower case)

a	Ellipsoid semi-axis perpendicular to film plane
$\hat{a}$	Lattice constant
a_o	Bohr radius
b	Ellipsoid semi-axis perpendicular to film plane
c	Ellipsoid semi-axis perpendicular to film plane
d	Film thickness
d_F	Feibelmann parameter or spill-out parameter: planar geometry
e	Charge on electron
g	Surface stress coefficient
k	Extinction coefficient
$< k >$	Pseudo-extinction coefficient
$\mathbf{k}$	Vacuum wave vector
k_F	Fermi momentum
k_u	Urbach absorption parameter

l	Multi-pole order
m_e	Electron mass
n	Absolute index of refraction
$< n >$	Pseudo-index of refraction
n_+	Ion core charge
n_e	Electron density
δn_e	Induced electron density
p	Metal volume fraction
$\hat{p}$	Polarization in the plane of incidence
$\mathbf{p}$	Dipole moment
r^j	Fresnel reflection coefficients
$\mathbf{r}$	Spatial coordinate
r_s	Wigner-Seitz electron density parameter
$\hat{s}$	Polarization perpendicular to the plane of incidence
t^j	Fresnel transmission coefficients
x	Non-overlap between conduction and d-electrons

Symbols – Roman (Upper case)

A	Surface plasmon resonance broadening parameter
A_T	Cross-sectional area of particle
A_c	Cauchy dispersion parameter
B_c	Cauchy dispersion parameter
C_c	Cauchy dispersion parameter
C_{abs}	Single particle absorption cross-section
C_{ext}	Single particle extinction cross-section
C_{sca}	Single particle scattering cross-section
$\mathbf{D}$	Electric displacement

$C_{\perp,\parallel}$	Lattice structure parameters
$\mathbf{E}$	Electric field vector
E	Electric field amplitude
E_F	Fermi energy of metal
$\mathbf{E}_{loc}$	Local electric field vector
F	Effective depolarization factor
L	Depolarization factor
N	Complex index of refraction
N_v	Number of particles per unit volume
N_p	Number of particles
$\mathbf{P}$	Dipole moment per unit volume
P	Working gas pressure
P_θ	Azimuthal angle
R	Particle radius
R^j	Reflectance
S	Particle surface area
T^j	Transmittance
T_m	Melting temperature
U_b	Applied bias
U_B	Self-bias potential
U_p	Plasma potential
V_p	Particle volume

Introduction

From a classical electrodynamic point of view, a metal particle is, in essence, a bounded electron gas. The most fascinating aspect in this respect is that the particles can support natural oscillations in the electron density at their surface, so-called surface plasmons, SPs. Unlike their plane surface counterpart, which can only be excited optically through surface modification (surface roughness, diffraction grating grooves) or using evanescent waves (attenuated total reflection), the spherical confinement of the electrons in particles allows direct coupling of the SPs to photons.[1]

This coupling produces dips in transmission spectra corresponding to the excitation of different modes of oscillation of the electrons, the dipole mode being the so-called surface plasmon resonance, SPR. Faraday[2] in 1857 was the first to note the brilliant colours exhibited by metal particles and Wood[3] in 1902 was the first to associate these colours with a new resonant absorption mechanism at work in the particles. Models describing the optical response of metal particles quickly followed: Maxwell-Garnett[4] in 1904 and Mie[5] in 1908, the former considering the particles as polarizable points within the quasi-static approximation, the latter solving Maxwell's equation for the scattering and absorption of light by a spherical particle of arbitrary size. Both of these models are general in that the dielectric constant of the metal is incorporated simply as an input parameter.

From a quantum mechanical point of view, a metal particle is a many electron system confined in a spherically symmetric potential which automatically gives rise to a spherical shell structure in which the electrons successively fill the degenerate energy

levels. The idea that the conduction band in metal particles is split into discrete levels (the so-called quantum size effect, QSE) was first proposed by Fröhlich[6] in 1937 and a theoretical model based on a statistical description of the level spacing was introduced in 1962 by Kubo.[7] The currently accepted model of the electronic structure of the conduction electrons in metal particles was developed by Ekardt[8] in 1984 in which the electrons are described within the density functional formalism and the ionic core structure as a uniform positive background within the jellium approximation. The shell structure predicted by this latter model has been repeatedly observed[9] in mass-abundance spectra of free cluster beams. (The particles in the cluster beam are analyzed in a mass spectrometer, and the expected drops in mass-abundance spectra after each shell closing due to the instability of open-shell clusters are observed.)

From a thermodynamic point of view, the most intriguing aspect of metal particles is the role of the surface in determining the minimum energy structure. Recent high resolution transmission electron microscopy (HRTEM) studies[10] have revealed a series of structural phase transitions that occur in small metal particles with decreasing size, in particular, the transition from FCC type single crystals to multiply twinned particles (MTPs), followed by a region of instability consisting of rapid structural transformations between different crystal geometries (so-called quasi-melting, QM), and the eventual melting of the particle at temperatures below the bulk point.

The basic rationale[11] behind the transition to MTPs, which are compact structures based upon packing of tetrahedra of different symmetries (i.e. icosahedral, decahedral), is that they have total lower surface energy compared to simple single crystals because of more low energy (111) faces. The transformation to MTPs comes at the expense of internal strain, the energy cost of which is outweighed by the net gain in surface energy for smaller particles. The basic rationale[12] behind the depression of the thermodynamic melting point lies in the fact that small particles have a higher proportion of surface atoms, atoms which have fewer nearest neighbours and are thus more weakly bound and less constrained in their thermal motion.

The structural transformations that take place in small particles also have implications concerning the electronic structure of both core and conduction electrons. Changes in the lattice parameter induced by MTP formation or, in general, by surface stress, will affect the electronic band structure of the metal.[13,14] Increasing disorder and full-fledged melting will affect changes in the electron-phonon interaction and in the nature of optical excitations, from direct inter-band transitions with conservation of energy and crystal momentum, to local, or nondirect transitions, with only energy conservation being important.[15] The increasing number of surface atoms, distinct in their electronic structure compared to volume atoms by virtue of their reduced coordination,[16,17] will also affect the overall electronic response of the particle.

Aside from the purely academic interest arising from the rich variety of physical phenomena described above, metal particles are also of interest due to their current and potential technological importance. The most obvious optical application concerns their spectrally selective properties. The ability to tailor the optical response depending on the embedding material, the metal, and the size, shape, concentration and state of coagulation of the particles has led to such applications as:[18] decorative glasses, selective solar absorbers for photothermal conversion of solar energy, foils for radiative cooling, coatings for energy efficient windows, and coatings for infrared furtivity.

A more recent optical application relevant to the telecommunications industry concerns the intrinsic third-order susceptibility (χ_m^3) of metal particles.[19,20] The SP-induced local field enhancement of the already large χ_m^3 values yields effective third-order susceptibilities of metal/dielectric composites (χ_{eff}^3) which appear to be sufficient to construct photonic devices for optical switching and computing.[21] The major hurdle to overcome prior to the deployment of such devices is the high absorption coefficient (α) inherent to the resonant optical nonlinearity. In particular, the figure of merit α/χ_{eff}^3 needs to be minimized to allow sufficient transmission in a waveguiding device for signal detection, while at the same time, sufficient nonlin-

earity to allow switching. One potential solution to the α/χ^3_{eff} bottle-neck is the use of non-spherical particles combined with a nonlinear embedding material.[22,23] In an alternative approach, the local field effects are utilized to enhance the response of nonlinear chromophores attached to the particle surface.[24,25]

The most important non-optical application of metal clusters has been in the field of heterogeneous catalysis where particles are deposited on a supporting substrate and exposed to a reactant gas. The striking, and as yet not understood,[26] difference in catalytic behaviour between metal films and particles is exemplified by gold: In the bulk form, gold shows strong affinity only for sulfur and sulfur containing compounds, whereas particles exhibit extraordinary catalytic combustion, partial oxidation of hydrocarbons, hydrogenation of unsaturated hydrocarbons, reduction of nitrogen oxides, and photocatalytic production of hydrogen.[26,27] One clue to the origin of the enhanced catalytic activity might be its strong dependence on the type of support,[28] usually a metal oxide (Al_2O_3, Co_3O_4, Fe_2O_3, SiO_2, TiO_2).

More exotic applications related to nanoscale electronics are based on the ability to control the charge in the particles, a possibility suggested by X-ray photoelectron spectroscopy (XPS) studies[29] and optical spectroscopy[30-32]. A particular example of charge control is the Coulomb blockade[33] where one has observed discrete electron charging of metal particles arising from tunneling across ultralow capacitance ($C < 10^{-16}$F) junctions. The change in electric potential when an electron tunnels across the dielectric/metal junction is large enough to impede the next electron from tunneling. The blockade can be overcome through sequential $(2n + 1)e/2C$ increases in voltage, incrementally charging the particle by single electrons, producing a junction with a straircase current-voltage curve.

The present study concerns the optical properties of metal/dielectric nanocomposite materials in a thin film format. On one hand, it consists of the development of a characterization methodology that allows extraction of the detailed microstructural characteristics of the film based entirely on optical methods (e.g. without the

need to resort to additional methods such as TEM, QCM, profilometry, etc.). Such a characterization methodology is relevant to the development of nanocomposite thin film applications with regard to both a better understanding of the physics involved, and from an optimization perspective.

On the other hand, it consists of the characterization of the physical phenomena arising from the finite size of the particles, in particular, the role of the surface in determining the structural and electronic properties by virtue of their influence on the optical properties. As such, it is a complement to other (more invasive) characterization techniques used to study the properties of small particles, most notably HRTEM[10] and photoemission spectroscopy,[34,35] as well as other standard (i.e. extended X-ray absorption fine-structure (EXAFS) spectroscopy,[36] electron diffraction,[37] X-ray diffraction (XRD)[38]) and more novel (field-ion microscopy,[39] variable energy positron spectroscopy,[40] scanning probe microscopy[41]) techniques. It is also complementary to other optical characterization methods that have recently been applied to the study of metal particles, in particular, femtosecond transient absorption spectroscopy[42] and scanning near-field optical microscopy.[43]

The utility of optical spectroscopy to characterize metal/dielectric nanocomposites lies in the excitation of SPs, and their inherent sensitivity to both microstructure and finite size effects. The plausibility is provided by the use of parametric models to describe the optical response of both the metal (i.e. Drude[44]) and the dielectric (i.e. Cauchy dispersion/Urbach absorption[45]), as well as their response when combined to form an effective medium (i.e. Maxwell-Garnett[4]). Applying these models to optical spectra through fitting of the relevant parameters is made possible by using both ellipsometric and photometric data. The sensitivity of ellipsometric measurements to the optical constants of materials, especially in the case of a thin film deposited on a substrate having a similar index of refraction, is essential in finding the global minimum during the fitting procedure. Including photometric data allows the collection of all the information contained in the reflected/transmitted light beam, and is

essential in reducing parameter correlations during fitting.

To make the characterization tractable requires a film microstructure that can be described using an effective medium model as simple as possible. The greatest concern in this respect is the structure of the metal/dielectric interface: (*i*) is it homogeneous or does it consist of the metal surface, dielectric grain boundaries, and inter-dispersed voids? and (*ii*) is it abrupt or has a reaction between the metal and dielectric led to the formation of an 'interphase'? The former concern is minimized by use of PECVD coatings as embedding materials. The compact and amorphous structure inherent to PECVD films[46] should not only minimize void content at the metal/dielectric interface, but also approach the ideal of a structureless host material assumed in the Maxwell-Garnett model.[4]

The concern of a metal/dielectric reaction is minimized by using the inert metal gold as the embedded particles. The use of a noble metal also increases the sensitivity of the optical response to finite size-induced structural and electronic changes due to the presence of a filled d-band. (The optical response of alkali metals, for example, is little affected by changes in the core, as evidenced by the agreement with the response predicted by the classical Drude model which only considers the conduction electron response.[44]) Of the three noble metals, gold is exceptional in that the inter-band transition edge coincides with the SPR for a low index embedding material. (For Ag, the transition edge is at higher energy, while for Cu, it is at lower energy compared to that of the SPR.[47])

This thesis is comprised of two introductory chapters and five articles. The first chapter describes in detail the classical electrodynamic optical response of a collection of metal particles. Emphasis is placed on an optical model based on the Maxwell-Garnett effective medium in combination with the Drude description of metals. The influence of finite size and matrix effects on the optical response are also included, and the models that exist to account for these effects are described. The second chapter outlines the experimental methodolgy, in particular, how the films are prepared, how

and what optical measurements are made, and how parametric modeling applied to the measured optical data can be used to determine the optical constants of materials and to extract relevant microstructural parameters.

The first article deals with gold particles embedded in a PPFC matrix. The ability to extract microstructural parameters using the Maxwell-Garnett model applied to the optical spectra is demonstrated, and emphasis is placed on the dependence of the film microstructure on glow discharge parameters and post-deposition thermal treatments. The model limitations with respect to the minimum particle size and maximum metal volume fraction are identified, the former limit attributed to the classical description of the conduction electron response, and the latter due to particle coagulation effects.

The second article concerns gold particles embedded in SiO_2 matrices. The SiO_2 matrix differs from the PPFC in two major respects: (*i*) it is thermally more stable and (*ii*) the absorption edge is at higher energy. The former allows post-deposition thermal treatments to be carried-out at much higher temperatures, so that liquid-like coalescence is not restricted to very small particles. As such, particle growth, not coagulation, is observed, allowing identification of the large particle limit of the Maxwell-Garnett model. The lack of matrix absorption in the uv allows a clearer view of the gold core response. The observed particle size dependence of the core response is identified as a contributing factor to the small particle limit of the model.

The third article is a short letter which addresses the particle size dependence of the core response. A correspondence is observed between spectra measured as a function of particle size and spectra measured as a function of temperature. This correspondence suggests that the disappearance of long range-order that occurs upon transition to the liquid state is responsable for the observed changes in the core response in particles.

The fourth article applies the characterization methodology developed for 3-D films to discontinuous 2-D films consisting of substrate-supported particles. This

format allows a direct comparison between the optical spectra and TEM images of the same samples, a luxury that outweighs the added complexity involved in modeling the optical response of a 2-D array of particles and that allows the shift and broadening of the SPR with particle size to be quantified. This article also demonstrates the influence of image charges on the optical response by using different arrangements of dielectric/discontinuous film/dielectric structures with dielectrics SiO_2, TiO_2, and 'void'.

The last article concerns the morphological changes that occur in discontinuous films with post-deposition thermal treatments. These changes, obvious from optical spectroscopy, are used to clarify core-level binding energy shifts observed from XPS measurements. This article also demonstrates the possibility of charge transfer between the particles and the substrate, and how this charge transfer affects both the optical and the core-level spectra.

Chapter 1

Optical Properties of Metal Particles

1.1 Introduction

Studies of the optical properties of metal particles date back to Faraday in 1857[2] who associated the brilliant colours exhibited by very thin gold films to their discontinuous nature. The extraordinary spectral response arises from the excitation of plasmon polaritons (resonant coupling of the incident field with quanta of collective conduction electron plasma oscillations) with resonant energies across the uv-visible spectrum. The full electrodynamic boundary problem was solved by Mie in 1908[5] and is equivalent to the Fresnel equations for spherical geometry. It is a general solution: it gives the total extinction (i.e. both absorption and scattering) due to polariton states (i.e. modes of oscillation) of arbitrary multipole order.

The Mie theory is only exact for a single particle, and is, thus, restricted to very dilute concentrations where the particles act as independent scattering centres and there is no multiple scattering. An alternative to the exact electrodynamic solution was proposed by Maxwell-Garnett in 1904[4] where the optical properties of the metal particles are calculated by considering an effective medium consisting of the particles and the surrounding medium. Being an electrostatic solution, it is applicable to particles with sizes such that the field of the incident light is constant across the particle

(i.e. $<< \lambda$). The Maxwell-Garnett theory is nothing more than the Clausius-Mosotti relation (or, as it is known in optics, the Lorentz-Lorenz relation), calculated using the polarizability of a sphere. It therefore includes the interaction between particles within the framework of local field effects. This extends the range of applicability to particles in much higher concentration than is allowed by the Mie theory.

The optical response of the metal is incorporated in these optical models only as an input parameter. As such, any discrepancies between the measured and modeled response can be traced to a particle size dependence of the optical constants of the metal, so-called finite size effects. Such a dependence is expected from the simple fact that the solid-state description of the optical response of a metal particle must converge, in the small particle limit (i.e. one atom), with the atomic response.

All the modeling in this thesis is performed within the framework of the Maxwell-Garnett theory. However, to stress the limitations of the model with respect to the particle size, a brief outline of the Mie theory is included (Section 1.2). The extinction spectra for particles of arbitrary size is presented, with additional calculations made in the quasi-static limit in which only the dipolar mode is excited. The factors influencing the resonance energy and width of this mode are discussed. In section 1.3, the Maxwell-Garnett (Clausius-Mosotti) equation is derived, and the influence on the dipolar resonance due to particle interaction is shown. This section also includes a discussion of the dependence of the optical response on the detailed mirco-geometry of the particles. In Section 1.4, the recent advances in the understanding of finite size effects are presented. How these different effects are expected to affect the optical response is demonstrated. Finally, a brief discussion on the influence of the matrix material is included in Section 1.5.

1.2 Mie Theory

In this section, the Mie equations[5] describing the total extinction cross-section of a collection of spherical particles of arbitrary size are presented. A detailed outline of their derivation can be found in the review article by Perenboom *et al*,[48] or the book by Kreibig and Vollmer[47] and a complete solution is given in the book by van de Hulst.[49] The extinction spectra as a function of particle size are given in Section 1.2.1 for a typical Drude free electron metal. The simplification of the Mie equations in the small particle limit is presented in Section 1.2.2. Within this limit, the explicit dependence of the optical response on the dielectric function of the embedding matrix and on the type of metal (i.e. alkali versus noble) is demonstrated.

1.2.1 Particles of Arbitrary Size

The Mie theory consists of solving for the extinction of an incident beam, $I(z) = I_o e^{-\tilde{\alpha} z}$, after passing a distance z through a material containing a volume fraction, or filling, p, of scattering centres. The total extinction coefficient, $\tilde{\alpha}$, in the limit of independent scattering centres is given by the extinction by a single particle, C_{ext}, times the filling:

$$\tilde{\alpha} = pC_{ext} = p[C_{abs} + C_{sca}], \tag{1.1}$$

where the extinction by each particle consists of an absorption term, C_{abs}, and a scattering term, C_{sca}. The extinction and scattering by each particle is given by

$$C_{ext} = -\frac{2\pi}{\epsilon_h k^2} \sum_{l=1}^{\infty} (2l+1) \Re[a_l + b_l], \tag{1.2}$$

$$C_{sca} = \frac{2\pi}{\epsilon_h k^2} \sum_{l=1}^{\infty} (2l+1) [\mid a_l \mid^2 + \mid b_l \mid^2], \tag{1.3}$$

where $k = 2\pi/\lambda$ is the vacuum wavevector, ϵ_h is the dielectric function of the embedding material, l is the multipole order, and a_l and b_l are the Mie coefficients for the lth multipole:

$$a_l = -\frac{\epsilon_m \psi_l(\epsilon_m x)\psi_l'(\epsilon_h x) - \epsilon_h \psi_l'(\epsilon_m x)\psi_l(\epsilon_h x)}{\epsilon_m \psi_l(\epsilon_m x)\eta_l'(\epsilon_h x) - \epsilon_h \psi_l'(\epsilon_m x)\eta_l(\epsilon_h x)}, \tag{1.4}$$

$$b_l = -\frac{\epsilon_h \psi_l(\epsilon_m x)\psi_l'(\epsilon_h x) - \epsilon_m \psi_l'(\epsilon_m x)\psi_l(\epsilon_h x)}{\epsilon_h \psi_l(\epsilon_m x)\eta_l'(\epsilon_h x) - \epsilon_m \psi_l'(\epsilon_m x)\eta_l(\epsilon_h x)}, \tag{1.5}$$

where $x = kR$, R being the particle radius. ϵ_m is the dielectric function of the metal and ψ_l and η_l are Ricatti-Bessel functions for spherical geometry.

Calculation of the extinction cross-section requires as input parameters ϵ_h and ϵ_m. Concerning the metal dielectric function, the Drude theory for free electron (intraband) absorption can be used:[44]

$$\epsilon_m = 1 - \frac{\omega_p^2}{\omega(\omega + i/\tau_B)}, \tag{1.6}$$

where $\omega_p^2 = n_e e^2/\epsilon_o m_e$ is the bulk plasma frequency and τ_B is the free electron relaxation constant. The alkali metals (Li, Na, K, ...) are well described by the Drude model since the optical response is dominated by conduction (s-band) electrons. For demonstrative purposes, ϵ_m corresponding to sodium, for which[44] $\omega_p^2 = 5.7\,\mathrm{eV}^2$ and $\tau_B = 3.2 \times 10^{-14}$ seconds, shall be used since the experimental dielectric function agrees within 4% with that predicted by Eq. 1.6.[50]

The extinction cross-section for Na particles in vacuum ($\epsilon_h = 1$) as a function of R is shown in Fig. 1.1(a). For the smallest sizes ($R < 20\,\mathrm{nm}$), only the dipolar mode is excited. This mode is shifted to longer wavelengths (red-shifted) as the particle size increases: from $\lambda \sim 400\,\mathrm{nm}$ for $R = 20\,\mathrm{nm}$ to $\lambda \sim 500\,\mathrm{nm}$ for $R = 60\,\mathrm{nm}$ to $\lambda \sim 650\,\mathrm{nm}$ for $R = 100\,\mathrm{nm}$. This shift is due to the increasing variation of the incident field across the particle (i.e. phase retardation). With increasing R, one also

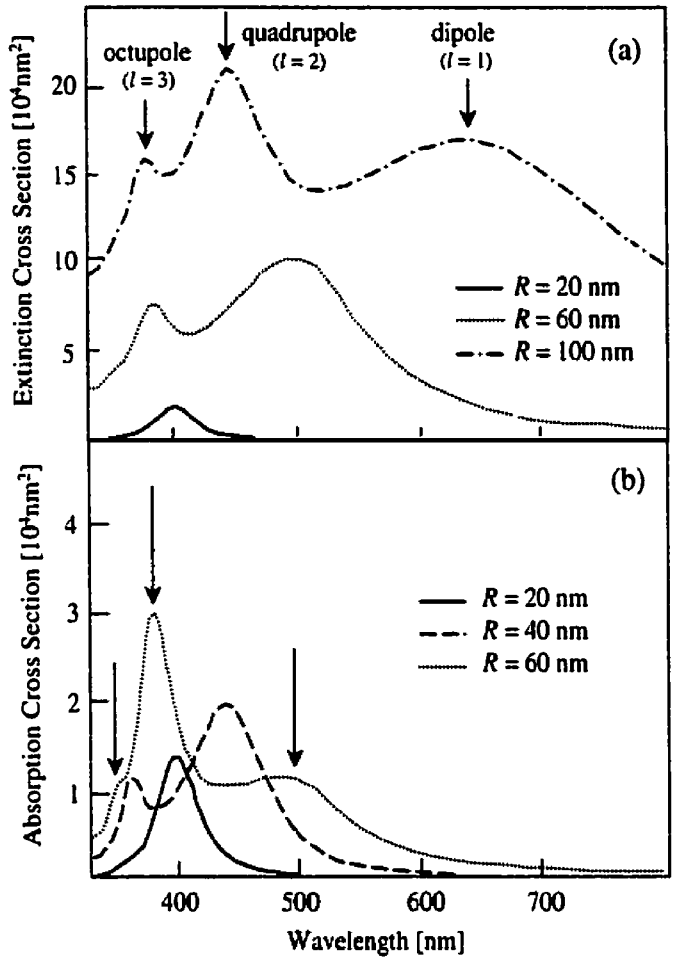

Figure 1.1: Mie (a) total extinction and (b) absorption cross sections for Na particles in vacuum as a function of size (adapted from Ref. [47]).

observes the apprearance of higher order excitations at higher energy: the quadrupole mode is fully visible at $\lambda \sim 380\,\text{nm}$ for $R = 60\,\text{nm}$ and the octupole mode is fully visible at $\lambda \sim 375\,\text{nm}$ for $R = 100\,\text{nm}$. These modes will be similarly red-shifted with increasing R.

As well as being shifted, all modes will be broadened as R increases. This is due, in part, to phase retardation, and, in part, to scattering. The latter is evident from the absorption cross-section shown in Fig. 1.1(b) obtained by subtracting Eq. 1.3 from Eq. 1.2. For example, the absorption cross-sections for $R = 60\,\text{nm}$ shows three distinct

peaks correpsonding to $l = 1, 2, 3$, while in the extinction cross-section, the dipole and quadropole modes are severly broadened and the octupole mode is completely washed out.

1.2.2 Quasi-static Limit

The optical response is drastically simplified for $\lambda/2R > 10$ as a consequence of (i) negligible scattering, (ii) negligible phase retardation, and (iii) excitation of only the dipolar mode. (I will adopt the convention in the literature and refer to this excitation simply as the surface plasmon resonance). In this small particle, long wavelength limit, or quasi-static limit (QSL), the Mie extinction reduces to simple absorption given by:

$$\alpha(\omega) = 9\frac{\omega}{c}p\epsilon_h^{3/2}\frac{\Im[\epsilon_m]}{[\Re[\epsilon_m] + 2\epsilon_h]^2 + \Im[\epsilon_m]^2}. \tag{1.7}$$

Eq. 1.7 describes a lorentzian absorption band resonant for $\Re[\epsilon_m] = 2\epsilon_h$, damped by $\Im[\epsilon_m]$. For ϵ_m given by Eq. 1.6, the resonant frequency occurs at $\omega_M = \omega_p/\sqrt{\epsilon_h + 2}$ while the width is determined by τ_B.

The simplified response in the QSL can be used to show the explicit dependence of the SPR on the host matrix and on the type of metal. The dependence on the matrix material (i.e. the red-shift of the resonance with increasing ϵ_h), which arises from the screening of the incident field, is shown in Fig. 1.2(a). Fig. 1.2(b) shows the metal dielectric function (i.e. Eq. 1.6 with parameters relevant to Na) used in the calculation.

The dependence of the SPR on ϵ_m for metals which are well described by the Drude equation arises simply from the dependence of ϵ_m on ω_p and τ_B.[44] In particular, a higher bulk plasma frequency (i.e. a higher electron density, n_e, or lower electron effective mass, m_e) will result in a blue-shifted SPR, while a smaller relaxation constant will reduce the SPR width. More striking is the difference between the SPR of alkali

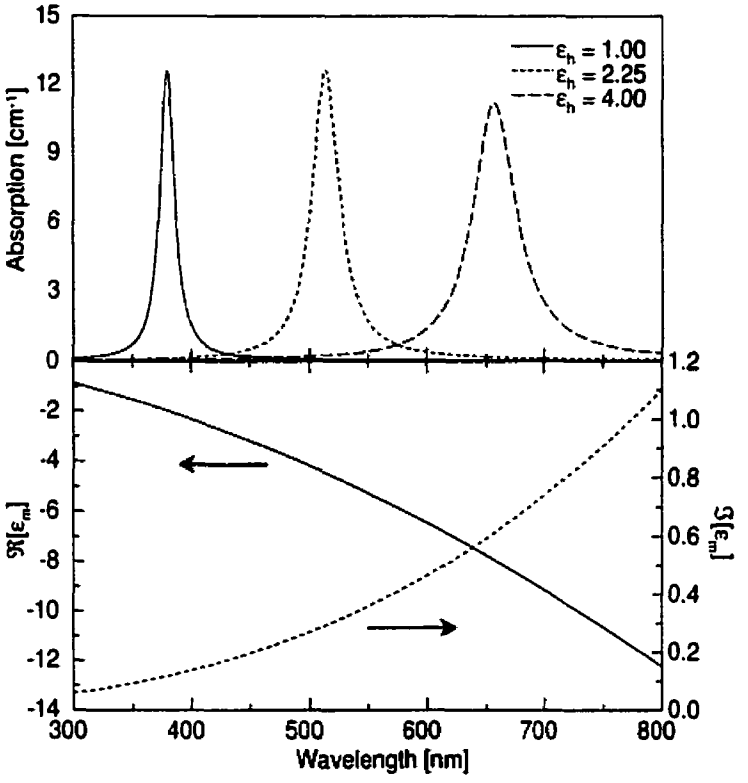

Figure 1.2: (a) SPR of metal particles having a dielectric function given in (b) for different values of ϵ_h. The absorption is calculated with $p = 10^{-4}$ %.

and noble metals. The latter do not adhere well to the response predicted by Eq. 1.6 due to the presence of d-band electrons, absent in the former.[44] To account for the influence of these electrons on the dielectric function of noble metals, an inter-band, or core, response term must be added to the Drude equation :

$$\epsilon_m = \epsilon_{core} + 1 - \frac{\omega_p^2}{\omega(\omega + i/\tau_B)}, \tag{1.8}$$

where $\Re[\epsilon_{core}]$ accounts for the screening by the d-electrons and $\Im[\epsilon_{core}]$ accounts for absorption from inter-band transitions between the d- and s-bands. These are, of course, related through the Kramers-Kronig (KK) relations. The SPR is now located at $\omega_M = \omega_p/\sqrt{\epsilon_h + 2 + \Re[\epsilon_{core}]}$ while the width is given by $\Gamma = 1/\tau_B + \Im[\epsilon_{core}]$.

The influence of the d-band electrons on ϵ_m for the specific case of gold in shown in Fig. 1.3. The polarizabiltiy ($\Re[\epsilon_m]$) is increased by ~ 10 at $\lambda \sim 500\,\text{nm}$ with respect to the Drude equation while inter-band absorption substantially increases $\Im[\epsilon_m]$ for $\lambda < 650\,\text{nm}$, which marks the onset of inter-band transitions.[51] The influence of the d-band electrons on the SPR band are most clearly demonstrated by comparing the spectra obtained with and without core effects. For example, if only the Drude term is considered, the SPR is located at $\lambda \sim 235\,\text{nm}$ (see Fig. 1.3(a)), which is at higher energy compared to Na ($\lambda \sim 385\,\text{nm}$) due to the higher plasma frequency of gold ($\omega_p = 8.9\,\text{eV}$). Including the additional screening provided by the d-electrons ($\Re[\epsilon_{core}]$) results in a dramatic red-shift of the SPR to $\lambda \sim 500\,\text{nm}$. Adding inter-band absorption ($\Im[\epsilon_{core}]$) severly broadens the SPR and markedly increases the asymmetry of the band.

1.3 Effective Medium Theory

In the QSL, two-phase composite materials can be regarded as a homogeneous material possessing an effective dielectric function. This is due to the fact that $\lambda >> R$ and so the incident light does not probe the inhomogeneous microscopic structure, but rather the spatially averaged structure. The effective dielectric function is written in terms of the dielectric functions of the constituents, the exact formulation depending on the assumed microscopic structure. In the small filling limit, these theories reduce to the Mie response in the QSL. However, unlike the Mie theory, they can be applied to higher fillings by using local field corrections to account for the interaction between the dipole fields of the particles.

The two most widely used effective medium theories (EMTs) are the Maxwell-Garnet (M-G) EMT[4] and the Bruggeman EMT,[52] more commonly known simply as the effective medium approximation (EMA). The former is derived assuming a coated sphere microstructure (one of the constituents is in small concentration with

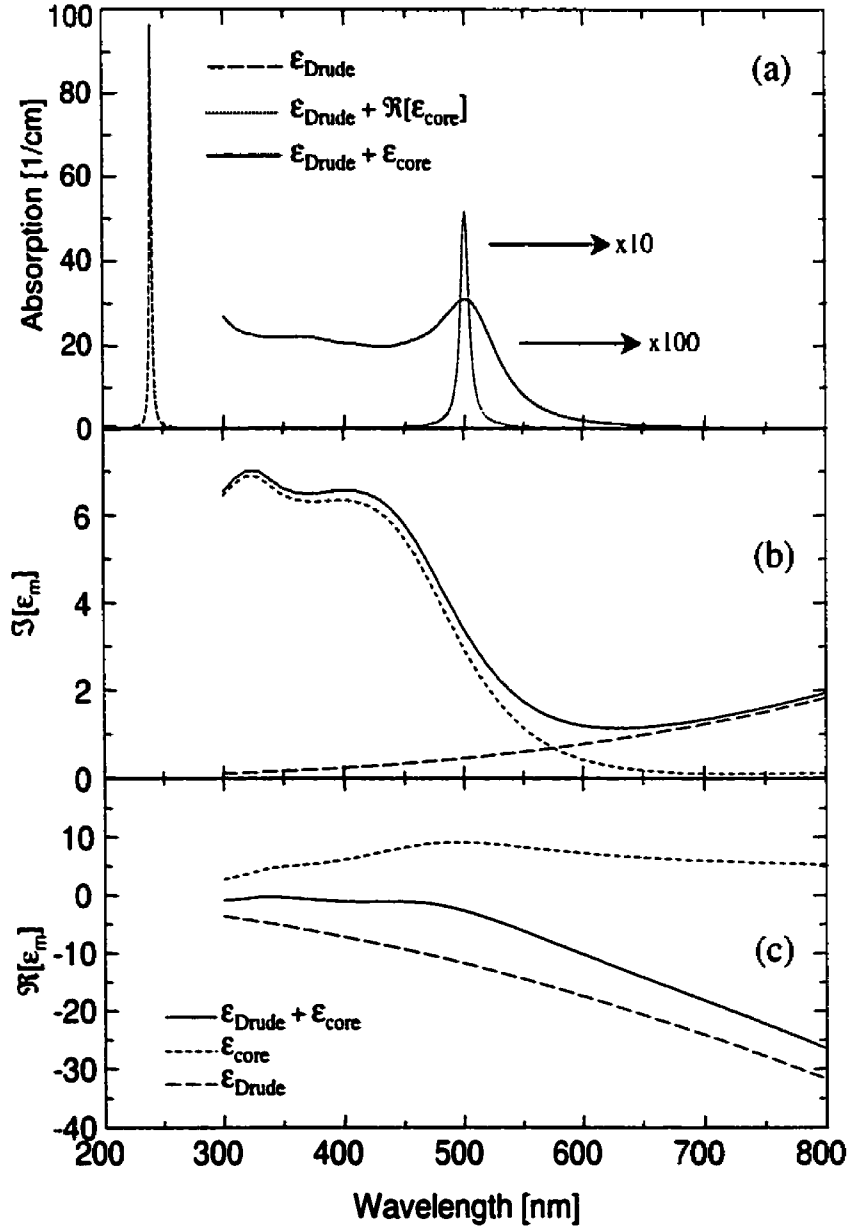

Figure 1.3: (a) The SPR of Au particles for $p = 10^{-4}\,\%$ and $\epsilon_h = 1$ with and without core effects. (b) Imaginary and (c) real parts of the core and Drude ($\omega_p = 8.9\,\text{eV}$, $\tau_B = 5 \times 10^{-14}\,\text{seconds}$) contributions to the dielectric function of gold.

respect to the other, and thus competely surrounded by the other). The EMA, on the other hand, is derived assuming an aggregate microstructure, where both phases are treated on equal footing. An alternative EMT was more recently developed by Ping Sheng[53] which takes into account the dependence of the microstructure on the filling of the inclusions, absent in both the M-G EMT and the EMA, and offers a compromise between the two theories. Detailed discussions concerning the relationship between the film microstructure and the EMTs can be found in articles by Lamb *et al*,[54] Niklasson *et al*,[55] and Aspnes.[56]

The M-G EMT, for which the implied microstructure is equivalent to that assumed in the Mie theory, is used exclusively in this thesis. It is based on the Clausius-Mosotti (C-M) relation derived using electrostatic equations and allows one to relate the macroscopic dielectric function of a material to the microscopic quantities of atomic polarizabilities. The effective dielectric function of a collection of particles follows naturally by incorporating the polarizability of a spherical particle. In Section 1.3.1 a text book[57,58] derivation of the C-M relation (M-G EMT) is presented. The sensitivity of the optical response to the microstructure is also included in Section 1.3.2 where the SPR predicted by the M-G EMT and the EMA are compared. In Section 1.3.3, the extenstion of the M-G EMT to non-spherical particles is presented.

1.3.1 Maxwell-Garnett Effective Medium

Consider a collection of N_v polarizable points per unit volume in vacuum with polarizability $\hat{\alpha}$ and subject to an applied field $\mathbf{E}$. The points may be atoms on a lattice, molecules of a liquid, or small particles. To include the influence of the polarization of nearby points, the dipole moment per point is written as

$$\mathbf{p} = \hat{\alpha}\mathbf{E}_{loc} \tag{1.9}$$

using the local field, $\mathbf{E}_{loc}$, instead of the applied field, $\mathbf{E}$. The local field is generally derived using a fictitious cavity cut out of a uniformly polarized material[57] and is given by:

$$\mathbf{E}_{loc} = \mathbf{E} + \frac{\mathbf{P}}{3\epsilon_o}, \tag{1.10}$$

where $\mathbf{P} = N_v\mathbf{p}$ is the dipole moment per unit volume. Using the definition of the electric displacement:

$$\mathbf{D} = \epsilon_{eff}\epsilon_o\mathbf{E} = \epsilon_o\mathbf{E} + \mathbf{P}, \tag{1.11}$$

one can solve for the effective dielectric function, ϵ_{eff}, of the collection of points in vacuum to obtain the C-M equation:

$$\frac{\epsilon_{eff} - 1}{\epsilon_{eff} + 2} = \frac{N_v\hat{\alpha}}{3\epsilon_o}. \tag{1.12}$$

Alternatively, the polarizable points may, themselves, be surrounded by a polarizable medium with dielectric constant ϵ_h. In this case, the local field must be calculated by removing only the points when cutting out the fictitious cavity, leaving in place the embedding material. This gives a generalized C-M equation:

$$\frac{\epsilon_{eff} - \epsilon_h}{\epsilon_{eff} + 2\epsilon_h} = \frac{N_v\hat{\alpha}}{3\epsilon_o}, \tag{1.13}$$

The polarizability of a spherical particle with dielectric constant ϵ_m embedded in a host material having ϵ_h is given by:[59]

$$\hat{\alpha} = 4\pi\epsilon_o R^3 \frac{\epsilon_m - \epsilon_h}{\epsilon_m + \epsilon_h}. \tag{1.14}$$

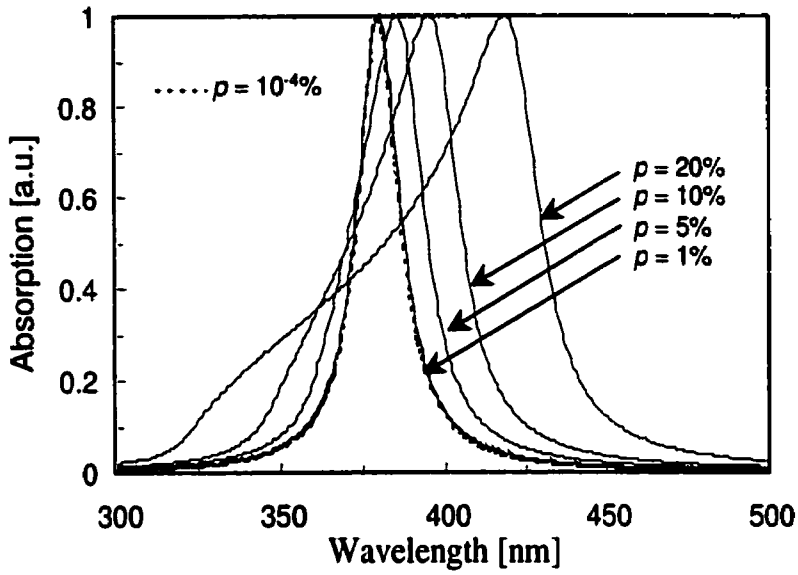

Figure 1.4: The dependence of the SPR on filling according to the M-G EMT for $\epsilon_h = 1$ and ϵ_m corresponding to Na.

Incorporating Eq. 1.14 into Eq. 1.13 defines the M-G effective medium:[4]

$$\frac{\epsilon_{eff} - \epsilon_h}{\epsilon_{eff} + 2\epsilon_h} = p\frac{\epsilon_m - \epsilon_h}{\epsilon_m + 2\epsilon_h}, \tag{1.15}$$

where $p = 4\pi N_v R^3/3$ is the filling.

For very low fillings, Eq. 1.15 reduces to the Mie theory in the quasi-static limit (i.e. Eq. 1.7). At higher fillings ($> 0.1\%$), a red-shift and broadening of the SPR is predicted and is shown in Fig. 1.4 for the Drude metal in Fig. 1.2(b). The asymmetry of the band that develops with increased filling is due to the frequency dependence of $\Im[\epsilon_m]$.

1.3.2 Bruggeman Effective Medium

The M-G EMT implies a coated-sphere microstructure by virtue of the choice of ϵ_h as the embedding material (this was invoked in going from Eq. 1.12 to Eq. 1.13).

To see this more clearly, the inclusions and matrix can be put on equal footing by considering both constituents placed in a third material, ϵ:

$$\frac{\epsilon_{eff}-\epsilon}{\epsilon_{eff}+2\epsilon}=p\frac{\epsilon_m-\epsilon}{\epsilon_m+2\epsilon}+(1-p)\frac{\epsilon_h-\epsilon}{\epsilon_h+2\epsilon}. \tag{1.16}$$

In this form, it is easily demonstrated how the implied microstructure is dictated by the choice of ϵ. For example, if it is assumed that a small concentration of metal inclusions are dispersed in the matrix, then the natural choice is to set $\epsilon=\epsilon_h$, which gives the M-G effective medium, Eq. 1.15. Alternatively, if $p\sim 0.5$, then neither plays the role of the host. In this case, one can choose $\epsilon=\epsilon_{eff}$:

$$0=p\frac{\epsilon_m-\epsilon_{eff}}{\epsilon_m+2\epsilon_{eff}}+(1-p)\frac{\epsilon_h-\epsilon_{eff}}{\epsilon_h+2\epsilon_{eff}}, \tag{1.17}$$

which defines the Bruggeman effective medium. The implied microstructure in this case is that of an aggregate model, where the two constituents are mixed on a random basis.

The sensitivity to microstructure is shown in Fig. 1.5 where the SPR band predicted by the two models are compared for different fillings, using, again, $\epsilon_h=1$ and ϵ_m from Fig. 1.2(b). At 10^{-2}%, the two theories begin to diverge, with the EMA predicting an SPR band having a successively smaller maximum absorption and a larger width with increased filling.

1.3.3 Particle Shape Effects

The influence of the shape of the particle on the SPR band can be incorporated into the M-G EMT by substituting Eq. 1.14 with the expression for the polarizability of an ellipsoid:[49]

$$\hat{\alpha}_j=\epsilon_o V_p\frac{\epsilon_m-\epsilon_h}{\epsilon_h+L_j(\epsilon_m-\epsilon_h)}, \tag{1.18}$$

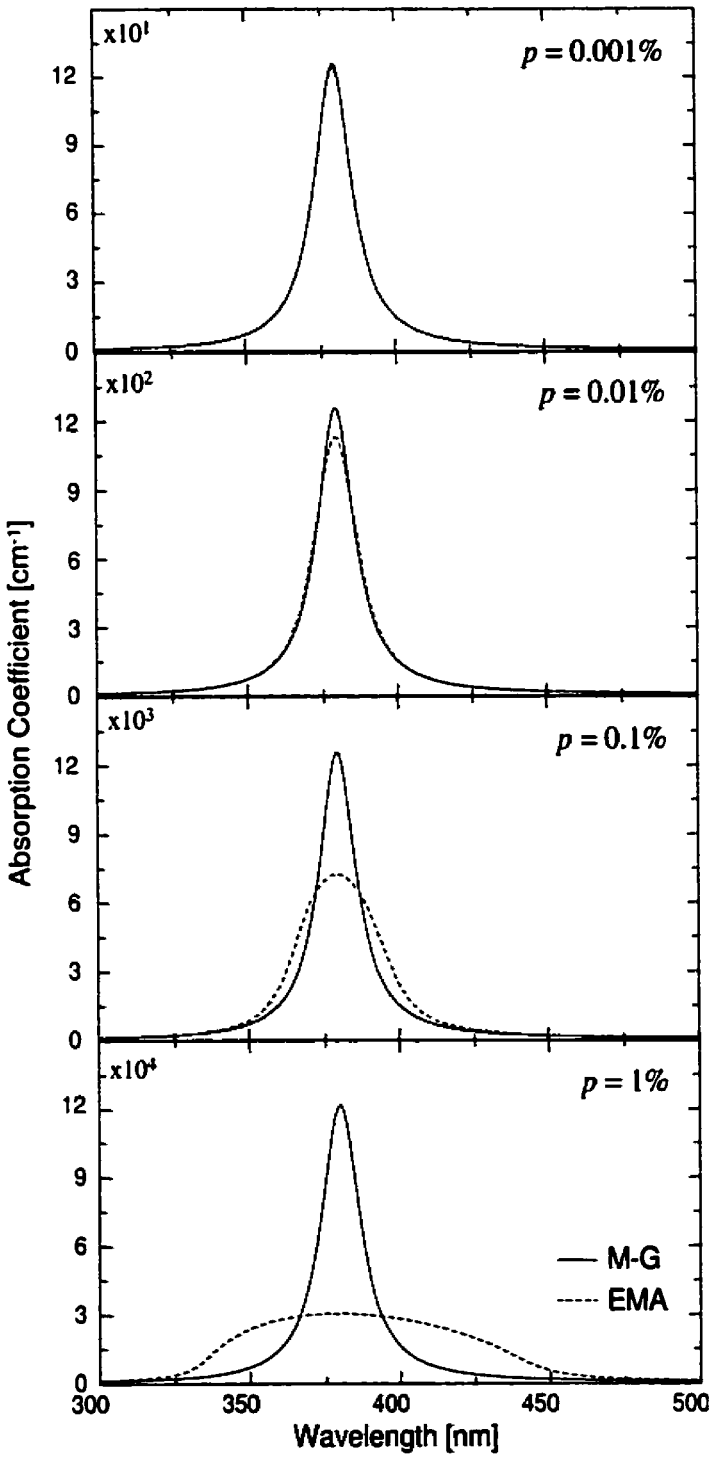

Figure 1.5: Comparison of the SPR predicted by the M-G EMT and the EMA for $\epsilon_h = 1$ and ϵ_m corresponding to Na.

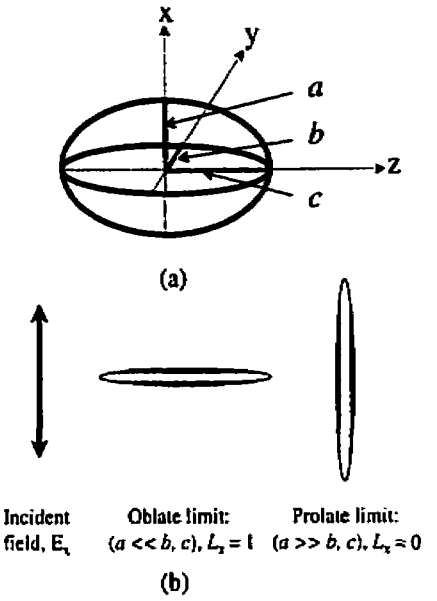

Figure 1.6: (a) Ellipsoid with the major axes alligned to the coordinate system. (b) Oblate and prolate limits with respect to an incident field in the x direction.

where the polarizability is now a tensor and j represents one of the three major axes of the ellipsoid. The L_j's are three depolarization factors which depend on the ratio of the semiaxes of the ellipsoid (a, b and c, see Fig. 1.6(a)) according to:

$$L_x = \int_0^\infty \frac{abc}{2(s+a^2)^{3/2}(s+b^2)^{1/2}(s+c^2)^{1/2}} ds, \tag{1.19}$$

with L_y and L_z obtained by performing cyclical changes. Note $L_x + L_y + L_z = 1$ always holds.

For the special case of spheroids ($b = c$) the above integration reduces to the following simple formulae: For prolate spheroids ($a > b, c$):

$$L_x = \frac{1-e^2}{e^2}\left[\frac{1}{2e}\ln\frac{1+e}{1-e} - 1\right], \tag{1.20}$$

where $e^2 = 1 - (b^2/a^2)$. For oblate spheroids ($a < b, c$):

$$L_x = \frac{1+f^2}{f^2}\left[1 - \frac{1}{f}\arctan(f)\right], \tag{1.21}$$

where $f^2 = (b^2/a^2) - 1$. In the limit of flat elliptical disks ($a << b, c$) one obtains $L_x = 1$ and $L_y = L_z = 0$, while in the limit of long elliptical cylinders ($a >> b, c$), one obtains $L_x = 0$, $L_y = c/(b+c)$ and $L_z = b/(b+c)$.

Using the polarizability of an ellipsoid, Eq. 1.18 instead of Eq. 1.14, the M-G effective medium becomes:[60]

$$\frac{\epsilon^j_{eff} - \epsilon_h}{\epsilon^j_{eff} + 2\epsilon_h} = 3p\frac{\epsilon_m - \epsilon_h}{L_j\epsilon_m + (1 - L_j)\epsilon_h}. \tag{1.22}$$

The superscript j on ϵ_{eff} is used to indicate that the effective dielectric function is now a tensor (i.e. the medium is anisotropic).

Eq. 1.22, however, is inconsistent in the limits of flat disks and long cylinders (see Fig. 1.6(b)). For example, for incident fields parallel to the particle boundaries ($L_j = 0$), Eq. 1.22 should give a simple weighted average of ϵ_m and ϵ_h:

$$\epsilon_{\|} = p_m\epsilon_m + (1 - p_m)\epsilon_h, \tag{1.23}$$

since there is no induced polarization field outside the particle, and, therefore, no modification of the applied field. For incident fields normal to the particle boundaries ($L_j = 1$), Eq. 1.22 should give:

$$\epsilon_{\perp} = [p_m/\epsilon_m + (1 - p_m)/\epsilon_h]^{-1}, \tag{1.24}$$

as in an array of capacitors arranged in series (see, for example, Ref. [56]). Eqs. 1.23 and 1.24 are known as the no screening and maximum screening Wiener bounds,[61] respectively, and occur in any two-phase composite regardless of composition or

microstructure.[56,62]

These inconsistencies arise because the local field calculation (Eq. 1.10) still pertains to a spherical cavity. Cohen *et al*[63] remedied the inconsistencies by calculating the local field using a cavity that is congruent with the shape of the particle:

$$\frac{\epsilon_{eff}^{j} - \epsilon_h}{L_j\epsilon_{eff}^{j} + (1 - L_j)\epsilon_h} = p\frac{\epsilon_m - \epsilon_h}{L_j\epsilon_m + (1 - L_j)\epsilon_h}. \tag{1.25}$$

The absorption spectrum according to Eq. 1.25 for randomly oriented ellipsoids with $L_1 = 0.42, L_2 = 0.33$ and $L_3 = 0.25$ in vacuum is shown in Fig. 1.7(a). The three peak structure results from the dependence of the resonance frequency on the direction in which the collective electron excitations are driven. For example, for the ellipsoids in which the electric field is parallel to the minor axis ($L > 1/3$), the SPR is blue-shifted with respect to the $L = 1/3$ case, while for those in which the field is parallel to the major axis, ($L < 1/3$) it is red-shifted. To see this more clearly, consider alligned spheriods with circular cross-section ($b = c$) and an incident field parallel to a. Increasing a from that which gives a oblate spheriod ($a < b, c$: $L > 1/3$) to that which gives a prolate spheroid ($a < b, c$: $L < 1/3$) results in a shift of the SPR from $\omega_{sp} > \omega_p/\sqrt{3}$ to $\omega_{sp} < \omega_p/\sqrt{3}$, as shown in Fig. 1.7(b). Alternatively, the spheroid orientation can be constant, and p-polarized transmission measurements versus angle of incidence can be used to probe the different axes of the ellipsoid as shown in Fig. 1.7(c).

1.4 Finite Size Effects

For small enough particles, ϵ_m begins to diverge from its bulk (or thin film) value, resulting in a particle size dependence of the energy and width of the SPR, so-called finite size effects. This divergence is anticipated since the dielectric function is a solid state description of the optical properties of the metal, whereas small metal particles

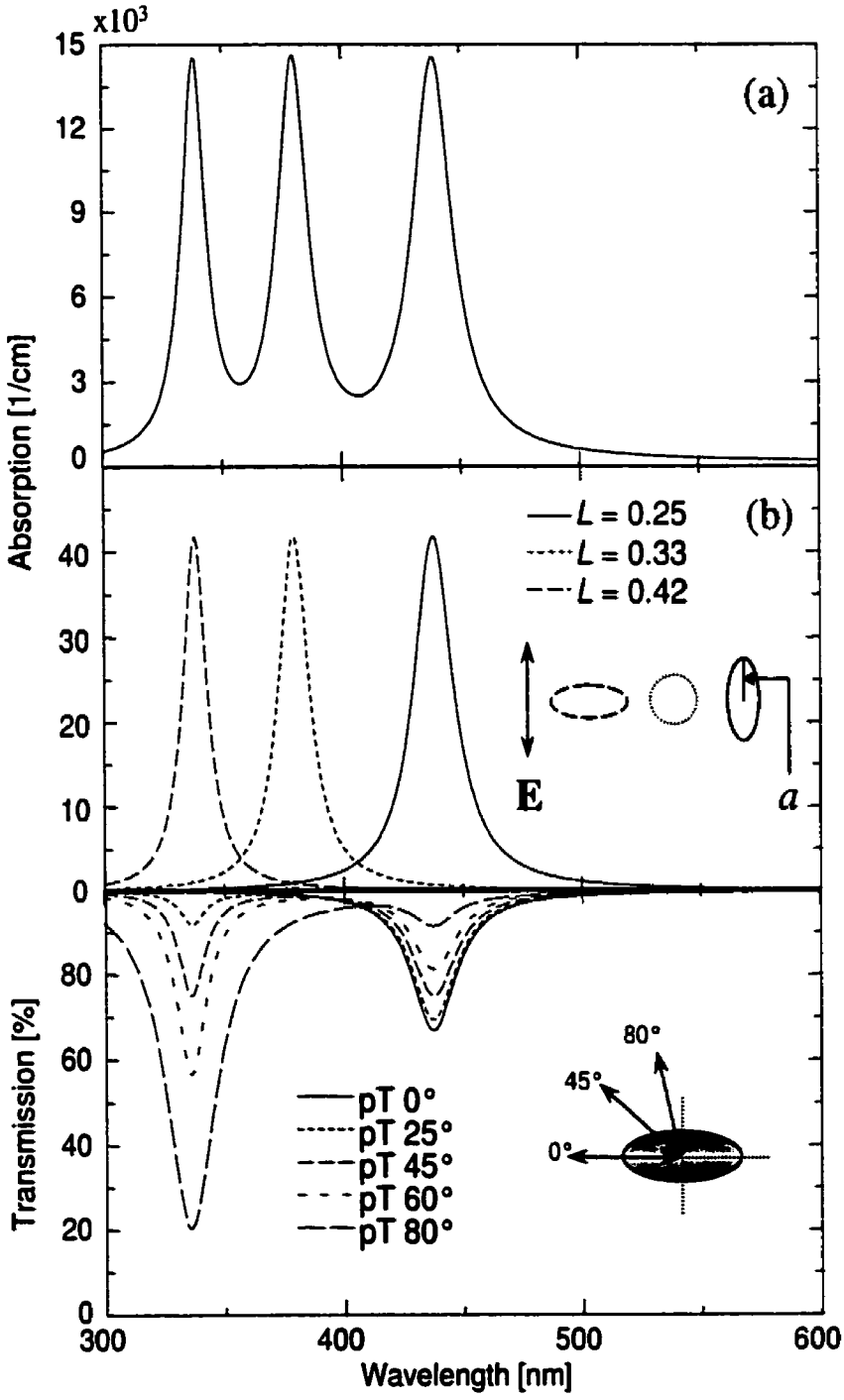

Figure 1.7: Absorption of spheroids with $L_1 = 0.42, L_2 = 0.33$ and $L_3 = 0.25$: (a) randomly oriented, (b) alligned in different orientations, and (c) alligned versus angle of incidence. Parameters used are: $p = 1\%$, $\epsilon_h = 1$ and ϵ_m corresponding to Na.

can be regarded as a transition state, the properties of which must eventually converge with the atomic response as the number of atoms in the particle decreases to one. The most appropriate approach in the large particle limit of this transition region is to consider the changes in the optical response in terms of the increasing role played by the surface of the particle. Hence, the most appropriate parameter is the surface to volume ratio ($S/V \sim 1/R$).

Experimentally, the effect of the finite size of the particles on ϵ_m results in a shifting and broadening of the SPR with decreasing particle size relative to the resonance expected using the bulk metal dielectric function. The broadening follows a $1/R$ dependence for larger particles,[32] and breaks down for particles with only a few hundred atoms.[64] The shift of the SPR also follows a $1/R$ dependence, which continues, in this case, to particles containing less than a hundred atoms.[50] The direction of the shift depends on the type of metal. It shifts to lower energy ($\omega_{sp} < \omega_M$) for alkali metals: sodium,[65-68] potassium,[66,69] cesium,[70] and lithium,[71] and to higher energy ($\omega_{sp} < \omega_M$) for noble metals: silver[30,72-74] and gold.[75-78]

The first attempt to account for the above effects dates back to 1958[79] where the broadening of the SPR was described in terms of classical scattering of the electrons by the particle surface. Shortly after, in 1966, a quantum mechanical interpretation was provided by Kawabata and Kubo.[80] The last two decades have been particularly fruitful in providing an improved understanding of the optical properties of small metal particles, as evidenced by the numerous review articles: Perenboom *et al* in 1981,[48] Kreibig and Genzel in 1985,[81] Halpern in 1986,[82] de Heer *et al* in 1987,[83] Kresin in 1992[84] and de Heer in 1993.[9]

In this section, the different phenomenon which occur are presented. These include those which pertain solely to the conduction electron response, namely, the limited mean free path effect, the quantum size effect, and conduction electron spill-out, as well as those which concern both the conduction and the core responses, namely, the interaction between them (the core-polarization-free surface layer) and the influence

of the atomic structure. The possibility of metal/matrix interactions, and how these will affect the SPR, is also discussed.

1.4.1 Limited Electron Mean Free Path

The broadening of the SPR was originally interpreted in terms of conduction electron scattering from the particle surface as R decreased below the electron mean free path,[79] the so-called limited mean free path (LMFP) effect. The additional source of scattering can be incorporated within the Drude expression for ϵ_m by replacing τ_B^{-1} in Eq. 1.6 with an effective collision frequency Γ:[85]

$$\Gamma = \tau_B^{-1} + \frac{A\nu_F}{R}, \tag{1.26}$$

where ν_F is the conduction electron Fermi velocity. The broadening parameter, A, depends on whether the scattering is isotropic ($A = 1$) or diffuse ($A = 0.75$).[85]

Eq. 1.26 predicts the expected linear increase in the width of the SPR versus $1/R$ and a red-shift of the resonance with decreasing particle size.[86] The absorption spectrum as a function of R is shown in Fig. 1.8 using $\nu_F = 1.07 \times 10^8$ cm/sec, corresponding to Na,[44] and considering isotropic scattering (i.e. $A = 1$).

1.4.2 Quantum Size Effect

Already in 1937, Frohlich[6] shed doubt on the classical interpretation by pointing out that the continuous conduction band of metals should break up into observable discrete states when the dimensions of the metal becomes small enough, the so-called quantum size effect (QSE). This problem was formulated quantitatively in 1962 by Kubo,[7] and, in 1966, Kawata and Kubo[80] demonstated that the $1/R$ dependence of the SPR width could also be obtained from a quantum mechanical treatment of the conduction electrons in which the discrete nature of the conduction 'band' was included. In their calculation, the particle surface is not considered to act as a

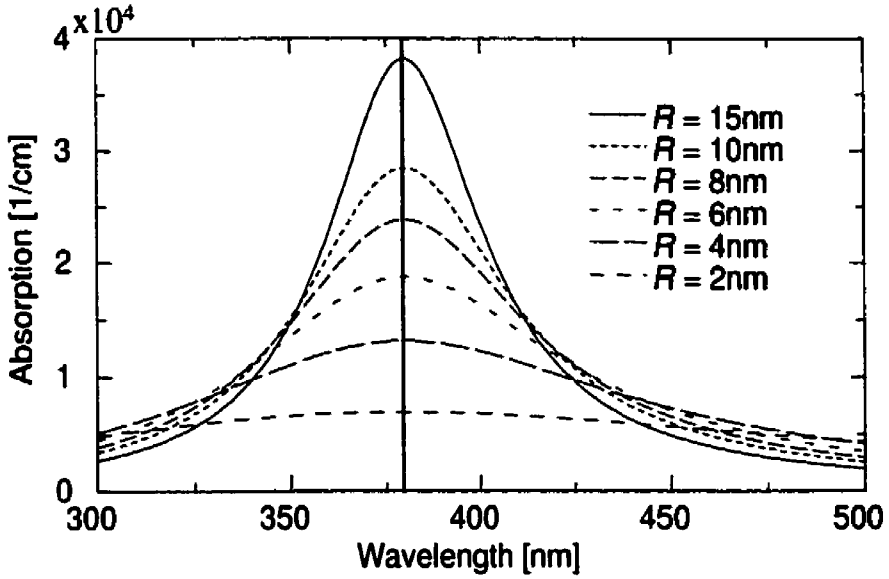

Figure 1.8: Particle size dependence of the SPR according to the LMFP effect (Eq. 1.26) with isotropic scattering ($A = 1$). Parameters used are: $p = 1\%$, $\epsilon_h = 1$, and ϵ_m corresponding to Na.

scatterer, but rather serves to define the boundary conditions for a particle in a box problem, and, as such, determines the eigenstates of conduction electrons in the finite volume of the sphere. The broadening in this interpretation results from the coupling of the surface plasmon with single electron excitations (i.e. Landau damping).

In order to determine the quantum mechanical optical response of a set of N electrons in a potential ϕ_{eff}, one first solves Schrödinger's equation for the ground-state electron density $n_e(\mathbf{r}) = \sum_{i=1}^{N} \mid \psi_i(\mathbf{r}) \mid^2$:

$$\left[-\frac{\nabla^2}{2} + \phi_{eff}[\mathbf{r}, n_e(\mathbf{r})]\right] \psi_i(\mathbf{r}) = E_i \psi_i(\mathbf{r}), \tag{1.27}$$

where $\psi_i(\mathbf{r})$ and E_i are the single particle eigenfunctions and eigenenergies, respectively. The response to an applied field, $V_{ext}(\mathbf{r}, \omega)$, can then be obtained using the

random phase approximation (RPA) in which the polarizability is given by:

$$\tilde{\alpha}(\omega) = \int \delta n_e(\mathbf{r},\omega) V_{ext}(\mathbf{r},\omega) d\mathbf{r}, \tag{1.28}$$

where the induced electron density, $\delta n_e(\mathbf{r},\omega)$, is given by

$$\delta n_e(\mathbf{r},\omega) = \int \chi(\mathbf{r},\mathbf{r}',\omega) V_{ext}(\mathbf{r}',\omega) d\mathbf{r}'. \tag{1.29}$$

$\chi(\mathbf{r},\mathbf{r}',\omega)$ is the frequency dependent response function for the interacting electron system which is determined by $n_e(\mathbf{r})$. The methods used to solve Eq.1.27 applied to metal particles can be found in the review by Brack.[87]

The solution of Kawata and Kubo,[80] and similar subsequent calculations,[64,86,88–91] (for a review, see Kreibig[81]) were done assuming an infinite barrier potential outside the particle (i.e. $\phi_{eff} = \infty$) such that the electron density drops to zero. In this approximation, the broadening of the SPR can be incorporated into the Drude expression in the same fashion as for the LMFP effect, except that in this case the broadening parameter is frequency dependent:[64]

$$A(\omega) = \beta g(\zeta), \tag{1.30}$$

where $\zeta = \hbar\omega/E_F$ and E_F is the metal Fermi energy. Depending on the details of the calculations, different prefactors, β, and functions, $g(\zeta)$, have been obtained by different authors (see, for example, Tran and Ekardt[90]). The prefactor calculated by Kawata and Kubo[80] is $\beta = 6/\pi^2$, while the most recent calculation by Yannouleas[64] gives $\beta = 3/4$. The slightly different functions, $g(\zeta)$, from these two calculations are shown in Fig. 1.9.

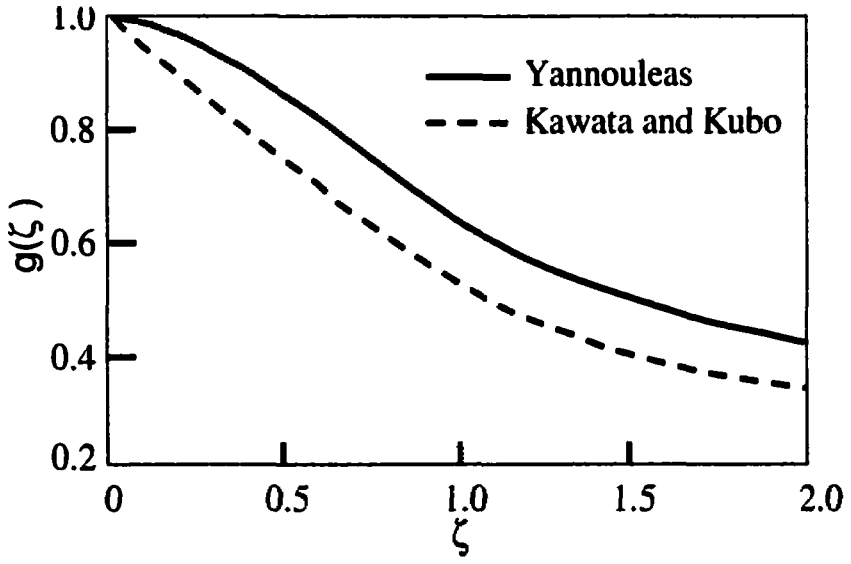

Figure 1.9: The functions $g(\zeta)$ where $\zeta = \hbar\omega/E_F$ used to determine the broadening parameter in the quantum mechanical polarizability of a metal sphere calculated using an infinite barrier.

1.4.3 Conduction Electron Spill-Out

The infinite barrier models generally (although not always[91]) predict a blue-shift of the SPR with decreasing R, which is opposite to the experimentally observed red-shift in alkali metal particles.[9] The flaw in these models was revealed by self-consistent microsopic solutions to Eqs. 1.27 and 1.28, initially obtained by Ekardt[8,92,93] in the early eighties and subsequently by others[94,95]. In this case, the potential ϕ_{eff} consists of a Coulomb term provided by the positive jellium background ($n_+ = 3/4\pi r_s^3$, where r_s is the Wigner-Seitz electron density parameter) and exchange-correlation potential. The use of this type of potential is the so-called local density approximation (LDA), or, if solving for $\delta n_e(r)$, the time-dependent (TD) LDA.[87]

These more accurate numerical solutions demonstrated the importance of the ground-state electron density in determining the conduction electron response. In particular, the electron density in small particles extends beyond the cluster radius

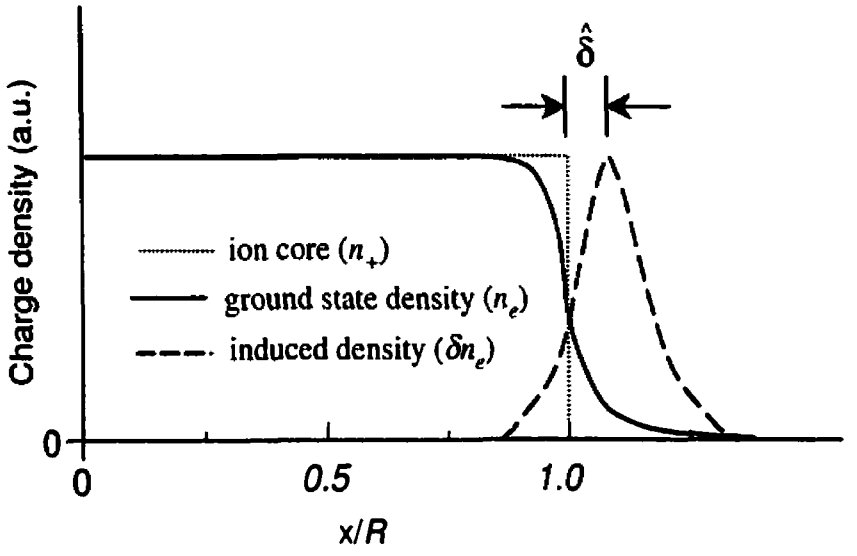

Figure 1.10: Schematic representation of conduction electron spill-out.

as defined by the ion core, so-called spill-out, shown schematically in Fig. 1.10. As a consequence, the centroid of the induced charge density is located outside the ion-core at a distance $\hat{\delta}$, a so-called spill-out parameter, giving rise to an increased polarizability (i.e. the effective radius of the particle is larger), the effect of which red-shifts the SPR with decreasing R.

The microscopic theories have been indispensable in the understanding the oscillations in the electronic and optical properties of particles consisting of less than a few hundred atoms, so-called shell effects.[9] These very small particles do not behave like little pieces of metal, but rather like giant molecules, where the conduction electrons occupy QSE induced shells with energy level spacing of a few tenths of an eV.[84] Application of these theories to larger particles ($R > 2\,\mathrm{nm}$) is, however, not feasible due to their complexity, and the consequent computational effort required.

A variety of simplified approaches have been proposed to treat larger particles. These include analytical theories, where the electron density is described using various modifications to the Thomas-Fermi approximation,[84,96–98] as well as asymptotic

approaches,[31,99,100] originally developed by Apell *et al*,[101-103] whereby the complex TDLDA calculations are restricted to the surface of the particle. In the former approach, the shift of the SPR is given in terms of an analytically determined spill-out parameter:[98]

$$\frac{\omega_{sp}}{\omega_M} = 1 - \frac{3}{2}\frac{\hat{\delta}}{R} - \frac{21}{8}\left[\frac{\hat{\delta}}{R}\right]^2 - \cdots \tag{1.31}$$

In the asymptotic approaches, the response of metal is written in terms of a classical bulk term, $\epsilon_m = 1 - \omega_p^2/\omega$, and a surface term, $\epsilon_s(\omega) = 1/3\omega^2 \sum(\omega)$, so that the dielectric function of the metal becomes:[99]

$$\epsilon_m = 1 - \frac{\omega_p^2}{\omega^2 + \sum(R,\omega)}. \tag{1.32}$$

$\sum(R,\omega)$ is a so-called self-energy in which the influence of the quantum size effect and conduction electron spill-out are incorporated. A simple expression for $\sum(R,\omega)$ is obtained if one approximates the surface of the particle by a plane:[100]

$$\sum(R,\omega) = \frac{1}{R} d_F(\omega)(\omega_p^2 - \omega^2). \tag{1.33}$$

where $d_F(\omega)$ is the so-called Feibelman parameter for a plane metal surface,[104-106] and is readily calculated within the TDLDA. In this case, the shift of the SPR is given in terms of $\Re[d_F(\omega)]$, which is the planar equivalent of the spill-out parameter:[100,103]

$$\frac{\omega_{sp}}{\omega_M} = 1 - \frac{\Re[d_F(\omega_{sp})]}{R} - \cdots \tag{1.34}$$

A further benefit of this approach is that the response has been formulated into a Drude-like expression, allowing the broadening of the SPR to be described in terms

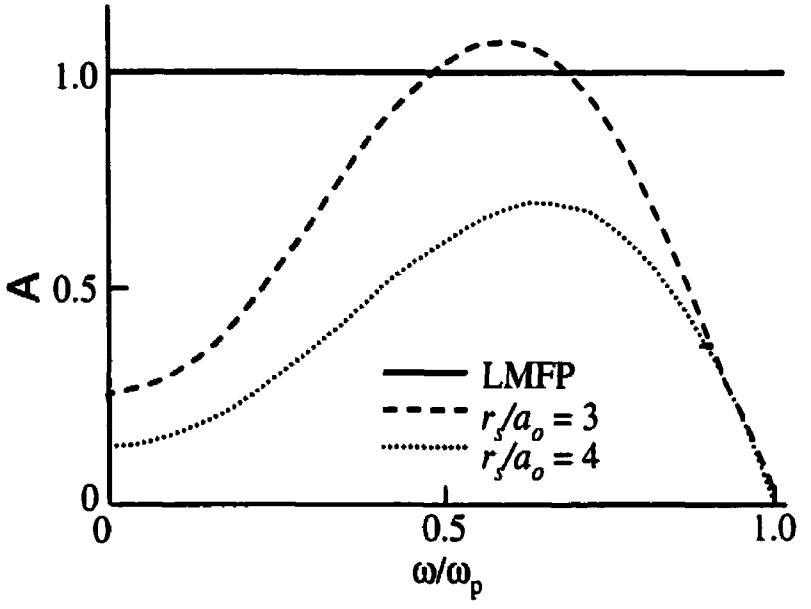

Figure 1.11: Frequency dependence of A after Ref. [101] for two electron density parameters. r_s is given in units of the Bohr radius, $a_o = \hbar^2 me^2$.

of the parameter A, now defined as:[101]

$$A(\omega) = \left(\frac{4}{9\pi}\right)^{2/3} (3r_s^{1/2}) \left(\frac{\omega_p}{\omega} - \frac{\omega}{\omega_p}\right) \Im(-d_F(\omega)k_F), \tag{1.35}$$

where k_F is the Fermi momentum and $\Im[d_F]$ accounts for single-particle (electron-hole) excitations (i.e. QSE). The frequency dependence of A according to the Eq. 1.35 is shown in Fig. 1.11 for two electron density parameters. Zaremba and Persson[31,99] have performed a similar calculation without the assumption of planar geometry, however they do not give the frequency dependence, only the value at $\omega = \omega_M = \omega_p/\sqrt{3}$ for which $A = 0.3$ for an $r_s/a_o = 3$ metal (i.e. Au and Ag).

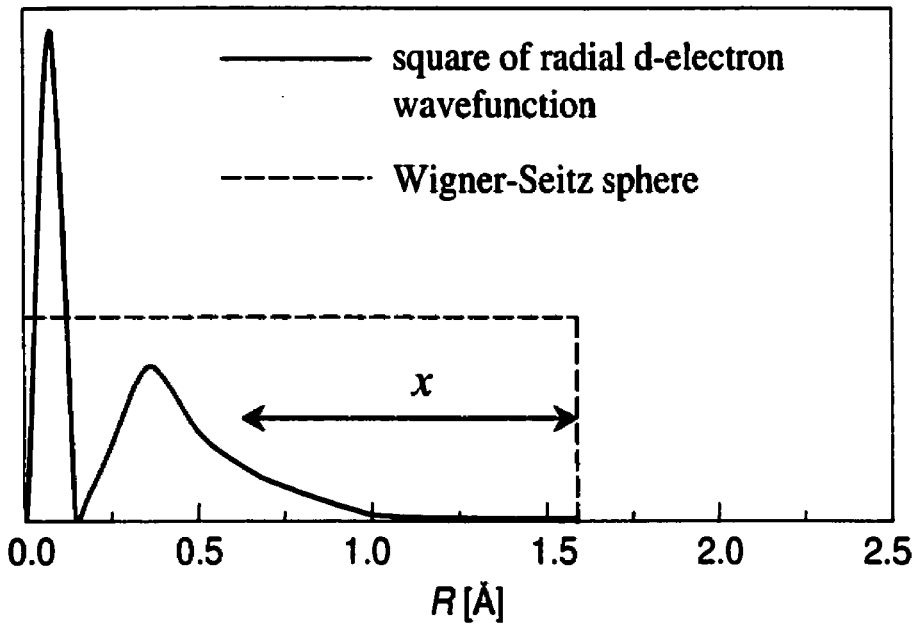

Figure 1.12: d-electron wave function compared to Wigner-Seitz sphere for a noble metal atom showing region of non-overlap, x. After Ref. [107].

1.4.4 Core-Polarization-Free Surface Layer

In the case of noble metals, the SPR blue-shifts with decreasing R, opposite to the observed spill-out induced red-shift for the alkali metals. The different behaviour is associated with the d-electrons in noble metals, absent in the alkali metals. The d-electrons, through their screening, red-shift the SPR, as discussed in Secton 1.2.2. If one looks, however, at an atom of a noble metal, there exists a region of non-overlap between the d-electron wave function and the conduction electron, as shown in Fig. 1.12. In the body of a metal cluster, this non-overlap is averaged over the unit cell. This is not the case, however, for the atoms on the surface of the cluster.[100]

One can therefore expect, as the S/V ratio increases, that the screening provided by the d-electrons will diminish, hence, blue-shifting the SPR.[100,107] Classically, the influence of a core-polarization-free layer at the surface of a particle can be modeled by considering a two region particle:[49,60] an inner sphere having a dielectric function

corresponding to the bulk metal and an outer shell where the core polarizability is absent. This gives a blue-shift of the SPR which can be calculated from:[107]

$$\left[\frac{\epsilon_{NC}}{\epsilon_h}+2\right]\left[\frac{\epsilon_{WC}}{\epsilon_{NC}}+2\right]=2\left[1-\frac{x}{R}\right]^3\left[\frac{\epsilon_{WC}}{\epsilon_{NC}}-1\right]\left[1-\frac{\epsilon_{NC}}{\epsilon_h}\right] \tag{1.36}$$

using ϵ_{WC} given by Eq. 1.8 (i.e. with core) and ϵ_{NC} given by Eq. 1.6 (i.e. no core) and solving the resulting quadratic equation in $\Omega=[\omega/\omega_p]^2$ at $\omega=\omega_{sp}$.

1.4.5 Atomic Structure

Until now, the discussion of the finite size effects has been restricted to the conduction electron response assuming that the atomic structure was equivalent to its bulk counterpart. However, it is natural to expect that the increasing role of the surface in small particles will have an effect on the atomic structure of the metal, and, consequently, the electonic bandstructure.

The most obvious influence of the surface in small particles concerns the state of the surface with respect to stress.[108] The simplest manifestation of the effect of surface stress in small particles is a change in the lattice constant, $\Delta\hat{a}$[37]:

$$\frac{\Delta\hat{a}}{\hat{a}}=-\frac{2}{3}g\kappa/R, \tag{1.37}$$

where $\hat{a}$ is the bulk lattice constant, κ is the compressibility coefficient, and g is the surface stress coefficient defined by

$$g=\sigma_s+S\frac{\partial\sigma_s}{\partial S}. \tag{1.38}$$

σ_s is the surface tension and S is the surface area such that the surface energy is given by $\sigma_s S$. The behaviour predicted by Eq. 1.37 has been observed in small gold particles from lattice constant measurements using electron diffraction[37,76,108] and EXAFS spectroscopy.[36] In particular, the surface is in a state of dilation ($g>\sigma_s$) so

that $\Delta\hat{a}$ is negative, (i.e. the lattice is contracted).

More sophisticated theoretical treatments of the minimum energy structures of small particles[11,109–111] predict lattice distortion rather than simple contraction. Specifically, the distortion is described in terms of either (*i*) non-uniform contraction in a single crystal,[109] (*ii*) lattice deformation resulting from internal strain upon formation of MTPs,[11] or (*iii*) completely amorphous structures.[111]

In the extreme, one can no longer speak of a disordered lattice, but rather a liquid particle. The depression of the melting temperature in small metal particles was predicted in 1909 by Pawlow[112] and has since been described using thermodynamic models,[113,114] simulated using molecular dynamics,[115–118] and observed using a variety of experimental techniques.[114,119–122] Lower melting temperatures with decreasing particle size are ultimately attributable to the increasing proportion of surface atoms which are more weakly bound and less constrained in their thermal motion by virtue of their lower coordination. The distinctly different behaviour of surface atoms is manifest in the occurrence of surface premelting, which is responsible for the liquid-like coalescence of particles well-below the melting point,[123] and which has even been observed using real time HRTEM in an *in situ* evaporation facility.[124]

One can expect the following structural transitions to occur with decreasing particle size:[10] (*i*) decreasing mean lattice constant and increasing disorder, (*ii*) change in crystal structure from FCC single crystals to MTPs, (*iii*) rapid oscillations amongst various multiply twinned structures of different polyhedral morphologies (i.e. QM), and (*iv*) surface pre-melting, followed by full-fledged melting at temperatures below the bulk point. How these structural changes affect the optical properties depends critically on the type of metal. The atomic structure, through its effect on the electronic bandstructure, will influence predominantly the core response.

Alkali metals, the optical response of which is little affected by the core, will thus not depend critically on the atomic structure, aside from a contraction-induced increase in n_e, and, hence, ω_p. In fact, the core of free alkali metals, which are

produced by cluster beam sources[9] and are, thus, at relatively high temperatures with respect to their melting points, are likely in a liquid state.[125] This actually increases the applicability of TDLDA modeling since these calculations are done within the jellium approximation where the core is considered as a structureless sphere providing only a uniform background charge density.

The core response of noble metal clusters, on the other hand, plays a crucial role in determining the optical response, which will, therefore, be very sensitive to any transitions in the atomic structure. One can, for example, compare the dramatic differences between the optical constants of liquid[126] and crystalline gold.[127] The limited experimental studies concerning the core response in gold particles[75, 128–130] have shown that the inter-band transition edge is dependent on particle size. In particular, both the threshold energy and the band edge slope decrease with decreasing R.

These effects are usually explained in terms of lattice contraction and d-band distortion. The former is based on the bandstructure calculations of Christensen and Seraphin[13] which predict a decrease of the onset of inter-band transitions for a contracted lattice. The latter is based on XPS studies (see, for example, Mason[34] and Wertheim[131] and references therein) which have shown d-band narrowing and a shift of the density of states (DOS) to lower binding energy in small clusters, effects attributed to the redistribution of s- and d-electrons, similar to that observed in plane metal films.[16, 17] As well as band-edge changes, optical measurements also suggest the occurrence of a structural phase transition at $R \sim 1.5\,\mathrm{nm}$, [75, 128] which can tentatively be ascribed to particle melting.[114]

1.5 Matrix Effects

A final effect which needs to be considered is the influence of the matrix material. Even assuming an abrupt interface between the metal and the dielectric, the

host matrix will influence the spill-out of conduction electrons through screening of the electron-electron interaction,[132,133] in particular, an increase in the extent of the spill-out is expected for higher index materials. There is also the possibility of metal-adsorbate charge transfer excitations at the metal/matrix interfacial region. On one hand, these reactions can lead to the formation of a two-region particle, which can be trivially treated using an appropriate EMT.[60] As an example, exposure of Ag particles to sulphur results in the formation of a shell of Ag_2S around the particle.[134,135]

Alternatively, the metal/matrix interaction does not lead to the formation of a different material, to which a dielectric function can be identified, but, rather, results only in adsorbate-induced resonant states above E_F and close to the frequency of the SPR.[31] The influence on the SPR of Ag particles in these types of reactive matrices has been extensively studied,[30,72] and results in a severe broadening of the SPR, so-called chemical interface damping[32] (CID). According to a model proposed by Persson,[31] the effect of CID on the optical response can be accounted for simply by including an adsorbate-induced contribution (ΔA) to the broadening parameter: $A \rightarrow A + \Delta A$.

1.6 Summary

The optical response of larger particles in dilute concentration can be described using the theory of Mie with the bulk metal dielectric function, as well as that of the host material, as input parameters. The spectrum consists of a series of absorption bands corresponding to different modes of oscillation of the conduction electrons. The particle size dependence of the energy and width of these bands is determined by scattering and phase retardation. For smaller particles, EMTs can be used to describe the optical response. Although these theories are derived using electrostatic equations, and are thus limited to particles within the quasi-static limit, they are applicable to a collection of particles in higher concentration than that allowed by

the Mie theory.

For still smaller particles, an influence of the finite size of the particles on the optical response is expected. The signature of finite size effects are a broadening and shifting of the SPR and can be ascribed to a particle size dependence of the conduction and core electron responses. The former arises from a combination of the QSE, conduction electron spill-out, and the interaction between the conduction and core electrons. The latter is a consequence of the particle size dependence of the atomic structure, and hence the electronic bandstructure, of the metal. For the smallest particles, shell effects will dominate the optical properties, with the collective conduction electron response vanishing completely for particles containing just a few atoms.

This thesis concerns, for the most part, the optical response of gold particles in the size range within the quasi-static limit, but large enough so that the conduction band can be considered a quasi-continuum (i.e. no shell effects). This size domain allows one to ascribe a broadening parameter to the width of the SPR. In Table 1.1, the A values specific to gold (where applicable) obtained from the different models are compiled, along with the assumptions made in each model. The TDLDA models refer to calculations done in the asymptotic limit.

In Fig. 1.13, the various particle size dependencies of the energy of the SPR predicted by the different models are compiled. The LMFP-induced red-shift is calculated from Eq. 1.26 assuming a broadening parameter $A = 1$. The spill-out-induced red-shifts given by Eqs. 1.31 and 1.34 were calculated using theoretical spill-out parameters: $\hat{\delta} = 1.3\,\text{Å}$[104] and $\Re[d_F] = 0.54\,\text{Å}$,[136] respectively. The blue-shift induced by the presence of the core-polarization-free surface layer (Eq. 1.36) was calculated using $x = 1\,\text{Å}$.[107] The full TDLDA predictions are after Palpant *et al*[78,132] in which the spill-out corresponds to an embedding medium having $\epsilon_h = 2.0$ and $x = 1\,\text{Å}$.

Table 1.1: Broadening parameters according to different theories. A is given for $\hbar\omega = 2.34\,\mathrm{eV}$ (unless otherwise stated) which corresponds to the Mie resonance of gold particles in SiO_2 ($\epsilon_h = 2.25$).

Theory	Comments	A
LMFP[85]	isotropic scattering	1.0
LMFP[85]	diffuse scattering	0.75
QSE[80]	∞ barrier	0.5
QSE[64]	∞ barrier	0.675
TDLDA[101]	∞ barrier	0.1
TDLDA[101]	with spill-out	0.6
TDLDA[99]	$\omega = \omega_p/\sqrt{3}$	0.3

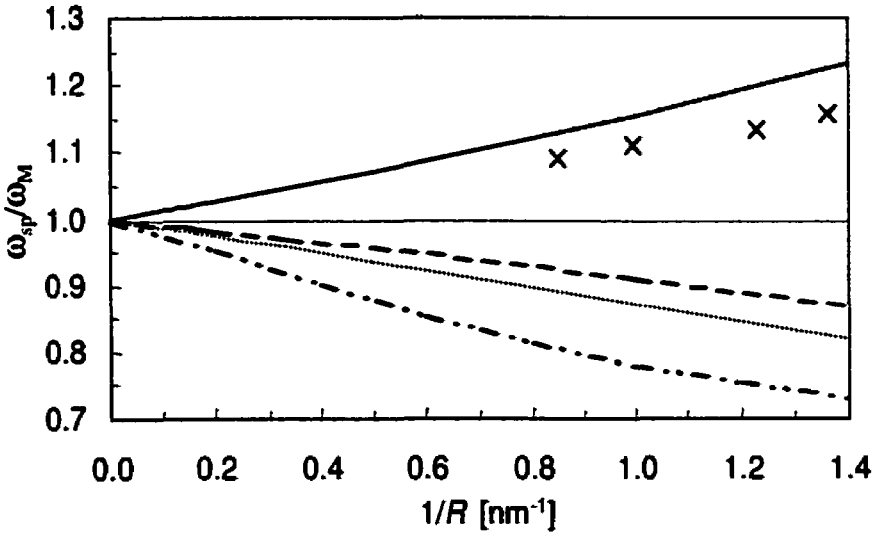

Figure 1.13: SPR shifts: dashed-dotted line: LMFP effect, solid line: core-polarization-free surface layer, dashed line: spill-out (Eq. 1.31), dotted line: spill-out (Eq. 1.34), crosses: full TDLDA calculations.

Chapter 2

Experimental Methodology

2.1 Film Deposition

2.1.1 Introduction

There exists an extensive list of deposition methods that have been utilized for the fabrication of metal/dielectric composite films, including: (*i*) vacuum techniques,[137] (*ii*) metal ion implantation into a dielectric,[138–142] (*iii*) the sol-gel technique,[143–145] (*iv*) deposition from metal colloid solutions,[146] and (*v*) electrodeposition.[147] Of these, vacuum deposition methods are the most frequently used, in particular, co-sputtering of the metal and dielectric from separate targets,[148–151] as well as a variety of hybrid methods combining sputtering, evaporation, and PECVD, (see, for example, Biederman and Martinu[152]).

In this thesis, hybrid methods utilizing glow discharges have been employed for composite film deposition, in particular, the PECVD of dielectric matrices and the magnetron sputtering (MS) of gold. The amorphous nature of dielectric films produced by PECVD have important implications with respect to the assumed microstructure of the composite films. The ability to deposit a material which serves only as a structureless host for the metal particles is crucial in the application of the

M-G EMT. For polycrystalline matrices, for example, one has to consider the grain structure of the matrix, the presence of voids, and, in particular, the possibility of a non-homogeneous interface at the metal/dielectric boundary.

In this section, the principal mechanisms responsible for film growth using glow discharges are outlined. More detailed accounts can be found in the handbooks edited by Bunshah[153] and Vossen and Kern[154]. Application of glow discharges for the deposition of the specific materials used in this thesis is given. A detailed discussion concerning MS of metals can be found in the book by Ohring[155] while a detailed review concerning PECVD of dielectric materials for optical application is given by Martinu and Poitras[46]. Finally, a discussion of how these techniques can be combined in hybrid systems for the deposition of composite films is given.

2.1.2 Glow Discharges

A glow discharge is a partially ionized gas consisting of electrons, ions, neutrals, free radicals, and other excited species (i.e. a plasma). Using a glow discharge allows the creation of free radicals and excited species in concentrations normally obtained only at flame temperatures. The lower activation energies for surface and gas-phase reactions of these species greatly enhances the kinetics and allows film formation at reduced temperatures.

The plasma state is created by introduction of energy, via electric or magnetic fields, which couples to the electrons in the gas. The energy gained by the accelerated electrons is, in turn, passed to the neutrals through collisions. Steady-state charge effects then set-in which allow glow discharges to be utilized for film deposition. Consider, for example, the immersion of an isolated surface into a plasma. Charged particle impingement (electrons and ions), and subsequent neutralization, gives rise to a transient current density at the surface. The much higher electron current relative to the ion current (due to the latter's larger mass, and consequent lower mobilty), will result in the surface charging progressively negative, reducing the electron current

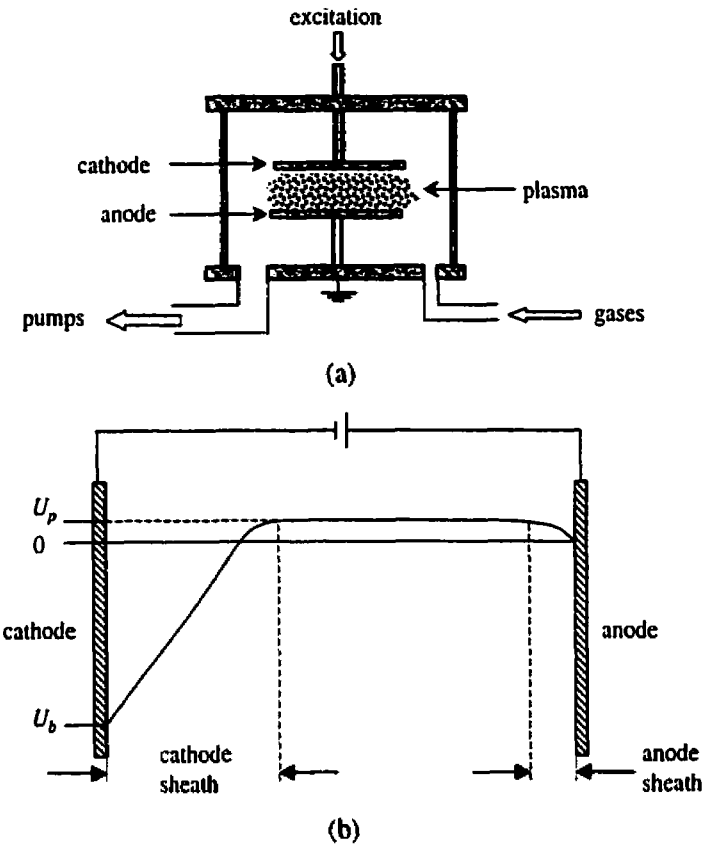

Figure 2.1: (a) A typical parallel-plate electrode reactor.
(b) Potential across the electrodes in a DC discharge.

density and creating a space-charge region, until a steady-state is reached.

The steady state potential that develops across two electrodes in a typical reactor in which the plasma is excited through application of a DC bias is shown in Fig. 2.1. The above charging effects restrict the electric fields to the electrodes, so that the reactor behaves electrically like a diode. The potential across the space charge region (sheath) at the powered electrode is given by $U_p - U_b$, where U_p is the plasma potential and U_b is the applied voltage.

In the case of an insulating electrode, application of a bias results in a build-up of charge at the cathode. In this case the reactor acts like a capacitor as opposed to the diode behaviour in Fig. 2.1 due to the negligible current density across the cathode.

If, however, an AC signal is applied (i.e. RF (13.56 MHz) or MW (2.45 GHz)), the charge build-up will be neutralized during each half-cycle. Furthermore, the slower neutralization by the positive ion bombardment during the negative half-cycle results in the development of a negative potential on the electrode, a so-called self-bias, U_B, such that the potential across the electrodes is as in the case of a DC discharge.

In either case, the unique steady state conditions arising from the disparity in the masses of electrons and ions provide a mechanism whereby energy can be ultimately transferred to the neutral species in the gas. The typical reactions that take place upon injection of electrons into the plasma, via the space-charge field, are:

- Ionization: $A_2 + e \longrightarrow A_2^+ + 2e$
- Excitation: $A_2 + e \longrightarrow A_2^* + e$
- Dissociation: $A_2 + e \longrightarrow 2A + e$
- Dissociative attachment: $A_2 + e \longrightarrow A_2^- \longrightarrow A + A^-$

The ionzation process is responsible for the creation of the plasma, the reverse of which (i.e. by neutralization processes such as recombination of charge carriers though collisions with surfaces) necessitates a continuous input of energy to sustain the plasma. Possible excitation processes include rotational, vibrational, and electronic, the latter being responsible for the plasma glow as the atoms de-excite through emission of photons. The dissociative processes produce atoms and free radicals that can be long-lived in the gas-phase and that are highly reactive when striking a surface.

The plasma can be utilized in a variety of ways depending on the configuration of the system and on the nature of the gas discharged. The use of inert gases gives rise to film deposition via physical sputtering of a target material. In the case of reactive gases, films can either be deposited (i.e. reactive sputtering and PECVD),

or etched (i.e reactive ion etching). In this study, the intended role of the plasma is film deposition via a combination of physical sputtering and PECVD.

The film growth rate, morphology, and composition for a specific working gas composition will be dependent on (*i*) the specific internal plasma characteristics (electron density and electron energy distribution function) which determine the different species in the plasma, and (*ii*) plasma-surface interactions and substrate surface conditions.[46] The former are determined by the external parameters, namely power, pressure, gas flow, and excitation frequency, while the latter by ion bombardment and substrate temperature.

2.1.2.1 Physical Sputtering

In the case of physical sputtering, the material to be deposited comes from a target placed on the powered electrode. The plasma is used as a source of inert ions, and a noble gas (e.g. argon) is used in the discharge. The electric field at the cathode accelerates ions that diffuse there towards the target. This ion bombardment results in the ejection of target atoms by momentum transfer. The subsequent diffusion of the ejected target material and condensation on a substrate placed at the anode forms the thin film.

The sputtering rate depends not only on the material to be sputtered, but also on the sputtering gas and energetic conditions, and hence, will be sensitive to the external plasma parameters mentioned above. Enhanced sputtering rates can be obtained by use of a magnetron in which magnets are placed beneath the target in order to form a closed or an open magnetic field. The Lorentz force experienced by the electrons in the dual field environment results in a prolonged electron residence time in the plasma and thus an enhanced probability of ion collision. In particular, the parallel component of the magnetic field, with respect to the target, results in a helical trajectory of the emitted electrons. Thus, the use of a magnetron not only leads to larger discharge currents and increased sputter deposition rates relative to the simple

diode-sputtering configuration, but also localizes the plasma so that only a limited number of electrons strike the substrate. The use of an open magnetic field, so-called unbalanced magnetron sputtering,[156] also permits control of the ion-to-neutral flux ratio at the substrate.

The most important characteristic of sputtered metal films is the grain morphology (i.e. size, shape, orientation, and boundary structure), generally studied using TEM techniques (see Ch. 5 in Ohring[155] and references therein). Besides the substrate temperature and the use of an unbalanced magnetron, the morphology of the deposited film can be controlled by applying a negative bias to the anode in order to promote ion bombardment. This bombardment has a dramatic influence on the microstructure of the growing film, in particular, the disruption of the columnar grain structure for that of a denser, fine-grained film with much lower pin-hole density. Such are the benefits of ion bombardment that most films sputtered today are done using ion assisted deposition (IAD) methods in which a broad-beam ion source is added to the deposition system.

2.1.2.2 PECVD

In PECVD, the material which makes up the film comes from the reactive species created in the plasma by virtue of the dissociation processes mentioned above. This being the case, plasma kinetics play a much more important role in determining the chemical composition of the deposited film. Furthermore, there is generally a choice of precursors from which the film may be obtained,[46] which will, again, influence the film composition. Finally, since the discharged gas will contain not only electrons, ions, and neutrals, but also free radicals and molecular fragments, the surface reactions that give rise to film deposition will inherently be more complicated.

Since both electrodes are available for substrate placement (i.e. there is no target material), PECVD has the inherent option of ion bombardment of the growing film simply by placing the substrate on the powered electrode. As in the case of

MS with a biased anode, this bombardment has dramatic effects on the film morphology and chemical composition, in particular, film densification and desorption of weakly bonded gases, and will also influence the surface reactions that give rise to film formation.[46]

The first matrix material studied in the course of this work was a plasma polymerized fluorocarbon which is a polymer deposited by PECVD using an organic monomer as the precursor gas, so-called plasma polymerization. In the case of fluoropolymers, the input gas is a fluorocarbon (i.e. a freon), producing the free radicals $(CF_2)_n$ and CF_x, which are considered to be the plasma polymerization precursors.[157] Since atomic fluorine is also present in the discharge, the plasma has the potential to etch and it is the $[CF_x]$:[F] ratio that will determine whether polymerization or etching takes place. This ratio is not only influenced by the external plasma parameters, but also by the choice of monomer (i.e. CF_4, C_2F_6, C_3F_8, $\cdots$) as well as the introduction of additional gases (i.e. H_2 for enhanced polymerization, O_2 for enhanced etching).[158]

Plasma polymerization occurs in four steps:[159] (i) initiation of reaction by formation of free radicals in gas phase, (ii) diffusion to adjacent surfaces, (iii) propagation of short segments of polymer chains, and (iv) chain termination. The last two steps occur on the surface forming a solid polymer deposit. A simple representation of the reactions at the surface are:[152]

- $ion + (polymer)_m \longrightarrow (polymer)^*_m$
- $(CF_2)_{n(g)} + (polymer)^*_m \longrightarrow (polymer)_{m+n}$
- $CF_{x(g)} + (polymer)_m \longrightarrow (polymer)_{m+1}$

where the asterisk indicates activated (i.e. by charged particle bombardment) polymer sites.

The most important characteristics of the deposited polymers are the [C]:[F] ratio, the carbon and fluorine bonding configurations, and the degree of cross-linking. These are usually compared to that of teflon, for which the [C]:[F] ratio is exactly two

(i.e. only -CF_2 bonds are present). The most utilized methods for characterizing the chemical structure and composition of these films have been Fourier transform infrared spectroscopy and XPS (see, for example, d'Agnostino *et al*[158] and references therein).

The second matrix material studied in this work was SiO_2. As in the case of the fluoropolymer, there exists an extensive choice of precursors and feed mixtures available, including Si containing organic precursors (i.e. TEOS, HMDSO, TMDSO) as well as silane (SiH_4) combined with O_2, CO_2, or N_2O.[46] For example, the basic reaction using SiH_4 in mixture with N_2O is

- $SiH_4 + 4N_2O \longrightarrow SiO_2 + 4N_2 + 2H_2O$

The intermediate steps leading to this reaction are difficult to ascertain and requires identification of the deposition precursors as well as the possible surface reaction pathways.[160] The deposited films are generally amorphous, with 5-15 at.% hydrogen content, and may contain carbon or nitrogen, depending on the precursor.

The critical structural characteristics of the films are the mean Si-O-Si bond angle, $\hat{\theta}$, and the density, ρ. Low values of $\hat{\theta}$ may result in stress accumulation leading to network relaxation and the formation of defect centres, the former of which may result in the creation of pores, and, hence, changes in ρ. These structural characteristics are intimately related to the chemical composition, in particular, the incorporation of H which exists mostly in the form of -OH. The OH groups affect the film properties in a variety of ways, including (*i*) stabilization of low-angle Si-O-Si bonds, (*ii*) passivation of dangling bonds, and (*iii*) reaction with H_2O present in pores (see, for example, Martinu and Poitras[46] and references therein).

2.1.3 Hybrid Deposition of Metal/Dielectric Composite Films

The above two deposition methods (MS of metals and PECVD of dielectrics) can be readily combined in a hybrid deposition system for the fabrication of composite

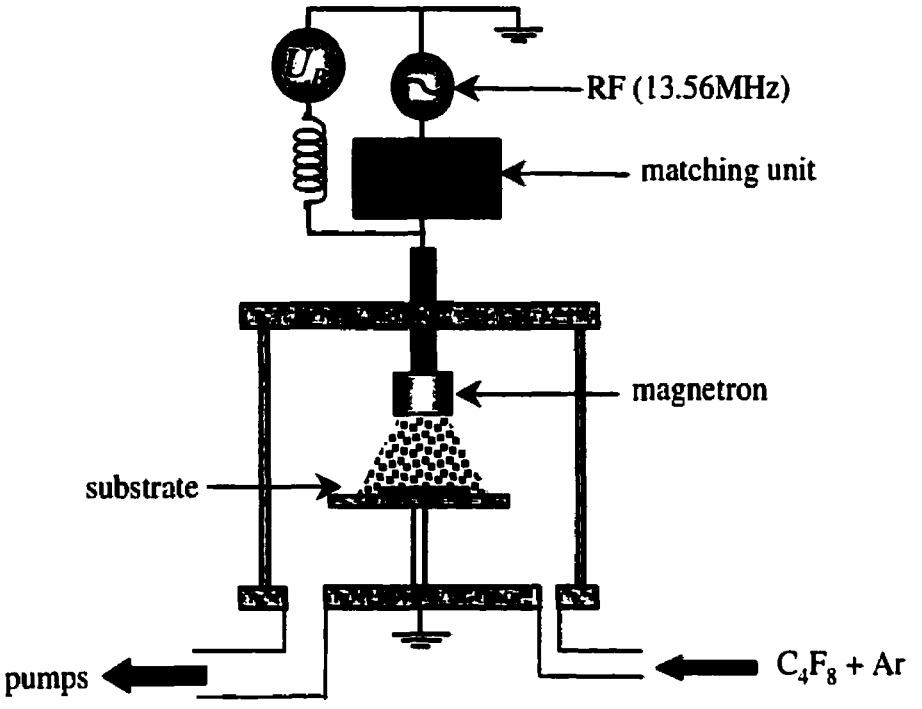

Figure 2.2: Schematic of the reactor used for Au/PPFC composite film deposition.

films.[152] In this thesis, two methods were used: The first consists of simultaneous plasma polymerization and sputter etching[161–163] used to produce Au/PPFC films. The second method is a rather novel approach using dual RF discharges for the deposition of Au/SiO_2 films.

2.1.3.1 Au/PPFC Films

A schematic of the deposition system used for Au/PPFC composite film deposition is shown in Fig. 2.2. It consists of a parallel-plate electrode reactor equipped with a 50 mm diameter balanced circular magnetron. The discharge is excited by an RF signal capacitively coupled via a matching network to the magnetron, and the substrate is placed on the grounded electrode. Octa-fluoro-cyclobutane (C_4F_8) was used as the precursor gas.

Without the use of the magnetron, the reactor would operate as a simple plasma

polymerization system for the deposition of PPFC films. The enhanced sputtering yield available by using the magnetron, together with the addition of argon to the gas mixture, allows for both sputtering of the target material (i.e. gold), and, simultaneously, the discharge of the fluorocarbon gas. The subsequent diffusion of the gold atoms and free radicals to the substrate surface results in the formation of the Au/PPFC films.

The microstructural characteristics of the deposited films (concentration and size of the embedded gold particles) are determined by the relative deposition rates of the gold and the fluoropolymer, which, in turn, are dependent on the external plasma parameters. Substrate temperature will further alter the film morphology, in particular, the decreased polymerization rate for heated substrates,[158] combined with the enhanced surface diffusion of the gold atoms, will result in higher filling, larger particle films.

2.1.3.2 Au/SiO_2 Films

A schematic of the deposition system used for Au/SiO_2 deposition is shown in Fig. 2.3. Again, the reactor is in a simple parallel-plate electrode configuration using a capacitively coupled RF excitation. In this case, however, the sample is placed on the powered electrode. Furthermore, the reactor is complemented by a magnetron powered from a separate RF supply. The precursor gas used was SiH_4 in mixture with N_2O.

As before, the system works as a simple PECVD reactor for the deposition of SiO_2. The inclusion of the magnetron and addition of argon into the gas mixture allows for the simultaneous incorporation of the gold atoms into the discharge. Formation of the Au/SiO_2 composite film then takes place at the substrate. The crucial requirement for the deposition method to work is a sufficiently high RF bias on the magnetron so that Au sputtering, and not SiO_2 deposition, prevails at the target. The concern of oxide on the target was such that the magnetron was always powered first, and

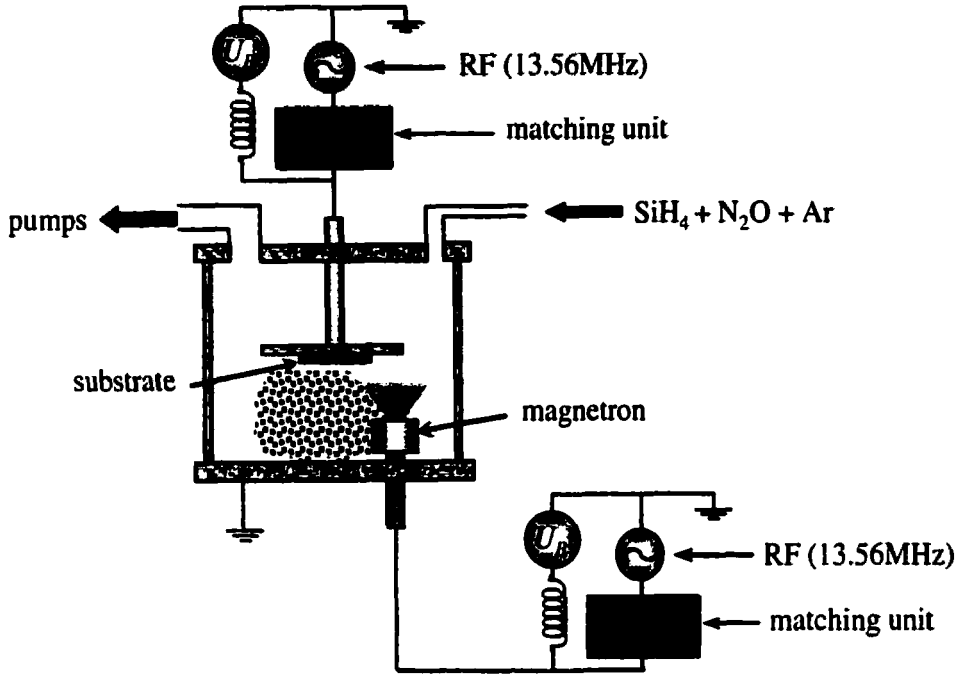

Figure 2.3: Schematic of the reactor used for Au/SiO_2 composite film deposition.

then allowed to sputter clean prior to powering the substate electrode. During this procedure, a shutter was placed over the target to prevent deposition on the substrate.

It can be noted in the figure that the magnetron is placed off-centre with respect to the substrate. This was done in order to obtain a gradient in the gold filling across the substrate. As such, multiple microstructures could be obtained in a single deposition on the same sample.

2.2 Optical Characterization using Ellipsometry

2.2.1 Introduction

The standard method used in the optical characterization of metal/dielectric materials is photometry, and, in particular, measurement of the normal or near-normal incidence transmission spectra.[63] Modeling is generally limited to a comparison of the experimental SPR energy (e.g. the minimum in the transmission spectrum) to that predicted by the Mie or M-G theories. In the case of bulk samples, the dielectric function of the nanocomposite material can be calculated from the transmission data using the Kramers-Kronig relations.[164] In the case of thin films, the dielectric function is determined from the Fresnel equations using both transmission and reflection spectra.[165,166]

The workhorse used for the optical characterization of the films in this thesis was ellipsometry. It differs fundamentally from photometric measurements in that the ratio of the electric field amplitudes are measured, not their intensities. This makes ellipsometric measurements relatively insensitive to such things as intensity fluctuations of the light source, temperature drifts of the electronic components, and, in particular, macroscopic surface roughness. The latter results in light loss by scattering of the incident radiation out of the field of the instrument. In photometry, this effect can go unchecked, resulting in large errors in the calculated optical constants.[167] In ellipsometry, macroscopic scattering does not influence the spectra, and the true bulk constants of the material are determined. On the other hand, if it is this very surface roughness that is of interest, then photometry in a scattering set-up (i.e. either angle-resolved, or using an integrating sphere) is essential.

A second important, though not fundamental, distinction is that ellipsometry is inherently an oblique-angle measurement. This allows for the determination of two independent quantities, unlike normal-incidence measurements where the parallel and perpendicular components of the reflection and transmission coefficients are equal. In

the case of a substrate, this allows sufficient information to be obtained in one measurement to uniquely determine the dielectric function without the need to resort to a K-K analysis. For more complicated multi-layer structures, spectroscopic measurements are necessary in that they allow application of dispersion models. In this case, the two quantites measured at different angles of incidence provide sufficient constraints on a multi-layer optical model so that the dielectric function of the films can be determined with a high level of confidence.

In this section, the basic elements of ellipsometry are presented. More detailed discussions are available in several books devoted to the subject,[168-171] in particular, the classic book of Azzam and Bashara,[168] which provides a detailed theoretical description, and the very recent book by Tompkins and McGahan,[171] in which a more applied approach is taken. The connection between ellipsometry and the optical properties of materials as provided by the Fresnel equations[172] is also presented. The section is concluded with some typical examples which are relevant to this thesis, and which demonstrate the power of parameterized models applied to spectroscopic measurements in determining the optical constants of materials.

2.2.2 Ellipsometry

Ellipsometry is the measurement of the change in polarization upon reflection of an incident electromagnetic wave from a surface. Why this measurement is called ellipsometry relates to the state of polarization. The polarization of an electromagnetic wave is best described by considering the electric field vector, $\mathbf{E} = \mathbf{E}_o \exp(\omega t - \mathbf{k}\cdot\mathbf{r} + \delta)$, in terms of two mutually perpendicular components, one parallel to the plane of incidence, the p wave, and the other perpendicular, the s wave. The incident electric field can then be written as $\mathbf{E}_i = E_i^p \hat{p} + E_i^s \hat{s}$ with

$$E_i^p = E_{io}^p \exp(\omega t - \mathbf{k}_i \cdot \mathbf{r} + \delta_i^p), \tag{2.1}$$

$$E_i^s = E_{io}^p \exp(\omega t - \mathbf{k}_i \cdot \mathbf{r} + \delta_i^s). \tag{2.2}$$

Similarly, for the reflected field, $\mathbf{E}_r = E_r^p \hat{p} + E_r^s \hat{s}$ with

$$E_r^p = E_{ro}^p \exp(\omega t - \mathbf{k}_r \cdot \mathbf{r} + \delta_r^p), \tag{2.3}$$

$$E_r^s = E_{ro}^s \exp(\omega t - \mathbf{k}_r \cdot \mathbf{r} + \delta_r^s). \tag{2.4}$$

$\mathbf{k}_i$ and $\mathbf{k}_r$ are the propagation vectors of the incident and reflected beams, respectively, $\mathbf{r}$ is the spatial coordinate, ω is the angular frequency, and the δ's are the phases of each component.

Using these equations, the locus of end points of the incident and reflected electric field vectors when viewed in a stationary plane perpendicular to the direction of propagation is given by[169]

$$[E_{jo}^s]^2[E_j^p]^2 + [E_{jo}^p]^2[E_j^s]^2 - 2E_{jo}^p E_{jo}^s E_j^p E_j^s cos\delta_j = [E_{jo}^p]^2[E_{jo}^s]^2 sin^2\delta_j, \tag{2.5}$$

where $j = i$ (r) for the incident (reflected) wave, respectively. Eq. 2.5 is that of an ellipse inscribed into a rectangle whose sides are parallel to the coordinate axes, $\hat{p}$ and $\hat{s}$, and have magnitude $2E_{jo}^p$ and $2E_{jo}^s$, respectively. The shape of the ellipse (ellipticity) together with its orientation define the state of polarization and is determined the phase difference between the s and p components of the field: $\delta_j = \delta_j^p - \delta_j^s$. Ellipsometry, then, is the measurement of the change in ellipticity upon reflection, hence its name, first coined in 1945.[173]

The reflection process is shown schematically in Fig. 2.4. To determine the change in polarization upon reflection, it is necessary to know the complex amplitude attenuations, $\tilde{\rho}^p = E_i^p/E_r^p$ and $\tilde{\rho}^s = E_i^s/E_r^s$, of the p- and s-waves, respectively:

$$\tilde{\rho}^p = \frac{E_{io}^p}{E_{ro}^p} \exp i(\delta_r^p - \delta_i^p), \tag{2.6}$$

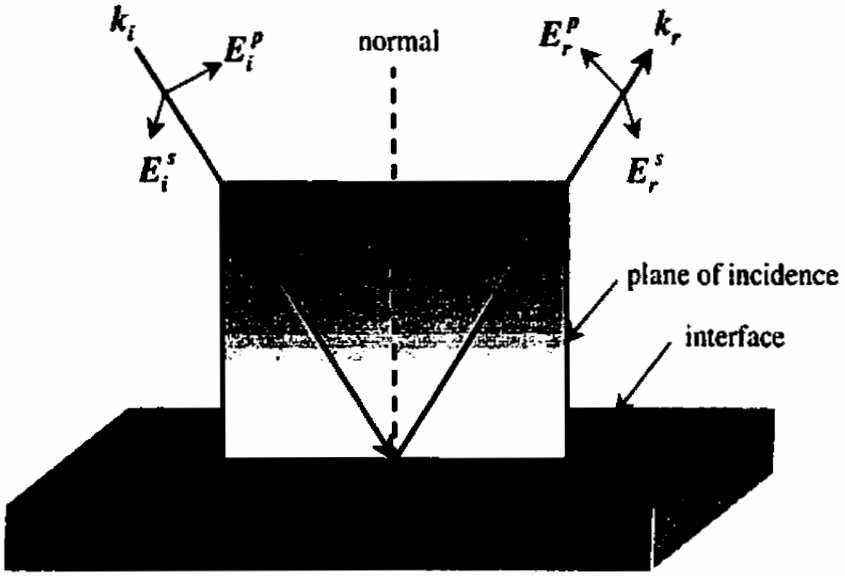

Figure 2.4: Reflection from an interface showing the parallel and perpendicular components of the electric field vectors.

$$\tilde{\rho}^s = \frac{E_{io}^s}{E_{ro}^s} \exp i(\delta_r^s - \delta_i^s), \tag{2.7}$$

where use has been made of Eqs. 2.1 through 2.4. The phase changes, $\delta_r^p - \delta_i^p$ and $\delta_r^s - \delta_i^s$, are not directly measurable. However, the ratio of p and s wave complex amplitude attenuations, $\tilde{\rho} = \tilde{\rho}^p/\tilde{\rho}^s$, yield measurable quantities. Defining the ratio of the absolute amplitude attenuations upon reflection as

$$\tan \Psi = \frac{|\tilde{\rho}^p|}{|\tilde{\rho}^s|} = \frac{E_{ro}^p}{E_{io}^p}\frac{E_{io}^s}{E_{ro}^s}, \tag{2.8}$$

and the change in phase difference upon reflection as

$$\Delta = \delta_r - \delta_i = (\delta_r^p - \delta_r^s) - (\delta_i^p - \delta_s^s), \tag{2.9}$$

then it is possible to write the complex attenuation ratio as

$$\tilde{\rho} = \frac{E_{ro}^{p}}{E_{ro}^{s}} \frac{E_{io}^{s}}{E_{io}^{p}} \exp i(\delta_r - \delta_i) = \tan \Psi \exp i\Delta. \tag{2.10}$$

Eq. 2.10 is the fundamental equation of ellipsometry, and the angles Ψ and Δ are the data which are actually measured. The measurement process is discussed in the next section.

2.2.3 Ellipsometers

How Ψ and Δ are actually measured depends on the type of ellipsometer, of which there are three general configurations: (*i*) null, (*ii*) rotating element, and (*iii*) polarization modulation ellipsometry, each one differing with respect to whether the incident or reflected (or both) polarization states are controlled. In null ellipsometry, the combination of a rotating polarizer (i.e. an optical element that allows transmission only through one axis thus producing linearly polarized light) and a rotating compensator (i.e. a phase retarder such as a quarter-wave plate) are utilized to adjust the polarization of the incident light so that the reflected light is linearly polarized and can be subsequently "nulled" by using an analyzer (i.e. polarizer placed in the reflected beam path).

In rotating element ellipsometers, a polarizer and analyzer are utilized to linearly polarize both the incident and reflected light. In this case, however, either the polarizer or the analyzer is continuously rotated so that the light reaching the detector varies with time and can be Fourier analyzed to determine Ψ and Δ. In polarization modulation ellipsometry, the incident light is linearly polarized, then modulated (by means other than a rotating element) so that the incident light has a time-dependent elliptical polarization. The *s*- and *p*-polarized components of the reflected beam are split (i.e. with a Wollaston prism) and the intensities are measured with two separate detectors.[171]

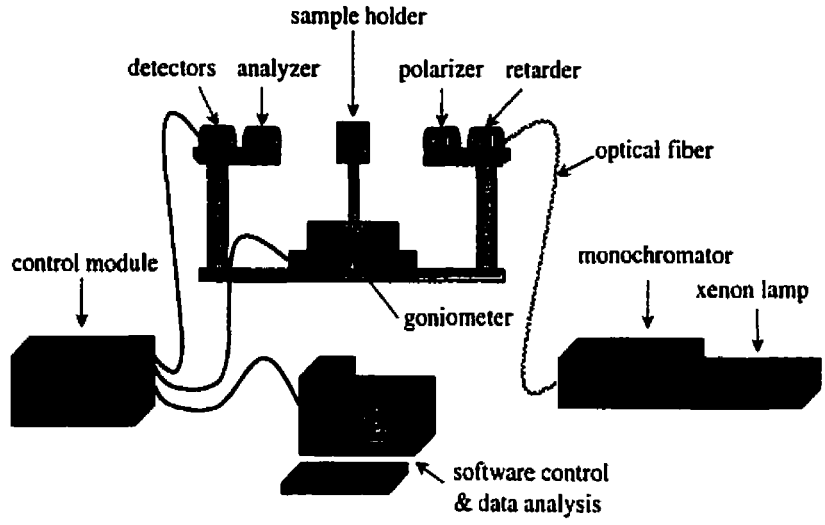

Figure 2.5: Schematic of variable-angle spectroscopic ellipsometry system from J. A. Woollam Co. Inc.

In this thesis a rotating analyzer system was used and is shown schematically in Fig. 2.5. A xenon lamp is used as a light source and monochomatic light from a monochromator is coupled with an optical fiber to a fixed polarizer producing linearly polarized light incident on the sample. The reflected light is passed through an analyzer rotating at a frequency ω producing linearly polarized light incident on the detector.

The polarization of the analyzed light takes on the time dependence given by the rotating analyzer, and, as such, the intensity measured by the detector is determined by the polarization of the light incident on the analyzer. For example, for linearly polarized reflected light, the output at the detector is a sine wave at 2ω as the analyzer goes from 100% transmission when the axis is lined up with the polarization of the reflected light, to 0% transmission 180° later. Alternatively, for circularly polarized reflected light, there is always a component that is transmitted through the analyzer, resulting is a constant DC signal from the detector.

In general, the reflected light will be elliptically polarized, and the output of the

detector is a sinusoid with a DC offset:

$$V(t) = V_o + a\cos(2\omega t) + b\sin(2\omega t), \tag{2.11}$$

where a and b are the Fourier coefficients. For a given orientation of the linearly polarized incident light with respect to the plane of incidence (i.e. the azimuthal angle, P_θ), the Fourier coefficients are determined by Ψ and Δ according to:[174,175]

$$\frac{a}{V_o} = \frac{\tan^2\Psi - \tan^2 P_\theta}{\tan^2\Psi + \tan^2 P_\theta}, \tag{2.12}$$

$$\frac{b}{V_o} = \frac{2\tan\Psi\cos\Delta\tan P_\theta}{\tan^2\Psi + \tan^2 P_\theta}. \tag{2.13}$$

The primary drawback of the system described above is the diminished accuracy in the case of linearly polarizied reflected light (i.e. $\Delta = 0°$ or $180°$). A second, less crucial, drawback is the inability to distinguish the handedness of the reflected beam (i.e. the quadrant Δ lies in). As such, all Δ values from $180°$ to $360°$ are mapped into the $0°$ to $180°$ range. Both of these drawbacks are inherent to the rotating element configuration. Both, however, can be simply alleviated by use of a rotating retarder placed in the input beam. It functions in a similar fashion as in the null configuration, except, in this case, the purpose is to shift the measured Δ values to regions of improved accuracy. Measurements using the retarder take significantly longer, and, as such, one has the option of not using it in cases where it is not necessary.

2.2.4 Complex Index of Refraction

In this section the connection is made between the experimentally determined quantity $\tilde{\rho}$ (i.e. ellipsomteric angles Ψ and Δ) and material properties via the Fresnel reflection coefficients. Reflection and refraction are governed by the electromagnetic

nature of light, in particular, by the requirement that the tangential components of **E** and **B** be continuous across boundaries between media. These boundaries are a consequence of material polarization effects[57] which are included within Maxwell's equations through the electric displacement, **D**, previously discussed in Ch. 1 and reiterated here:

$$\mathbf{D} = \epsilon_o \mathbf{E} + \mathbf{P} = \epsilon \epsilon_o \mathbf{E}. \tag{2.14}$$

In the context of reflection and refraction, it is more frequent to use the complex index of refraction, N, to account for material polarization:

$$N = \sqrt{\epsilon} = n - jk \tag{2.15}$$

where n is the absolute index of refraction, or simply the index of refraction, and k is the extinction coefficient, which defines the absorption coefficient $\alpha = 4\pi k/\lambda$ used in Lambert's law: $I = I_o \exp[-\alpha z]$.

From Maxwell's equations with appropriate boundary conditions, the complex amplitude coefficients for reflection from the interface of two materials having N_1 and N_2 are given by the well-known Fresnel reflection coefficients:[172]

$$r_{12}^p = \frac{E_r^p}{E_i^p} = \frac{N_2 \cos\phi_1 - N_2 \cos\phi_2}{N_1 \cos\phi_1 + N_1 \cos\phi_2} \tag{2.16}$$

$$r_{12}^s = \frac{E_r^s}{E_i^s} = \frac{N_2 \cos\phi_1 - N_2 \cos\phi_2}{N_1 \cos\phi_1 + N_2 \cos\phi_2} \tag{2.17}$$

where ϕ_1 is the angle of incidence and ϕ_2 is the angle at which the light is transmitted, as shown in Fig. 2.6, the two being related by Snell's law: $N_1 \sin\phi_1 = N_2 \sin\phi_2$.

Using Eqs. 2.6 and 2.7 and the Fresnel equations, one can write the complex

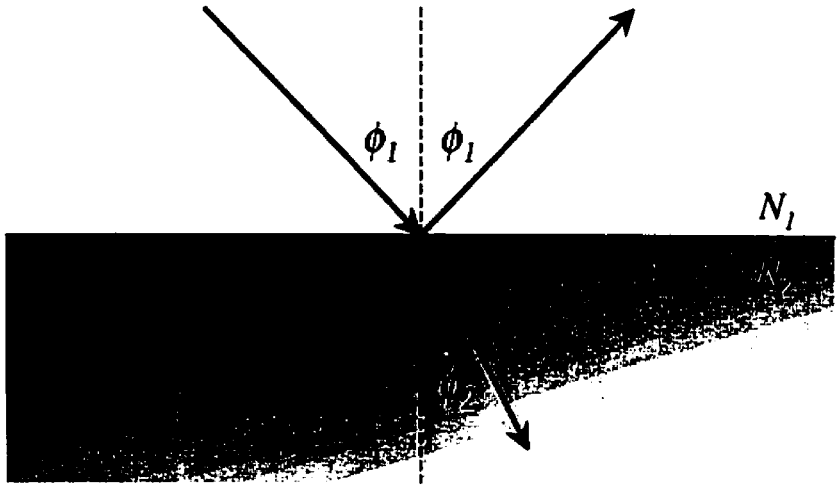

Figure 2.6: Reflection and refraction at the interface of two media having indices N_1 and N_2.

indices in terms of electric field amplitudes and phases:[176]

$$N_1 - N_2 = \tan\phi_1 \sqrt{1 - \frac{4\tilde{\rho}\sin^2\phi_1}{(\tilde{\rho}+1)^2}} \tag{2.18}$$

For the particular case of reflection from a substrate, $N_1 = n_1 = 1$ (i.e. ambient is air), Eq. 2.18 becomes[177]

$$n_2^2 - k_2^2 = n_1^2 \sin^2\phi_1 \left[1 + \frac{\tan^2\phi_1(\cos^2 2\Psi - \sin^2\Delta \sin^2 2\Psi)}{(1+\sin 2\Psi\cos\Delta)^2}\right] \tag{2.19}$$

and

$$2n_2k_2 = \frac{n_1^2 \sin^2\phi_1 \tan^2\phi_1 \sin 4\Psi \sin\Delta}{1+\sin 2\Psi\cos\Delta)^2} \tag{2.20}$$

using Eq. 2.10. Thus, in the case of a substrate, the complex index can be uniquely determined from the measured Ψ and Δ values.

For a multi-layer structure, this correspondence does not hold. Consider the simplest case, a three layer air/film/substrate structure, having indices N_1, N_2, and N_3,

respectively. In this case there are two interfaces to contend with, and, correspondingly, two sets of Fresnel equations: r_{12} for the ambient/film interface and r_{23} for the film/substrate interface. The complex amplitude coefficients are now given by:[168,172]

$$\tilde{\rho}^p = \frac{r_{12}^p + r_{23}^p \exp(-j2\beta)}{1 + r_{12}^p r_{23}^p \exp(-j2\beta)}, \tag{2.21}$$

$$\tilde{\rho}^s = \frac{r_{12}^s + r_{23}^s \exp(-j2\beta)}{1 + r_{12}^s r_{23}^s \exp(-j2\beta)}, \tag{2.22}$$

where $\beta = 2\pi(d/\lambda)N_2 \cos\phi_2$. Even if the index of the substrate, N_3, is known, there is no unique solution for the film index, N_2, due to the additional unknown, d, the film thickness. As mentioned in Section 2.2.1, this is not a critical limitation. It does, however, necessitate the use of parametric modeling which requires spectroscopic measurements. Furthermore, measurements at multiple angles of incidence are generally needed in order to constrain the model during the fitting procedure used to extract parameters.

Expressions for $\tilde{\rho}$ for any number of interfaces can be easily derived, usually using matrix methods.[174] For correct optical constant determination, it is crucial to adhere to the assumptions made when deriving the Fresnel equations, in particular, that each interface is plane and parallel. This requires careful consideration of both the surface morphology, and the structure of each underlying interface.[178]

Deviations from the ideal surface can be classified in three ways: (*i*) thickness non-uniformity, (*ii*) macroscopic roughness, and (*iii*) microscopic roughness. Thickness non-uniformity on the scale of the diameter of the probing beam has the effect of depolarizing the reflected light (i.e. the phase of the light is dependent on the location from which it is reflected). The influence of this effect can be simulated by calculating data for the structure using a series of slightly different thickness. Light incident on a surface which is macroscopically rough (i.e. having a critical dimension larger than the probing wavelength) is scattered out of the field of the detector, as mentioned in

Section 2.2.1. It does not, therefore, play a role in ellipsometric measurements, aside from, perhaps, a noiser signal due to the diminished light intensity incident on the detector.

Microscopic surface roughness (i.e. having a critical dimension much less than the probing wavelength), may, however, have a significant influence on the calculated constants since it mimics the effects of a very thin surface layer of reduced index. Incorporating this 'layer' into the optical model is particularly important in the analysis of transparent substrates since surface roughness effects can be mistaken for absorption. This can be done by modeling the layer as an effective medium (see Ch. 1), in particular, the Bruggeman model using, for example, 50% rough material and 50% over-lying material. The additional constraint on the calculated extinction coefficient provided by the incorporation of transmission spectra in the analysis is highly desired.

2.2.5 Dielectric Substrates and Films

The two main substrates used in this thesis were glass and quartz slides. The analysis of the quartz substrate will be discussed first since it provides the simplest example of ellipsometric determination of the optical constants of a material, being non-absorptive in the spectral region of interest. It also serves to point out some of the salient features in the Ψ and Δ spectra of substrate materials.

The ellipsometric spectra of quartz is shown in Fig. 2.7 together with a transmission spectrum taken at normal incidence. Ψ for a substrate material ranges from 0° to 45° (see Eqs. 2.8, 2.16, and 2.17), depending on ϕ_1, and any variation at the same ϕ_1 is due to material dispersion (i.e. wavelength dependence of the index of refraction). In the case of quartz, Ψ ranges from close to 0° at $\phi_1 = 55°$ to almost 30° at $\phi_1 = 75°$, with some dispersion evident from the variation at smaller wavelengths.

From Eqs. 2.16 and 2.17, Δ for a non-absorbing substrate is either 0° or 180° (i.e. linearly polarized incident light remains linearly polarized upon reflection), the orientation depending on whether the ϕ_1 is greater or less than the Brewster angle,

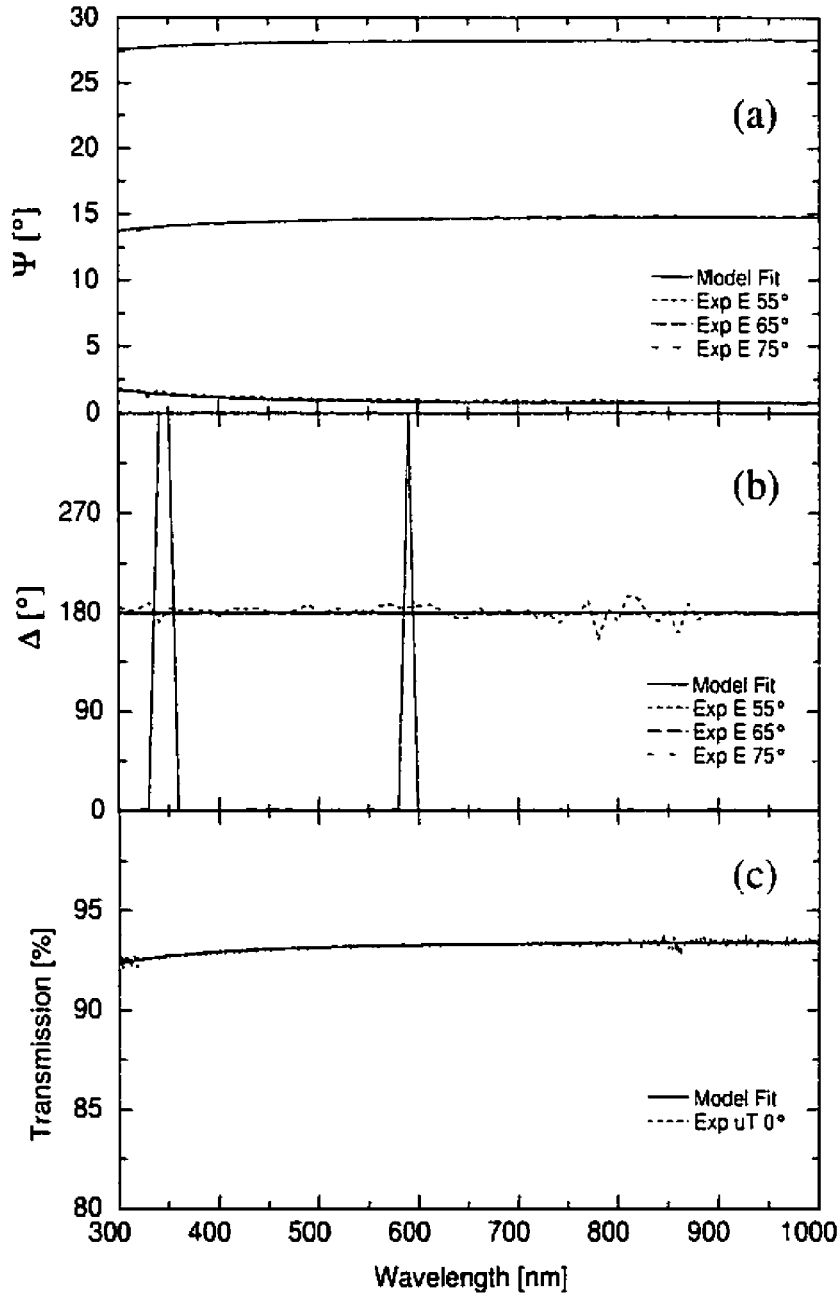

Figure 2.7: Ellipsometric (a) Ψ and (b) Δ values and (c) transmission spectrum for a quartz substrate.

ϕ_B:

$$\tan \phi_B = \frac{n_2}{n_1}, \tag{2.23}$$

at which r^p, and, hence, Ψ, are equal to zero. In the case of quartz, $55° < \phi_B < 65°$ since it is between these angles that Δ changes form 180° to 0°. Note that the jumps in Δ for $\phi_1 = 65°$ are 360° and, therefore, represent the same polarization state.

Since the measured spectra are for a substrate, and since only reflections from the surface have been collected (i.e. the substrate back-surface has been sanded), then the optical constants are simply obtained from Eqs. 2.19 and 2.20. This calculation for the spectra taken at $\phi_1 = 55°$ is shown in Fig. 2.8. The wavelength to wavelength variation in these constants is simply noise, and can be improved by increasing the averaging during measurement. This, however, substantially increases the measurement time. Alternatively, dispersion models can be applied to the measured spectra, and it is this option that lies at the heart of the power of spectroscopic measurements.

For a non-absorbing materials, there are numerous empirical models to describe the wavelength dependence of n.[179] In this thesis, the dispersion relation proposed by Cauchy[180] has been employed:

$$n(\lambda) = A_c + \frac{B_c}{\lambda^2} + \frac{C_c}{\lambda^4} + \cdots, \tag{2.24}$$

where A_c, B_c, C_c are constants to be determined. Evaluation of the dispersion parameters is usually performed via a fitting procedure whereby a merit function is defined and minimized. In this thesis, the Levenberg-Marquardt algorithm is employed to minimize a standard χ^2 type function (i.e. sum of the squares of the differences) with the difference between each measured and modeled data point weighted by the standard deviation of the data point. Applying Eq. 2.24 to the measured spectra gives the model fits shown in Fig. 2.7 and the n and k given in Fig. 2.8, the latter of which is, of course, 0, since no absorption term was included.

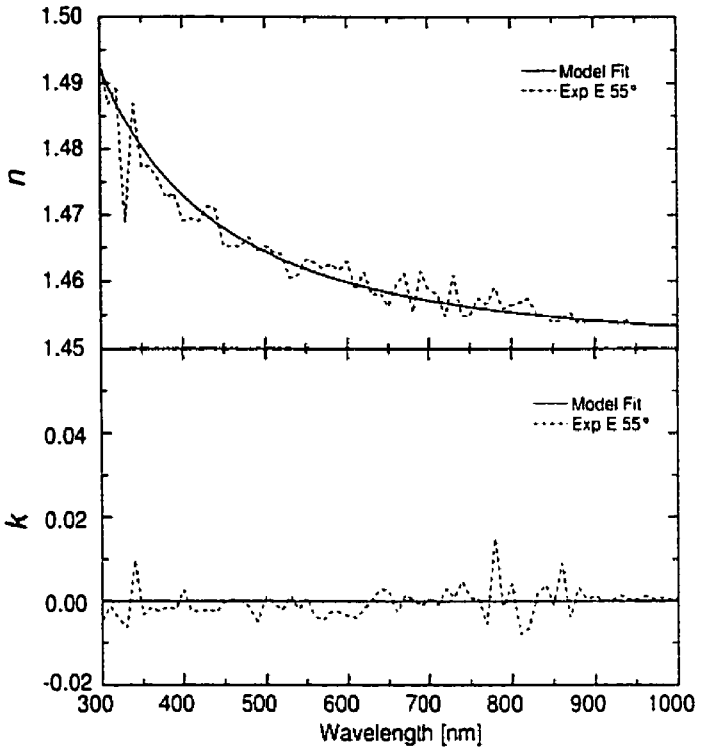

Figure 2.8: Optical contants of quartz obtained from inversion of Ψ and Δ data measured on a bulk substate. The modeled constants were obtained using a Cauchy dispersion.

The second substrate extensively used was glass, which differs from quartz in that it possesses a slightly higher index, and, more significantly, begins to absorb in the spectral region of interest. The ellipsometric and photometric data for the glass substrate are shown in Fig. 2.9. Δ and Ψ are very similar to those obtained for quartz, the small difference in index resulting in a slight shift in Ψ values. An important difference, however, is observed in the transmission spectrum, which drops rapidly for $\lambda < 350\,\text{nm}$, marking the absorption edge of glass.

Proceeding as before, n and k can be calculated from Eqs. 2.19 and 2.20, as shown in Fig. 2.10 for $\phi = 55°$. The calculated k values, however, would give 0% transmission across the visible for a 1 mm thick substrate, which is definitely not

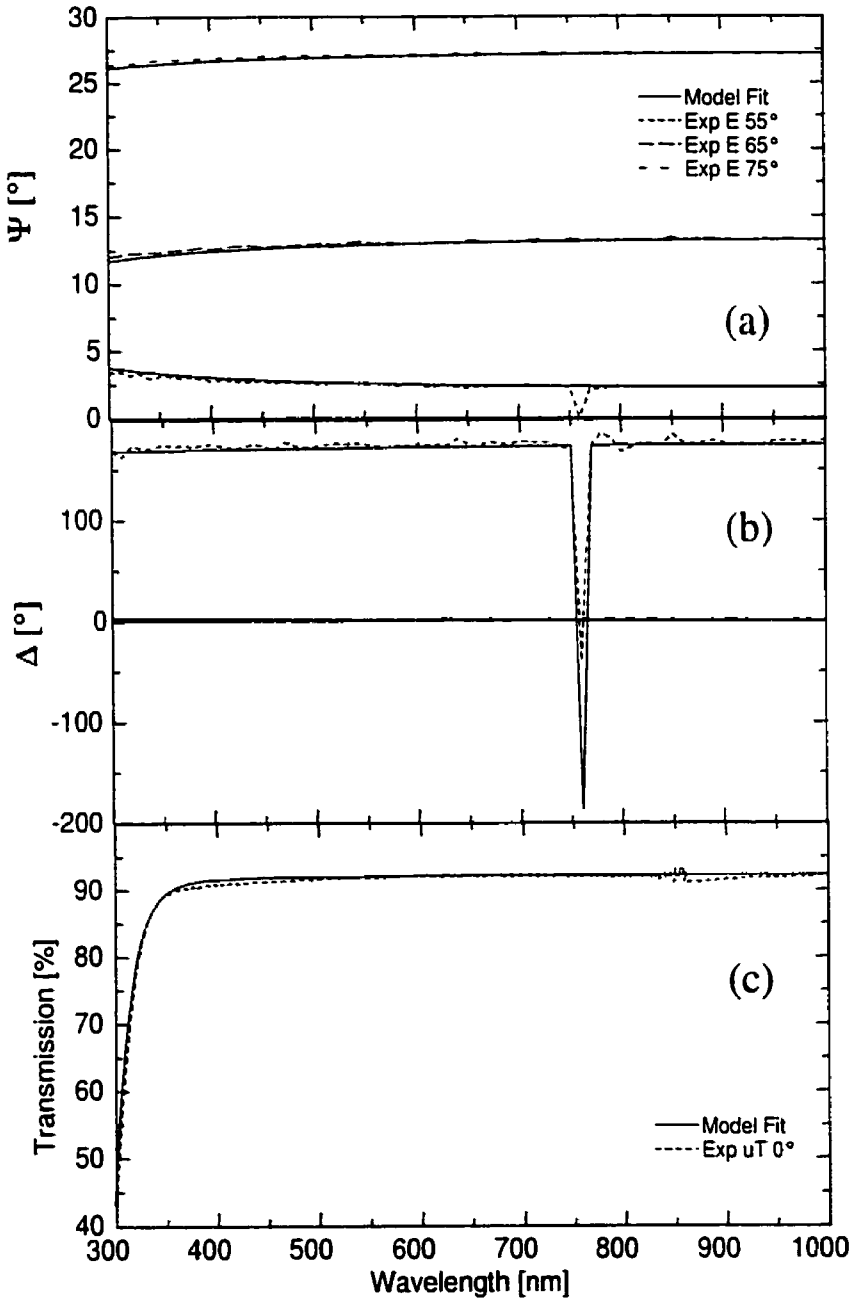

Figure 2.9: Ellipsometric (a) Ψ and (b) Δ values and (c) transmission spectrum for a glass substrate.

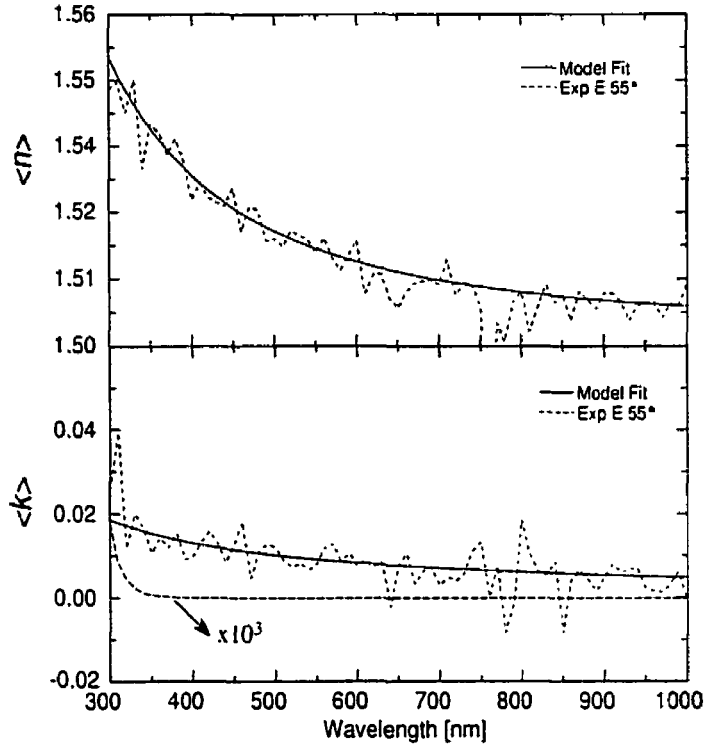

Figure 2.10: Pseudo-optical contants of glass obtained from inversion of Ψ and Δ data measured on a bulk substate. The model pseudo-constants were obtained from a two layer model comprised of a Cauchy dispersion with an Urbach absorption edge and a 2 nm Bruggeman surface roughness layer. The real k of glass is indicated by the long-dashed curve.

correct (see Fig. 2.9(c)). This error is a consequence of microscopic surface roughness which renders the assumption of a single interface invalid, To obtain the correct optical constants of glass, a model is required that accounts not only for real absorption, but also considers the influence of a surface roughness layer. (Incidently, n and k, when calculated under the incorrect assumption of a single interface, as in Fig. 2.9, are referred to as the pseudo-optical constants, $< n >$ and $< k >$).

The modeling of absorption in amorphous materials is dictated by the absence of long-range order which broadens the inter-band features and extends absorption below the band-edge. The absorption at the band-edge can be modeled in a number

of ways (see Forouhi and Bloomer[181] and Jellison and Modine[182] and references therein). Here, however, the absorption below the band-edge is of primary concern, which is usually modeled as an exponential,[183–185] the so-called Urbach tail:[186]

$$k = k_u \exp \beta_u \left[12400 \left(\frac{1}{\lambda} - \frac{1}{\gamma_u} \right) \right], \tag{2.25}$$

where k_u, β_u and γ_u are constants to be determined. Combining Eqs. 2.24 and 2.25 and inserting into a two-layer optical model with a Bruggeman surface roughness top layer gives the fitted curves shown in Fig. 2.9 and the pseudo-optical constants shown in Fig. 2.10. The latter figure also shows the true extinction coefficient of glass. (The true absolute index is indiscernible from $< n >$).

To characterize the dielectric materials which served as the embedding matrices (i.e. PPFC and SiO_2), thin films of the pure material were deposited on silicon. Although the use of silicon as the substrate prevents the inclusion of transmission spectra in the analysis, it greatly increases the sensitivity of Ψ and Δ as compared to measurements on glass or quartz due to the much higher index contrast. The typical spectra of a dielectric film on Si is shown in Fig. 2.11 for an 800 nm PPFC film. The film was deposited in an RF discharge of C_4F_8 at 250 mTorr using a gas flow of 24 sccm and an input power of 8 W. In contrast to substrate spectra, Ψ can range from 0° to 90° due to interference effects. Furthermore, the oscillations in Ψ with λ correspond to interference fringes, even though the thickness is constant, due to the equivalence of λ and d (see β in Eqs. 2.21 and 2.22).

Δ for of a film/substrate spectrum can vary, in general, from 0° to 360°. However, since $\Delta \neq 0°$ or 180°, there was no need for the retarder as in the case of the quartz and glass substrates. This being the case, Δ is limited to the range 0° to 180°, with values betweeen 180° and 360° folded back to the 0° to 180° domain. It is for this reason that the spectra in Fig. 2.11 show cusps whenever Δ approaches 180°, and equivalent cusps would be present if Δ were to approach 0°.

Analysis of the film is as before: a Cauchy dispersion model including an Urbach

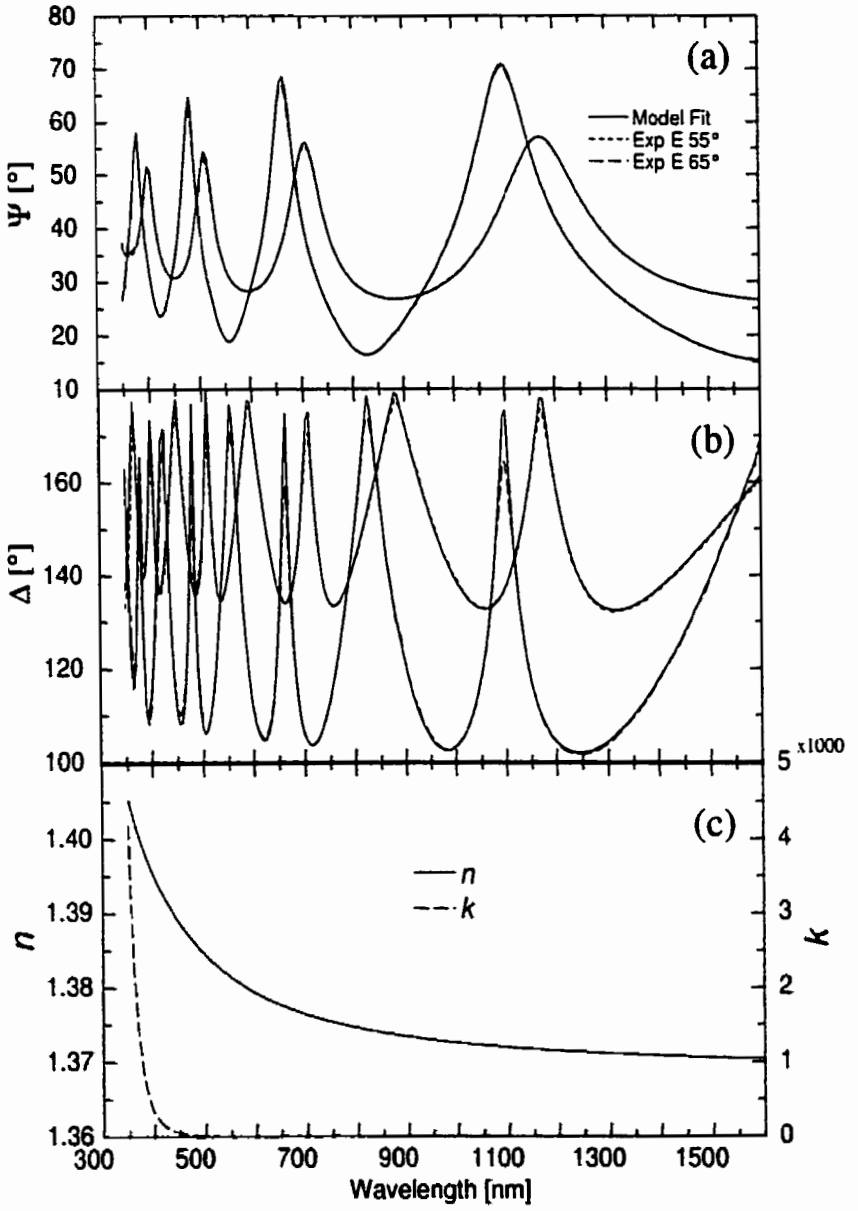

Figure 2.11: Ellipsometric (a) Ψ and (b) Δ spectra of PPFC on silicon. (c) Optical contants of PPFC determined using the Cauchy/Urbach model.

Table 2.1: Cauchy and Urbach parameters obtained form ellipsometric characterizaiton of substrate and matrix materials. Also listed are the indices of refraction at $\lambda = 633\,\text{nm}$. (At this wavelength, $k \sim 0$ in all cases.)

Material	A_c	$B_c \times 10^{-3}$	$C_c \times 10^{-5}$	k_u	β_u	n
Quartz	1.449	3.07	8.24	0	—	1.457
Glass	1.502	4.87	-2.12	6.82×10^{-7}	5.53	1.514
PPFC	1.369	3.32	15.0	4.19×10^{-3}	5.76	1.378
SiO_2:H	1.497	8.11	-28.4	0	—	1.516

absorption tail. In this case, however, the Si optical constants are required, and are taken from literature.[187] The calculated optical constants of PPFC are shown in Fig. 2.11(c). In this case, model assumptions concerning surface properties are not as crucial since reflections from the Si/PPFC interface are included in the measured Ψ and Δ values, and so no erroneous results concerning film absorption are calculated.

The results of the model analysis of the two substrate materials (quartz and glass) and the two matrix materials (PPFC and SiO_2) are summerized in Table 2.1. A note concerning β_u and γ_u in the expression for the Urbach absorption: these two parameters are obviously 100% correlated. In this thesis, the value of γ_u was always set to 3500, with only β_u used as a fit parameter. It is for this reason that only β_u is listed in Table 2.1.

2.2.6 Absorbing Film: Gold

The Ψ and Δ spectra for an RF sputtered gold film on glass are shown in Fig. 2.12. Since gold is highly absorbing in the visible, a thin film suffices to produce spectra corresponding to a substrate material (i.e. the maximum transmission of a 100 nm film is $\sim$ 1%). As such, the optical constants can be determined from direct calculation, and are also shown in the figure. Note that in this case, the permittivity, not the complex index, has been plotted, as is generally the case when describing the optical

properties of metals (see Eqs. 1.6 and 1.8).

The true optical constants of gold (i.e. of a perfect single crystal specimen) are determined by conduction electron and the inter-band transition excitations. The latter requires integration over the Brillouin zone of all possible inter-band transitions using approriate transition matrix elements. The former can be described by the theory of Drude (see Eq. 1.6) with the relaxation process determined by electron-electron and electron-phonon interactions. The constants shown in Fig. 2.12, however, correspond to a polycrystalline thin film having an unknown grain morphology, the influence of which must be addressed.

Considering first the intra-band response, the relaxation constant now contains additional contributions from grain-boundary and surface scattering. Grain-boundary scattering in the case of uniform, randomly oriented grains is not critical in that it can simply be incorporated within an effective relaxation constant. Oriented grains, however, will lead to an anisotropic response, and, if not uniform thoughout the film, a dependence on thickness. Surface scattering may or may not affect the response depending on whether the scattering is diffuse or specular, respectively,[155] which will be determined by the surface morphology.

With regard to the inter-band response, the most critical effects of polycrystallinity are void content and strain-induced lattice deformation. The effect of void content is to reduce the amount of polarizable material per unit volume, resulting in a decrease in $\Im[\epsilon_m]$.[188] Strain, on the other hand, will influence the inter-band edge,[13] and, more significantly, broaden features in the imaginary inter-band spectrum related to inter-conduction band transitions.[14] Surface roughness will also influence the inter-band spectrum, resulting, in particular, in smaller calculated $\Im[\epsilon_m]$ values.

Modeling of these effects is not, in itself, difficult, if there exists a simple expression describing the true optical reponse. In the intra-band region, there exists such an expression: the Drude equation (i.e. Eq. 1.6). In this case, film anisotropy, under the assumption of a columnar grain structure, can be simply treated using a uniax-

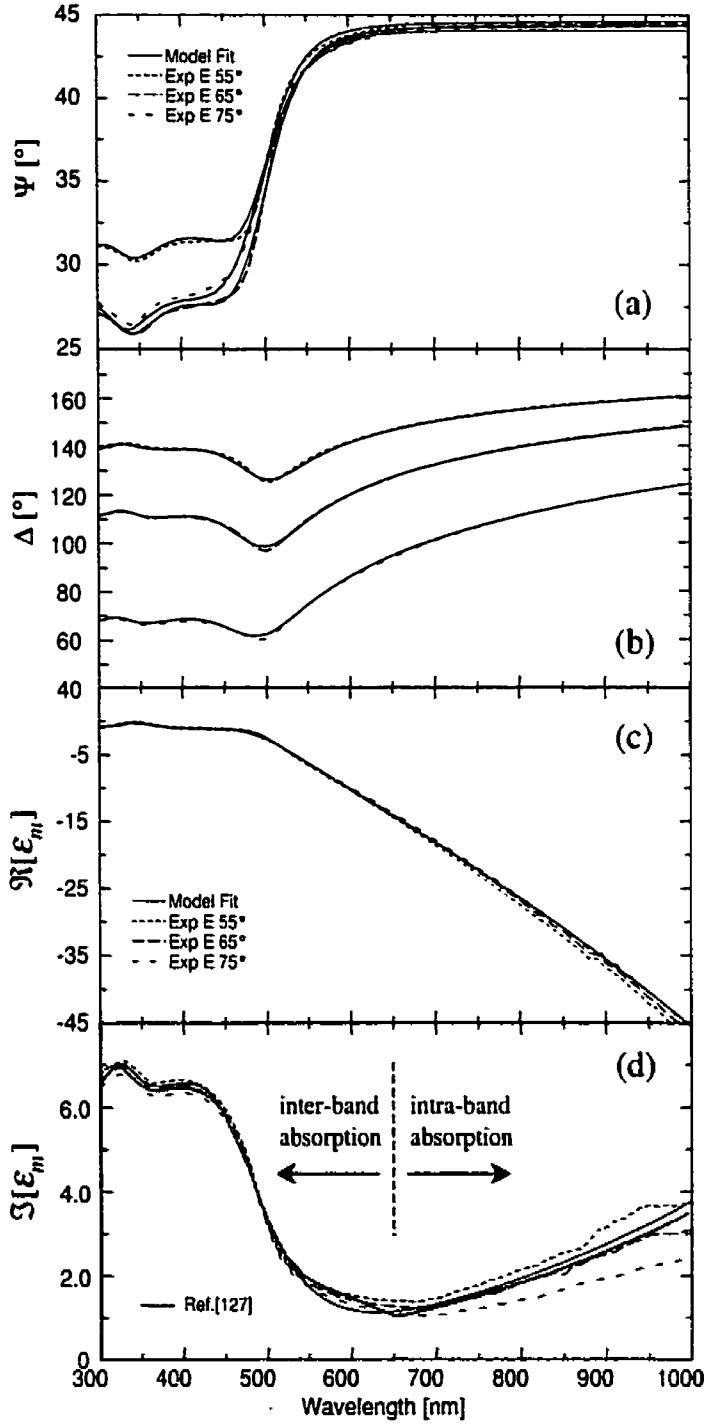

Figure 2.12: Ellipsometric (a) Ψ and (b) Δ spectra of an RF sputtered gold film on glass. (c) Optical contants determined from direct calculation. The model curves correspond to fits of the $\phi_1 = 65°$ spectra.

ial dielectric function with two relaxation constants describing the electron motion parallel to and in the plane of the film. Combined with the use effective mediums to account for both the void content and surface roughness would account for most of the observed effects. In the inter-band region, however, such an expression does not exist, and the above effects cannot be incorporated into an optical model. As such, one must be content with using the pseudo-reponse given in Fig. 2.12.

There is, however, an angle dependence in both inter- and intra-band regions of the pseudo-response. Whether this is a material property (i.e. anisotropy) or a consequence of the assumptions of a plane, smooth surface is not clear. It is more than likely a combination of the two (i.e. oriented grains under strain and a surface roughness layer). From the above discussion, the response which gives the largest values for $\Im[\epsilon_m]$ in the inter-band region and the lowest values in the intra-band region should be most representative of the true constants of gold. From Fig. 2.12, the best inter-band response is obtained from the $\phi_i = 55°$ scan while the best intra-band response is given by the $\phi_i = 75°$ scan. The reponse predicted from the spectra at $\phi_i = 65°$ have been used as the optical constants of gold since these most closely resemble the generally accepted literature values of $\Im[\epsilon_m]$ for gold[187] as measured by Thèye,[127] also shown in Fig. 2.12.

To 'model' the inter-band response (i.e. ϵ_{core} in Eq. 1.8) a series of six Lorentz oscillators were fit to the Ψ and Δ spectra at $\phi_i = 65°$ by varying their widths and amplitudes. The intra-band term was incorporated using the Drude equation (i.e. Eq. 1.6) with ω_p and τ_B as fit parameters. The best fit to the experimental Ψ and Δ data, as well as the model dielectric function, are shown in Fig. 2.12. The inter- and intra-band contributions to the the dielectric function have already been presented in Ch. 2 (see Fig. 1.3).

2.3 Additional Characterization Techniques

2.3.1 Photometry

Photometry is the measurement of the change in intensity (i.e. the square of the electric field amplitude) upon reflection from and transmission through a material, in particular, the reflectance, $R^j = \frac{|E_r^j|^2}{|E_i^j|^2}$, and the transmittance, $T^j = \frac{|E_t^j|^2}{|E_i^j|^2}$, where the superscript j indicates the polarization (i.e. p- or s-wave). The relation to material properties are obtained from the absolute squares of the Fresnel reflection and transmission coefficients, the former of which have already been presented in Section 2.2.4, while the latter are given by[172]

$$t_{12}^p = \frac{E_t^p}{E_i^p} = \frac{2N_1 \cos\phi_1}{N_2 \cos\phi_1 + N_1 \cos\phi_2}, \tag{2.26}$$

$$t_{12}^s = \frac{E_t^s}{E_i^s} = \frac{2N_1 \cos\phi_1}{N_1 \cos\phi_1 + N_2 \cos\phi_2}. \tag{2.27}$$

For a single interface (see Fig. 2.6), $R^j = \mid r_{12}^j \mid^2$ and $T^j = \mid t_{12}^j \mid^2$. In the case of a film covered substrate, the reflectance and transmittance for each polarization become[172]

$$R = \frac{\mid r_{12} \mid^2 + \mid r_{23} \mid^2 e^{j2(\beta^* - \beta)} + r_{12}^* r_{23} e^{-j2\beta} + r_{12} r_{23}^* e^{j2\beta^*}}{1 + \mid r_{12} \mid^2 \mid r_{23} \mid^2 e^{j2(\beta^* - \beta)} + r_{12} r_{23} e^{-j2\beta} + r_{12}^* r_{23}^* e^{j2\beta^*}} \tag{2.28}$$

and

$$T = \frac{N_3}{N_1} \frac{\mid t_{12} \mid^2 \mid t_{23} \mid^2 e^{j(\beta^* - \beta)}}{1 + \mid r_{12} \mid^2 \mid r_{23} \mid^2 e^{j2(\beta^* - \beta)} + r_{12} r_{23} e^{-j2\beta} + r_{12}^* r_{23}^* e^{j2\beta^*}}, \tag{2.29}$$

respectively, with β as before (see Eqs. 2.21 and 2.22). Since the intensity is crucial in photometric measurements, spectrophotometers are generally dual beam instruments, one beam used as a reference, and the other incident on the sample. The measurements are usually made at near-normal incidence (e.g. $\phi_1 \sim 7°$), and are,

for all intent and purposes, polarization insensitive (i.e. $R^p = R^s$ and $T^p = T^s$ at $\phi_1 = 0$).

Spectrophotometric measurements were utilized in this work in a variety of ways. Transmission spectra were always used in the analysis of the composite films since they provided an additional constraint on the optical model. They also helped visualize the surface plasmon absorption band since, in the absence of strong interference effects and severe scattering, a transmission spectrum is simply an inverted absorption spectrum (i.e. $R + T + S = 1 - A$). Oblique-incidence polarized transmission measurements were also used to investigate film anisotropy (see Fig. 1.7). Finally, measurements were made using an integrating sphere with which one can determine the reflection due to both specular and diffuse scattering,[189] the latter of which becomes important for large particle films (see Fig. 1.1).

2.3.2 Transmission Electron Microscopy

Transmission electron microscopy (TEM) was used in this thesis solely as an imaging tool to determine the metal particle size, in-plane shape, and concentration. The analysis of the images is straightforward due to the disparity in electron transmission between the matrix material and the metal particles (i.e. for 100 kV electrons, a 50 nm thick film of matrix material is still highly transmitting, whereas a few nanometers of gold is completely opaque).

The analysis was restricted to films containing one mono-layer of metal particles to avoid complications arising from a 3-D dispersion. Sample preparation consisted of the deposition of the films to be analyzed on standard carbon-coated copper grids. The images were taken with a Philips CM-30 microscope operated in bright-field mode. 100 – 300 kV electrons were used and images were taken at 52k to 550k times magnification. Although some electron beam effects were observed in the case of the Au/PPFC films (the matrix material shriveled up), no *in situ* variation of the particle size or shape was observed.

2.3.3 X-ray Photoelectron Spectroscopy

X-ray photoelectron spectroscopy, also known as electron spectroscopy for chemical analysis (ESCA), utilizes the photoelectric effect to determine the binding energy, BE, of electrons in atomic orbitals:

$$KE = h\nu - BE - \phi_s, \tag{2.30}$$

where KE is the kinetic energy of the emitted electron, $h\nu$ is the energy of the incident photon, generally Mg Kα (1253.6 eV) or Al Kα (1486.6 eV) x-rays, and ϕ_s is the work function of the spectrometer. Although the penetration depth of soft x-rays is of the order of micrometers, escape depths for electrons is limited to a few nanometers (e.g. the mean free path for 1.5 keV electrons in gold is 2 nm[190]), hence the measured binding energies correspond to electrons emitted from the first few atomic layers.

Typical spectra consist of a series of peaks corresponding to emission from different core levels (i.e. s, p, d, and f), the latter three of which form doublets due to spin-orbit splitting (i.e. $p_{1/2}$, $p_{3/2}$, $d_{3/2}$, $d_{5/2}$, $f_{5/2}$, $f_{7/2}$). For metals, there are also low intensity peaks $10 - 20$ eV below E_F correponding to emission from solid-state energy bands (i.e. the valence band). The linewidths are determined by the convolution of the natural linewidth (i.e. the lifetime of the 'hole' resulting from the photo-ionization process), the spectral width of the x-ray beam, and an instrumental contribution. For metals, the linewidths can exihibit considerable asymmetry due to coupling with conduction electrons.

XPS has been particularly useful in studying the electronic properties of small metal particles (see, for example, Mason[34] and references therein). In particular, the core-level BE and linewidth as well as the width and centre energy of the valence band have been shown to be particle size-dependent. The origin of these effects, which are both metal and matrix dependent, still remains somewhat of a controversy.[131,191–195]

Chapter 3

Article 1: Au/Fluoropolymer Films

The emphasis of this article is on the determination of the microstructural dependence of nanocomposite films on glow discharge parameters and post-deposition thermal treatments using the all-optical characterization method. Finite size effects in core response of the gold are not discussed; there is a single comment in this regard, stating only that 'the agreement between model and experimental spectra is poorer at shorter wavelengths'.

Compared to the other systems studied, the Au/PPFC films contained the smallest particles. For the specific fabrication conditions used, particle growth arising from atomic migration on the growing film surface during deposition was limited. Furthermore, particle growth arising from atomic or particle diffusion during anneal was limited by the thermal stability of the polymer. In particular, the results of the article suggest that at 160°C liquid-like coalescence of particles larger than $\sim 5\,\mathrm{nm}$ is supressed when embedded in a PPFC matrix. This can be compared to the behaviour observed in the supported particle system (Chapter 5), in which much larger particles could be obtained for a similar thermal treatment. These results illustrate the important role played by the matrix material with regard to atomic migration on the particle surface, responsible for the liquid-like coalescence of solid particles.

Spectroellipsometric Characterization of Plasma-Deposited Au/Fluoropolymer Nanocomposite Films

Dan Dalacu and Ludvik Martinu

Recieved 13 November 1998; accepted 5 February 1999
J. Vac. Sci. Technol. A, **17**(3), 877-883, May/June 1999

3.1 Abstract

Nanocomposite thin film structures are presently being studied because of their interesting nonlinear optical properties. The microstructure of plasma-deposited nanocomposite films consisting of gold particles embedded in a plasma-polymerized fluorocarbon matrix was fully characterized using a generalized Maxwell-Garnett effective medium approach applied to ellipsometric data. The particle size dependence of the dielectric properties of gold was treated classically using a broadening parameter, A, equal to 0.25, as determined from TEM analysis. In general, the model predicted correctly the dependence of microstructural characteristics on glow discharge parameters and post-deposition thermal treatments. However, careful interpretation of the model fit parameters is necessary in both the high gold volume fraction limit and small particle size limit. For the former, misleading results with respect to particle size and shape may be obtained due to aggregation effects, the onset of which was determined to occur at a gold volume fraction of about 30%. For the latter, deviations from the classical description of the permittivity of gold nanoparticles (occurring for particles smaller than 9 nm) can lead to misleading results with respect to particle shape.

3.2 Introduction

Metal nanoparticles embedded in dielectric matrices have been produced for centuries for their aesthetic value as colored art glassware. More recently their spectrally selective properties have been considered for such applications as photothermal conversion[196] and infrared furtivity.[18] The peculiar optical response of these materials stems from the excitation of surface plasmons[197] in the metal particles which is resonant in the uv or visible part of the spectrum. The exact frequency of the surface plasmon resonance is dependent on the dielectric properties of the metal and the surrounding matrix, as well as on the detailed microstructural characteristics of the nanocomposite.

Currently, these nanocomposites are of interest for their nonlinear optical properties as they possess a large effective third-order nonlinear optical susceptibility,[19] χ^3_{eff}, due to an enhanced local electric field inside the metal nanoparticles at the SPR. The value of χ^3_{eff} will depend on the nonlinear susceptibility of the metal itself, the volume fraction of the metal incorporated in the matrix, and on the local field enhancement factor; the latter being sensitive to the detailed microstructure of the nanocomposite film.

The primary interest in our laboratory is the nonlinear optical properties of dielectric matrices containing nanoparticles. Such nanocomposite materials can be fabricated by hybrid vacuum methods using a simultaneous combination of the deposition techniques such as evaporation, sputtering, plasma polymerization and plasma-enhanced chemical vapour deposition (for a review see, for example, Abeles[137] and Biederman and Martinu[152]). In order to obtain desirable nonlinear properties, the film microstructure has to be optimized in terms of the concentration, size and shape of the metal particles. This, in turn, requires a precise knowledge of the effect of fabrication conditions on the microstructural characteristics, and availability of a straightforward method to evaluate this microstructure.

In the present work the nanocomposite materials were obtained by simultaneous

plasma polymerization of a fluorocarbon gas, and magnetron sputtering of gold.[157, 198] We apply variable angle spectroscopic ellipsometry as a sensitive, non-invasive method ideal for microstructural characterization. Further benefits of ellipsometric characterization include the facility of measurement (as compared to TEM analysis where sample preparation can be arduous and measurements destructive), and no restriction on film thickness (as compared to transmission measurements where the thickness is limited by the film absorption). The aim of the study is thus two-fold: first to verify the feasibility of ellipsometric measurements as a useful technique for microstructural characterization of nanocomposite films, and second, to characterize the effect of deposition parameters and post-deposition annealing on the film microstructure.

3.3 Experimental Methodology

3.3.1 Film Preparation

The composite films were prepared by simultaneous plasma polymerization of a fluorocarbon (octa-fluoro-cyclobutane, C_4F_8) and sputtering of gold onto glass substrates. The depositions were performed in a simple RF (13.56 MHz) diode reactor (see, for example, Martinu[198]) consisting of a 50 mm diameter RF-powered magnetron head with a gold target, and a grounded substrate holder placed at a distance of 50 mm. The experiments were carried out at a total gas flow rate of 20 sccm. Fragments (free radicals) of the C_4F_8 are formed in the plasma due to inelastic collisions of electrons, and they contribute to the formation of an amorphous fluorocarbon plasma polymer matrix into which gold atoms are simultaneously incorporated.[152]

The microstructure of these nanocomposite films depends on the arrival rate of the principal film constituents (mostly CF_x radicals and gold atoms), and the surface conditions such as substrate temperature and energy of bombarding energetic particles. In the present study the main parameters used to control the film microstructure were the RF input power (20 to 30 W), the gold target negative bias voltage, U_B (-55

to −70 V), the working gas pressure (10 to 20 mTorr), and the C_4F_8:Ar flow ratio (1:9 to 1:4).

The films were subjected to a 10 hour post-deposition anneal at 100°C (unless otherwise stated) to avoid aging effects.[199] Specifically, the microstructure of these types of nanocomposite films have been observed to change with time due to the diffusion of atomic gold or very small gold grains and subsequent coalescence resulting in the growth of larger particles at the expense of smaller ones. This phenomenon was seen to occur at room temperature over a period of months.[199] In our study, the post-deposition anneal has thus two purposes: (i) stabilization of the film with respect to microstructure, and (ii) narrowing of the particle size distribution.

3.3.2 Film Characterization

The optical data (ellipsometric angles Ψ and Δ) were measured from 300 nm to 1600 nm using a variable-angle spectroscopic ellipsometer (model VASE from the J.A. Woollam Co., Inc). Additional normal-incidence transmission measurements were made using a double-beam spectrophotometer (model Lamda 19 from Perkin-Elmer). Transmission electron microscopy was performed on samples deposited on carbon-coated copper grids using a Philips CM30 microscope. X-ray photoelectron spectroscopy analysis of the fluoropolymer matrix was performed in a VG ESCALAB 3 Mark II instrument with a non-monochromated MgK_α source (1256.6 eV) and a 0.8 eV resolution.

3.4 Microstructural Characterization using the Effective Medium Approach

The high gold volume fraction of the films in this study necessitates the use of an effective medium for characterization as opposed to the exact treatment of Mie.[5] Therefore, the optical response was modeled using the Maxwell-Garnett[4] effective

medium theory modified by Cohen et al:[63]

$$\frac{\epsilon_{eff} - \epsilon_h}{L\epsilon_{eff} + (1-L)\epsilon_h} = p\frac{\epsilon_m - \epsilon_h}{L\epsilon_m + (1-L)\epsilon_h}, \tag{3.1}$$

where p is the volume fraction of gold, and ϵ_{eff}, ϵ_m and ϵ_h represent the dielectric response of the effective medium, the gold inclusions, and the fluoropolymer host, respectively. Note that this model assumes that the filling is low enough so that the particles are well isolated (i.e. no aggregation effects) and that the particle size is small compared to the probing wavelength so that there are no retardation effects (i.e. quasi-static approximation).

The depolarization factor L is an average screening parameter to account for variations in particle shape, and it defines the Wiener limits, namely $L = 0$ for no screening (all particle boundaries parallel to the applied field) and $L = 1$ for maximum screening (all boundaries perpendicular to the applied field).[62] The original M-G equation is obtained for spherical particles (i.e. $L = 1/3$). The incorporation of a depolarization factor into the model is necessary since the composite films may, in general, be slightly uniaxial with the axis of symmetry normal to the film plane. We justify the use of Eq. 3.1 at different angles of incidence by considering that for weakly anisotropic films the deduced dielectric response obtained assuming isotropy is most representative of the response in the plane of the film (i.e. $\epsilon_{eff} \approx \epsilon_{||}$).[200]

The dielectric functions of the two components in the effective medium, as well as the glass substrate, were determined separately from ellipsometric measurements. The dielectric properties of the polymer was modeled by a three-term Cauchy dispersion with an Urbach absorption edge in the uv region:

$$\epsilon_h^{1/2} = A_c + \frac{B_c}{\lambda^2} + \frac{C_c}{\lambda^4} - ik_u \exp\left[\beta_u(12400(\frac{1}{\lambda} - \frac{1}{\gamma_u}))\right]. \tag{3.2}$$

The optical response of gold was modeled separately in the inter-band and intra-band regions, the former being described by a series of Lorentz oscillators, and the latter

by the Drude free electron model:

$$\epsilon_m = \epsilon_{core} + 1 - \frac{\omega_p^2}{\omega(\omega + i/\tau_B)}, \tag{3.3}$$

where ω_p is the plasma frequency and τ_B is the free electron relaxation lifetime determined by scattering processes in the bulk material.

When Eq. 3.3 is applied to metal nanoparticles with radii comparable with or smaller than the electron mean free path, collisions of the conduction electrons with the particle surface become important. To account for this additional source of scattering, $1/\tau_B$ in Eq. 3.3 is replaced by an effective collision frequency, Γ:[85]

$$\Gamma = \frac{1}{\tau_B} + \frac{A\nu_F}{R}; \tag{3.4}$$

ν_F is the electron Fermi velocity (1.39×10^8 cm/sec[44]), R is the particle radius, and A is a constant which depends on the details of the scattering process at the particle surface ($A = 1$ for isotropic scattering, and 0.75 for diffuse scattering). Note that the model described by Eqs. 3.3 and 3.4 assumes that the inter-band response of the metal nanoparticles is the same as in the bulk material. It has been shown that this is the case for particles larger than about 2 nm.[75]

Equations 3.1 through 3.4 can be incorporated into a multilayer optical model (air/film/substrate)[168] with four free parameters which can be fit (i.e. using the Levenberg-Marquardt method) to the ellipsometric data in order to extract the microstructural characteristics, namely film thickness, d, gold filling, p, particle radius, R, and depolarization, L.

An example of such a fitting procedure for $\Psi(\lambda)$ and $\Delta(\lambda)$ measured at 55°, 65° and 75° is shown in Fig. 3.1. The extracted parameters are $d = 85.1$ nm, $p = 27.3\%$, $R = 16.8$ nm, $L = 0.377$ and the mean square error (MSE) of the fit was 3.1. To verify that the best-fit result obtained from the modeling process is unique, the correlation between each parameter was calculated from the covariance matrix.[174] Strong corre-

lation exists between the particle size parameter and the film thickness, and between the filling and the depolarization factor. Including transmission data in the fitting routine decreases these correlations, especially for the former pair, without significant changes in the extracted parameters. For the latter pair, significant correlation persists, but it is not severe enough to render the solution not unique.

The particle size above was calculated assuming isotropic scattering of the electrons at the metal surface (i.e. $A = 1$ in Eq. 3.4). Fig. 3.1 also shows the measured and calculated (using the dielectric function from the fit) normal incidence transmission, T(λ). All three spectra show very good agreement across the entire wavelength range measured, except for a slightly poorer agreement at shorter wavelengths ($\lambda < 500$ nm).

Comparison of particle size extracted from the ellipsometric data with those obtained from TEM micrographs revealed a systematic discrepancy, the former being approximately four times larger. In order to obtain correct particle size from the ellipsometric data it was found necessary to use a value of $A = 0.25$ in Eq. 3.4. More will be said about this choice in Section 3.6.

3.5 Results

The microstructural characteristics (d, p, R, L) extracted from the fit of Eq. 3.1 to the ellipsometric data for films grown under different deposition conditions are summarized in Table 3.1. Using this approach a systematic investigation of the influence of different glow discharge parameters (input power, working pressure, gas flows) on the microstructure was performed. These parameters are represented in Table 3.1 by the target bias (U_B), working pressure (P), percent fluorocarbon (%FC), and percent argon (%Ar). Table 3.1 also lists the MSE for each fit which are, for the most part, between 3 and 4, as is the value for the fit in Fig. 3.1. This demonstrates that, in general, the model is able to reliably reproduce the dielectric function of the films.

The different discharge parameters can be classified into two groups; (i) those

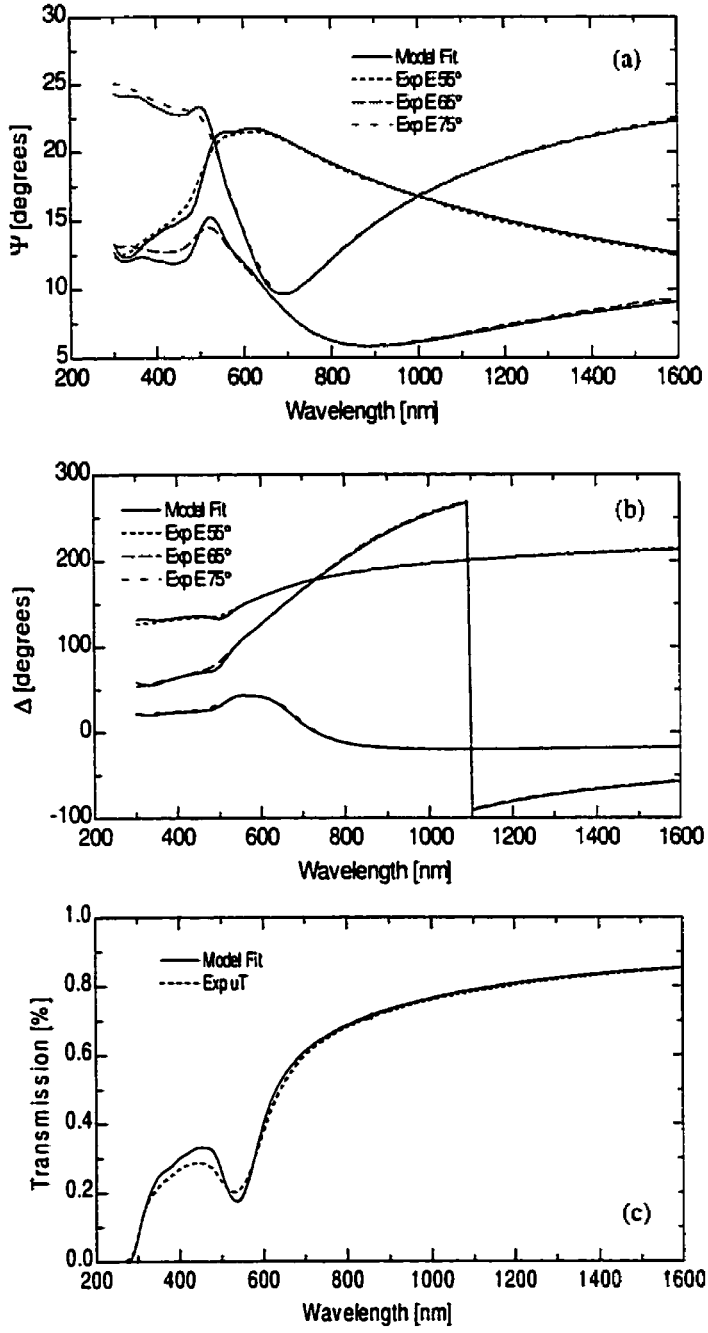

Figure 3.1: Measured ellipsometric data and model fit for sample J25D: (a) Ψ, (b) Δ, and (c) normal incidence transmission.

Table 3.1: Results of microstructural characterization for samples grown under different deposition conditions. All films were annealed at 100°C for 10 hours.

Sample	U_B (V)	P (mT)	%Ar	%FC	MSE	d (nm)	p (%)	L	R (nm)
J25F	-55	10	90	10	3.3	76.1	19.0	0.421	3.3
J25E	-60	10	90	10	3.8	73.6	25.3	0.355	3.6
J25D	-65	10	90	10	3.1	85.1	27.3	0.377	4.2
J25B	-70	10	90	10	4.5	101.8	29.9	0.330	4.3
J22A	-70	10	85	15	3.1	166.3	20.9	0.388	3.5
J22B	-70	10	80	20	3.8	187.4	18.8	0.391	3.0
J24B	-70	10	85	15	4.1	236.8	18.4	0.446	3.1
J24C	-70	10	80	20	11.4	286.5	16.8	0.502	2.6
F14A	-65	15	90	10	4.0	124.5	20.3	0.372	2.9
F14B	-65	20	90	10	4.7	153.0	15.9	0.423	2.7

which primarily affect the plasma polymerization rate (%FC, %Ar, P), and (ii) those which primarily affect the gold sputtering rate (U_B). The gold filling dependence on deposition rate for the first group is shown in Fig. 3.2a. It is seen that the deposition rate increases most significantly with increased monomer flow as expected for a polymerization reaction limited by monomer supply. Decreasing the argon flow has a similar effect since deposition at the same pressure requires a relative increase in the concentration of monomers. Increased pressure results in an increased plasma polymerization rate through an increase in the concentration of CF_x radicals. For this case, however, the increased scattering of sputtered gold atoms with increased pressure results in a smaller filling for equal deposition rates.

Alternatively, the gold filling can be varied at a nearly constant deposition rate (case ii) through the input power. The extracted fillings are comparable with those determined from the frequency changes in a quartz crystal microbalance measured for films grown under similar deposition conditions.[198] The gold filling dependence on U_B is shown in Fig. 3.2b. Also shown in this figure is the increase in particle size with increased input power as expected from previous results.[201]

The details of the particle size dependence on the deposition parameters is washed

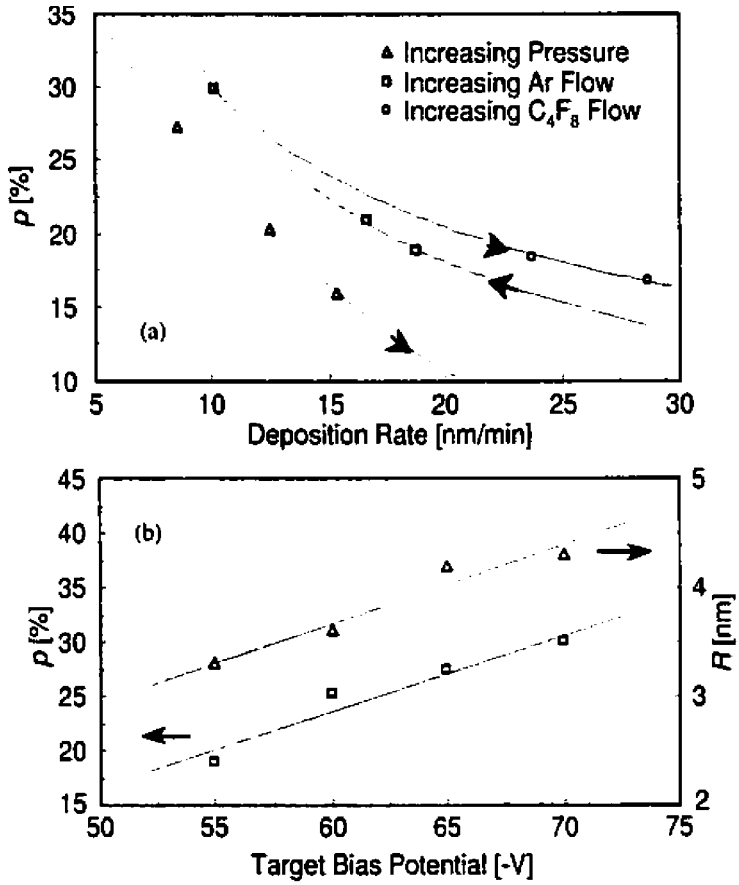

Figure 3.2: Evolution of gold volume fraction as a function of glow discharge parameters: (a) filling related to the plasma polymerization rate, and (b) filling related to the gold sputtering rate.

out due to the post-deposition annealing. However, the size of embedded clusters was generally observed to increase for increased filling values in agreement with previous results.[202] The radii for all samples versus filling are shown in Fig. 3.3a. A general dependence of the depolarization factor on gold filling was also observed. For low filling films, the depolarization factor was greater than 1/3 and decreased with increased filling. The depolarization versus filling for all samples is shown in Fig. 3.3b.

A study of the effect of thermal annealing on film microstructure was undertaken. The thermal treatment was carried out at the glass transition temperature of the

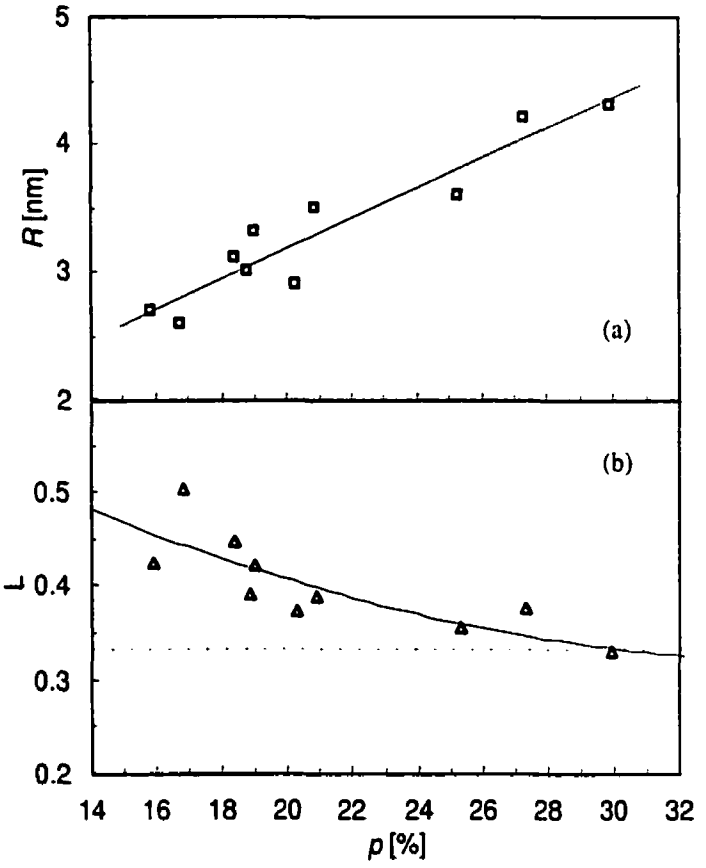

Figure 3.3: Dependence of (a) particle radius and (b) depolarization factor on the gold volume fraction. Dotted line shows expected depolarization factor for spherical particles (i.e. $L = 1/3$).

polymer, ~160°C.[162] At this temperature, a densification of the polymer occurs as a consequence of a rearrangement and possibly a curing effect in the crosslinked structure of the plasma fluoropolymer.[203] The thermal treatment also results in some defluorination of the films. This latter effect was quantified by XPS analysis which showed a decrease in the [F]/[C] ratio from 1.56 to 1.45 for a two hour anneal. Neither of the above two effects were significant enough to alter the optical properties of the fluoropolymer matrix as determined ellipsometrically.

The parameters extracted from ellipsometric measurements on a film subjected

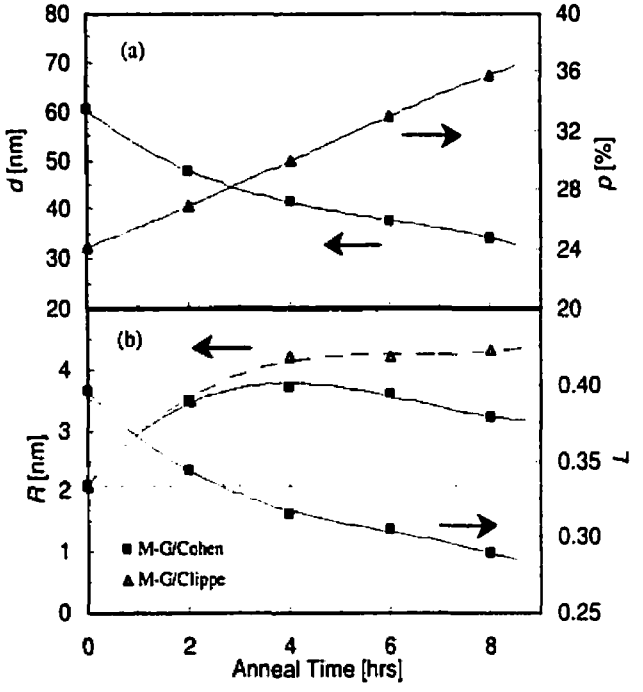

Figure 3.4: Evolution of microstructural parameters with post-deposition annealing time at 160°C: (a) film thickness and gold filling and (b) particle radius and depolarization. Calculation of corrected R values (triangles) is discussed in Section 3.6. Dotted line shows expected depolarization factor for spherical particles (i.e. $L = 1/3$).

to a post-deposition anneal for various durations are shown in Fig. 3.4. The polymer densification is evident from the decrease in film thickness, and it results in an increasing gold filling with increasing anneal duration (Fig. 3.4a). The particle radius is seen to increase sharply with the first anneal then it peaks after four hours, and it subsequently decreases for fillings greater than 30% (Fig. 3.4b). Note that the particle size extracted from the as deposited film is fictitiously low due to additional SPR broadening as a consequence of the larger distribution in particle size. The depolarization, on the other hand, is seen to continually decrease from values greater than 1/3, to values less than 1/3 as the filling increases above 30%.

3.6 Discussion

The general trend in the microstructure evolution with filling (whether the filling is varied through glow discharge parameters or post-deposition annealing) for gold/fluoropolymer films is well documented.[166,204] The particles are spherical and well separated at low fillings and increase in size with increased filling, becoming more irregular in shape as the size increases. As the filling approaches the threshold for percolation worm-like clusters develop which evolve into a labyrinth-type structure for fillings at and above percolation.

The influence of these microstructural changes on the optical properties of the films is exemplified by their effect on the shape and position of the SPR band. To elucidate this point, we have calculated the absorption spectra, $\alpha(\lambda)$, for a series of samples, which span the entire range of microstructures evaluated in this study, from the dielectric function obtained directly from the ellipsometric data without using the parametric model. The results are shown in Fig. 3.5.

The main features of the SPR band in going from high to low filling are a shift in the peak position to higher energies and a general increase in the bandwidth. The shift of the SPR beyond that predicted by the unmodified M-G EMT is reproduced by the parametric model through the depolarization factor. In particular, values of $L < 1/3$ indicate that the SPR occurs at a lower energy than predicted (i.e red-shifted), while values of $L > 1/3$ indicate a blue-shift.

To verify that the observed shifts of the SPR are indeed due to variations in particle shape, as predicted by the model, we have performed generalized ellipsometric measurements[205] on selected samples. The anisotropy expected for films with non-spherical particles was not observed and so the interpretation of the depolarization as a shape factor is incorrect. Therefore it is necessary to account for origin of shifts ($L \neq 1/3$) of the SPR.

One possible explanation for the red-shift with increased filling is the appearance of particle aggregation effects expected to occur as the filling approaches the threshold

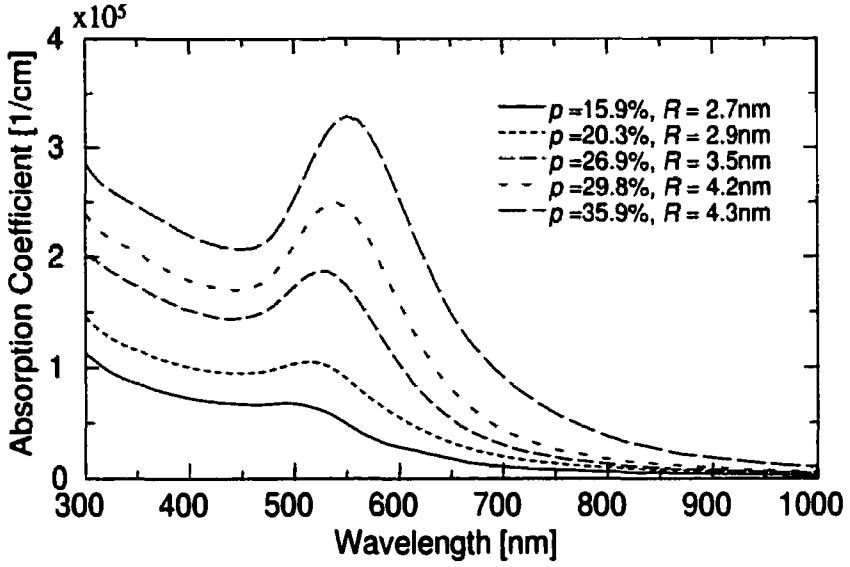

Figure 3.5: Absorption spectra of selected samples spanning the entire range of microstructures: low filling, small particle films to high filling films exhibiting significant particle aggregation effects.

for percolation (~40%)[152,206]. This is supported by the TEM observations of high filling samples, as illustrated in Fig. 3.6. The microstructural characteristics extracted from ellipsometric data for this particular sample were $d = 7.9\,\text{nm}$, $p = 33.7\%$, $L = 0.274$ and $R = 2.5\,\text{nm}$. (Note that the particle size is lower than would be expected for such a high filling sample (see Fig. 3.3a) and is a consequence of the reduced thickness of the film necessary for TEM analysis). The inset in Fig. 3.6 shows the particle coagulation in the form of double-sphere structures that is in violation of the M-G EMT.

To take these geometric effects into account within the M-G formalism, we have used an approach proposed by Granqvist and Hunderi[60] to describe discontinuous gold films. In their model a set of depolarization factors used to describe ellipsoidal shapes[207] were interpreted as effective depolarization factors to account for the detailed geometric configuration of the particles according to the theory of Clippe *et*

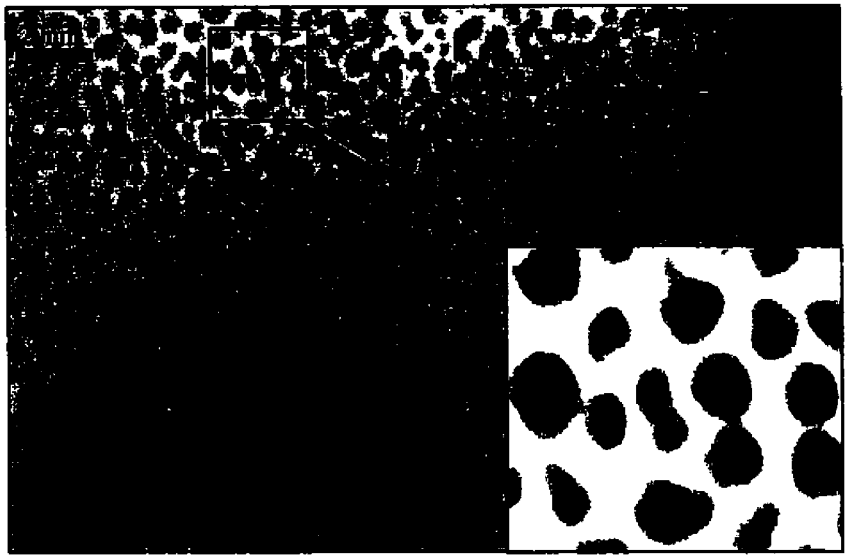

Figure 3.6: Transmission electron micrograph of a high filling sample, M12C ($p = 33.7\%$, $R = 2.5$ nm, $L = 0.274$).

al.[208] The effective dielectric response in their model is written as

$$\epsilon_{eff} = \epsilon_h \frac{1 + \frac{2}{9}\sum_{j=1}^{3} p_j \sum_{i=1}^{3} \frac{\epsilon_m - \epsilon_h}{\epsilon_h + L_i(\epsilon_m - \epsilon_h)}}{1 - \frac{1}{9}\sum_{j=1}^{3} p_j \sum_{i=1}^{3} \frac{\epsilon_m - \epsilon_h}{\epsilon_h + L_i(\epsilon_m - \epsilon_h)}}, \tag{3.5}$$

where the L_i's are given in sets to describe different geometrical configurations, for example (i) single spheres: $L_1 = L_2 = L_3 = 1/3$, (ii) double spheres: $L_1 = 0.250$, $L_2 = L_3 = 0.375$, and (iii) infinite linear chain: $L_1 = 0.133$, $L_2 = L_3 = 0.435$. Note that for $L_1 = L_2 = L_3$, Eq. 3.5 reduces to Eq. 3.1.

The results of applying this model to the annealed film with three different fillings, one for each geometrical configuration, are given in Table 3.2. After four hours of annealing, non-zero volume fractions of double-sphere structures and of infinite chains are observed. Note that the total filling is almost unchanged compared to Fig. 3.4a. The particle size, however, does not decrease with anneal but rather "levels-off" as expected.[203] The corrected particle sizes are shown in Fig. 3.4b.

The Clippe theory predicts the splitting of the SPR resonance into two absorption

Table 3.2: Evolution of microstructural parameters with post-deposition annealing time at 160°C taking into consideration the geometric configuration of the gold particles; ss: single sphere, ds: double sphere, ic: infinite chain. Only corrected particle sizes are shown.

time (hrs)	p_{tot} (%)	p_{ss} (%)	p_{ds} (%)	p_{ic} (%)	R (nm)
0	24.1	24.1	0	0	2.1
2	26.9	26.9	0	0	3.5
4	29.8	24.3	5.0	0.5	4.2
6	33.4	25.5	7.0	0.9	4.2
8	35.9	19.4	14.7	1.8	4.3

peaks (modes) for each geometrical configuration, the exact frequency of each mode being dependent on geometry. We have not observed such a multi-peak absorption. However, as we are mostly concerned with double-sphere structures, the mode frequencies of which are close to the SPR frequency, we assume the additional peaks are buried by the particle size distribution. As such, particle coagulation appears as a red-shifted and broadened SPR, the latter effect being responsible for the extraction of a decreasing particle size with increased filling.

Although this model is not expected to apply to films at higher fillings, where the concept of particle size loses meaning, it does close the gap between the cermet structure and the labyrinth structure expected at percolation.[204] For microstructural characterization of films at and above percolation it is necessary to use an EMT more representative of the aggregate structure of the film.[52,53]

Next we consider the blue-shift of the SPR with decreasing cluster size which was seen to occur for particles smaller than 9 nm. We have described the particle size-dependent broadening of the SPR in terms of the classical limited mean free path effect[79,85,209] (Eq. 3.4) which predicts no significant shift in the peak position for particles larger than 4 nm (although there is a slight red-shift for smaller particles). This approach loses validity with decreasing particle size due to the splitting of the conduction electron band into discrete energy levels.[6] More appropriate models

have been developed[86,88,89] (for a review see Kreibig[81]) to describe these so-called quantum size effects where the dielectric function of the metal is derived quantum mechanically within the random-phase approximation. These are based on the original work of Kawabata and Kubo[80] which treat the particle surface not as a scatterer, but rather to determine the eigenstates of electrons which are bound states in the finite volume of a sphere. These theories do predict a blue-shift with decreasing particle size, however, they neglect the details of the electron density at the surface (due to the use of an infinite ionization potential) which become important for small particles.

More recently, Ekardt[93] has carried out a full quantum-mechanical calculation using a generalized RPA in which the diffuseness of the electron density at the particle surface is automatically included. When an accurate electron density profile, which extends outside the particle radius as defined by the ion core (so called 'spill-out'), is taken into account, the SPR is seen to red-shift with decreasing particle size. This calculation was done for simple metals. In noble metals, the s-d interaction, as described by Liebsch,[100] is absent for the conduction electrons which 'spill-out' of the particle, and thus they oscillate with an unscreened plasma frequency (i.e. at higher frequency). As this effect becomes more pronounced with increasing surface-to-volume ratio, it leads to a blue-shift with decreasing particle size. Very recently, the method of Ekardt was applied to gold nanoparticles and it was shown that a blue-shift with decreasing particle size is indeed obtained.[78]

In Section III the constant A in Eq. 3.4 was arbitrarily set to 0.25 so that extracted particle sizes agreed with TEM results. In the original quantum mechanical models,[80,86,88,89] the dielectric function of the metal is given in a form similar to Eqs. 3.3 and 3.4 with A being a model-dependent broadening parameter in the range of 0.29 to 1. A more recent model,[99] that also expresses the dielectric function in the above form (but does not assume an infinite ionization potential and is in good agreement with the results of Ekardt), gives an A value of 0.3, similar to the one obtained in this study. Using experimental A values to support a particular model, however,

needs a word of caution as the broadening parameter is also a matrix-dependent parameter. For example, A for silver particles embedded in different matrices ranges from 0.25 to 1.[30,32,72,86] Persson[31] accounted for the variation in A in terms of the details of the metal/matrix interfacial region (i.e. metal-adsorbate charge transfer excitations). The observed increase in A for more reactive matrices was attributed to so-called chemical interface damping.[32] A more detailed study of the influence of the metal/matrix interface is presently ongoing in our laboratory, in particular, the influence on A of SiO_xN_y matrices with composition ranging from SiO_2 to Si_3N_4.[210]

3.7 Summary and Conclusions

We have used variable-angle spectroscopic ellipsometry measurements to characterize the microstructure of gold/fluoropolymer nanocomposite films and to determine its dependence on deposition conditions and post-deposition thermal treatments. We have modeled the optical response of the films using a modified Maxwell-Garnett effective medium approach. By allowing a depolarization factor and a broadening parameter as fit variables, as well as the film thickness and the gold volume fraction, we were able to reproduce the measured spectra with high accuracy for fillings ranging from 15 to 35%.

However, the good fits in the low filling (small particle) and high filling limits were artificial in that they were a consequence of the adjustable depolarization factor included in the model to account for deviations in particle shape from that of a sphere. These deviations were not observed and, as such, the depolarization factor was reinterpreted as a gauge to quantify model applicability.

Depolarization factors less than 1/3 represent a red-shifted SPR and indicate that particle aggregation effects are present. If the detailed geometric configuration of the particles for films with $L < 1/3$ are not taken into account, extracted particle sizes are fictitiously small due to the broadening of the SPR that accompanies aggregation.

The onset of particle aggregation effects was found to occur at a filling of about 30%. Values of $L > 1/3$ represent a blue-shifted SPR and indicate that the motion of the electrons in the particles can no longer be described by the classical LMFP theory. The small particle limit was determined to be about 9 nm. Useful microstructural information can still be obtained below this limit since the width of the SPR band, although blue-shifted, is still related to the particle size.

Acknowledgments

The authors wish to acknowledge the expert technical assistance of Mr. Gilles Jalbert, the help with selected computations of Mr. Thomas Gervais and complimentary XPS measurements of Ms. Jolanta E. Klemberg-Sapieha. We would also like to thank Mr. Daniel Poitras for the many helpful discussions (as well as being our TEXpert). This work was supported by the Natural Sciences and Engineering Research Council (NSERC) of Canada.

Chapter 4

Article 2: Au/SiO_2 Films

The main emphasis of this article concerns finite size effects, in particular the particle size dependence of the core response of gold. Two more general objectives concern the demonstration of the influence of dipole-dipole interaction predicted by the M-G model and the identification of the limits of the M-G model with respect to the quasi-static approximation.

The particle sizes studied in this article are much larger than those in the Au/PPFC system and were obtained by performing thermal treatments at 900°C as opposed to 160°C. At this temperature, the stability of the SiO_2:H structure is of concern, in particular, changes related to the role of H in the film as discussed in Secion 2.1.2.2 (i.e. $\hat{\theta}$ and ρ), as well as possible crystallization.

Both of these effects will influence the optical constants of the SiO_2. However, it is crystallization, rather than restructuring of the amorphous matrix, that is of concern, since it could potentially obscure the observation of the effects listed above behind a complicated metal/dielectric interface morphology. To verify the crystalline state of the matrix, a grazing incidence XRD spectrum was taken of a Au/SiO_2 film that had been annealed for 10 hours. The spectrum, shown in Fig. 4.1, possesses sharp diffraction peaks corresponding only to reflections from Bragg planes in gold having no preferred orientation.[211] The broad hump at $2\theta \sim 20°$ is representative

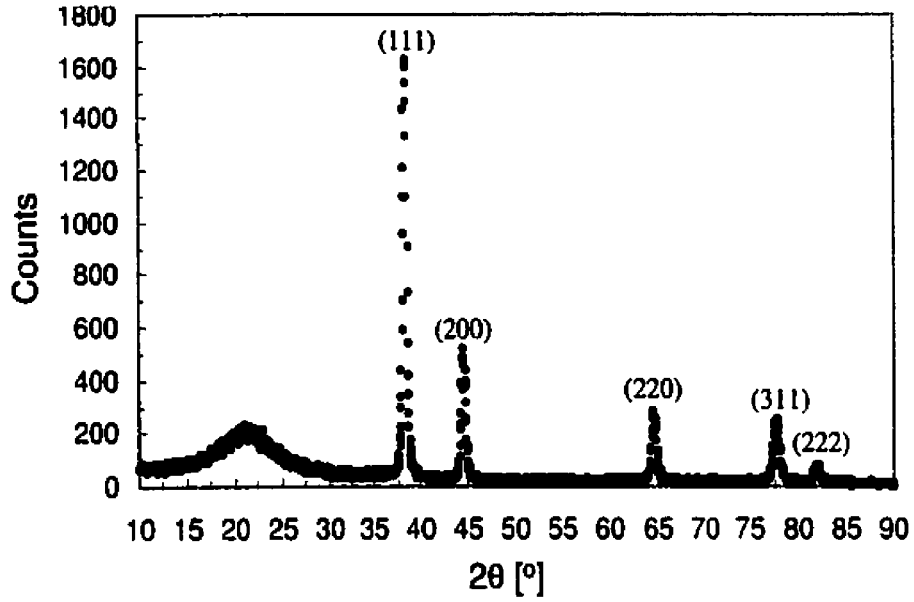

Figure 4.1: Grazing incidence XRD spectrum of a Au/SiO_2 film with $R > 20\,nm$ deposited on quartz.

of an amorphous material and corresponds to the spectrum taken of an as-deposited pure SiO_2 film (not shown).

To take into account any possible thermally-induced changes in the optical constants of the matrix resulting from restructuring, pure SiO_2 films were annealed together with the Au/SiO_2 nanocomposites. These films were measured ellipsometrically and a decrease in index amounting to ~ 0.03 was observed after 10 hours at 900°C. In modeling the annealed Au/SiO_2 films, an ϵ_h corresponding to a pure SiO_2 film annealed for the same duration was used, even though the slight change in ϵ_h did significantly influence the extracted fit parameters.

Spectroellipsometric Characterization of Plasma-Deposited Au/SiO_2 Nanocomposite Films

Dan Dalacu and Ludvik Martinu

Recieved 20 August 1999; accepted 24 September 1999

J. Appl. Phys. **87**(1), 228-235, January 2000

4.1 Abstract

Nanocomposite films consisting of metal nanoparticles embedded in a dielectric matrix were fabricated by simultaneous sputtering of a gold target and plasma-enhanced chemical vapour deposition of hydrogenated SiO_2. The optical constants of the films were determined from spectroscopic ellipsometry measurements and were modeled using the Maxwell-Garnett effective medium theory. The particle size dependence of the free electron absorption was included according to the limited electron mean free path effect using a broadening parameter $A = 0.15$ determined from the comparison of the measured spectra with TEM micrographs. Using bulk inter-band optical constants for gold, very good agreement was obtained between the model and the measured spectra but only in the narrow particle size range ~ 10 to 20 nm, the latter of which marks the onset of phase retardation effects. For smaller particles, the energy of the surface plasmon resonance was progressively blue-shifted with respect to the predicted value. This was interpreted by a size dependence of the inter-band transitions as a result of strain-induced variation of the lattice constant within the particle.

4.2 Introduction

The optical properties of bulk noble metals are due to inter-band (d-band to the s-p conduction band) transitions at shorter wavelengths and intra-band (free electron) absorption at longer wavelengths. In metal nanoclusters the intra-band contribution is modified due to the confinement of the electrons within the particle. Instead of monotonically increasing with wavelength, the absorption spectrum is dominated by the resonant coupling of the incident field with quanta of collective conduction electron plasma oscillations, so-called surface plasmons.[197] The frequency and the shape of the surface plasmon resonance band is dependent on the concentration, size, and shape of the metal clusters, as well as the dielectric properties of the surrounding medium. This dependence allows for the extraction of microstructural characteristics of the nanocomposite material from their optical properties. This can be done, for example, by fitting the measured dielectric function of the metal clusters with the calculated response using the Mie theory,[5] or, for larger metal volume fractions where dipole-dipole interactions become important, with the response predicted by effective medium theories.[4,52,53]

This type of microstructural characterization is becoming increasingly important considering the recent demonstration of the dramatic difference in the optical nonlinearity of gold clusters as compared to bulk.[19] First, confinement of the conduction electrons results in a situation similar to that of a molecule[212] and, as such, the clusters are expected to possess a non-zero electric dipole third-order nonlinear susceptibility. Second, the excitation of surface plasmons results in a large local electric field in the clusters which will enhance any intrinsic nonlinearity. The enhancement was first shown by Ricard et al[19] for Ag and Au clusters from degenerate four wave mixing (DFWM) experiments. The origin of the intrinsic nonlinearity was, however, attributed to Fermi smearing[20] (i.e. non-equilibrium electron population) due to 'hot electrons' which dominated over any non-linearity due to the dipole nature of the particles.[213] Since then a large experimental ef-

fort has been undertaken to investigate the nonlinearity of metal clusters, in particular gold/dielectric nanocomposite materials. The different matrices studied include SiO_2,[138,139,143,148,150,214,215] Al_2O_3,[149] TiO_2,[151] and $BaTiO_3$,[216] with deposition methods including co-sputtering,[148–151,215,216] ion implantation,[138,139] and the sol-gel technique,[143] as well as hybrid approaches combining plasma-enhanced chemical vapour deposition and laser evaporation.[214]

In the above experiments, an effective optical nonlinearity is measured, from which the intrinsic nonlinearity of the metal is calculated. This type of analysis relies critically upon the ability to evaluate the detailed microstructure of the films as it is the microstructure that determines the enhancement factor. In previous articles[166,217] we have demonstrated the applicability of the effective medium approach applied to spectrophotometry and spectroscopic ellipsometry measurements to extract microstructural information of Au/plasma polymerized fluorocarbon nanocomposite films. In this study we extend our previous work to include Au/SiO_2 nanocomposite films. The SiO_2 matrix allows us to study in more detail the inter-band region of the gold particles since we are not limited by the absorption edge of the fluoropolymer matrix ($\sim 350\,nm$). With this region of the spectrum available for characterization and considering the sensitivity inherent to ellipsometric techniques, insight can be obtained into the structural changes that occur in small particles through the effect that these changes have on the optical properties. This study will complement similar investigations which utilize more invasive characterization techniques to study small particles, namely high resolution transmission electron microscopy,[10] photoemission spectroscopy,[218–220] x-ray absorption spectroscopy,[36] and electron diffraction experiments.[37,76,108]

4.3 Film Preparation and Characterization

Nanocomposite thin films can be fabricated by hybrid vacuum methods using a simultaneous combination of deposition techniques such as evaporation, sputtering, plasma polymerization and PECVD (for a review see, for example, Abelès[137] and Biederman and Martinu[152]). For this work, we adopt a rather novel hybrid deposition method using two RF sources in a parallel-plate electrode arrangement, one for the PECVD of the SiO_2 matrix and another for the sputtering of a gold target. In this way, a more independent control of the SiO_2 and gold deposition rates can be obtained.

The PECVD of the SiO_2 matrix is performed using SiH_4/N_2O chemistry.[221,222] Fused quartz substrates were placed on an RF-powered (13.56 MHz) circular electrode, 18 cm in diameter. Gas flows used were 10 sccm, 40 sccm, and 65 sccm for SiH_4, N_2O and Ar, respectively. The depositions were made at a pressure of 80 mTorr with an RF input power of 100 W for a self-bias potential of -300 V. The above configuration was complemented by a 50 mm diameter magnetron head powered by a separate RF supply, also at 13.56 MHz. The gold target was positioned facing the substrate holder at a vertical distance of 70 mm, and the axis of the magnetron was displaced from the axis of the substrate holder by 115 mm. In this way a gradient in the concentration of gold incorporated into the SiO_2 matrix was obtained, allowing for multiple measurements on the same sample. The RF input power on the magnetron was 200 W for a self-bias potential of -300 V.

Following a detailed optimization of the deposition process and the characterization methodology, three representative samples, A, B and C, were prepared. They were positioned at different locations on the substrate holder so that sample A was closest to the gold target and sample C was farthest away. In this way a large variation in the gold content was achieved using the same fabrication conditions. The deposition times were adjusted accordingly to maintain the minimum transmission of the SPR band around 50% (i.e. 1, 4, and 8 minutes for samples A, B, and C,

respectively). Different measurements on each sample were designated by number, increasing with increasing distance from the magnetron and hence decreasing gold content (i.e. A1, A2, A3...).

As-deposited films obtained in this way are brownish in color; they consist, most likely, of atomic gold or sub-nanometer gold clusters and do not exhibit a SPR. To promote cluster growth, via diffusion of the gold atoms and small clusters through the SiO_2 matrix and subsequent coalescence (Ostwald ripening[223]) the films were annealed at 900°C in air. At this temperature, it is expected that the gold clusters will experience a rapid liquid-like coalescence in which neck formation and particle reshaping occurs on a time scale of ~ 70 ms.[123]

The optical characterization of the films was performed using a variable-angle spectroscopic ellipsometer (model VASE from the J.A. Woollam Co., Inc.). Additional normal-incidence transmission measurements were made using a double-beam spectrophotometer (model Lambda 19 from Perkin-Elmer). Scattering measurements were also made on selected samples using an integrating sphere module of the spectrophotometer (Labsphere RS19, 15 cm diameter). Transmission electron microscopy was performed on samples deposited on carbon-coated copper grids using a Philips CM30 microscope.

4.4 Microstructural Characterization using the Effective Medium Approach

The microstructural characteristics were determined by incorporating a parameterized (i.e. film thickness, d, gold volume fraction, p, and particle radius, R) structural model into a multilayer optical model (air/film/substrate).[168] The free parameters were fitted to the optical data using the Levenberg-Marquardt method. Both the ellipsometric and photometric data were used in the fitting procedure to minimize correlations between fit parameters. To model the optical response of the

nanocomposite films we employed the Maxwell-Garnett[4] effective medium theory:

$$\frac{\epsilon_{eff} - \epsilon_h}{\epsilon_{eff} + 2\epsilon_h} = p\frac{\epsilon_m - \epsilon_h}{\epsilon_m + 2\epsilon_h}, \tag{4.1}$$

where ϵ_{eff}, ϵ_m and ϵ_h represent the dielectric response of the effective medium, the gold inclusions, and the SiO_2 host, respectively. This model assumes spherical particles which have dimensions small compared to the probing wavelength (i.e. quasi-static approximation[47] (QSA)) and which are well separated (i.e. no aggregation effects).

The dielectric functions of the two components in the effective medium, as well as the fused quartz substrate, were determined separately from ellipsometric measurements. The dielectric properties of the SiO_2 were modeled by a simple three-term Cauchy dispersion. The optical response of the gold was modeled separately in the inter-band and intra-band regions, the former being described by a series of Lorentz oscillators, and the latter by the Drude free electron model:

$$\epsilon_m = \epsilon_{core} + 1 - \frac{\omega_p^2}{\omega(\omega + i\Gamma)}, \tag{4.2}$$

where ω_p is the plasma frequency and Γ is the free electron collision frequency. When Eq. 4.2 is applied to a pure gold thin film, the collision frequency is determined by the scattering processes in the bulk material (i.e. $\Gamma = 1/\tau_B$). For metal nanoparticles, however, Γ has to be modified according to:[85]

$$\Gamma = \frac{1}{\tau_B} + \frac{A\nu_F}{R}, \tag{4.3}$$

where ν_F is the electron Fermi velocity (1.39×10^8 cm/sec).[44] The origin of the additional term can be interpreted in two ways: (i) classically, due to scattering of the conduction electrons from the particle surface as R becomes comparable to or smaller than the electron mean free path, the so-called limited mean free path

effect;[79] (*ii*) quantum mechanically, due to dipole transitions between sp-electron eigenstates which become discrete as a result of the small dimensions of the particle.[80] The parameter A is a measure of the slope in a plot of the SPR bandwidth versus reciprocal particle size; it is dependent on the model used to derive Eq. 4.3 (see, for example, Kreibig and Genzel[81]) and, experimentally, it has been found to depend on the particular metal/matrix system being studied (see, for example, Hovel et al[32]). As such, the best approach[164] is to determine A by comparison of the width of the SPR band with the particle size as determined from TEM analysis for each metal/matrix combination.

As such, a detailed TEM analysis of several samples was performed to determine the parameter A, the results of which will be published elsewhere[224]. It was found that for small particle size distributions (standard deviation less than 25%), a value of $A = 0.15$ is required to extract the correct particle size. A typical TEM micrograph of a thin ($\sim$13 nm) Au/SiO_2 film is shown in Fig. 4.2 demonstrating the nearly circular and well isolated particles with a narrow size distribution (inset) as required by Eq. 4.1.

As an example of the agreement between the predicted and measured optical constants, we show in Fig. 4.3 the results of the fitting procedure from a measurement on sample A after a one hour anneal at 900°C. The figure shows the ellipsometric spectra (angles $\Psi(\lambda)$ and $\Delta(\lambda)$) and model fit from 300 nm to 1000 nm measured at incident angles of 55°, 65° and 75° as well as normal-incidence transmission ($T(\lambda)$) from 300 nm to 850 nm. The fit parameters from the model fit in this particular case were $d = 53.9$ nm, $p = 7.7\%$, and $R = 9.7$ nm.

4.5 Results and Discussion

Two distinct dependencies on anneal time were observed and are illustrated in Fig. 4.4. The optical constants of the high filling film, sample C, were correctly

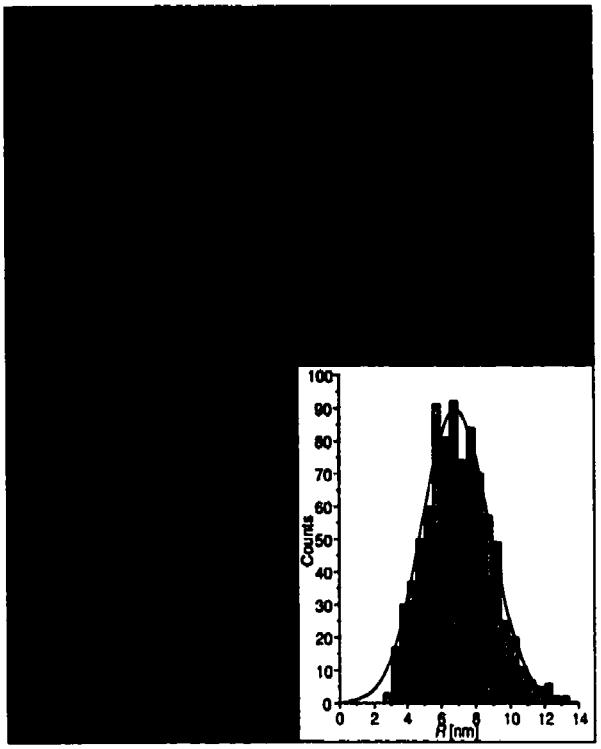

Figure 4.2: TEM of a nanocomposite film for which model fit parameters are $d = 12.9\,\text{nm}$ and $p = 23.1\%$. The inset shows the particle size distribution.

predicted by Eq. 4.1 after a 1 hour anneal. Extended annealing, however, resulted in the red-shifting and broadening of the SPR beyond that predicted by the M-G EMT as shown in Fig. 4.4(a). These trends in the shape and position of the SPR are caused by phase retardation effects which occur for particles larger than the quasi-static limit ($R \sim 20\,\text{nm}$).[47] This was supported by the observation of significant scattering (up to 6% after 10 hours at 900°C for the sample in Fig. 4.4(a)) that is expected by particles significantly larger than those covered by QSA.

For the lower filling films, samples B and C, annealing resulted in a narrowing SPR band as shown in Fig. 4.4(b), indicative of particle growth within the QSA. The band, however, was blue-shifted with respect to the value predicted by Eq. 4.1, the blue-shift decreasing with anneal time, and thus with increasing particle size.

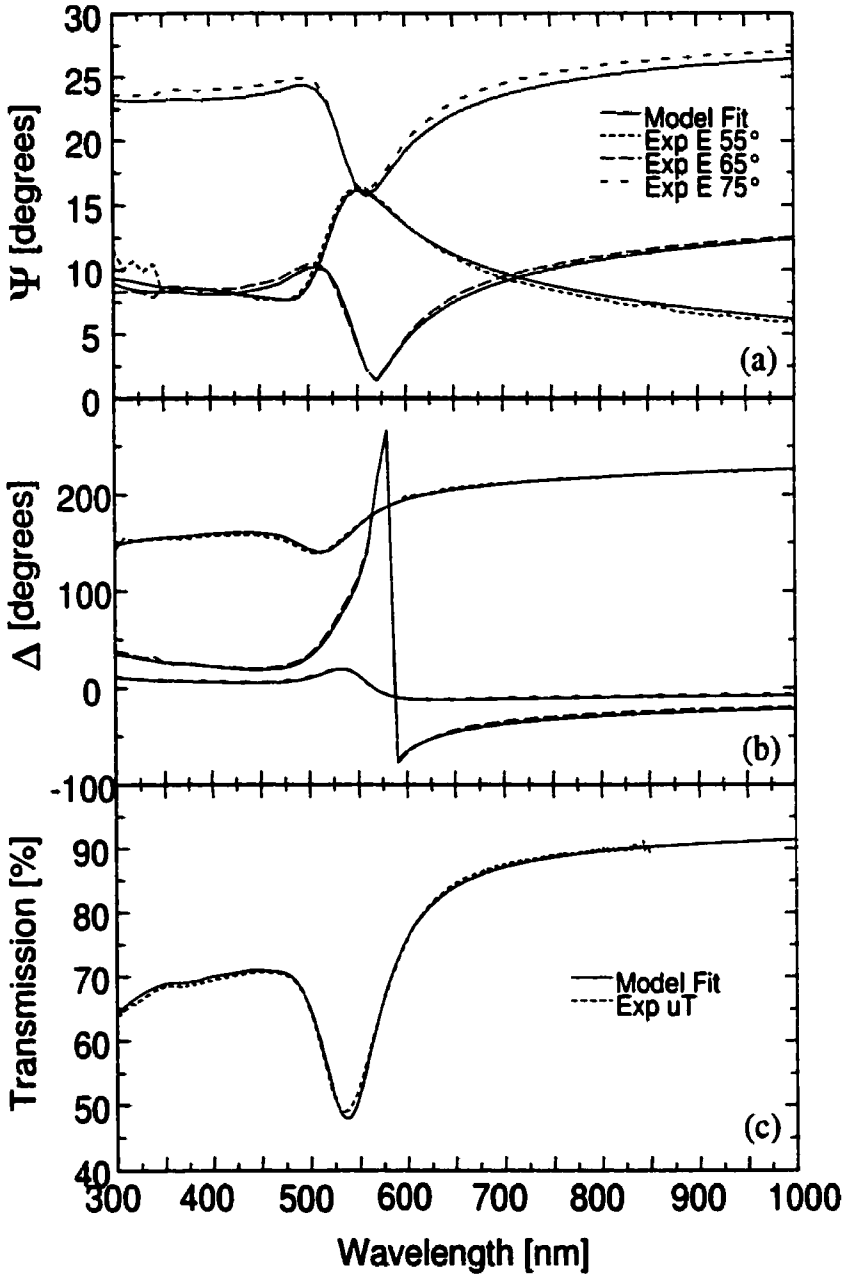

Figure 4.3: Measured ellipsometric data and model fit for sample A4: (a) $\Psi(\lambda)$, (b) $\Delta(\lambda)$, and (c) $T(\lambda)$ at normal incidence.

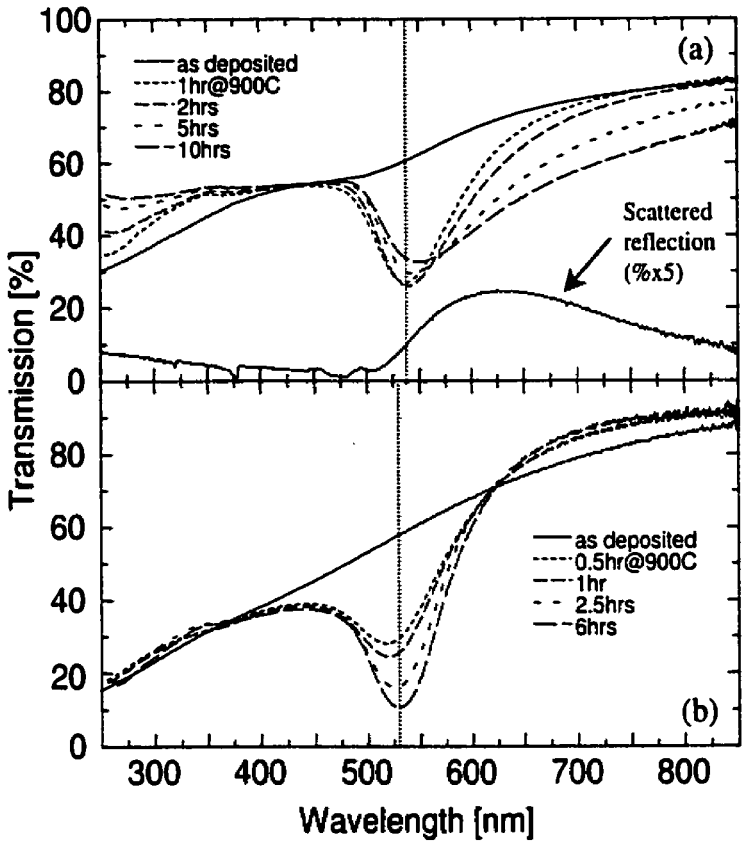

Figure 4.4: Normal incidence transmission spectra after different anneal times for (a) sample A2 ($p = 13.8\%$, $d = 77.8\,\text{nm}$) and (b) sample B2 ($p = 6.9\%$, $d = 228.7\,\text{nm}$). The dotted vertical lines indicate the position of the SPR expected from Eq. 4.1. For sample A2 the integrated scattered reflection after 10 hours at 900°C is also shown.

Anneals of 6 and 9 hours for samples B and C, respectively, were required before good agreement between measured and modeled optical constants was obtained.

The dependence of p on the distance from the magnetron axis is shown in Fig. 4.5 together with the variation in the film deposition rate. The filling and deposition rate were determined from the fits to the samples after sufficient annealing so that their optical constants were described well by Eq. 4.1 (i.e. 1, 6 and 9 hours for samples A, B and C, respectively). The gold filling varied from $\sim 14\%$ for sample A1 to less than 1% for C3. The increase in the deposition rate with p is well beyond the increase

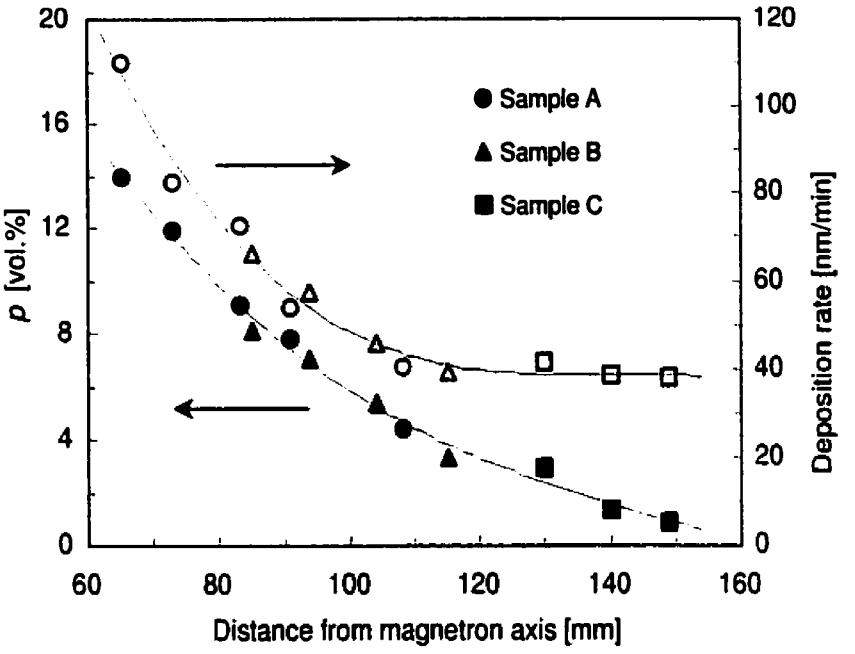

Figure 4.5: Dependence of the gold filling and film deposition rate on the distance from the magnetron axis.

expected from the added volume of gold (i.e. the deposition rate of pure SiO_2 with a shutter over the gold target was $\sim 40\,\text{nm/min}$) and is due to the increasing plasma density close to the magnetron.

The particle size calculated using Eq. 4.3 for films which possessed the narrowest SPR bandwidths exceeded $R = 20\,\text{nm}$, for which QSA is not expected to be valid.[47] As no red-shifting of the SPR was observed at these bandwidths, it appears that the particle size according to Eq. 4.3 is over-estimated. This is, most likely, a consequence of an inappropriately low bulk relaxation constant used in Eq. 4.3 (i.e. $\tau_B = 5\times10^{-14}\text{s}$) as the contribution to electron scattering from crystal imperfections and impurities are not expected to be present due to the high temperature annealing.[128] We therefore make the assumption that $\tau_B \ll R/A\nu_F$ and neglect the bulk scattering term in Eq. 4.3 when calculating R. This does not affect the constant A since the SPR bandwidth of the samples from which A was determined was broad enough so that

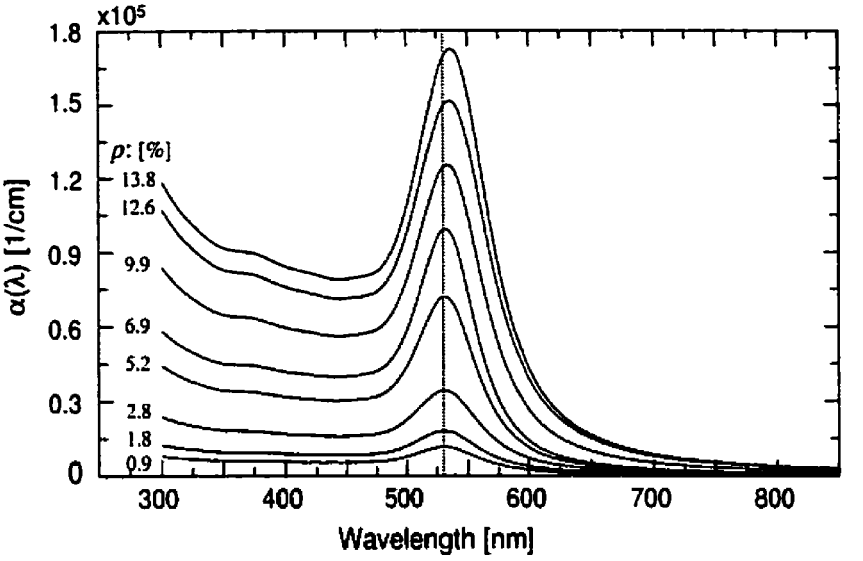

Figure 4.6: Absorption spectra calculated from the model fit for films with gold fillings from $\sim$ 1% to $\sim$ 14%. The dotted vertical line indicates the position of the SPR in the low-filling limit.

the bulk scattering did not significantly affect the extracted particle size.

Fig. 4.6 shows the variation in the absorption coefficient with p. The shift of the resonance from its position in the low filling limit (dashed vertical line) to longer wavelengths with increased filling is a measure of the dipole-dipole interaction between particles. This shift demonstrates the necessity of using the M-G equation as opposed to the Mie equation, the latter being based on the extinction by a single particle; it does not contain a p-dependence of the resonant frequency.

In order to model the optical response of the films for which the position of the SPR band is not in agreement with Eq. 4.1 (i.e. over the entire range of particle sizes obtained in this work), we adopt the approach applied in our previous study of Au/PPFC films[217] in which a generalized M-G model was employed:[63]

$$\frac{\epsilon_{eff} - \epsilon_h}{L\epsilon_{eff} + (1-L)\epsilon_h} = p\frac{\epsilon_m - \epsilon_h}{L\epsilon_m + (1-L)\epsilon_h}. \tag{4.4}$$

The additional parameter, the depolarization factor (L), is an average screening parameter[62] that defines the Wiener limits: $L = 0$ for no screening (all particle boundaries parallel to the applied field), and $L = 1$ for maximum screening (all boundaries perpendicular to the applied field). Eq. 4.4 reduces to the M-G equation for spherical particles for which $L = 1/3$. The depolarization factor, then, is intended to account for any variations in particle shape, and thus, in film anisotropy. These deviations have the effect of shifting resonant frequency of the SPR: to lower energy for oblate spheroids ($L < 1/3$) and to higher energy for prolate spheroids ($L > 1/3$).

Transmission measurements using p-polarized light at large angles of incidence, which are sensitive to anisotropy,[225] have shown the films to be isotropic, even when $L \neq 1/3$. As such, deviations from $L = 1/3$ and the shifts in the SPR that they entail are not a consequence of non-spherical particles, but rather indicate violations of the assumptions made when applying Eq. 4.1. In the previous study,[217] the red-shift ($L < 1/3$) observed in films with $p > 30\%$ was attributed to aggregation effects, while the blue-shift ($L > 1/3$) for films with $R < 4.5$ nm was associated with the validity of the LMFP effect. In this study, $L < 1/3$ signifies the presence of phase retardation effects rather than aggregation as the fillings are much lower. We will also show that $L > 1/3$ does not necessarily signify the small particle limit of Eq. 4.3, but rather, is related to a particle size dependence of the inter-band optical constants of gold.

Applying Eq. 4.4 to samples A, B and C revealed no significant variation in d or p with anneal. The dependence of R and L with anneal for sample locations A4, B2, and C1 is shown Fig. 4.7. Phase retardation is evident in the higher filling films (A4 and B2) from the decrease of L to values below 1/3 (i.e. SPR red-shifting). The onset of retardation effects occurs at $R \sim 11$ nm and is indicated in the figure by the dotted vertical lines. Particle sizes determined using Eq. 4.3 are no longer valid beyond this limit since they are fictitiously small due to the SPR broadening that accompanies retardation, hence the decreasing R with anneal time observed for A4 and B4.

From Fig. 4.7(a) it is seen that the particle growth rate increases with increased

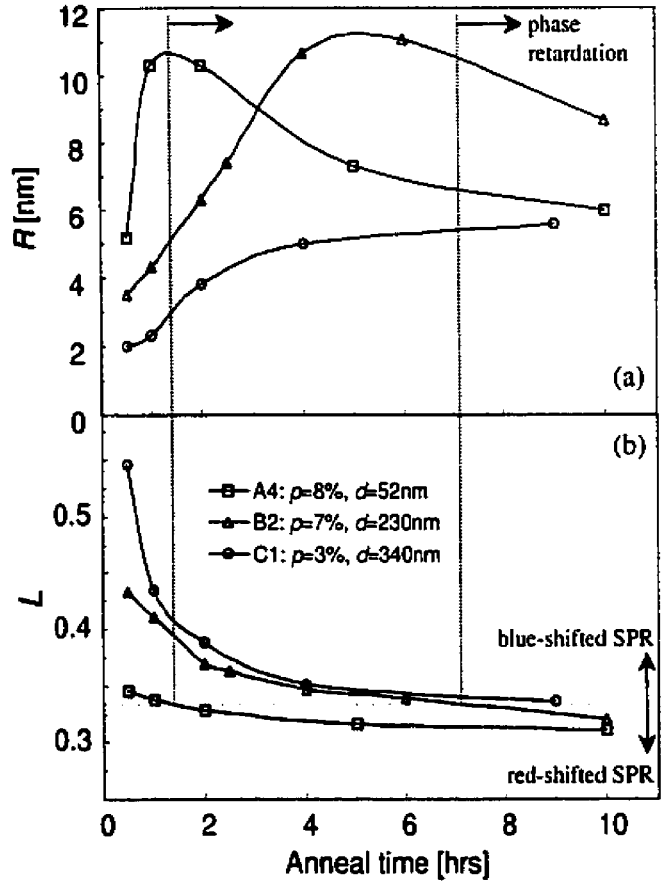

Figure 4.7: Extracted fit parameters using Eq. 4.4 after different anneal times: (a) R and (b) L. The onset of retardation effects is indicated in (a) by the dotted vertical lines and the depolarization factor expected for spherical particles is indicated in (b) by the dotted horizontal line.

filling and decreased film thickness. The former trend is expected from a growth model dependent on the diffusion of gold atoms through the SiO_2. The dependence on thickness is surprising. We speculate that oxygen absorbed from the air during anneal plays a crucial role in determining the diffusion rate of atomic gold through the matrix. This is supported by the fact that a much reduced growth rate was observed when annealing in nitrogen (not shown here), in agreement with similar results in literature.[138]

The onset of the blue-shifting of the SPR with decreasing particle size occurs at

$R \sim 5\,\text{nm}$, seen most clearly from the low filling sample (C1) for which the particle growth was slowest. This blue-shift is now a well document trend for both gold[76–78,217] and silver[73,74,100,107] clusters though there is still current discussion as to its origin. It has been interpreted[78,100,107] in terms of an increase in the sp-electron population that is not screened by the polarizable inner medium of the ion core as a consequence of electron spill-out beyond the cluster edge and is based on calculations done in the framework of the time-dependent local-density approximation.

This interpretation is well justified for silver[100,107] where the inter-band edge (4d $\rightarrow$ 5sp) is at higher energy than the position of the SPR. For gold, however, the inter-band edge, defined by the onset of a weak 5d $\rightarrow$ 6sp transition at 1.94 eV near the symmetry point X in the Brillouin zone, and a stronger one at 2.45 eV near L,[51] coincides with the position of the SPR. This being the case, any dependence of the inter-band optical constants on particle size will influence the shape and position of the SPR and, thus, must be taken into consideration.

Most publications consider this region to be size-independent down to $\sim 10^3$ atoms ($R \sim 1.5\,\text{nm}$) based on two articles by Kreibig[75,128] in which a structural phase transition from cluster matter to solid-state was shown to occur at this particle size and was attributed to the increase in the number of surface atoms compared to volume atoms (and thus an increase in the number of atoms with lower coordination numbers). The transition was characterized as abrupt even though the data[75] indicated a more gradual change starting at $R \sim 2.4\,\text{nm}$ ($\sim$4000 atoms). This smearing of the transition was attributed by the author as resulting from the particle size distribution.

We feel, however, that the transition is not necessarily abrupt, or, at least, there exists a gradual transition which follows an abrupt one, prior to the inter-band optical constants attaining their bulk value. This is based on the observed changes in the transmission for $\lambda < 375\,\text{nm}$ (see Fig. 4.4(b)). Although far enough removed from the SPR energy so as to not affect its shape or position, the spectrum in this region continues to develop for particle radii much larger than 2.4 nm. A broad transition,

even a series of transitions, should be expected as the particle size increases beyond 1.5 nm, at which size the clusters attain metallic properties.[218] These transitions can by identified with: (i) the influence of a quasi-molten state,[124] (ii) the influence of the surface atoms on the total density of states[226], and (iii) the influence of lattice contraction on the electronic bandstructure.[130]

In order to account for a possible change of the optical constants in the inter-band region, Eq. 4.1 was applied to the measured optical data with the amplitudes and linewidths of the six Lorentz oscillators, which make up ϵ_{core} in Eq. 4.2, set as fit parameters. The microstructural parameters d, p, and R were also fit though they were not found to change significantly from those extracted using Eq. 4.4. The results for sample B2 are shown in Fig. 4.8. The real part of ϵ_m ($\Re[\epsilon_m]$) is seen to decrease with decreasing particle size (Fig. 4.8(a)), the same trend that was obtained by Quinten[164] and Kreibig[128] from a Kramers-Kronig analysis of the measured extinction spectra. This decrease in $\Re[\epsilon_m]$ is due to a decrease in the real part of ϵ_{core} ($\Re[\epsilon_{core}]$) and is responsible for the observed blue-shift of the SPR.

In the context of reduced screening, $\Re[\epsilon_{core}]$ can be interpreted as describing an effective core polarization with both bulk and surface terms, and the decrease with R results from an increase in the contribution of the polarization-free surface layer. Attributing the changes in $\Re[\epsilon_{core}]$ solely to the influence of a polarization-free surface layer cannot, however, be consolidated with the particle size dependence of the imaginary part of ϵ_m ($\Im[\epsilon_m]$), shown in Fig. 4.8(b), together with the bulk values of Thèye.[127] The observed variation in $\Im[\epsilon_m]$ at shorter wavelengths are indicative of changes in the electronic structure of the particle which will also affect the core polarization. In order to gain some insight into the driving force behind these changes, we have examined more closely the particle size dependence of $\Im[\epsilon_m]$ throughout the measured spectral region.

For $\lambda > 500$ nm, $\Im[\epsilon_m]$ is determined mostly by free electron absorption (though there is a small contribution from inter-band transitions near X), and the increase

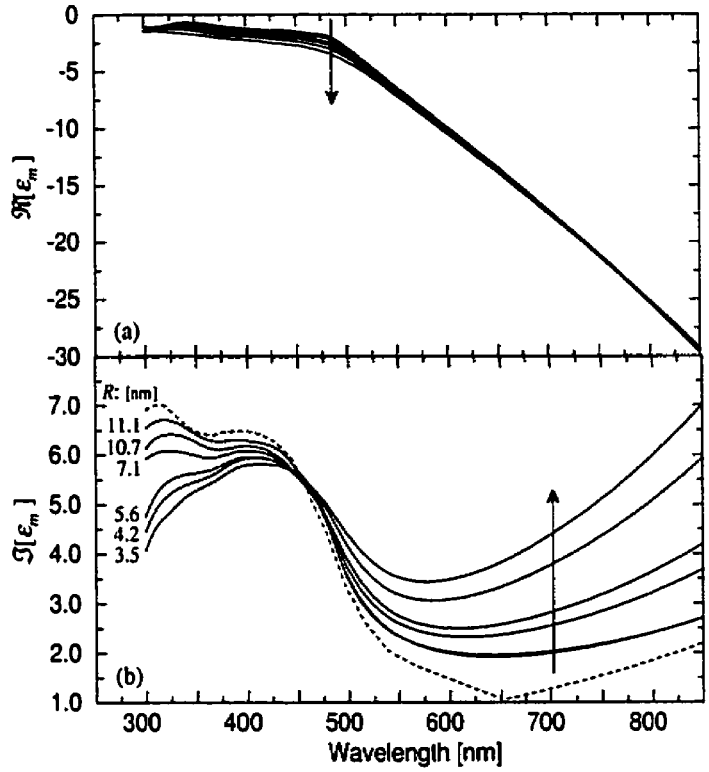

Figure 4.8: Dependence of the optical constants of gold on particle size: (a) $\Re[\epsilon_m]$ and (b) $\Im[\epsilon_m]$. The dashed line in (b) is the bulk data of Thèye.[127] The arrows indicate decreasing R.

observed with decreasing R is, of course, due to the second term in Eq. 4.3.

For 375 nm$< \lambda <$ 500 nm, $\Im[\epsilon_m]$ has contributions from both inter-band transitions near L and free electron absorption. The decreasing height of the peak at $\sim$425 nm with decreasing R is due to a decrease in the imaginary part of ϵ_{core} ($\Im[\epsilon_{core}]$). This trend has also been observed by Yamaguchi et al,[129] however, it is in disagreement with the calculations of Quinten[164] and Kreibig[128], both of whom obtained an increase in $\Im[\epsilon_{core}]$ with decreasing R. The optical constants determined from ellipsometric measurements should be more reliable than those calculated from a K-K analysis of extinction spectra since K-K integrals have to be approximated in the spectral regions where measured data are not available.

To study the dependence of $\Im[\epsilon_{core}]$ on R in this region, we have subtracted the intra-band contribution and have plotted $[\Im[\epsilon_{core}](\hbar\omega)^2]^2$ versus $\hbar\omega$ which is expected[127] to be linear in the range from 2.45 eV to 3.3 eV (i.e. the transition near L has the form $\Im[\epsilon_{core}] \sim (\omega - \omega_o)^{1/2}/(\hbar\omega)^2$, where the $\hbar\omega_o$ is the onset energy). This plot is shown in Fig. 4.9(a). Fig. 4.9(b) shows the dependence of the bandedge slope and onset energy on the particle size taken from a least squares fit to the data in Fig. 4.9(a). The results show the same trends as those of Kreibig's,[128] namely a decrease in both the bandedge slope and the onset energy with decreasing particle size, from $\sim$5000 and $\sim$2.43 eV to $\sim$3500 and $\sim$2.40 eV, respectively, as R decreases from 11.1 nm to 3.5 nm. However, the decrease of the slope in Kreibig's data was only observed for $R < 2$ nm, with a constant value of $\sim$5000 for larger particles while the onset energy was 2.45 eV already for $R \sim 7$ nm. Extrapolating our results to bulk values and assuming a continuing linear dependence, we obtain an onset energy of $\sim$2.44 eV and bandedge slope of $\sim$5600 compared to Thèye's values[127] of 2.45 eV and 6000, respectively.

The most dramatic change in $\Im[\epsilon_m]$ in Fig. 4.8(b) is the increase in the height of the peak around 315 nm with increasing R. The same result[14] has been observed when annealing pure gold thin films; in fact, the similarity between Fig. 4.8(b) and Fig. 3 in Ref. [14] is remarkable. Attributing the variation in the peak height to a particular effect for a polycrystalline gold film is difficult as there are many contributing factors (see, for example, Aspnes[188]). For embedded particles, however, all of these can be ruled out, with the exception of strain-induced lattice deformation.

The lattice contraction of gold nanoparticles is now well established[37,76,108] and has been attributed to the surface of the particle being in a state of stress, specifically, dilated.[37] The peak at $\sim$315 nm has contributions from:[227] (*i*) inter-band transitions (3d, 4d $\rightarrow$ 6sp), and (*ii*) inter-conduction band transitions (6sp $\rightarrow$ 7sp). The latter transitions are very sensitive to lattice distortions.[14] In particular, the strain-induced variation of the lattice spacing will cause the peak to broaden and lower. Although it

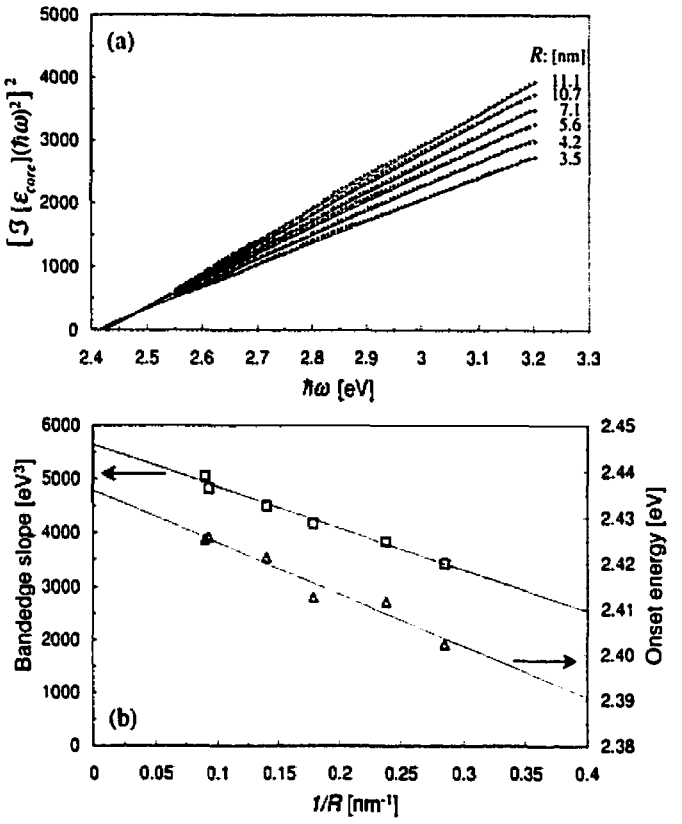

Figure 4.9: (a) Particle size dependence of the inter-band edge for transitions near L and (b) change in the inter-band edge slope and shift of the onset energy versus reciprocal particle size.

is difficult to quantify the internal strains present in a pure polycrystalline film, the difficulty being compounded by substrate effects, the situation for embedded particles is clear: the decrease of the peak height is a consequence of the increasing disparity between the lattice constant at the surface and in the inner particle. This is the same conclusion drawn by Picozzi et al[130] to account for the particle size dependence of the vuv reflectivity of gold clusters.

As mentioned above, changes in the absorption spectrum at 315 nm are not expected to influence the shape or position of the SPR. However, changes in the band-structure that they entail will influence, to a lesser or greater extent, changes in the

absorption throughout the uv-visible spectrum. This particle size dependence of the bandstructure is expected from the variation in the atomic arrangement as determined by the state of the particle surface with respect to stress. Minimum energy structure considerations (in which surface stress plays a crucial role) together with HRTEM studies has led Marks[10] to envision a phase map for gold nanoparticles. According to the map, the gold particles go through a transition from a quasi-molten state to particles having a multiply-twinned structure at $R \sim 2\,\text{nm}$ for temperatures of $\sim 300\text{K}$. This is followed by a transition to single crystals at $R \sim 7\,\text{nm}$. The first transition corresponds well with that observed by Kreibig,[75,128] while the transition to single crystals occurs at the minimum particle size for which the position of the SPR was found to be correctly predicted using bulk gold values for ϵ_{core}. Furthermore, the transition to single crystals is expected to be a gradual one due to the presence of thermodynamically unstable structures as a consequence of particle growth kinetic effects.

4.6 Summary and Conclusions

Au/SiO_2 nanocomposite films were fabricated using a hybrid deposition technique in which gold sputtering and PECVD were utilized. The optical constants of the films were determined from VASE measurements and modeled using the M-G EMT. The particle size dependence of the gold free electron absorption was included according to the LMFP effect with the broadening parameter $A = 0.15$, as determined from the comparison of the measured spectra to TEM micrographs.

The model predicted correctly the optical response of the films, but only in the narrow size range $5.6\,\text{nm} < R < 11.1\,\text{nm}$, the large particle limit being the well known limit of the QSA. For $R < 5.6\,\text{nm}$ the energy of the SPR was blue-shifted with respect to model predictions. The blue-shift with decreasing particle size was attributed to a size dependence of the inter-band transitions near L in the Brillouin zone as a result of

strain-induced variation of the lattice constant within the particle. This is supported by changes in the inter-band spectra at $\lambda \sim 315\,\mathrm{nm}$ where $\Im[\epsilon_m]$ is determined in part by 6sp $\rightarrow$ 7sp inter-conduction transitions which are more sensitive to lattice deformations. The small particle limit is larger than previously determined and its observation is due to the sensitivity of the ellipsometric technique together with the fact that particle size distributions in the films studied were narrow.

Acknowledgments

The authors wish to acknowledge the expert technical assistance of Mr. Gilles Jalbert. This work was supported by the Natural Sciences and Engineering Research Council (NSERC) of Canada.

Chapter 5

Article 3: Au/SiO_2 Films at High Temperature

This article is a short letter reiterating the particle size-dependence of the core response of gold presented in Chapter 4. *In situ* transmission measurements as a function of temperature are also performed, taking advantage of the thermal stability of the Au/SiO_2 films. The size- and temperature-induced changes in ϵ_{core} are compared to elucidate the origin of the size-dependence, namely the loss of long-range order arising from surface atom migration and crystal structure distortion.

Temperature dependence of the surface plasmon resonance in Au/SiO_2 nanocomposite films

Dan Dalacu and Ludvik Martinu

Recieved 23 August 2000; accepted 23 October 2000

Appl. Phys. Lett. **77**(26), December 2000

5.1 Abstract

The optical response of Au/SiO_2 nanocomposite films at temperatures spanning the transition to the liquid state has been measured. The change in the optical constants of gold from those corresponding to the crystalline material to those of the liquid occurs gradually and at temperatures below the bulk melting point. The similarity of the temperature-induced changes in the Au inter-band absorption edge to that observed with decreasing particle size suggests that a gradual transition to the liquid phase also occurs in small particles.

5.2 Results

The optical response of gold particles is exceptional in that the dipolar mode of the collective conduction electron plasma oscillations (i.e. surface plasmon resonance) coincides with the dominant inter-band transition edge. Optical spectroscopy, therefore, provides a probe of the particle size dependence of both the valence and conduction electrons. The particle size dependence of the conduction electron response is relatively well understood: the width of the SPR band increases linearly with particle size as a consequence of Landau damping[64] while the energy is determined by the combined effects of spill-out[93] and reduced s-d interaction for surface atoms,[100,107] resulting in a blue-shift of the SPR with decreasing size.[78]

The particle size dependence of the inter-band transition edge is less clear and has generally been described in terms of surface stress-induced changes of the lattice constant and the reduced coordination of the surface atoms.[129,228] The effect of the latter is a narrowing of the valence band[219,220,229] and a shift of the center of gravity to lower energy,[16] though the observed shift in small particles is to higher energy as a consequence of particle charging.[29] The former is based on the observed lattice constant changes in gold particles[36,37,108] and corresponding changes expected in the electronic band-structure.[13,230] For example, the onset energy of the $5d \rightarrow 6s$ transitions near symmetry points L and X in the Brillouin zone are predicted to shift by $-0.40\,\mathrm{eV}$ and $-0.45\,\mathrm{eV}$, respectively, for a 0.053Å dilation, equivalent to a 920°C temperature rise. However, the predicted shift of the Fermi energy is $-0.43\,\mathrm{eV}$, so that only minor overall changes are expected.

A more appropriate description of the atomic structure of small metal particles requires consideration of surface atom migration (so-called surface pre-melting), structural fluctuations (so-called quasi-melting), and mixed liquid/solid phases (so-called pseudo-crystallinity), as revealed by recent electron microscopy studies.[10,120,124] These effects are all precursors to the eventual melting of the particle at a temperature (T_m) below that of the bulk material. The reduction of T_m with decreasing particle size

is an old idea that has been described in terms of phenomenological thermodynamic models,[112,113] and, more recently, simulated using molecular-dynamics.[115–118] Experimental evidence of the reduced T_m has been demonstrated repeatedly by a variety of techniques.[114,119–122]

In this work, we measure the optical response of Au particles over a temperature range that includes T_m. Microstructural changes are avoided by stabilizing the films in a SiO_2 matrix and performing extended anneals at 900°C prior to taking the measurements such that the heat treatments are fully reversible. One important finding of this study is the absence of an abrupt change in both the inter- and intra-band response, indicative of a broadened phase transition. We also compare the particle size dependence of the optical response with that of the temperature dependence. The correspondence between the two, which has already been implied by the phase diagram of Ajayan and Marks,[231] suggests a gradual melting of the ion core with decreasing particle size.

The Au/SiO_2 nanocomposite films were deposited on quartz substrates by simultaneous RF sputtering of a gold target and plasma-enhanced chemical vapour deposition of SiO_2.[210] The samples were annealed in air in a simple quartz tube furnace, and *in situ* transmission measurements were made using an Oriel diode-array spectrophotometer. Additional *ex situ* measurements over a wide spectral range were taken using a VASE ellipsometer (J. A. Woollam Co.) and a Lambda 19 spectrophotometer (Perkin-Elmer).

The film thickness (d) and gold volume fraction (p) were determined by applying the Maxwell-Garnett model[4] to the *ex situ* optical data.[210] The optical response of the gold particles was described using a modified Drude dielectric function[224] consisting of a size-dependent core polarizability to account for the shift of the SPR and an effective collision frequency:[85]

$$\Gamma = 1/\tau_B + A\nu_F/R, \tag{5.1}$$

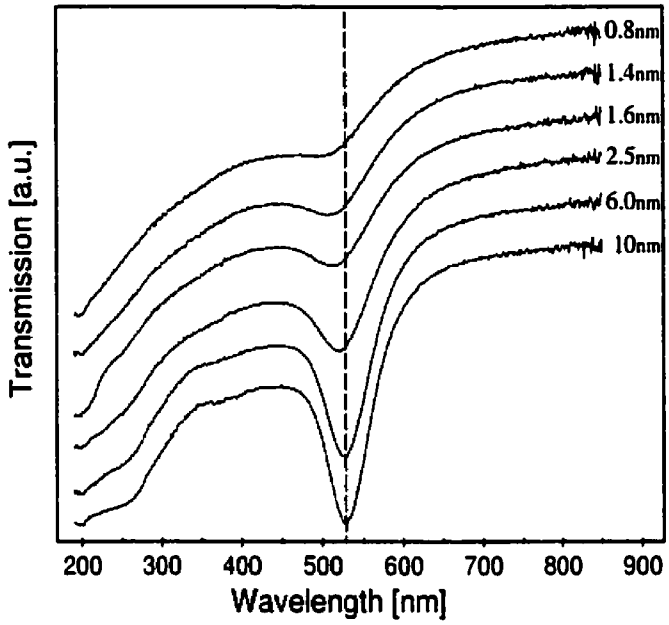

Figure 5.1: Transmission spectra as a function of R obtained from successive anneals at 900°C of a Au/SiO_2 film with $p = 1.5\%$ and $d = 300\,nm$.

which describes the size-dependent width of the SPR in terms of the particle radius (R), the electron velocity (ν_F), and a broadening constant (A).[64] The particle size was estimated from Eq. 5.1 using $A = 0.15$.[224]

Fig. 5.1 shows the transmission spectra as a function of particle radius obtained by successive 900°C anneals of the same sample. The particle size dependence of the conduction electron response is evident from the blue-shift and broadening of the SPR with decreasing R. The increasing asymmetry of the band, on the other hand, is due to changes in the inter-band response. In particular, analysis of the measured absorption and ellipsometric spectra have shown that both the slope and the onset energy of the absorption edge due to the d- to s-band transition near L decreases with decreasing R.[129,210,228] An additional particle size dependence is evident from the increasing dip in the transmission between 250 and 350 nm, a feature which has been identified with inter-conduction band transitions and its broadening associated with lattice deformation.[14]

Fig. 5.2(a) shows the transmission spectra as a function of temperature for a $R = 2\,\text{nm}$ film which is expected to undergo a transition to the liquid phase within the temperature range measured. For example, for this particle size molecular-dynamic simulations[117] predict $T_m \sim 600°\text{C}$, while electron diffraction experiments[114] suggest $T_m \sim 700°\text{C}$. The broadening of the SPR arises from the temperature dependence of τ_B, in particular, the electron-phonon contribution (i.e. $1/\tau_{el-ph} \sim T$ for temperatures greater than the Debye temperature, $\theta_D = -103°\text{C}$[44]). We attribute the increasing asymmetry of the band to the melting of the ion core. For comparison, we have also plotted the transmission expected at 900°C using the ambient temperature optical constants of bulk gold but with Γ obtained from a fit of the low energy flank of the SPR band of the 900°C spectrum.

The inter-band changes observed in Fig. 5.2 are very similar to those observed in Fig. 5.1. In fact, a comparable decrease in the slope of the inter-band absorption edge observed with decreasing R has also been observed upon transition to the liquid phase from optical measurements on bulk gold.[126] Even the interconduction-band absorption, seen to disappear in Fig. 5.1, is presumably supressed in the liquid phase.[126] The striking difference between the optical measurements of bulk gold and those of Fig. 5.2 is that the transition to the liquid phase for particles is gradual. There is no abrupt change in neither the inter- nor intra-band responses, the latter of which is also expected to change significantly upon transition due to a two-fold decrease in τ_B.[232]

Since the transition to the liquid phase is broadened, changes in the optical response of particles are expected at temperatures below T_m. This is indicated from the observed changes in the asymmetry of the SPR band for the $R = 8\,\text{nm}$ film in Fig. 5.2(b). The broadening also makes it difficult to observe an abrupt change in the optical constants of gold even for much larger particles. For example, Fig. 5.2(c) shows the transmission spectra for a $R = 15\,\text{nm}$ film taken below and above the bulk melting point, $T_m = 1063°\text{C}$, providing some evidence of an abrupt transition.

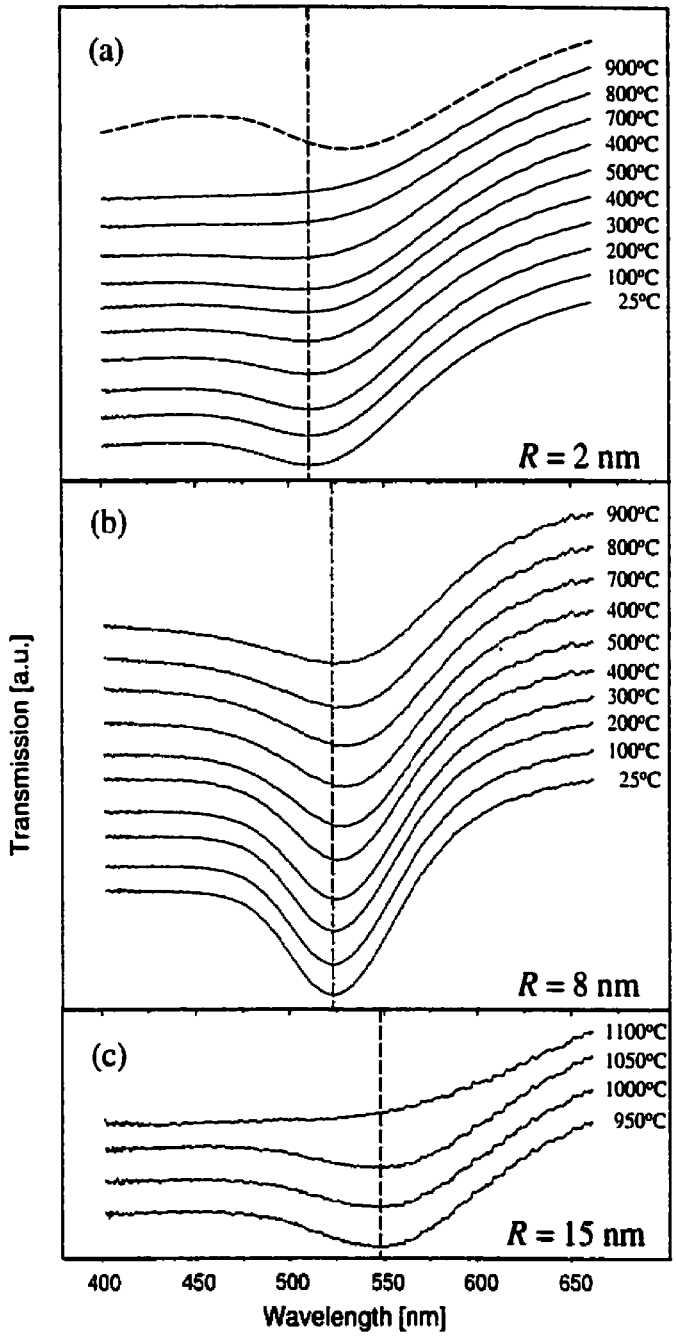

Figure 5.2: Transmission spectra as a function of temperature for Au/SiO_2 films with (a) $R = 2\,nm$, $p = 3.7\%$, $d = 375\,nm$, (b) $R = 8\,nm$, $p = 2.2\%$, $d = 325\,nm$, and (c) $R = 15\,nm$, $p = 6.3\%$, $d = 50\,nm$. The dashed curve in (a) represents a model spectrum using the ambient temperature bulk gold inter-band response and Γ corresponding to the 900°C transmission.

A melted ion core will also have implications concerning the energy of the SPR. In particular, a blue-shift is expected from the reduction in the core polarizability observed from the measurements on bulk liquid gold.[126] This is apparently more than compensated by the red-shift resulting from large Γ values seen from the calculated transmission in Fig. 5.2 and from lattice dilation, which decreases the electron density, and, hence, the plasma frequency, $\omega_p = n_e e^2/\epsilon_o m_e$. In the case of the R dependence, the decrease in core polarizability will add to the effect of decreased s-d interaction, resulting in the distinct blue-shift with decreasing R observed in Fig. 5.1.

In conclusion, we have measured the temperature dependence of the optical response of gold particles, revealing a gradual transition of the inter-band response to that of the liquid material. We have also observed a correspondence between the temperature and particle size dependence of the inter-band response, suggesting that the same effects that occur with increasing T also occur with decreasing R. A similar correspondance has also been observed from photoemission studies[15,219] which have revealed the disappearance of the dependence of the energy distribution curves on excitation frequency upon transition to the liquid phase and with decreasing particle size, indicative of a change from direct to indirect inter-band transitions.

The authors wish to acknowledge the expert technical assistance of Mr. G. Jalbert. This work was supported by the Natural Sciences and Engineering Research Council (NSERC) of Canada.

Chapter 6

Article 4: Discontinuous Au Films

The study of substrate-supported particles was performed with two objectives in mind: The first one consisted of applying the results of the study of the 3-D Au/SiO_2 system to discontinuous films. In particular, the particle size dependence of the core response of gold observed in the 3-D system was used to account for the particle size dependence of the SPR energy in the 2-D system for which the inter-band absorption edge is less visible due to the minute thickness of the films. The second objective was the determination of the exact relation between the width of the SPR and the particle size (i.e. the value of A), which was needed in the study of the 3-D Au/SiO_2 system. This was accomplished by analyzing identical samples using both optical spectroscopy and TEM. The TEM analysis performed here differs from that done in the Au/PPFC study in that a mono-layer of particles was analyzed, allowing a more accurate statistical approach to be used to determine the particle size.

The luxury of the dual optical/TEM analysis comes at the expense of a more complicated optical response inherent to a 2-D array of particles, in particular, a local field which gives rise to uniaxial anisotropy. The anisotropy is evident from oblique incidence transmission spectra which show absorption bands corresponding to two SPRs since the local field, and hence the local field-induced shift, depends on direction. This is shown in Fig. 6.1 where the blue-shift and broadening of the

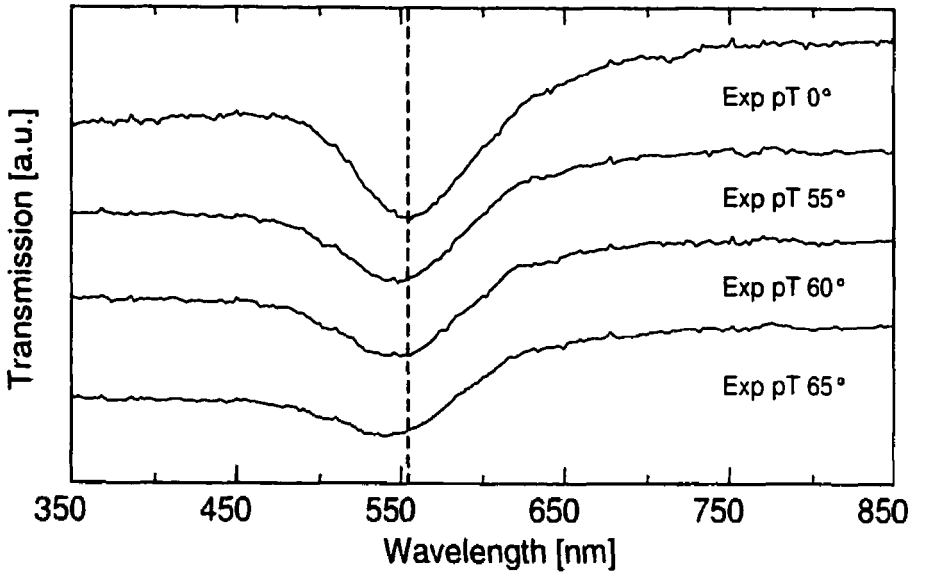

Figure 6.1: Oblique incidence p-polarized transmission spectra of a discontinuous gold film ($p = 23.1\%$, $R = 6.9\,\text{nm}$).

'SPR' with increasing incidence angle for p-polarized light arises from the appearance of a second SPR at oblique incidence, resonant at a slightly higher energy. There is probably a contribution to the observed blue-shift from particle deformation (i.e. oblate spheroids) which gives rise to a very similar behaviour (see Fig. 1.7).

This article also demonstrates the role of the matrix material with regard to the liquid-like coalescence of small particles. Although the annealing temperature used in this study was only slightly higher than that used in the Au/PPFC study (250°C compared to 160°C, respectively), liquid-like coalescence was observed for particles as large as 20 nm as compared to only 5 nm particles when embedded in PPFC. This observation suggests that surface atom migration is inhibited by the presence of the matrix material, previously mentioned in Chapter 3. The restriction of surface atom migration to smaller particles might also account for decrease in the SPR width that was observed in this study when the particles were embedded in a matrix.

Concerning the liquid-like coalescence of the unembedded larger particles, it was

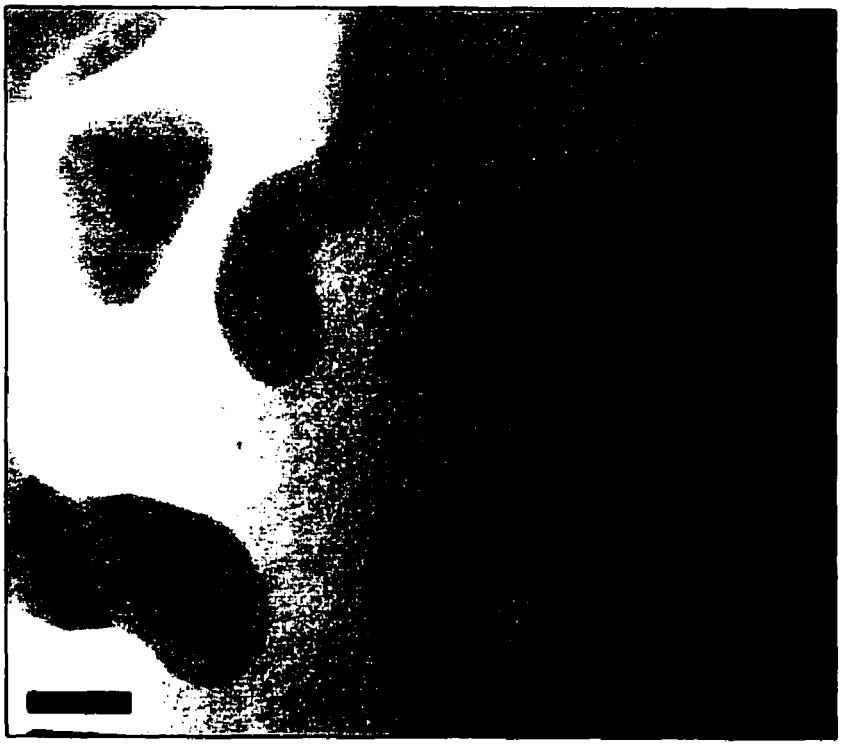

Figure 6.2: TEM micrograph of a large particle discontinuous film obtained by annealing a high p sample for 5 hours at 250°C. Bar indicates 20 nm.

noted that the reshaping that follows neck-formation does not occur after coalescence of particles larger than 20 nm, as shown in Fig. 6.2. For the anneal temperature used, it seems that at this particle size, two particles will form a grain boundary as opposed to reforming into something that resembles a sphere, either a single crystal (FCC-type cuboctahedra) or a MTP (icosahedra, decahedra).[233]

It is interesting to note that the substrate-dependent processes in the early stages of film growth (nucleation, migration, coalescence), studied extensively in the 1970's for the case of gold clusters on carbon[234] and NaCl,[235,236] is currently a topic of intense research.[237] Recent studies of the substrate dependence of gold cluster growth include the substrates SiO_2,[238,239], TiO_2,[240,241] MgO,[241,242] and Al_2O_3.[243]

Optical Properties of Discontinuous Gold Films: Finite Size Effects

Dan Dalacu and Ludvik Martinu

Recieved 6 June 2000; accepted 11 September 2000

J. Opt. Soc. Am. B. **18**(1), 85-92, January 2001

6.1 Abstract

The optical constants of discontinuous gold films consisting of both embedded and unembedded spherical particles in the size range 5 - 14 nm were determined from spectroellipsometric and spectrophotometric measurements. The optical response was modeled using the Yamaguchi anisotropic dielectric function. The energy and width dependence of the surface plasmon resonance due to the finite size of the gold particles was determined using a phenomenologically modified metal dielectric function. The expected blue-shift and broadening of the resonance with decreasing particle size was observed. The magnitude of the shift suggests that changes in the lattice constant in small gold particles, and the attendant effects on the core response, play an important role in determining the resonant energy. The width dependence on particle size was found to be well described by broadening parameters $A = 0.15$ and $A = 0.22$ for embedded and unembedded particles, respectively.

6.2 Introduction

The excitation of collective conduction electron plasma oscillations, the dipole mode of which is referred to as the surface plasmon resonance,[197] has made the optical properties of noble metal nanoparticles the subject of continued research since it was first noticed by Faraday in 1857.[2] The interest stems, in part, from the link which these particles provide between the atomic and solid states, and in part, from potential applications in the fields of spectrally selective coatings,[196] non-linear optics,[19] and heterogeneous catalysis.[26] Particles supported on substrates, so-called 'discontinuous films', relevant to the latter application, have received particular attention; this includes mainly the films consisting of gold[60,129,225,244-252] and silver[73,253-255] particles.

Optical characterization of discontinuous films is made very difficult due to the minute thickness of the film and the presence of the substrate. The former, being of the order of the particle size, necessitates the characterization of films with a high metal volume fraction where the dipole-dipole interactions cannot be neglected. As such, the exact electrodynamic treatment of Mie,[5] calculated for a single particle, cannot be applied and optical modeling must be done within the framework of effective medium theories.[18] The supporting substrate will further complicate the optical response by giving rise to image charge effects as well as to a deformation of the particles into spheroids of revolution. On the other hand, discontinuous films provide an easy method of preparation of particles with sizes in a range where the evolution of the particle size dependence of the optical constants of the metal (so called 'finite size effects'), can be followed from the convergence point with the bulk constants.

The finite size effects occur for particles with dimensions less than the electron mean free path and they signify the increasing importance of the particle surface. They result in a broadening and shifting of the SPR compared to predictions of the Mie theory, and they are a consequence of the discretization of the conduction electron eigenstates[80] (i.e. the so-called quantum size effect). The recent advances

in the understanding of the finite size effects in small metal particles based on the quantum mechanically derived response of the conduction electrons have led to the following general conclusions (see, for example, de Heer[9]): (*i*) The broadening of the SPR is a result of the coupling of the collective resonance with single-electron excitations[64] (i.e. Landau damping) and, for larger clusters, it is proportional to the inverse particle size;[85] (*ii*) the electron density extends outside the particle radius, as defined by the ion core, which red-shifts the SPR,[93] so-called electron 'spill-out'; and (*iii*) the amplitude of the d-electron wavefunction at the boundary of the Wigner-Seitz sphere is negligible for the surface atoms (i.e. there is a core-polarization-free surface layer);[100,107] as a result, part of the induced charge density oscillates with an unscreened plasma frequency (i.e. blue-shifted). Experimentally, the SPR of alkali metals is red-shifted[50] (i.e. effect (*ii*) is absent), while for gold and silver it is blue-shifted[30,74,78,210] (i.e. effect (*iii*) dominates).

An additional contribution to the observed finite size effects in the case of noble metals is the dependence on particle size of the dielectric function just below the Fermi level. For gold, the response in this region is determined by inter-band transitions from initial states in the d-bands and in the conduction band,[227] both of which are sensitive to lattice constant changes[13,14,230] known to occur in small gold particles.[36,37,76,108] Transitions from the d-bands will also be affected by band narrowing observed in X-ray photoelectron spectroscopy studies[220,229] and associated with the reduced coordination of the surface atoms.[131] In the quantum mechanically derived response, these effects are not included:[78,256] only the conduction electrons are treated (jellium approximation) using the bulk Wigner-Seitz radius, r_s, and the inter-band response is taken from the bulk constants.

In this study, we first demonstrate the influence of dipole-dipole interactions resulting from the particles themselves, as well as their image charges. This is accomplished by depositing the discontinuous gold films with varying filling in a multi-layer configuration (dielectric/gold/dielectric) using different dielectric materials. We then show

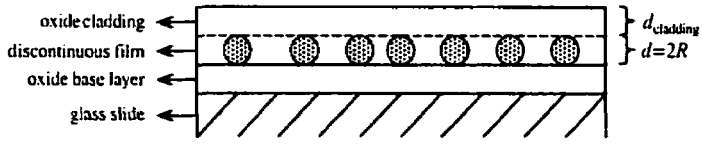

Figure 6.3: Schematic representation of the multi-layer dielectric/gold/dielectric structure.

that finite size effects can also be observed, and quantified, in the discontinuous films by accounting for the shift and broadening of the SPR due to the dipole and image charge interactions according to the theory of Yamaguchi.[257] The measured shifts of the SPR are compared with those predicted from the quantum mechanical response calculated by Palpant *et al*[78] where the electron density distribution is described in terms of the time-dependent local density approximation. The discrepancies observed demonstrate the importance of a dependence of the inter-band optical constants of gold on the particle size.

6.3 Film Preparation and Characterization

The samples studied in this work consisted of a dielectric/gold/dielectric structure, schematically shown in Fig. 6.3. The base and cladding layers were deposited by plasma-enhanced chemical vapour deposition using SiH_4/N_2O and $TiCl_4/O_2$ chemistries for the SiO_2 and TiO_2, respectively, described in detail elsewhere.[221,222] The discontinuous gold films were deposited by RF magnetron sputtering from a 50 mm gold target at 60 mTorr of Ar. The magnetron was displaced from the axis of the substrate holder to allow for a gradient in the filling along the sample, and, as such, multiple measurements on the same sample. An input RF power of 100 W was used, for a self-bias of -350 V. All films were annealed at 250° C for 5 hours prior to deposition of the cladding in order to obtain spherical, well-isolated particles with a narrow size distribution.

Optical characterization of the films was performed before and after deposition of the cladding layer. It consisted of variable-angle spectroellipsometric (model VASE from J.A. Woollam Co., Inc.), and normal-incidence transmission (model Lambda 19 from Perkin-Elmer) measurements. The $SiO_2/Au/SiO_2$ films were also deposited simultaneously on carbon-coated copper grids for transmission electron microscopy using a Philips CM30 microscope. Depositing the entire three layer structure on the grids ensures that the films studied optically are the same as those analysed by TEM (i.e. the base layer ensures that the morphology of the discontinuous films are indentical and the top layer minimizes the influence of the electron beam during analysis). The TEM images were analysed to extract different microstructural characteristics using the software package ImageTool developed at the University of Texas.

6.4 Optical Response of a 2-D Array of Metal Particles

For an ensemble of spherical particles of sufficiently large size (> electron mean free path) and in sufficiently low concentration (< 1%), the optical properties are described well by the Mie theory,[5] using the bulk metal optical constants. The maximum volume fraction is limited by the interaction of the dipole fields of the particles which results in a red-shift and broadening of the SPR. In the case of discontinuous films, the filling is not, in general, low enough to neglect dipole interactions, and the Mie theory no longer applies. Instead, an alternative approach, which describes the optical properties of an ensemble of metal particles by an effective dielectric constant, is used. Unlike the exact treatment of Mie, EMTs are derived in the electrostatic limit, and, as such, apply only to particles with dimensions small compared to the wavelength of the incident light (for gold the quasi-static limit occurs at a particle size of about 20 nm[210]). They are, however, readily modified to account for dipole-dipole interactions.

This can be achieved either by using the Lorentz local field as is the Maxwell-Garnett expression[4] which is applicable to 3-D films, or by direct calculation of a 2-D array of dipoles.[247,258] We have employed the theory of Yamaguchi[257-259] in which the uniaxial anisotropic response of a collection of oblate spheroids (minor axis a normal to the film plane, major axes $b = c$ in the film plane) is described in terms of two effective dielectric constants $\epsilon_{\|}$ and $\epsilon_{\perp}$ for electric fields parallel and perpendicular to the substrate, respectively:

$$\epsilon_{\|} = \epsilon_h \left[1 + \frac{p(\epsilon_m - \epsilon_h)}{\epsilon_h + F_{\|}(\epsilon_m - \epsilon_h)} \right], \tag{6.1}$$

$$\frac{1}{\epsilon_{\perp}} = \frac{1}{\epsilon_h} \left[1 - \frac{p(\epsilon_m - \epsilon_h)}{\epsilon_h + F_{\perp}(\epsilon_m - \epsilon_h)} \right], \tag{6.2}$$

where p is the gold filling, and ϵ_m and ϵ_h represent the dielectric response of the metal particles and the embedding matrix, respectively. The F's are effective depolarization factors given by:

$$F_{\|} = L_{\|} - \frac{\gamma^2}{24\eta^3} \frac{\epsilon_s - \epsilon_h}{\epsilon_s + \epsilon_h} - C_{\|} \frac{pd}{\zeta} \frac{2\epsilon_h}{\epsilon_s + \epsilon_h}, \tag{6.3}$$

$$F_{\perp} = L_{\perp} - \frac{\gamma^2}{12\eta^3} \frac{\epsilon_s - \epsilon_h}{\epsilon_s + \epsilon_h} + C_{\perp} \frac{pd}{\zeta} \frac{2\epsilon_s}{\epsilon_s + \epsilon_h}, \tag{6.4}$$

where $L_{\|,\perp}$ are real depolarization factors,[49] γ is the axial ratio (i.e. c/a), η represents the distance between the point dipole moment of a particle and its image charge, d is the film thickness, and ϵ_s is the dielectric function of the substrate. $C_{\|,\perp}$ are determined by the lattice structure of the 2-D array having inter-particle spacing ζ. Eqs. 6.3 and 6.4 allows one to account for the influence on the optical response due to particle shape (first term), image charge interaction (second term) and dipole interaction (third term).

The influence of these different effects can be observed using normal incidence transmission measurments. In this case, the optical response is given by $\epsilon_{\|}$ and the energy of the SPR is determined by ϵ_m, ϵ_h, and $F_{\|}$. In particular, the SPR is red-shifted for increasing ϵ_h and for decreasing $F_{\|}$. Dipole interaction, which will increase with increasing p, leads to a red-shift of the SPR due to a decrease of $F_{\|}$, while image charge interaction leads to either a red-shift or blue-shift, depending on whether $\epsilon_h < \epsilon_s$ or $\epsilon_h < \epsilon_s$, respectively.

In this study all these effects are observed by changing ϵ_h and ϵ_s using different combinations of base and cladding layers. The dielectric functions of the materials used for these layers (ϵ_{SiO_2}, and ϵ_{TiO_2}) as well as that of the glass substrate (ϵ_{glass}) were determined from ellipsometric measurements by fitting the Ψ and Δ data with a three-term Cauchy dispersion model. For the glass slide and TiO_2, an Urbach edge was included to account for the absorption in the near uv. The dielectric constants are shown in Fig. 6.4.

The dielectric function of gold, ϵ_m, determined from ellipsometric measurements of a continuous film, is also shown in the figure. The contributions to the dielectric function from the free electrons and bound core electrons have been separated by modeling the response of the former according to the Drude expression:

$$\epsilon_m = \epsilon_{core} + 1 - \frac{\omega_p^2}{\omega(\omega + i/\tau_B)}, \tag{6.5}$$

where ω_p is the bulk plasma frequency and τ_B is the free electron relaxation lifetime determined by scattering processes in the bulk material.

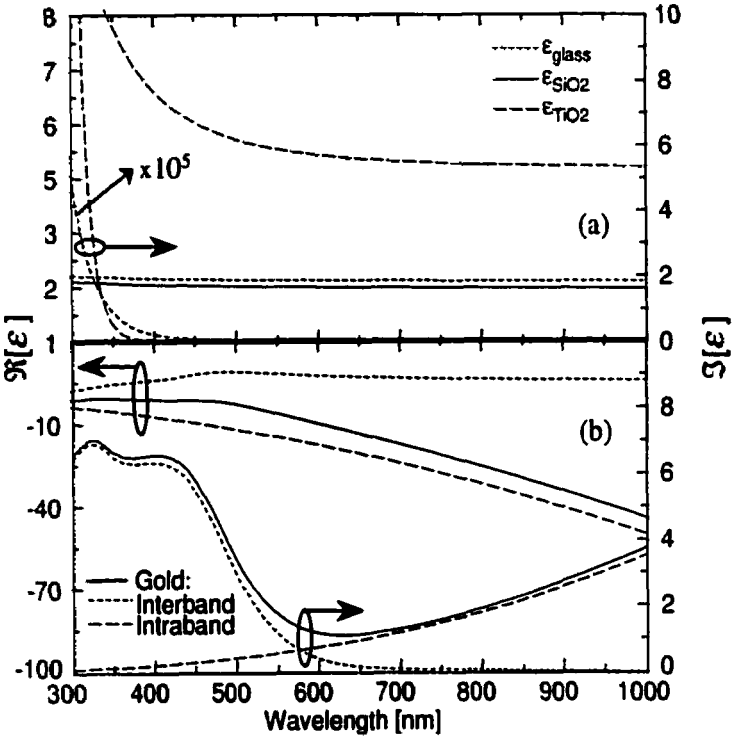

Figure 6.4: Optical constants of (a) glass, SiO_2, TiO_2 and (b) gold.

6.5 Results

6.5.1 TEM Characterization

Examples of TEM micrographs of the discontinuous gold films sandwiched between the two SiO_2 layers are shown in Fig. 6.5. The labels A, B, C, and D correspond to different distances from the magnetron axis, decreasing from A to D. The variation in particle size occurs as a consequence of the coalescence process during annealing,[123,223] with larger particles for films with higher gold filling (i.e. those located closer to the magnetron axis). Films with particles larger and smaller than those shown in Fig 6.5 were not studied, the former due to incomplete reshaping after coalescence resulting in irregular particles shapes, the latter due to the severe broadening of the SPR, resulting in rather featureless spectra.

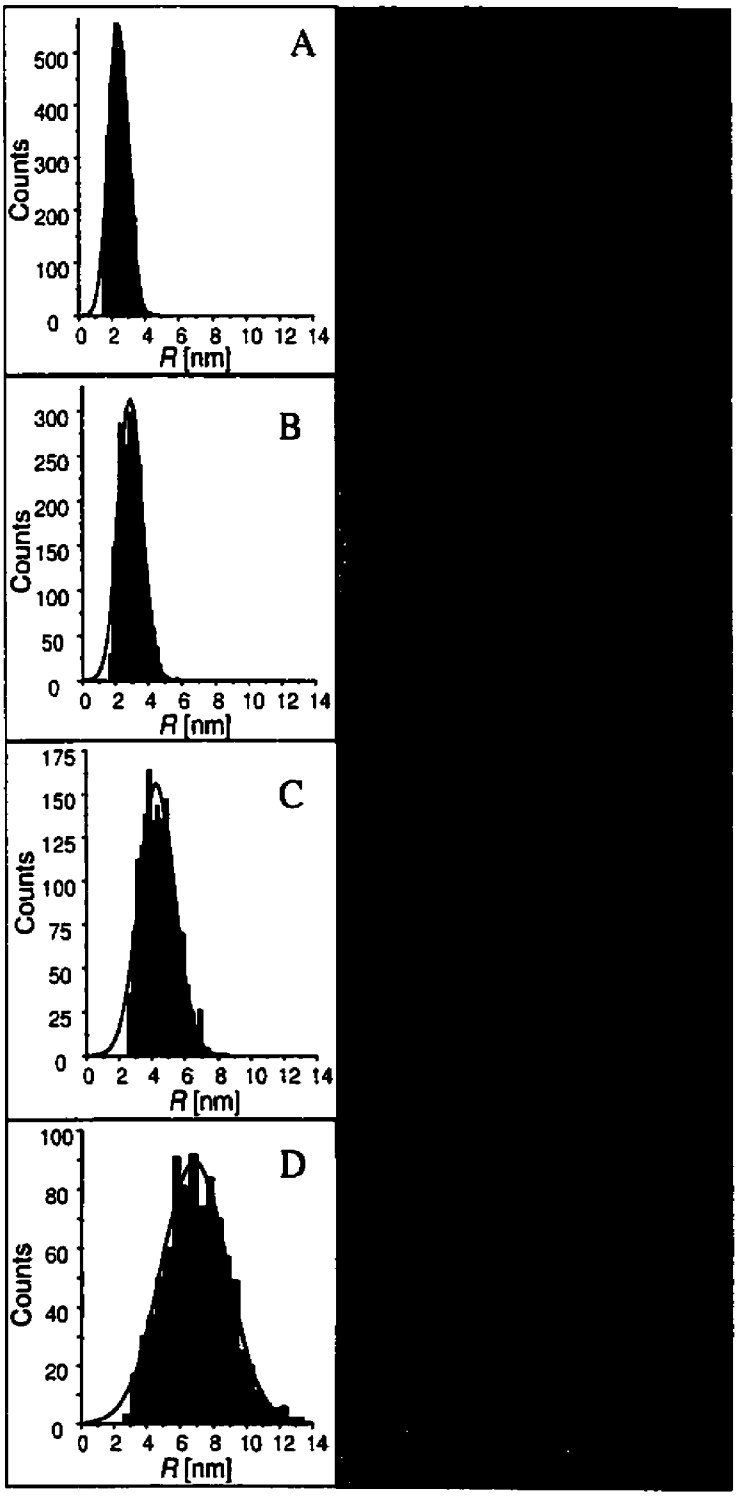

Figure 6.5: TEM micrographs and particle size distributions for the SiO_2/gold/SiO_2 samples.

The image analysis was performed on micrographs taken at lower magnification sampling an area of $A_T = 0.3786\,\mu m^2$. Particle sizes are calculated from the Feret diameter (i.e. $2R = \sqrt{A_p/\pi}$). The particle size distributions for the four films are shown in Fig. 6.5, and the results of the image analysis are summarized in Table 6.1. The particle sizes and standard deviations listed are obtained from gaussian fits to the histograms in Fig. 6.5. The axial ratio $b : c$ is also tabulated, and it indicates almost circular cross-sections for all the films, the lowest value of 1.17 most probably limited by the image resolution.

Table 6.1: Results of the image analysis performed on the TEM micrographs: N_p: number of particles sampled, R: particle radius, σ: standard deviation, b:c: major to minor axis ratio, p: gold filling.

Sample	N_p	R[nm]	σ[nm]	b:c	p[%]
A	3930	2.4	0.6	1.17	12.2
B	2800	2.9	0.7	1.17	13.3
C	1650	4.3	1.1	1.17	16.9
D	875	6.9	2.0	1.25	23.1

6.5.2 Optical Characterization

The transmission spectra of samples with different ϵ_h together with that of the substrate are shown in Fig. 6.6. These films have all been deposited on an SiO_2 base layer ($\epsilon_s = \epsilon_{SiO_2}$). In all cases the SPR blue-shifts as the distance from the magnetron axis increases. Part of the shift is a result of the decreasing dipole interaction as p decreases, and part is due to the blue-shift expected with decreasing R.

We have also indicated (by the vertical lines) the expected SPR energy in the Mie limit which excludes dipole and image charge interactions ($F_{\|} = L_{\|} = 1/3$ for spherical particles). For the uncladded samples ($\epsilon_h = 1$), the SPR energies are red-shifted relative to the Mie limit due to the shift from the image charge interaction for $\epsilon_h < \epsilon_s$. For the TiO_2 cladded samples, the SPR energies are blue-shifted since $\epsilon_h > \epsilon_s$. For the SiO_2 cladded samples, image charge interaction is absent and the

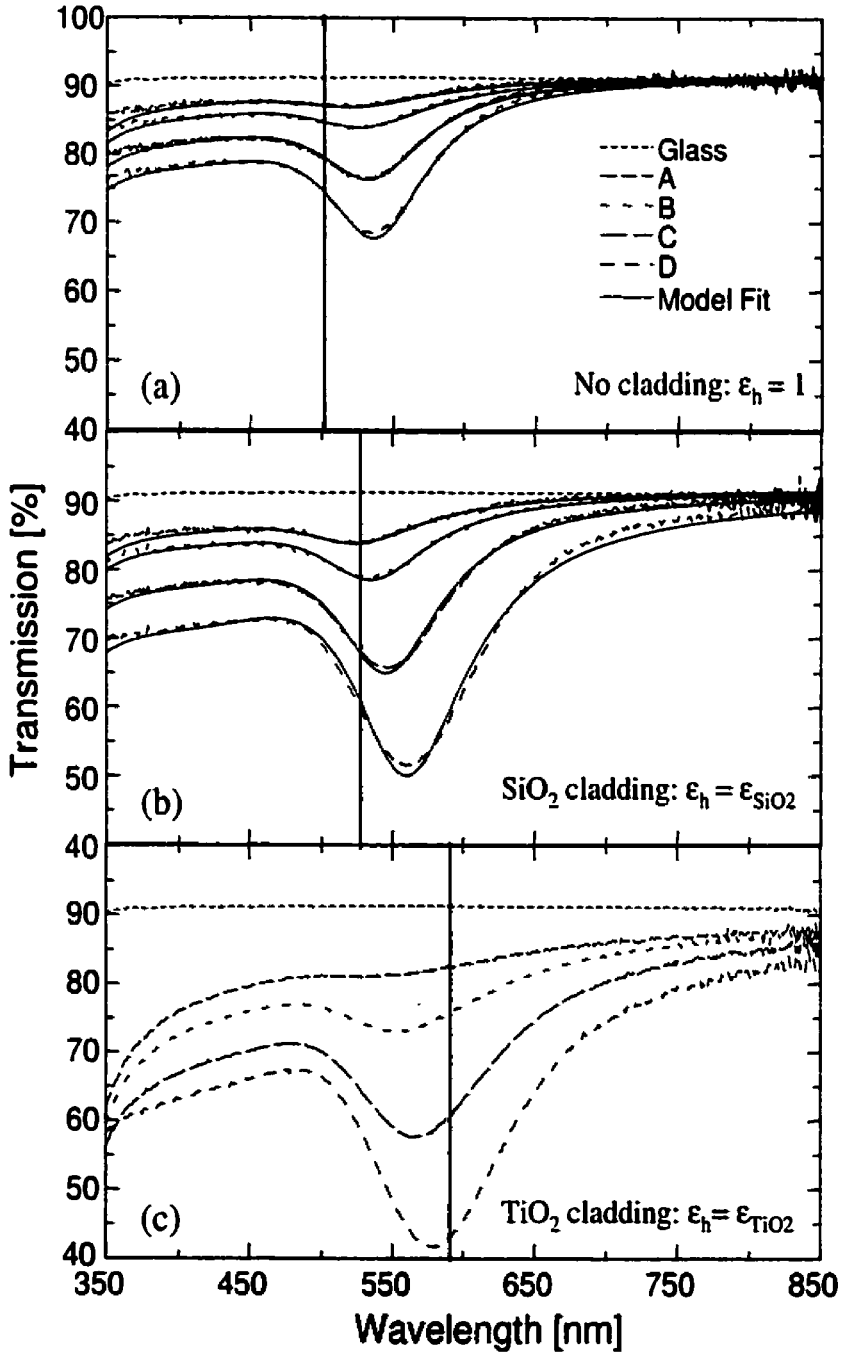

Figure 6.6: Transmission spectra of discontinuous gold films on a SiO_2 base layer with: (a) no cladding, (b) SiO_2 cladding, and (c) TiO_2 cladding.

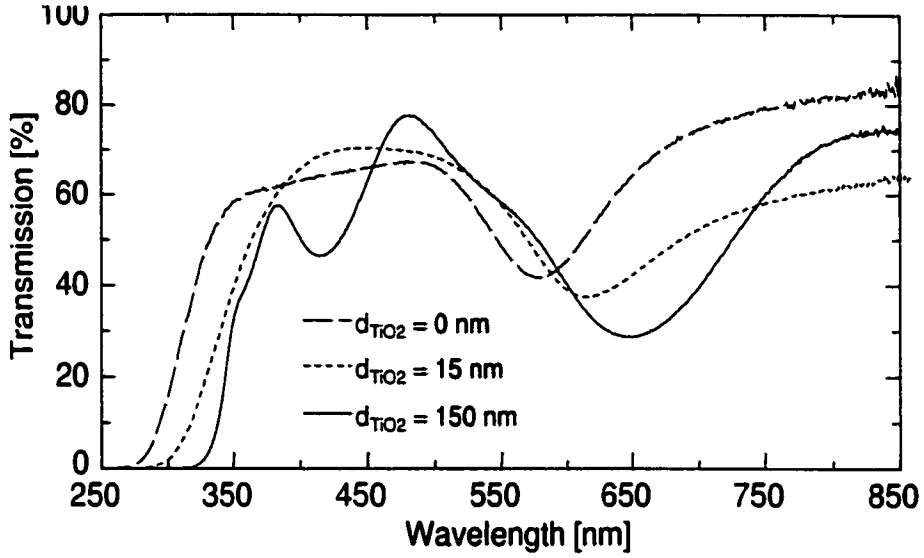

Figure 6.7: Transmission spectrum of sample C cladded with TiO_2 on TiO_2 base layers of different thickness.

SPR is found at lower energy for high p and at higher energy at low p. The latter is a consequence of the blue-shift due to finite size effects which becomes more important relative to the dipole interaction shift at lower p and smaller particle radii.

To demonstrate the influence of the image charge interaction more clearly, we have deposited TiO_2 cladded discontinuous films on base layers of TiO_2 of varying thickness, in effect varying η in Eqs. 6.3 and 6.4. The transmission of sample C films with TiO_2 base layers of 0, 15, and 150 nm are shown in Fig. 6.7. The image charge-induced blue-shift as the thickness of the TiO_2 layer decreases is clearly evident and amounts to $\sim$ 75 nm.

6.5.3 Finite Size Effects

To quantify the effect of the finite size of the particles on the optical response, we have applied Eqs. 6.1 and 6.2 to the ellipsometric and photometric data of the samples which correspond directly to the TEM images in Fig. 6.5 (i.e. SiO_2 base layer

with and without an SiO_2 cladding, Fig. 6.6(b) and (a), respectively). To account for the particle size dependence of the intra-band optical constants of gold (i.e. the linear dependence of the SPR width on inverse particle radius), $1/\tau_B$ in Eq. 6.5 is replaced by:[85]

$$\Gamma = \tau_B^{-1} + \frac{A\nu_F}{R}, \tag{6.6}$$

where ν_F is the electron Fermi velocity (1.39×10^8 cm/sec[114]). R is the particle radius, and A is a proportionality coefficient[64] that is, in this work, established experimentally by comparison of the measured spectra and the TEM micrographs.

Modeling of the shift of the SPR with decreasing particle size under the assumption of small spill-out suggests the use of a two-region particle[107] (i.e. an inner region using ϵ_{core} corresponding to bulk, and an outer rind with $\epsilon_{core} = 0$). However, to allow for the possibility of a size dependence of the core response, we shall model the shift by adjusting the core polarization over the entire particle (i.e. $\Re[\epsilon_{core}] + \delta_{core}$) . We ignore the variation in $\Im[\epsilon_{core}]$ which will result in some slight disagreement between modeled and measured spectra on the high energy flank of the SPR.

To obtain information regarding the particle dimensions perpendicular to the film plane, off-normal incidence transmission measurements were made. Supported clusters are, in general, oblate spheroids (i.e. minor axis perpendicular to the film plane). This gives rise to both surface plasmon mode along the major axis (Fig. 6.6) as well as a mode along the minor axis resonant at higher frequency.[225,250] Transmission measurements were made up to 80°, and no second minimum was observed for any of the samples, only a slight blue-shift and broadening of the resonance, more likely due to the third terms in Eqs. 6.3 and 6.4 as opposed to particle deformation (i.e. $L_\parallel \neq L_\perp \neq 1/3$). This is consistent with the results of Yamaguchi *et al*[129] in which cross-sectional TEM images of gold particles deposited on a heated substrate indicated $\gamma \sim 1.1$ for small particles.

Assuming spherical particles, we have set the film thickness to $d = 2R$ and have

calculated the filling from $p = N_p V_p / A_T$ where V_p is the volume of a sphere with radius R (see Table 6.1). For the cladded films, the oxide thickness was set to $d_{SiO_2} =$ 10 nm, as determined from a separate measurement on a sample without gold. The embedding matrix was set to $\epsilon_h = \epsilon_{SiO_2}$ and $\epsilon_h = 1$ for the cladded and uncladded films, respectively.

The dielectric functions corresponding to the glass slide, SiO_2 base layer, discontinuous film, and SiO_2 cladding layer were incorporated into a multilayer optical model[168] and the unknown parameters were fit to the measured spectra using the Levenberg-Marquardt method. The fit parameters were Γ, δ_{core}, $F_{\|}$ and $F_{\perp}$. The fit spectra are shown Fig. 6.6(a) and (b) and they demonstrate the ability of the model to reproduce the measured spectra. The agreement with the ellipsometric data Ψ and Δ for incident angles 55°, 65° and 75° is similarly good and is shown in Fig. 6.8 for sample C.

We note that the best-fit results are unique: parameter correlation calculated from the covariance matrix[174] was not significant for any of the above parameters. This was verified by the very poor agreement between the model fit the experimental data using only $F_{\|}$, $F_{\perp}$ and either Γ or δ_{core} as fit parameters. Since the depolarization factors are not correlated with Γ or δ_{core}, and since we can, at best, only roughly approximate the lattice structure parameters ($C_{\|}$, $C_{\perp}$, and ς) from the TEM images, we have not attempted to separate the different terms in Eqs. 6.3 and 6.4. (For an extensive treatment of the dependence of $F_{\|,\perp}$ on film microstructure, see Yamaguchi *et al*[129,255,257,258]).

The fit δ_{core} versus $1/R$ is plotted in Fig. 6.9(a) and, at least for the smaller particle films, is seen to gradually approach 0 in the bulk limit. The fit Γ versus $1/R$ is shown in Fig. 6.9(b). A was calculated using Eq. 6.6 with $\tau_B = 5 \times 10^{-14}$s, determined from the fit of the continuous film. The average values for the smaller particle films are $A = 0.15$ and $A = 0.22$ for the cladded and uncladded samples, respectively.

The slightly different behaviour of the larger particle film with respect to both

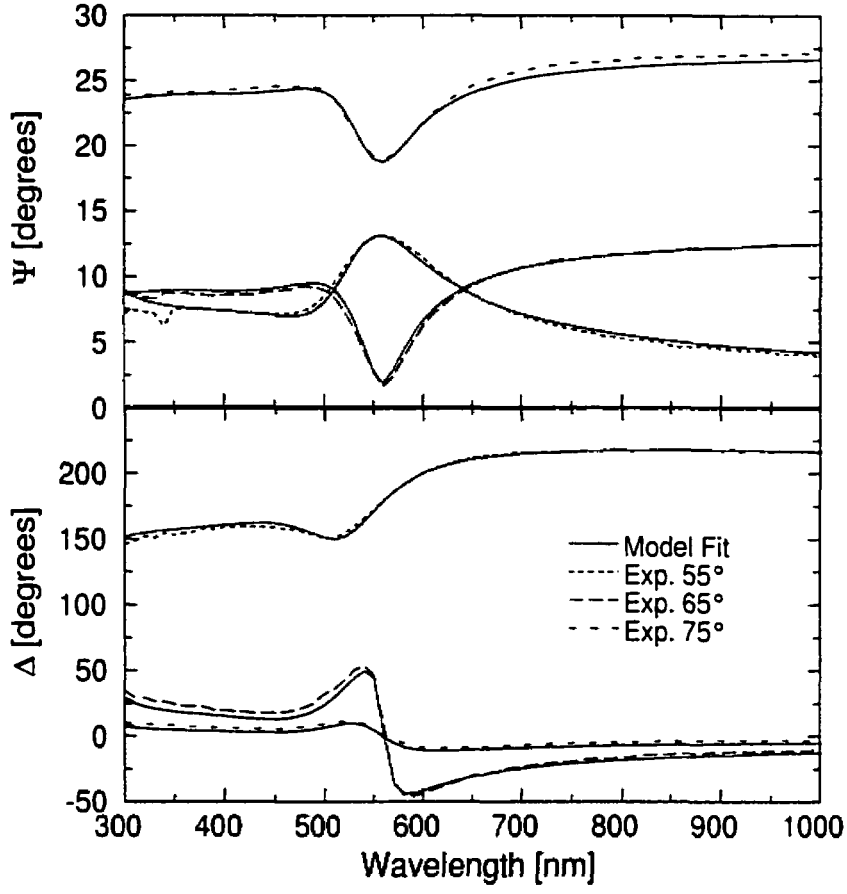

Figure 6.8: Ellipsometric data (a) Ψ and (b) Δ, and model fit for sample C with a base and cladding layer of SiO_2.

δ_{core} and Γ is related to the assumption concerning particle shape. The higher than expected δ_{core} is most likely due to $\gamma > 1$, resulting in a calulated p that is too low. Γ, on the other hand, is more sensitive to the particle shape in the plane of the film (i.e. $b : c$ in Table 6.5). The influence of $b : c \neq 1$ can be incorporated into the optical model by using two depolarization factors to describe the response in the film plane:[246] $\epsilon_{\|} = 1/2 \sum_{i=1}^{2} \epsilon_{\|}(F_{\|i})$. Applying this $\epsilon_{\|}$ to the response of sample D lowers both δ_{core}, and, more significantly, Γ. The decrease is indicated in Fig. 6.9 for the cladded sample by the full circles. The remaining discrepancy in Γ is most probably due to the larger particle size distribution for sample D.

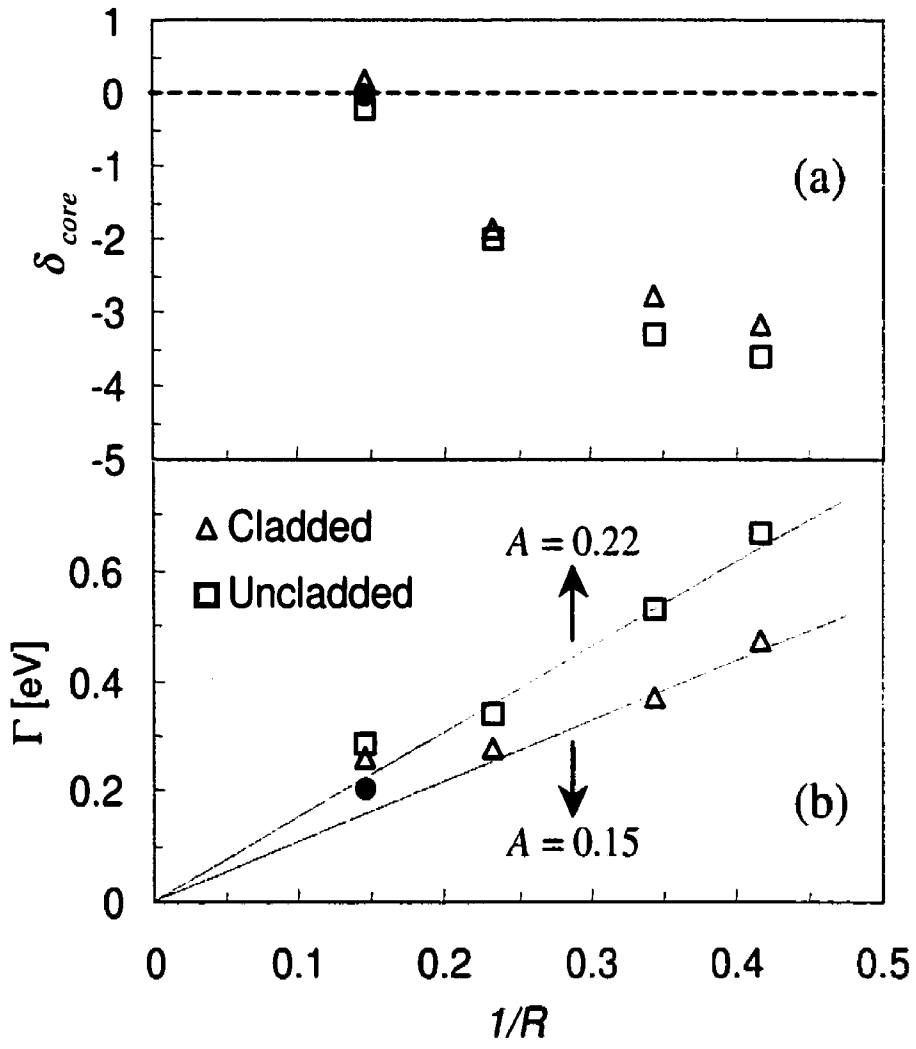

Figure 6.9: Dependence of (a) δ_{core} and (b) Γ on reciprocal particle size for the SiO_2/gold/SiO_2 and SiO_2/gold/vacuum samples corresponding to the TEM images in Fig. 6.5. The full circles represent the calculations for the cladded sample using two depolarization factors to describe $\epsilon_{\parallel}$.

6.6 Discussion

6.6.1 Blue-shift of SPR: ϵ_{core}

To demonstrate the importance of the inter-band region when accounting for the shift of the SPR, and to justfy our choice of a size-dependent ϵ_{core}, we compare our results with the quantum mechanically derived conduction electron response considering a realistic electron density distribution calculated in the TDLDA. In Fig. 6.10 we have plotted the finite size effect shift of the SPR versus $1/R$ calculated from the fit δ_{core} for the SiO_2 cladded films normalized with respect to the Mie limit. The additional data point corresponds to a sample with spectra too freatureless to be fit, but from which the resonance energy could still be determined. We have included in the figure the results of Palpant *et al*[78] for gold in porous alumina ($\epsilon_h = 2.6$), as well as our own results for Au/SiO_2 cermets.[210]

The shifts predicted by TDLDA calculations[132] for free and embedded 440 atom gold particles are shown in Fig. 6.10 as open circles and are much less than those determined experimentally. For the embedded particles, the calculated shift is smaller due to the screening of electron-electron interaction by the matrix[132,133] which results in a larger spill-out. This could account for the smaller shift observed in Palpant *et al*'s data since $\epsilon_{Al_2O_3} > \epsilon_{SiO_2}$. We note that the filling in their films ranged from 1.5-6%, so that the observed shift includes a small contribution from dipole interactions.

We attribute the discrepancy between the measured and predicted SPR energy on a particle size dependence of ϵ_{core}. Near the gold inter-band edge ϵ_{core} is determined by transitions from the d-bands to the s,p band (i.e. bands 3-5 to band 6) and from s,p states in band 6 to s,p-like states in band 7 (inter-conduction band transitions).[227] Both of these transitions will be affected by strain-induced lattice deformation,[14,230] resulting in a shift of the inter-band transition edge and a decrease in $\Im[\epsilon_{core}]$ at $\sim 4\,eV$. These changes in the inter-band absorption spectrum of small gold particles have been repeatedly observed.[128,129,164,210,228] The attendant decrease in $\Re[\epsilon_{core}]$,

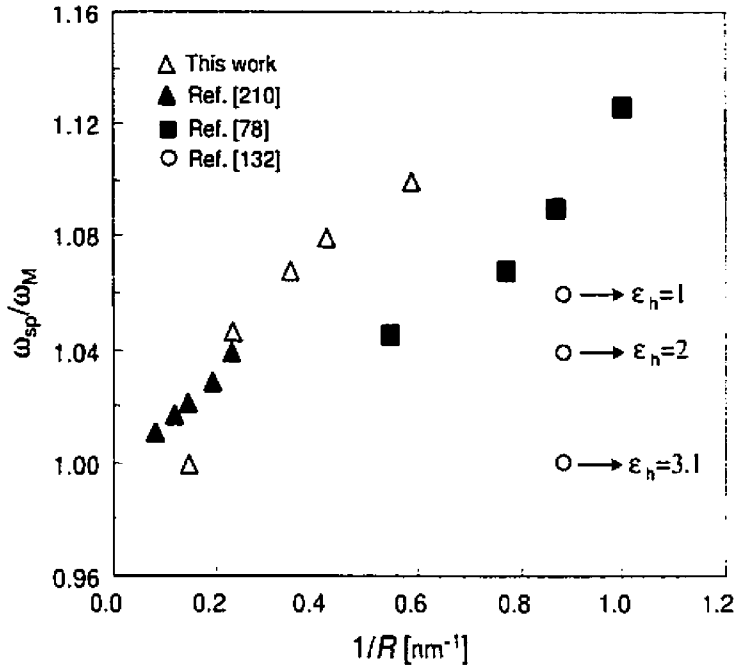

Figure 6.10: Normalized finite size effect shifts of the SPR of Au/SiO_2 films. Data for Au/Al_2O_3 cermets[78] are also included as well as the theoretical shifts predicted from TDLDA calculations using a 1 Å region of nonoverlap between conduction and d-electron wave functions.[132]

as determined from Kramers-Kronig analysis of absorption spectra,[164,228] as well as from ellipsometric measurements,[210] results in a blue-shift of the SPR with respect to that calculated using bulk inter-band optical constants.

6.6.2 Broadening of SPR: A

Since the TDLDA calculations are computationally expensive, they are limited to very small particle sizes where shell effects play an important role in determining the optical response.[9] The broadening parameter, A, however, can only be assigned to the SPR of larger particles, where the conduction band can be considered as a quasi-continuum.[64] The determination of A is therefore limited to asymptotic theories[99–102] where non-local effects (i.e. the electron density profile at the particle

surface) are included within a so-called "self-energy" term. The width dependence of the SPR on R from these models has the same form as the classical expression (Eq. 6.6), however, in this case, A is a function of both $\Omega = \omega/\omega_p$ and r_s, and will also depend on the centroid of the induced surface charge (i.e. spill-out).

For example, for $r_s = 3.0$ (i.e. gold and silver) Persson[31] calculated $A = 0.3$, which represents a much better agreement with our results ($A = 0.15 - 0.22$) than the classical value of $A = 1$ calculated considering isotropic scattering of electrons at the particle surface.[85] Furthermore, $A = 0.3$ is the value expected at $\Omega = 1/\sqrt{3}$ (i.e. the classical SPR frequency neglecting the d-electron screening), and a decrease in A is expected with decreasing frequency for $\Omega < 0.6$.[101] This is supported by the more significant broadening ($A = 0.25$) observed for free Ag clusters,[32] the resonance of which is at higher energy ($\omega_{sp} \sim 3.5\,\text{eV}$) as compared to our embedded Au clusters ($\omega_{sp} \sim 2.3\,\text{eV}$).

The reason for the larger broadening in the uncladded films is unclear. In fact, the opposite is expected considering that spill-out should be less severe in these particles since they are only partly in contact with the substrate. For example, from the calculations of Apell *et al.*[101] who considered spill-out effects in analogy to flat metal surfaces,[106] it is expected that A decreases with decreased spill-out, and it is predicted to approach $A \sim 0.1$ for an electron density that is terminated abruptly at the particle boundary.

As a final note, we mention the dependence of the SPR width on resonant states in the matrix which will enhance the broadening if these states are located above the Fermi energy and close to the frequency of the SPR[31] (so-called chemical interface damping[32]). For SiO_2 such a state exists at $\sim 3\,\text{eV}$ and is thought to be responsible for the very large broadening of silver in glass ($A \sim 1$) since the SPR for Ag in glass occurs at $\omega_{sp} \sim 3.1\,\text{eV}$. The absence of CID effects in our Au/SiO_2 films, as evidenced by the low A values, is simply due to the lower SPR energy ($\omega_{sp} \sim 2.3\,\text{eV}$) so that the coupling between the SPR and the resonant state in the matrix is negligible.

6.7 Summary and Conclusions

Discontinuous gold films consisting of nearly sphercial particles with varying size and filling were prepared. The crucial roles played by dipole-dipole and image charge interactions in determining the optical response of these films were demonstrated. In particular, the SPR red-shifts significantly with increased particle filling and its position relative to the Mie limit is dependent on the index of the substrate material. By accounting for these interactions according to the theory of Yamaguchi, we have determined the influence of the finite size of the particles on the optical properties of the films.

The finite size effects were quantified by applying two phenomenological parameters, δ_{core} and A, to describe, respectively, the shift and width of the SPR. Both cladded and uncladded films showed similar shifts, larger than expected from the TDLDA calculations of Lermé *et al*,[132] a discrepancy which we attribute to a particle size dependence of ϵ_{core} arising from strain-induced lattice deformation. From the particle size dependence of the width of the SPR, broadening parameters $A = 0.15$ and $A = 0.22$ were obtained for cladded and uncladded films, respectively.

Acknowledgments

The authors wish to acknowledge the expert technical assistance of Mr. G. Jalbert. This work was supported by the Natural Sciences and Engineering Research Council (NSERC) of Canada.

Chapter 7

Article 5: XPS Analysis

This article utilizes the expertise developed in the microstructural characterization of nanocomposite films to account for the observed electronic behaviour of the core electrons in gold determined using XPS. For the most part, the samples studied consisted of discontinuous gold films deposited on or embedded in SiO_2. A similar study [D. Dalacu *et al*, Mat. Res. Soc. Symp. Proc., **544**, 167. 1999] was performed on the 3-D Au/PPFC system.

Experiments were also performed on gold particles supported on ITO. On one hand, ITO is transparent in the visible (the band edge is located at $\sim 4\,eV$[260]), permitting the same optical characterization as in the case of SiO_2. On the other hand, it is a semi-conductor, and charge transfer between the ITO and gold will occur in order to allign the Fermi level.[261] Evidence of electron transfer across the ITO/gold interface was suggested by XPS and by the optical measurements, in which case it was described in terms of CID (see Section 1.5).

Substrate and morphology effects on photoemission from core-levels in gold clusters

Dan Dalacu, Jolanta E. Klemberg-Sapieha, and Ludvik Martinu

Recieved 8 August 2000; accepted 16 October 2000

Surf. Sci., 2001

7.1 Abstract

The combination of x-ray photoelectron spectroscopy and spectrophotometry of supported gold clusters on SiO_2 reveals the importance of cluster morphology in determining core-electron binding energies. As-deposited films show a discontinuous dependence of the binding energy on gold content, associated with a transition from coagulated or partially coalesced clusters to isolated clusters. In contrast, annealed films exhibit a smooth increase in binding energy down to very low gold content. Comparison of the photoemission from annealed clusters deposited on and embedded in the insulating SiO_2, as well as clusters deposited on a conducting ITO substrate, was used to highlight the contributing factors that determine the core-electron binding energy and line-width, namely: (*i*) initial-state effects relating to the electronic structure, (*ii*) final-state effects relating to relaxation processes, and (*iii*) the cluster charge, including the influence of image charge screening.

7.2 Introduction

The study of the electronic structure of small metal clusters has been indispensable in understanding the transition from the atomic to the solid state.[9] A good comprehension of the processes that occur in this transition region can help in the technological advancement of applications such as heterogeneous catalysis[26] and nonlinear optics.[19,150] The preeminent technique for probing the electronic structure of small metal clusters, in particular, the evolution of the valence-band and core-electron levels with cluster size, is photoelectron spectroscopy. This has resulted in numerous photoemission studies on supported metal clusters (see Mason[34] and references therein), which frequently use gold as a model material.[29,131,219,220,229,262-266]

A significant effort has been devoted to the study of the core-level binding energies (CBE) and line-widths determined by x-ray photoelectron spectroscopy in order to understand the changes in the initial-state electronic structure (valence-electron configuration) and final-state relaxation (extra-atomic response to the positively charged core hole created by photoionization) when going from bulk metal to atom (see, for example, DeCenzo and Wertheim[35]).

The cluster size dependence of the valence-electron configuration, and associated valence-band narrowing, has been compared to the configurational changes that occur for surface atoms in bulk samples.[16] In the latter case, the valence-band narrowing is understood to arise from an s-d redistribution consisting of a reduction of the delocalized s states and d bulk states of bonding character and enhancement of the localized d states of non-bonding and anti-bonding character.[17] The resulting decrease of the energy between the center of the narrowed surface atom d-band and the Fermi level pulls the density of states to lower binding energy together with the core-levels. A CBE shift to lower energy is also expected with decreasing cluster size by virtue of the increasing number of surface atoms in the clusters.

On the other hand, final-state relaxation processes in the bulk will decrease the CBE compared to that of an isolated atom.[34] This is expected from the decrease in

conduction electron screening of the core hole produced by photoionization due to the discretization of the conduction band with decreasing particle size.[80] A further reduction will occur as the screening provided by the cores of neighbouring atoms decreases due to a reduction of the effective coordination. The increase in the CBE with decreasing cluster size resulting from the disappearance of these bulk relaxation processes will be modulated by the substrate's ability to shield the final-state hole.

Competing with the above two fundamental processes is the possibility of cluster charging. If core-electron photoemission leaves the cluster with a unit positive charge, the resulting Coulomb energy will increase the CBE by an amount that depends on the shape of the cluster[29] and image charge screening.[267] Whether or not charging comes into play depends on the ability of the substrate to neutralize the cluster within the lifetime of the core hole. This depends on the substrate density of states at the Fermi energy as well as the shape of the cluster (i.e. the contact area with the substrate).

Both intial- and final-state effects mentioned above will also influence the core-level line-width. In the case of the former effect, the line-width is expected to pass through a maximum at a surface to volume ratio equal to one by virtue of the nonequivalence of the surface and volume atoms.[131] An increase in line-width is also expected with reduced screening, whether the reduction arises from a cluster size dependence of the conduction electron screening in the metal,[268] or due to the surrounding environment (see Fuggle *et al*[269] and references therein).

In this study, the CBE and line-width of gold clusters in the form of discontinuous films are investigated by XPS. The fundamental effects are distinguished from those produced by cluster charging through depositions on both insulating (SiO_2) and conducting (ITO) substrates as opposed to the more common amorphous carbon,[34] which is only poorly conducting. We also compare the trends in binding energy and line-width with the optical properties of the films. Optical characterization of discontinuous films provides fruitful information concerning film microstructure (i.e. cluster

size, shape, concentration...) as a consequence of the excitation of surface plasmons, and concomitant absorption band in the visible.[81] The dependence of the surface plasmon resonance on film microstructure is utilized to illustrate the distinctly different cluster morphologies that can occur in discontinuous films, which is important in understanding some of the observed trends in the XPS core-level energies and line-widths.

7.3 Experiment

The discontinuous gold films were deposited by radio-frequency magnetron sputtering from a 50 mm diameter gold target at 60 mTorr of Ar using an input RF power of 100 W for a self-bias of -350 V. To obtain films with different morphologies in a single deposition, the samples were displaced from the magnetron axis. This allowed us to control the volume fraction and size of the particles comprising the films, both of which decrease with increasing distance from the magnetron axis.[224] In the present work we refer to samples A, B, $\cdots$ H obtained at a sequentially increasing distance from the axis.

The films were deposited on glass substrates coated with $\sim$ 20 nm of either SiO_2 or ITO. Additional samples were prepared for transmission electron microscopy analysis on carbon-coated copper grids. One set of samples (including those for TEM) had an additional SiO_2 layer deposited on top. The SiO_2 layers were prepared by plasma-enhanced chemical vapour deposition using SiH_4/N_2O chemistry in a high frequency plasma system described elsewhere.[221,222] A commercial ITO-coated glass was used with a sheet resistance of $10\Omega/square$. Both annealed and as-deposited samples were studied. The post-deposition anneal was performed at 250° C in air for 5 hours.

XPS analysis was performed in a VG ESCALAB 3 Mark II instrument with a non-monochromated MgK_α source (1256.6 eV) and a 0.8 eV resolution. Optical transmission spectra were taken at normal incidence on a Perkin-Elmer Lambda 19 dual-beam

spectrophotometer. TEM was performed on the samples deposited on carbon-coated copper grids using a Philips CM30 microscope. Image analysis was done using ImageTool from the University of Texas.

7.4 Results and Discussion

7.4.1 Optical Characterization of Supported Clusters

The transmission spectra of as-deposited and annealed films on SiO_2 and annealed films on ITO are shown in Fig. 7.1 together with the respective substrates. In all the spectra the SPR band is clearly visible indicating that gold exists in the form of small particles. The dependence of the SPR band on the position of the sample relative to the magnetron axis is due to the variation in film microstructure. The increased transmission with increased distance is predominantly due to a reduced gold content in the film, and thus reduced inter-band absorption.[51]

The reduced gold content also contributes to the blue-shift that is observed with increasing distance from the axis and results from a decrease in dipole-dipole interactions.[129,224] A second contribution to the blue-shift arises from the presence of a core-polarization-free surface layer,[100,107,210] the influence of which increases with decreasing particle size. The observed broadening of the SPR with decreasing gold content is also an effect of the finite size of the particles. In particular, the width is expected to increase linearly with inverse particle size,[81] and is associated with the relaxation effects discussed in Section 7.2.[64,80]

The blue-shift and narrowing of the SPR upon annealing the samples on SiO_2 is indicative of a transition from flattened particles, perhaps coagulated or partially coalesced, to that of larger, well-isolated spherical particles with a narrower size distribution.[81,224,244] Similar changes were observed when annealing the ITO samples. The red-shifted and broadened SPR bands for the clusters on ITO compared to the samples on SiO_2 are not due to morphology effects. They result, rather, from

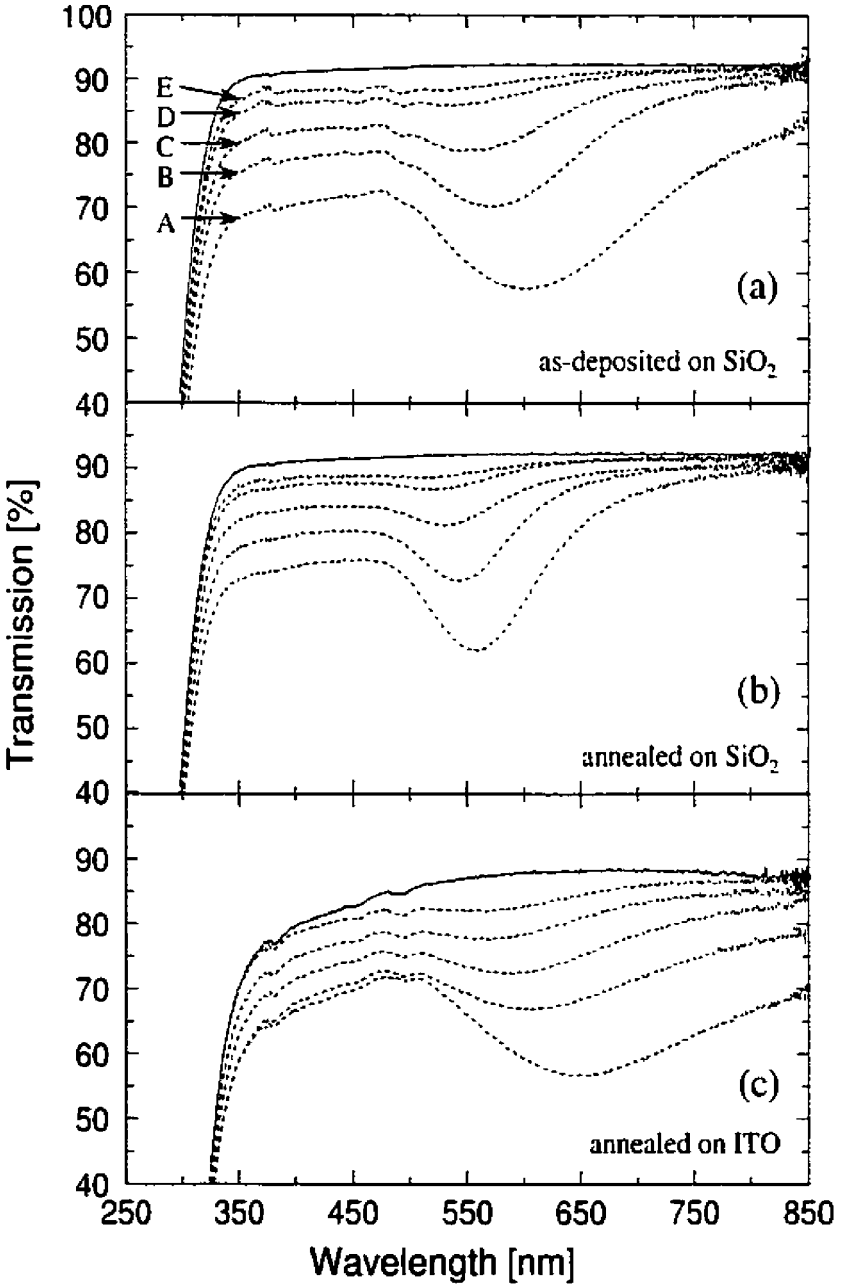

Figure 7.1: Optical transmission spectra of discontinuous films deposited at varying distances from the magnetron axis: (a) as-deposited on SiO_2, (b) annealed on SiO_2, and (c) annealed on ITO. Solid lines correspond to the respective substrate spectra.

the higher refractive index of the ITO compared to SiO_2 which affects the shape of the SPR through its influence on the image charge interaction.[224,257] A second contribution is the possibility of charge transfer reactions at the Au/ITO interface, so-called chemical interface damping.[32] CID effects have been used to account for the large broadening of the SPR for Ag in different reactive matrices.[31] and is especially pronounced in Ag/ITO cermets.[134]

7.4.2 XPS Characterization of Supported Clusters

The Au 4f core-level spectra for the annealed samples on SiO_2 are shown in Fig 7.2. Since the samples have been exposed to air, some degree of contamination is expected.[270] However, the 4f core-level spectra were well described using only two peaks corresponding to gold, as opposed to the multiple peaks required for gold present in its several characteristic oxidation states.[271] As such, we are confident that the peaks correspond to elemental gold.

The shift and the FWHM of the Au $4f_{7/2}$ core-level peak with atomic concentration for the as-deposited and annealed samples on SiO_2 and annealed samples on ITO are shown in Fig. 7.3. The atomic concentration was determined using peak area and peak height sensitivity factors corresponding to a homogeneous sample, and, as such, is qualitative, and indicates only the relative concentration of gold. The plotted shift is relative to the bulk binding energy (84.0 eV) and has been corrected for substrate charging using the adventitious hydrocarbon C 1s peak at 284.8 eV as reference.

The as-deposited samples on SiO_2 show both an increase in CBE and line-width but with a different dependence on concentration above and below 5 at.%. This concentration can be associated with a transition from a microstructure consisting of coagulated or partially coalesced flattened particles to that of a film consisting of isolated, more spherical clusters. We note that the CBE and line-width of the as-deposited films were sensitive to the x-ray flux. At higher flux, the CBE and line-width obtained corresponded to those of the annealed samples. We attribute

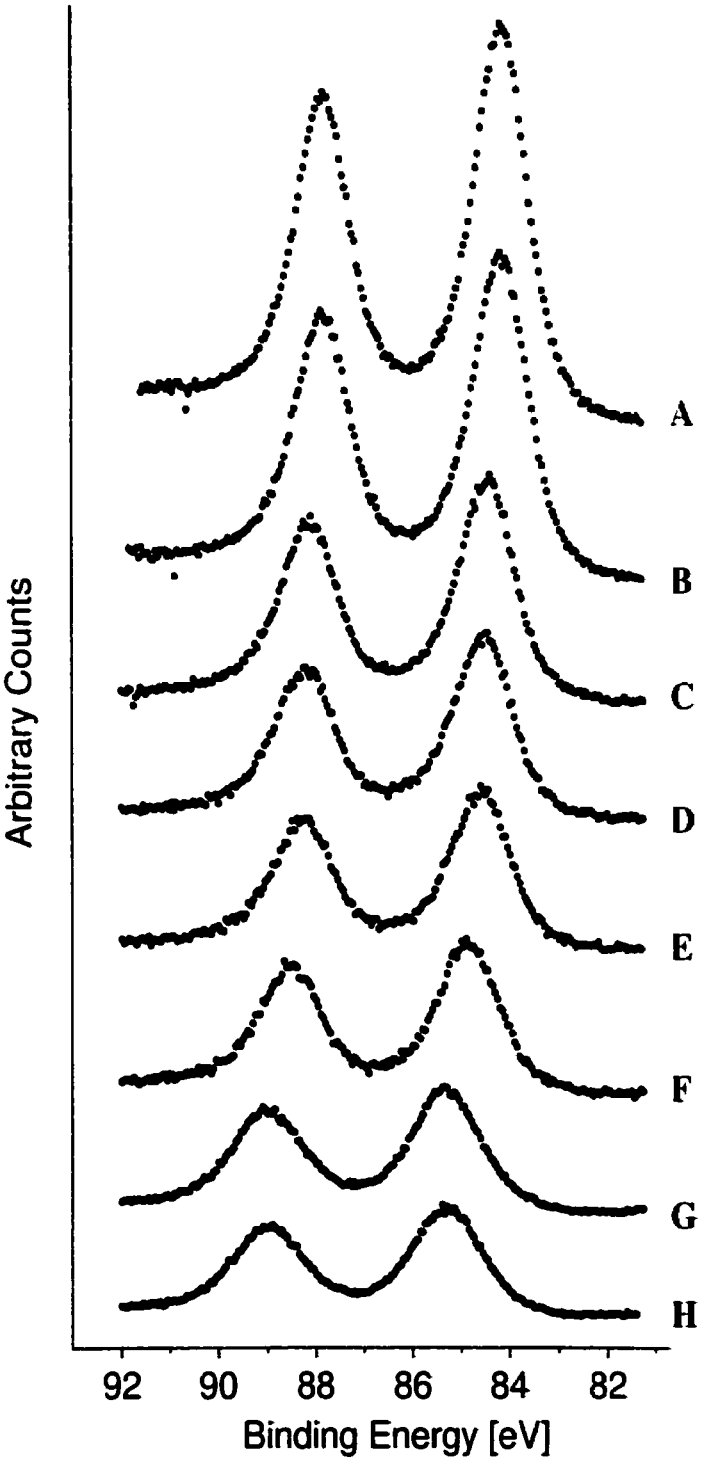

Figure 7.2: The dependence of the Au 4f core-level spectra on atomic concentration for annealed films on SiO_2.

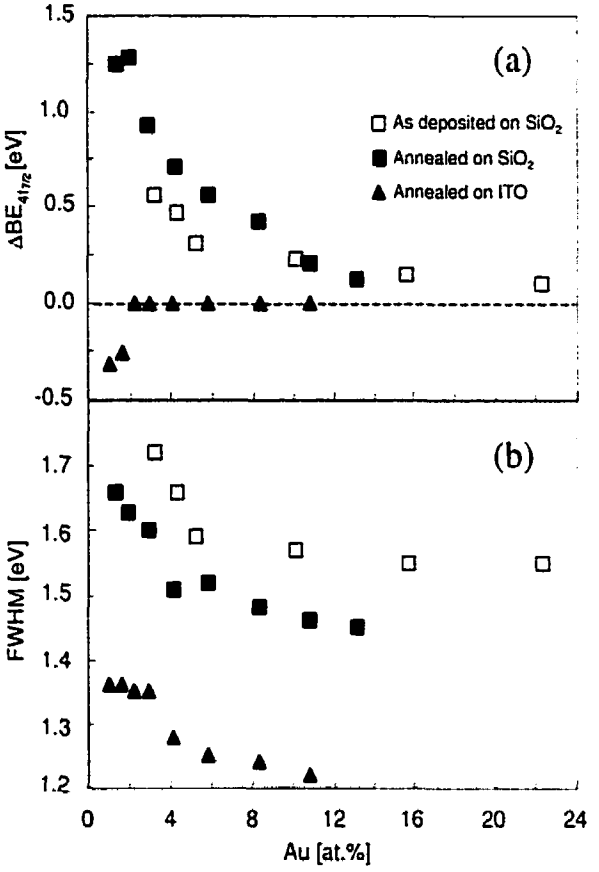

Figure 7.3: The dependence of the CBE and FWHM of the Au $4f_{7/2}$ peak on atomic concentration.

this to local heating due to the irradiation which effectively anneals the samples. In fact, discoloration of the analysed spot, indicative of a change in microstructure, was clearly observed for the films with higher gold content.

The changes that occur upon annealing can be understood from the morphological changes suggested by the transmission spectra. The measured gold content is reduced as a result of decreased surface coverage as the clusters become more spherical. This also results in larger CBE shifts due to the decreased contact area of the clusters with the substrate (and, thus, less efficient charge neutralization). The accompanying decrease in cluster size distribution results in reduced line-widths. The smooth increase

in the binding energy and line-width suggest that, unlike the as-deposited samples, the clusters here are well isolated, even at higher gold volume fractions. However, the samples on SiO_2 make evident a second transition at 2 at.% consisting of a negative CBE shift with decreasing concentration.

The transition at 2 at.% is more disctinct for the annealed films on ITO since, in this case, the positive CBE shift due to cluster charging is absent: the resevoir of electrons in the ITO is able to neutralize the clusters within the lifetime of the core hole. (We note that charge transfer was already suggested by the severely broadened SPR of these films.) The highly polarizable conduction electrons in the ITO will also mask any change in the final-state relaxation of the particles by providing efficient screening of the core hole. The CBE shift and line-width for the ITO samples is, thus, due to initial-state electronic structure effects, and the second transition marks a S/V at which the surface atoms begin to play an important role in determining the CBE. We note that the CBE shift of surface atoms in bulk gold is -0.4 eV,[16] compared to our value of -0.32 eV at 1 at.%.

7.4.3 XPS Characterization of Embedded Clusters

The embedded clusters were prepared by depositing an additional SiO_2 layer (< 10 nm) on top of the discontinuous films deposited on SiO_2. These $SiO_2/Au/SiO_2$ structures were simultaneously deposited on carbon-coated copper grids for TEM analysis. The multi-layer structure ensures identical sets of samples since they are both surrounded by SiO_2, which also serves to minimize the influence of the probing beams (i.e. both the x-rays in the XPS analysis and the electrons in the TEM analysis). The TEM micrographs for samples deposited at different distances from the magnetron axis are shown in Fig. 7.4. The particle radius, R, and size distribution obtained from a detailed image analysis of a 378600 nm^2 area (i.e. 400 to 4000 particles) are shown in Fig. 7.5.

The CBE shift and FWHM versus $1/R$ is shown in Fig. 7.6. We note that the

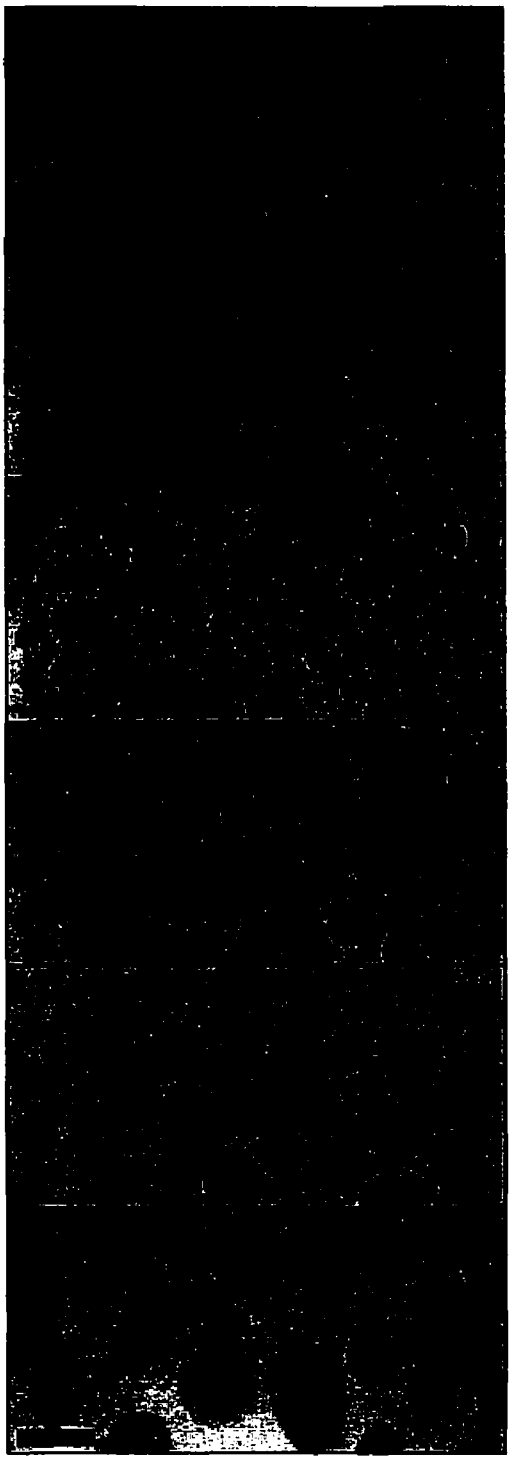

Figure 7.4: TEM micrographs of films deposited at varying distances from the magnetron axis. Bar indicates 20 nm.

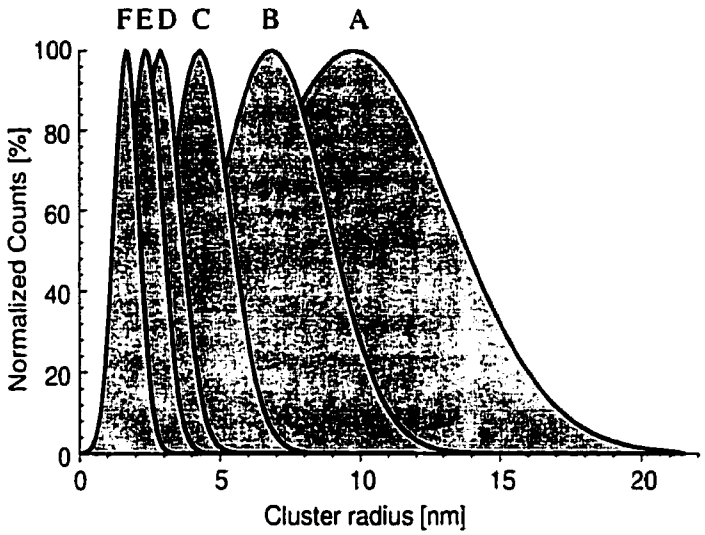

Figure 7.5: Particle size distributions obtained from image analysis of the samples in Fig. 7.4.

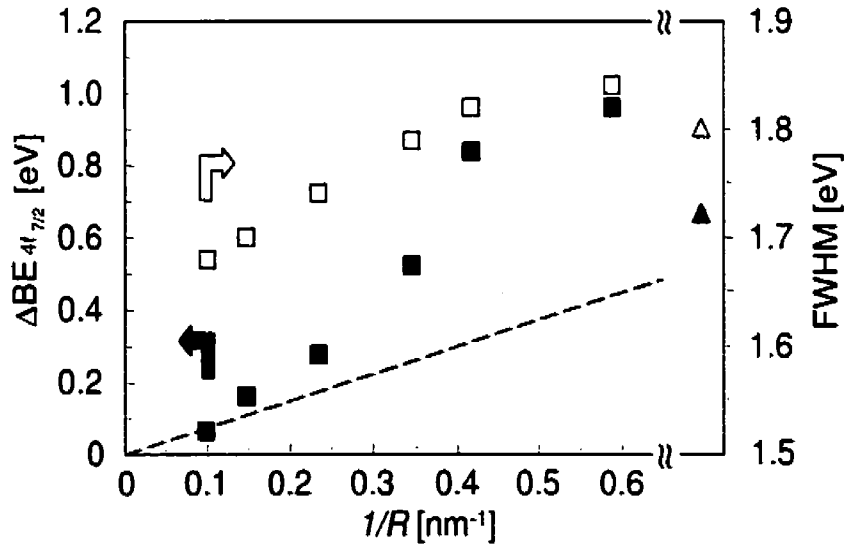

Figure 7.6: The dependence of the CBE and FWHM of the Au $4f_{7/2}$ peak on reciprocal particle size for clusters in SiO_2 corresponding to TEM micrographs in Fig. 7.4. Triangles represent measurements on the 3-D film. Dashed line corresponds to the charging-induced shift: $\Delta BE \sim e^2/2R$.

higher CBE shifts compared to the respective samples on SiO_2 arise from the absence of image charge screening which reduces the charging shift to about one-half.[267] A reduction of the charging due to the increased contact area with the SiO_2 is, apparently, of secondary importance. The CBE shift expected from the unit charge on a sphere ($e^2/2R$) is also shown in the figure, and does not account for the measured shift, suggesting that both relaxation effects and cluster charging have to be considered for the larger clusters.

The leveling-off of the CBE shift is indicative of the increasing importance of the surface atoms, and hence, initial-state effects. The initially linear dependence of the line-width on cluster size is a further indication of initial-state effects (i.e. $S/V \sim 1/R$), and the leveling-off at smaller clusters is suggestive of the peak anticipated for clusters with half the atoms on the surface and half in the volume, expected at $R \sim 1.2\,\text{nm}$.[75] A contribution to the leveling-off of the line-width with decreasing cluster size is also expected from the decreasing size distribution observed in Fig. 7.5.

We have also attempted to prepare isolated gold atoms embedded in SiO_2 using simultaneous RF sputtering of the gold and PECVD of the SiO_2,[210] thereby limiting particle growth that arises from migration of gold atoms across the substrate surface. The 3-D films produced in this way have shown the same core-level[272,273] and valence band[77] behaviour observed in the 2-D discontinuous films. A 230 nm thick film with a 7% gold volume fraction was deposited. The absence of gold particles consisting of more than a few atoms was verified from the transmission spectrum which showed no sign of the SPR (see Ref. 31, Fig. 3b).

Measurement of the CBE shift and FWHM of the $4f_{7/2}$ level of the 3-D film gave 0.66 eV and 1.8 eV, respectively, both of which are smaller than the corresponding measurements on sample F in Fig. 7.4. The initial-state effect suggested by the measurements on the supported samples (i.e. decrease in CBE with decreasing gold content) is, thus, also observed in the embedded samples. Furthermore, the peak in the line-width versus $1/R$, expected from the distinct nature of the surface and

volume atoms, is observed, and lies within the appropriate size range.

7.5 Summary and Conclusions

We have demonstrated the influence of the microstructure of discontinuous gold films on XPS core-level energies and line-widths. Identically prepared samples give vastly different results depending on post-deposition heat treatments. The same is true for the optical transmission spectra. We have applied the known dependence of the SPR absorption band on cluster morphology to draw the following conclusion: Annealed films consist of well-isolated clusters with a small size distribution and can be characterized in terms of cluster radii. This allows reliable information concerning the fundamental processes (initial- and final-state effects) that influence the CBE and line-width to be determined. On the other hand, as-deposited films are likely to consist of coagulated and/or partially coalesced small clusters, the effects of which dominate over the fundamental processes.

XPS characterization of annealed discontinuous films deposited on both insulating and conducting substrates, as well as embedded in an insulating matrix, has allowed us to identify specific effects related to (*i*) electronic structure, (*ii*) relaxation, and (*iii*) cluster charge, including the influence of image charge screening.

Acknowledgments

The authors wish to acknowledge the expert technical assistance of Mr. G. Jalbert. This work was supported by the Natural Sciences and Engineering Research Council (NSERC) of Canada.

Chapter 8

Conclusion

This work has demonstrated the ability to produce nanocomposite thin films possessing microstructures which adhere closely to that assumed in effective medium theories, namely isolated metal particles with a small size distribution embedded in a dielectric matrix which serves only as a structureless host material. Such nanocomposite films were realized through the use of PECVD materials (PPFC and SiO_2) as matrices, owing to their amorphous and compact structure, in combination with the use of gold as the embedded nanoparticles, owing to its chemical inertness.

The optical response of these nanocomposite films were used to illustrate two types of behaviour inherent to such systems: The first one concerns the effects prescribed by effective medium formalisms, namely the influence of dipole-dipole interaction at high particle concentrations, and image charge interaction in the presence of a substrate/matrix interface. It also concerns effects not included in effective medium theory, namely the observation of the onset of phase retardation and scattering.

The second one concerns the particle size dependence of the optical constants of gold. The ideal microstructure combined with sensitive ellipsometric as well as photometric optical measurements has permitted the observation of several important effects that occur with decreasing particle size: (*i*) a shift of the inter-band absorption edge to lower energy, (*ii*) a decrease in the slope of the edge, (*iii*) the broadening

of features due to inter-conduction band transitions, and (*iv*) a SPR width that is narrower for a given particle size than previously observed.

The particle size dependence of the core response was attributed to an increase in structural disorder with decreasing size. The increasing disorder in the atomic structure is understood to arise from a combination of stress-induced lattice deformation and the increasing percentage of surface atoms which are more weakly bound and less restricted in their thermal motion by virtue of their reduced coordination. This interpretation is supported by the similarity of the particle size-induced inter-band changes with those that occur upon transition to the liquid state.

The narrow SPR is attributed to a small particle size distribution combined with a non-reactive metal/dielectric interface. Attempts at quantifying the relation between the particle size and the SPR width has led to a calculated broadening parameter $A = 0.15$, much lower than those predicted by classical models, and more in-line, though still lower, than those predicted by quantum mechanical models. The value corresponding to the 2-D Au/SiO_2 system is quoted since is was obtained from a detailed image analysis of TEM micrographs, and is, thus, more accurate than the $A = 0.25$ determined from the 3-D Au/PPFC system, for which a statistical determination of the particle size could not be performed.

The identification of a broadening parameter is, to a small extent, arbitrary in that an assumption must be made with regard to the bulk contribution to the SPR width. For example, it was assumed that this contribution was negligible in the case of the 3-D Au/SiO_2 films owing to the high temperature anneal (i.e. 900°C), and supposed lack of lattice defects other than the deformation induced by the surface, where as a $\tau_B = 5 \times 10^{-14}$ seconds was assumed in the case of the discontinuous films which were only annealed to 250°C. The justification of this approach, and the accuracy of an A value of about 0.15 lies in the aggreement between the observed and predicted onset of phase retardation and scattering effects (i.e. at $R \sim 15 - 20\,\text{nm}$).

The results of this work are relevant on two accounts: the first one concerns the

characterization of finite size effects using a non-invasive spectroscopy which can be compared to more intrusive methods, in particular, TEM and XPS. The second concerns the current and potential applications of nanocomposite films. In regard to heterogeneous catalysis, the dependence of the electronic properties on the particle size and on the support material are essential for a better understanding of the enhanced activity inherent to small particle systems. In regard to nonlinear optical materials for telecommunications, the ability to fabricate a nanocomposite material in a thin film format that adheres to a microstructure assumed in effective medium models is essential in the optimization of the local field enhancement factor, and, hence, the device performance. In regard to nanoscale electronics, the observation of particle charging, as suggested by some of the experiments, implies the potential for manipulation of the electron density, usually ascribed only to semiconductors, and a concomitant wealth of potential applications. For example, one can envision the fabrication of transistors that are sensitive to the charge of a single electron by virtue of the ultralow capacitance of the particle/dielectric junction.

The natural continuation of this work consists of the extension of the characterization methodology to other metal/dielectric systems in order to provide additional experimental data on which to base theoretical models concerning finite size effects, in particular, the still unresolved questions of the magnitude and frequency dependence of A. Work in this regard has already commenced with the successful preparation of Ag/SiO_2 nanocomposite films using the dual MS/PECVD approach. A more novel system that can be envisioned is the fabrication of ITO particles which would possess a SPR in the ir by virture of the lower electron density.

In a different context, further research would consist of a more critical treatment of the microstructural dependence on fabrication conditions (glow discharge parameters and deposition system configuration). In particular, it is desirable to control the particle size without the need to resort to high temperature thermal treatments. This would open the door to the fabrication of novel vacuum-deposited matrix-embedded

metal/chromophore systems relevant to device application in the field of all-optical switching.

Bibliography

[1] R. H. Ritchie, "Surface plasmons in solids," Surf. Sci. **34,** 1 (1973).

[2] M. Faraday. "Experimental relations of gold (and other metals) to light," Phil. Trans. R. Soc. **147,** 145–181 (1857).

[3] R. W. Wood, "A suspected case of the electrical resonance of minute metal particles for light-waves. A new type of absorption," Phil. Mag. **3,** 396 (1902).

[4] J. C. Maxwell-Garnett, "Colours in metal glasses and in metallic films," Philos. Trans. R. Soc. London **203,** 385–420 (1904).

[5] G. Mie, "Beiträge zur Optik trüber Medien, speziell kolloidaler Metallösungen," Ann. Phys. (Leipzig) **25,** 377 (1908).

[6] H. Fröhlich, "Die spezifische Wärme der Elektronen kleiner Metallteilchen bei tiefen Temperaturen," Physica (Utrecht) **4,** 406 (1937).

[7] R. Kubo, "Electronic properties of metallic fine particles," J. Phys. Soc. Jap. **17,** 975 (1962).

[8] W. Ekardt, "Work function of small metal particles: self consistent spherical jellium-background model," Phys. Rev. B **29,** 1558 (1984).

[9] W. A. de Heer, "The physics of simple metal clusters: experimental and simple models," Rev. Mod. Phys. **65,** 611–676 (1993).

[10] L. D. Marks, "Experimental studies of small particle structures," Rep. Prog. Phys. **57,** 603 (1994).

[11] P. M. Ajayan and L. D. Marks, "Phase instabilities in small particles," Phase Transitions **24-26,** 229 (1990).

[12] M. Schmidt, R. Kusche, B. von Issendorft, and H. Haberland, "Irregular variations in the melting point of size-selected atomic clusters," Nature **393,** 238 (1998).

[13] N. E. Christensen and B. O. Seraphin, "Relativistic band calculation and the optical properties of gold," Phys. Rev. B **4,** 3321–3344 (1971).

[14] P. Winsemius, H. P. Lengkeek, and F. F. V. Kampen, "Structure dependence of the optical properties of Cu, Ag and Au," Physica B **79,** 529–546 (1975).

[15] D. E. Eastman, "Photoemission spectra for liquid and crystalline Au," Phys. Rev. Lett. **26,** 1108 (1971).

[16] P. Citrin, G. K. Wertheim, and Y. Baer, "Surface-atom x-ray photoemission form clean metals: Cu, Ag, and Au," Phys. Rev. B **27,** 3160 (1983).

[17] P. H. Citrin and G. K. Wertheim, "Photoemission from surface-atom core levels, surface densities of states, and metal-atom clusters: a unified picture," Phys. Rev. B **27,** 3176 (1983).

[18] S. Berthier and J. Lafait, in *Handbook of Optical Properties: Thin Films for Optical Coatings*, R. E. Hummer and K. H. Guenther, eds., (CRC Press, Boca Raton, 1995), Vol. 1, Chap. 11, pp. 305–352.

[19] D. Ricard, P. Roussignol, and C. Flytzanis, "Surface-mediated enhancement of optical phase conjugation in metal colloids," Opt. Lett. **10,** 511–513 (1985).

[20] F. Hache, D. Ricard, C. Flytzanis, and U. Kreibig, "The optical Kerr effect in small metal particles and metal colloids: the case of gold," App. Phys. A **47,** 347 (1988).

[21] J. R. F. Haglund, in *Handbook of Optical Properties: Optics of Small Particles, Interfaces, and Surfaces*, R. E. Hummel and R. Wibmann, eds., (CRC Press, Boca Raton, 1997), Vol. 2, Chap. 8, p. 191.

[22] J. W. Haus, N. Kalyaniwalla, R. Inguva, M. Bloemer, and C. M. Bowden, "Nonlinear-optical properties of conductive spheroidal particle composites," J. Opt. Soc. Am. B **6,** 797 (1989).

[23] J. E. Sipe and R. W. Boyd, "Nonlinear susceptibility of composite optical materials in the Maxwell Garnett model," Phys. Rev. A **46,** 1614 (1992).

[24] I. Vargas-Baca, M. P. Andrews, Y. Li, H. Vali, and M. G. Kuzyk, "Adsorption and enhanced optical response of a disulfide-functionalized chromophore on colloidal gold," unpublished .

[25] S. Muto, T. Kubo, Y. Kurokawa, and K. Suzuki, "Third-order nonlinear optical properties of Disperse Red 1 and Au nanometer-size particle-doped alumina films prepared by the sol-gel method," Thin Solid Films **322,** 233 (1998).

[26] M. Valden, X. Lai, and D. W. Goodman, "Onset of catalytic activity of gold clusters on titania with the apperance of nonmetallic properties," Science **281,** 1647–1650 (1998).

[27] M. Haruta, "Size- and support-dependency in the catalysis of gold," Catal. Today **36,** 153 (1997).

[28] M. Okumura, S. Nakamura, S. Tsubota, T. Nakamura, M. Azuma, and M. Haruta, "Chemical vapor deposition of gold on Al_2O_3, SiO_2, and TiO_2 for the oxidation of CO and H_2," Catal. Lett. **51,** 53 (1998).

[29] G. K. Wertheim, S. B. DiCenzo, and S. E. Youngquist, "Unit charge on cupported gold clusters in photoemission final state," Phys. Rev. Lett. **51,** 2310 (1983).

[30] K. P. Charlé, W. Schulze, and B. Winter, "The size dependent shift of the surface plasmon absorption band of small spherical metal particles," Z. Phys. D **12,** 471–475 (1989).

[31] B. N. J. Persson, "Polarizability of small spherical metal particles: influence of the matrix environment," Surf. Sci. **281,** 153–162 (1993).

[32] H. Hovel, S. Fritz, A. Hilger, U. Kreibig, and M. Vollmer, "Width of cluster plasmon resonances: bulk dielectric function and chemical interface damping," Phys. Rev. B **48,** 18178–18188 (1993).

[33] B. G. Levi, "Very small tunnel junctions sense the effect of single electrons," Phys. Today **41,** 19 (1988).

[34] M. G. Mason, "Electronic structure of supported small metal clusters," Phys. Rev. B **27,** 748 (1983).

[35] S. B. DiCenzo and G. K. Wertheim, "Supported clusters," Clusters and Molecules **1,** 361 (1990).

[36] A. Balerna, E. Bernieri, P. Picozzi, A. Reale, and S. Santucci, "A structural investigation on small gold clusters by EXAFS," Surf. Sci. **156,** 206–213 (1985).

[37] C. Solliard and M. Flueli, "Surface stress and size effects on the lattice parameter in small particles of gold and platinum," Surf. Sci. **156,** 487–494 (1985).

[38] W. Vogel, "X-ray diffraction from clusters," Cryst. Res. Technol. **33,** 1141 (1998).

[39] D. Lovall, M. Buss, P. Andres, and R. Reifenberger, "Resolving the atomic structure of supported nanometer-size Au clusters," Phys. Rev. B **58,** 15889 (1998).

[40] J. Xu, J. A. P. Mills, A. Ueda, D. O. Henderson, R. Suzuki, and S. Ishibashi, "Vacancy clusters on surfaces of Au nanoparticles embedded in MgO," Phys. Rev. Lett. **83,** 83 (1999).

[41] C. R. Henry, "Growth, structure and morphology of supported metal clusters studied by surface science techniques," Cryst. Res. Technol. **33,** 1119 (1998).

[42] H. Inouye, K. Tanaka, I. Tanahashi, and K. Hirao, "Ultrafast dynamics of nonequilibrium electrons in gold nanoparticle system," Phys. Rev. B **56,** 11334 (1998).

[43] T. Klair, M. Perner, S. Grosse, G. von Plessen, W. Spirkl, and J. Feldmann, "Surface-plasmon resonances in single metallic nanoparticles," Phys. Rev. Lett. **80,** 4249 (1998).

[44] N. W. Ashcroft and N. D. Mermin, *Solid State Physics* (Holt, Rinehart & Winston, New York, 1976).

[45] M. Born and E. Wolf, *Principles of Optics*, 6 ed. (Pegamon Press, New York, 1993).

[46] L. Martinu and D. Poitras, "Plasma deposition of optical films and coatings: A review," J. Vac. Sci. Technol. A, *in press* .

[47] U. Kreibig and M. Vollmer, *Optical Properties of Metal Clusters*, Vol. 25 of *Springer Series in Materials Science* (Springer-Verlag, New York, 1995).

[48] J. A. A. J. Perenboom, P. Wyder, and F. Meier, "Electronic properties of small metallic particles," Phys. Rep. **78,** 173 (1981).

[49] H. C. van de Hulst, *Light Scattering by Small Particles* (Dover Publications, Inc., New York, 1981).

[50] T. Reiners, C. Ellert, M. Schmidt, and H. Haberland, "Size dependence of the optical response of spherical sodium clusters," Phys. Rev. Lett. **74,** 1558–1561 (1995).

[51] M. Guerrisi, R. Rosei, and P. Winsemius, "Splitting of the interband absorption edge in Au," Phys. Rev. B **12,** 557 (1975).

[52] D. A. G. Bruggeman, "Berechnung verschiedener physikalischer Konstanten von Substanzen," Ann. Phys. (Leipzig) **24,** 636 (1935).

[53] P. Sheng, "Theory for the dielectric function of granular composite media," Phys. Rev. Lett. **45,** 60 (1980).

[54] W. Lamb, D. M. Wood, and N. W. Ashcroft, "Long-wavelength electromagnetic propagation in heterogeneous media," Phys. Rev. B **21,** 2248 (1980).

[55] G. A. Niklasson, C. G. Granqvist, and O. Hunderi, "Effective medium models for the optical properites of inhomogeneous materials," Applied Optics **20,** 26 (1981).

[56] D. E. Aspnes, "Local-field effects and effective-medium theory: A microscopic perspective," Am. J. Phys. **50,** 704 (1982).

[57] R. P. Feynman, R. B. Leighton, and M. Sands, *The Feynman Lectures on Physics* (Addison-Wesley, Reading, MA, 1964), Vol. 2.

[58] C. Kittel, *Introduction to Solid State Physics*, 7 ed. (John Wiley & Sons, Inc., New York, 1996).

[59] L. D. Landau and E. M. Lifshitz, *Electrodynamics of Continuous Media* (Addison-Wesley, Reading, MA, 1960).

[60] C. Granqvist and O. Hunderi, "Optical properties of ultrafine gold particles," Phys. Rev. B **16,** 3513–3534 (1977).

[61] O. Wiener, "Die theorie des Mischkörpers für das Feld der stationären strömung," Abh. Math. Phys. Kl Königl. Sächs. Ges. Wiss. **32,** 509 (1912).

[62] D. E. Aspnes, "Bounds to average internal fields in two-component composites," Phys. Rev. Lett. **48,** 1629 (1982).

[63] R. W. Cohen, G. D. Cody, M. D. Coutts, and B. Abeles, "Optical properties of granular silver and gold films," Phys. Rev. B **8,** 3689 (1973).

[64] C. Yannouleas and R. A. Broglia, "Landau damping and wall dissipation in large metal clusters," Ann. Phys. (NY) **217,** 105–141 (1992).

[65] M. A. Smithard, "Size effect on the Mie optical absorption of small sodium particles in sodium azide NaN_3," Solid State Commun. **14,** 407 (1974).

[66] V. Kresin, "Collective resonance frequencies of metal cluster ions," Phys. Rev. B **40,** 12507 (1989).

[67] K. Selby, M. Vollmer, J. Masui, V. Kresin, W. A. de Heer, and W. D. Knight, "Surface plasma resonances in free metal clusters," Phys. Rev. B **40,** 5417 (1989).

[68] C. Bréchignac, P. Cahuzac, F. Carlier, M. de Frutos, and J. Leygnier, "Optical excitation in small ionized sodium clusters: closed-shell and open-shell systems," Chem. Phys. Lett. **189,** 28 (1992).

[69] C. Bréchignac, P. Cahuzac, N. Kebaïli, J. Leygnier, and A. Sarfati, "Collective resonance in large free potassium cluster ions," Phys. Rev. Lett. **68,** 3916 (1992).

[70] H. Fallgren and T. P. Martin, "Photoabsorption of Cs_8 and $Cs_{10}O$ clusters," Chem. Phys. Lett. **168,** 233 (1990).

[71] Y. Wang, C. Lewenkopf, D. Tomáek, and G. Bertsch, "Collective electronic excitations and their damping in small alkali clusters," Chem. Phys. Lett. **205,** 521 (1993).

[72] K. P. Charlé, F. Frank, and W. Schulze, "The optical properties of silver microcrystallites in dependence on size and the influence of the matrix environment," Ber. Bunsenges. Phys. Chem. **88,** 350 (1984).

[73] Y. Borensztein, P. D. Andrès, R. Monreal, T. Lopez-Rios, and F. Flores, "Blue-shift of the dipolar plasma resonance in small silver particles on an alumina surface," Phys. Rev. B **33,** 2828–2830 (1986).

[74] J. Tiggesbäumker, L. Köller, K.-H. Meiwes-Broer, and A. Liebsch, "Blue shift of the Mie plasma frequency in Ag clusters and particles." Phys. Rev. A **48,** R1749–R1752 (1993).

[75] U. Kreibig, "The transition cluster-solid state in small gold particles," Solid State Comm. **28,** 767 (1978).

[76] R. Lamber, S. Wetjen, and G. Schulz-Ekloff, "Metal clusters in plasma polymer matrices: gold clusters," J. Phys. Chem. **99,** 13834–13838 (1995).

[77] R. Joerger, R. Gampp, A. Heinzel, W. Graf, M. Kohl, P. Gantenbein, and P. Oelhafen, "Optical properties of inhomogeneous media," Solar Energy Mat. **54,** 351 (1998).

[78] B. Palpant, B. Prével, J. Lermé, E. Cottancin, M. Pellarin, M. Treilleux, A. Perez, J. Vialle, and M. Broyer, "Optical properties of gold clusters in the size range 2-4nm," Phys. Rev. B **57,** 1963–1970 (1998).

[79] W. T. Doyle, "Absorption of light by colloids in alkali halide crystals," Phys. Rev. **111,** 1067 (1958).

[80] A. Kawabata and R. Kubo, "Electronic properties of fine metallic particles. II. Plasma resonance absorption," J. Phys. Soc. Jap. **21,** 1765–1772 (1966).

[81] U. Kreibig and L. Genzel, "Optical absorption of small metallic particles," Surf. Sci. **156,** 678 (1985).

[82] W. P. Halperin, "Quantum size effects in metal particles," Rev. Mod. Phys. **58,** 533 (1986).

[83] W. A. de Heer, W. D. Knight, M. Y. Chou, and M. L. Cohen, in *Electronic shell structure and metal clusters*, Vol. 40 of *Solid State Physics*, H. E. adn D. Turnbull, ed., (Academic, New York, 1987), Chap. 3, p. 93.

[84] V. V. Kresin, "Collective resonances and response properties of electrons in metal clusters." Phys. Rep. **220,** 1 (1992).

[85] U. Kreibig and C. von Fragstein, "The limitation of electron mean free path in small silver particles," Z. Phys. **224,** 307–323 (1969).

[86] L. Genzel, T. Martin, and U. Kreibig, "Dielectric function and plasma resonances of small metal particles," Z. Phys. B **21,** 339 (1975).

[87] M. Brack, "The physics of simple metal clusters: self-consistent jellium model and semiclassical approaches," Rev. Mod. Phys. **65,** 677 (1993).

[88] M. Cini and P. Ascarelli, "Quantum size effects in metal particles and thin films by an extended RPA," J. Phys. F **4,** 1998 (1974).

[89] A. A. Lushnikov and A. J. Simonov, "Surface plasmons in small metal particles," Z. Phys. **270,** 17 (1974).

[90] D. B. T. Thoai and W. Ekardt, "LIfe-time of surface plasmons in small metal particles," Solid State Commun. **41,** 687 (1982).

[91] D. M. Wood and N. W. Ashcroft, "Quantum size effects in the optical properties of small metallic particles," Phys. Rev. B **25,** 6255 (1982).

[92] W. Ekardt, "Dynamical polarizability of small metal particles: self-consistent spherical jellium background model," Phys. Rev. Lett. **52,** 1925 (1984).

[93] W. Ekardt, "Size-dependent photoabsorption and photoemission of small metal particles," Phys. Rev. B **31,** 6360–6370 (1985).

[94] M. J. Puska, R. M. Nieminen, and M. Manninen, "Electronic polarizability of small metal spheres," Phys. Rev. B **31,** 3486 (1985).

[95] D. E. Beck, "Self-consistent calculation of the eigenfrequencies for the electronic excitations in small jellium spheres," Phys. Rev. B **35,** 7325 (1987).

[96] G. Bertsch and W. Ekardt, "Application of sum rules to the response of small metal particles," Phys. Rev. B **32,** 7659 (1985).

[97] M. Brack, "Multipole vibrations of small alkali-metal spheres in a semiclassical description," Phys. Rev. B **39,** 3533 (1989).

[98] E. Engel and J. P. Perdew, "Theory of metallic clusters: asymptotic size dependence of electronic properties," Phys. Rev. B **43,** 1331 (1991).

[99] E. Zaremba and B. N. J. Persson, "Dynamic polarizability of small metal particles," Phys. Rev. B **35,** 596–606 (1987).

[100] A. Liebsch, "Surface-plasmon dispersion and size dependence of Mie resonance: silver versus simple metals," Phys. Rev. B **48,** 11317–11328 (1993).

[101] P. Apell and D. R. Penn, "Optical properties of small metal spheres: surface effects," Phys. Rev. Lett. **50,** 1316–1319 (1983).

[102] P. Apell and A. Ljungbert, "A General non-local theory for the electromagnetic response of a small metal particle," Physica Scripta **26,** 113–118 (1982).

[103] P. Apell and A. Ljungbert, "Red shift of surface plasmons in small metal particles," Solid State Commun. **44,** 1367 (1982).

[104] A. Liebsch, "Dynamical screening at simple-metal surface," Phys. Rev. B **36,** 7378 (1987).

[105] P. J. Feibelman, "Interpretation of the linear coefficient of surface-plasmon dispersion," Phys. Rev. B **40,** 2752 (1989).

[106] P. J. Feibelman, "Surface electromagnetic fields," Prog. Surf. Sci. **12,** 287–408 (1982).

[107] V. V. Kresin, "Collective resonances in silver clusters: role of d electrons and the polarization-free surface layer," Phys. Rev. B **51,** 1844–1849 (1995).

[108] C. W. Mays, J. S. Vermaak, and D. Kuhlmann-Wilsdorf, "On surface stress and surface tension," Surf. Sci. **12,** 134–140 (1968).

[109] J. L. Martins, R. Car, and J. Buffet, "Variational spherical model of small metallic particles," Surf. Sci. **106,** 265–271 (1981).

[110] C. L. Cleveland, U. Landman, M. N. Shafigullin, P. W. Stephens, and R. L. Whetten, "Structural evolution of larger gold clusters," Z. Phys. D **40,** 503 (1997).

[111] I. L. Garzón, L. Michaelian, A. Posada-Amarillas, P. Ordejón, E. Artacho, D. Sánchez-Portal, and J. M. Soler, "Lowest energy structures of gold nanoclusters," Phys. Rev. Lett. **81,** 1600 (1998).

[112] P. Pawlow, "Über die Abhängigkeit des Schmelzpunktes von der Oberflächenenergie eines festen Körpers," Z. Phys. Chem. **65,** 1 (1909).

[113] C. R. M. Wronski, "The size dependence of the melting point of small particles of tin," Br. J. Appl. Phys. **19,** 1731 (1967).

[114] P. Buffat and J.-P. Borel, "Size effect on the melting temperature of gold particles," Phys. Rev. A **12,** 2287 (1976).

[115] F. Ercolessi, W. Andreoni, and E. Tosatti, "Melting of small gold particles: mechanism and size effects," Phys. Rev. Lett. **66,** 911 (1991).

[116] H.-P. Cheng and R. S. Berry, "Surface melting of clusters and implications for bulk matter," Phys. Rev. A **45,** 7969 (1992).

[117] L. J. Lewis, P. Jensen, and J.-L. Barrat, "Melting, freezing, and coalescence of gold nanoclusters," Phys. Rev. B **56,** 2248 (1997).

[118] C. L. Cleveland, W. D. Luedtke, and U. Landman, "Melting of gold clusters," Phys. Rev. B **60,** 5065 (1999).

[119] T. Castro, R. Reifenberger, E. Choi, and R. P. Andres, "A field emission technique to measure the melting temperature of individual nanometer-sized clusters," Surf. Sci. **234,** 43 (1990).

[120] Y. Oshima and K. Takayanagi, "Solid-liquid phase transition of tin particles observed by UHV high resolution transmission electron microscopy: pseudocrystalline phase," Z. Phys. D **27,** 287 (1993).

[121] T. P. Martin, U. Näher, H. Schaber, and U. Zimmermann, "Evidence for a size-dependent metling of sodium clusters," J. Chem. Phys. **100,** 2322 (1994).

[122] M. Schimdt, R. Kusche, W. K. adn B. von Issendorft, and H. Haberland, "Experimental determination of the melting point and heat capacity for free cluster of 139 sodium atoms," Phys. Rev. Lett. **79,** 99 (1997).

[123] M. Miki-Yoshida, S. Techuacanero, and M. José-Yacamán, "On the high temperature coalescence of metallic nanocrystals," Surf. Sci. Lett. **274,** L569–L576 (1992).

[124] W. Krakow, M. Jóse-Yacamán, and J. L. Aragón, "Observation of quasimelting at the atomic level in Au nanoclusters," Phys. Rev. B **49,** 10591 (1994).

[125] N. Ju and A. Bulgac, "Finite-temperature properties of sodium clusters," Phys. Rev. B **48,** 2721 (1993).

[126] J. C. Miller, "Optical properties of liquid metals at high temperature." Phil. Mag. **20,** 1115 (1969).

[127] M.-L. Thèye, "Investigation of the optical properties of Au by means of thin semitransparant films," Phys. Rev. B **2,** 3060 (1970).

[128] U. Kreibig, "About a structural phase transition in minute gold particles embedded in glass," in *Growth and Properties of Metal Clusters.* J. Bourdon, ed., (Elsevier Scientific Publishing Company, The Netherlands, 1980), pp. 371-378.

[129] T. Yamaguchi, M. Takiguchi, S. Fujioka, and H. Takahashi, "Optical absorption of submonolayer gold films: size dependence of ϵ_{bound} in small island particles," Surf. Sci. **138,** 449–463 (1984).

[130] P. Picozzi, S. Santucci, M. D. Crescenze, F. Antonangeli, and M. Piacentini, "Vacuum ultraviolet reflectivity of small gold clusters." Phys. Rev. B **31,** 4023 (1985).

[131] G. K. Wertheim, "The insulator-metal transition in supported clusters," Phase Transitions **24-26,** 203–214 (1990).

[132] J. Lermé, B. Palpant, B. Prével, E. Cottancin, M. Pellarin, M. Treilleux, J. Vialle, A. Perez, and M. Broyer, "Optical properties of gold metal clusters: A time-dependent local-density-approximation investigation," Eur. Phys. J. D **4,** 95–108 (1998).

[133] A. Rubio and L. Serra, "Dielectric screening effects on the photoabsorption cross section of embedded metallic clusters," Phys. Rev. B **48,** 18223–18229 (1993).

[134] U. Kreibig, M. Gartz, A. Hilger, and H. Hövel, "Optical investigations of surfaces and interfaces of metal clusters," in *Advances in Metal and Semiconductor Clusters*, M. Duncan, ed., (JAI, Greenwich, 1998), Vol. 4, p. 345.

[135] C. G. Granqvist, N. Clander, and O. Hunderi, "Optical properties of ultrafine silver particles," Solid State Commun. **31,** 249 (1979).

[136] W. Ekardt and G. Penzar, "Collective excitations in open-shell metal clusters: Time-dependent local-density approximation applied to the self-consistent spheroidal jellium particle," Phys. Rev. B **43,** 1322 (1991).

[137] B. Abeles, "Granular metal films," in *Applied Solid State Science*, R. Wolfe, ed., (Academic Press, Inc., New York, 1976), Vol. 6, Chap. 1, p. 1.

[138] R. H. Magruder III, L. Yang, J. R. F. Haglund, C. W. White, L. Yang, R. Dorsinville, and R. R. Alfano, "Optical properties of gold nanocluster composites formed by deep ion implantation in silica," Appl. Phys. Lett. **62,** 1730 (1993).

[139] K. Fukumi, A. Chayahara, K. Kadono, T. Sakaguchi, Y. Horino, M. Miya, K. Fujii, J. Hayakawa, and M. Saton, "Gold nanoparticles ion implanted in glass with enhanced nonlinear optical properties," J. Appl. Phys. **75,** 3075 (1994).

[140] D. Ila, Z. Wu, C. C. Smith, D. B. Poker, D. K. Hensley, C. Klatt, and S. Kalbitzer, "Post bombarment enhanced optical absorption in gold implanted silica," Nucl. Inst. Instr. and Meth. B **127/128,** 570 (1997).

[141] Z. Liu, H. Li, X. Feng, S. Ren, H. Wang, Z. Liu, and B. Lu, "Formation effects and optical absorption of Ag nanocrystals embedded in single crystal SiO_2 by implantation," J. Appl. Physics **84,** 1913 (1998).

[142] Z. Dai, S. Yamamoto, K. Narumi, A. Miyashita, and H. Naramoto, "Gold nanoparticle fabrication in single crystal SiO_2 by MeV Au ion implantation

and subsequent thermal annealing," Nucl. Inst. Instr. and Meth. B **149,** 108 (1999).

[143] T. Yazawa, K. Kadono, H. Tanaka, T. Sakaguchi, S. Tsubota, K. Kuraoka, M. Miya, and W. De-Xian, "Preparation and optical property of monolithic silica gel uniformaly dipersed with gold colloid from aqueous solution," J. Non-Cryst. Solids **170,** 105 (1994).

[144] J. Matsuoka, R. Naruse, H. Nasu, and K. Kamiya, "Preparation of gold microcrystal-doped oxide optical coatings through adsorption of tetrachloroaurate ions on gel films," J. Non-Cryst. Solids **218,** 151 (1997).

[145] S. T. Selvan, Y. Ono, and M. Nogami, "Polymer-protected gold clusters in silica glass," Mat. Lett. **37,** 156 (1998).

[146] D. G. Duff, A. Baiker, and P. P. Edwards, "A new hydrosol of gold clusters. 1. Formation and particle size variation," Langmuir **9,** 2301 (1993).

[147] S. Banerjee and D. Chakravorty, "Optical absorption of composites of nanocrystalline silver prepared by electrodeposition," Appl. Phys. Lett. **72,** 1027 (1998).

[148] I. Tanahashi, Y. Manabe, T. Tohda, S. Sasaki, and A. Nakamura, "Optical nonlinearities of Au/SiO_2 composite thin films prepared by a sputtering method," J. Appl. Phys. **79,** 1244 (1996).

[149] H. B. Liao, R. F. Xiao, and G. K. L. Wong, "Large third-order nonlinear optical susceptibility of $Au\text{-}Al_2O_3$ composite films near the resonant frequency," Appl. Phys. B **65,** 673 (1997).

[150] H. B. Liao, R. F. Xiao, J. S. Fu, H. Wang, K. S. Wong, and G. K. L. Wong, "Origin of third-order optical nonlinearity in $Au{:}SiO_2$ composite films on femtosecond and picosecond time scales," Opt. Lett. **23,** 388 (1998).

[151] H. Liao, R. F. Xiao, H. Wong, K. S. Wong, and G. K. L. Wong, "Large third-order optical nonlinearity in Au:TiO_2 composite films measured on a femtosecond time scale," Appl. Phys. Lett. **72,** 1817 (1998).

[152] H. Biederman and L. Martinu, "Plasma polymer - metal composite films," in *Plasma Deposition: The Treatment and Etching of Polymers*, R. d'Agostino, ed., (Academic Press, Inc., New York, 1990), Chap. 4, p. 269.

[153] *Handbook of Deposition Technologies for Films and Coatings*, R. F. Bunshah, ed., (Noyes Publications, Park Ridges NJ, 1994).

[154] *Thin Films Processes*, J. L. Vossen and W. Kern, eds., (Academic Press, Inc., New York, 1991), Vol. 2.

[155] M. Ohring, *The Materials Science of Thin Films* (Academic Press, Inc., New York, 1992).

[156] I. Petrov, F. Adibi, J. E. Greene, W. D. Sproul, and W.-D. Münz, "Use of an externally applied axial magnetic field to control ion/neutral flux ratios incident at the substrate during magnetron sputter deposition," J. Vac. Sci. Technol. A **10,** 3283 (1992).

[157] E. Kay and M. Hecq, "Metal clusters in plasma polymerized fluorocarbon films: cobalt-aluminum," J. Vac. Sci. Technol. A **2,** 401 (1984).

[158] R. d'Agostino, F. Cramarossa, F. Fracassi, and F. Illuzzi, "Plasma polymerization of fluorocarbons," in *Plasma Deposition: The Treatment and Etching of Polymers*, R. d'Agostino, ed., (Academic, New York, 1990), Chap. 2, p. 85.

[159] D. K. Lam, R. F. Baddour, and A. F. Stancell, "A mechanisms and kinetics study of polymeric thin-film deposition in glow discharges," in *Plasma Chemistry of Polymers*, M. Shen, ed., (Dekkar, New York, 1976), p. 53.

[160] S. M. Han and E. S. Aydil, "Study of surface reactions during plasma enhanced chemical vapor deposition of SiO_2 from SiH_4, O_2, and Ar plasma," J. Vac. Sci. Technol. A **14,** 2062 (1996).

[161] E. Kay and M. Hecq, "Metal clusters in plasma polymerized matrices: Gold," J. Appl. Phys. **55,** 370 (1984).

[162] L. Martinu, H. Biederman, and J. Nedbal, "Dielectric properites of fluorocarbon and chlorofluorocarbon films plasma polymerized in an R.F. glow discharge," Thin Solid Films **136,** 11 (1986).

[163] L. Martinu and H. Biederman, "Plasma deposited composite polymer-metal thin films and their optical characteristics," Vacuum **36,** 477 (1986).

[164] M. Quinten, "Optical constants of gold and silver clusters in the spectral range between 1.5 eV and 4.5 eV," Z. Phys. B **100,** 211–217 (1996).

[165] P. Rouard and A. Meessen, "Optical properties of thin metal films," in *Progress in Optics*, E. Wolfe, ed., (North-Holland Publishing Co., Amsterdam, 1977), Vol. VX, Chap. 2, p. 78.

[166] L. Martinu, "Optical response of composite plasma polymer/metal films in the effective medium approach," Solar Energy Mat. **15,** 21 (1987).

[167] D. E. Aspnes, in *Handbook of Optical Constants of Solids*, E. D. Pallik, ed., (Academic Press, Inc., New York, 1985), Vol. 1, Chap. 5, p. 89.

[168] R. M. A. Azzam and N. M. Bashara, *Ellipsometry and Polarized Light* (North-Holland Publishing Co., Amsterdam, 1977).

[169] A. Roseler, *Infrared Spectroscopic Ellipsometry* (Akademi-Verlag, Berlin, 1990).

[170] H. G. Tompkins, *A User's Guide to Ellipsometry* (Academic Press, Inc., New York, 1993).

[171] H. G. Tompkins and W. A. McGahan, *Spectroscopic Ellipsometry and Reflectometry: A User's Guide* (John Wiley & Sons, Inc., New York, 1999).

[172] O. S. Heavens, *Optical Properties of Thin Film Solids* (Dover Publications, New York, 1965).

[173] A. Rothen, "The ellipsometer, an apparatus to measure thicknesses of thin films," Rev. Sci. Instr. **16,** 26 (1945).

[174] WVASE32, *Users Manual*, J. A. Woollam Co., Lincoln, NE, USA.

[175] A. Bergeron, Master's thesis, École Polytechnique de Montrél. Montréal, 1998.

[176] F. L. McCrackin, E. Passaglia, R. R. Stromberg, and H. L. Steinberg, "Measurement of the thickness and refractive index of very thin films and the optical properties of surfaces by elliposometry," J. Res. Nat. Bur. Sect. A. Physics and Chemistry **67,** 363 (1963).

[177] A. N. Saxena, "Changes in the phase and amplitude of polarized light reflected from a film-covered surface and their relations with the film thickness," J. Opt. Soc. Am. **55,** 1061 (1965).

[178] A. Bergeron, J. E. Klemberg-Sapieha, and L. Martinu, "Structure on the interfacial region between polycabonate and plasma-deposited $SiN_{1.3}$ and SiO_2 optical coatings studied by ellipsometry," J. Vac. Sci. Technol. A **16,** 3227 (1998).

[179] R. Maciejko, "Optoélectronique,", PHS6203 Course Notes, École Polytechnique de Montréal (1996).

[180] L. Cauchy, Bull. Sc. Math **14,** 9 (1830).

[181] A. R. Forouhi and I. Bloomer, "Optical dispersion relations for amorphous semiconductors and amorphous dielectrics," Phys. Rev. B **34,** 7018 (1986).

[182] J. G. E. Jellison and F. A. Modine, "Parameterization of the optical functions of amorphous materials in the interband region," Appl. Phys. Lett. **69,** 371 (1996).

[183] D. L. Wood and J. Tauc, "Weak absorption tails in amorphous semiconductors," Phys. Rev. B **5,** 3144 (1972).

[184] J. D. Dow and D. Redfield, "Toward a unified theory of Urbach's rule and exponential absorption edges," Phys. Rev. B **5,** 594 (1972).

[185] C. W. Greef and H. R. Glyde, "Anomalous Urbach tail in GaAs," Phys. Rev. B **51,** 1778 (1995).

[186] F. Urbach, "The long-wavelength edge of photographic sensitivity and the electronic absorption of solids," Phys. Rev. **92,** 1324 (1953).

[187] *Handbook of Optical Constants of Solids*, E. D. Palik, ed., (Academic Press, Inc., New York, 1985), Vol. 1.

[188] D. E. Aspnes, E. Kinsbron, and D. D. Bacon, "Optical properties of Au: sample effects," Phys. Rev. B **21,** 3290 (1980).

[189] A. Duparré, in *Handbook of Optical Properties: Thin Films for Optical Coatings*, R. E. Hummel and K. H. Guenther, eds., (CRC Press, Inc., Boca Raton, 1995), Vol. 1, Chap. 10, p. 273.

[190] *Handbook of X-ray Photoelectron Spectroscopy*, Perkin-Elmer Corporation, 1992.

[191] T. T. P. Cheung, "X-ray photoemission of small platinum and palladium clusters," Surf. Sci. **140,** 151 (1984).

[192] S. Kohiki and S. Ikeda, "Photoemission from small palladium clusters supported on various substrates," Phys. Rev. B **34,** 3786 (1986).

[193] W. Eberhardt, P. Fayet, D. M. Cox, Z. Fu, A. Kaldor, R. Sherwood, and D. Sondericker, "Photoemission from mass-selected monodispersed Pt clusters," Phys. Rev. Lett. **64,** 780 (1990).

[194] I. Jirka, "An ESCA strudy of copper clusters on carbon," Surf. Sci. **232,** 307–323 (1990).

[195] V. Vijayakrishnan and C. N. R. Rao, "An investigation of transition metal clusters deposited on graphite and metal oxide substrates by a combined XPS, UPS and Auger spectroscopy," Surf. Sci. Lett. **255,** L516 (1991).

[196] J. C. C. Fan, "Selective-black absorbers using sputtered cermet films." Thin Solid Films **54,** 139 (1978).

[197] U. Kreibig and P. Zacharias, "Surface plasma resonances in small spherical silver and gold particles," Z. Phys. **231,** 128 (1970).

[198] L. Martinu, "Deposition and structure of gold-containing plasma-polymerized halocarbon films," Thin Solid Films **140,** 307 (1986).

[199] H. Biederman, L. Martinu, and S. Nespurek, "Aging effects in composite plasma polymer/metal films," In *Proc. ISPC-8 Tokyo,* p. 1364 (1987).

[200] M. L. Jones, H. H. Soonpaa, and B. S. Rao, "Optical constants of bismuth tellurium sulfide from ellipsometric data." J. Opt. Soc. Am. **64,** 1591 (1974).

[201] H. Biederman, L. Martinu, O. Slavinska, and I. Chadacek, "Plasma deposition and properties of composite metal/polymer and metal/hard carbon films," Pure and App. Chem. **60,** 607 (1988).

[202] L. Martinu and H. Biederman, "Characterization of plasma deposited halocarbon polymer films containing small gold particles," J. Vac. Sci. Technol. A **3,** 2639 (1985).

[203] J. Perrin, B. Despax, and E. Kay, "Optical properties and microstructure of gold-fluorocarbon-polymer composite films," Phys. Rev. B **32,** 719 (1985).

[204] J. Perrin, B. Despax, V. Hanchett, and E. Kay, "Microstructure and electrical conductivity of plasma deposited gold/fluorocarbon composite films." J. Vac. Sci. Technol. A **4,** 46 (1986).

[205] M. Schubert, B. Rheinlander, J. A. Woollam, B. Johs, and C. M. Herzinger, "Extension of rotating-analyzer ellipsometry to generalized ellipsometry: determination of the dielectric function tensor from uniaxial TiO_2," J. Opt. Sci. Am. A **13,** 875 (1996).

[206] L. Martinu, "Electrical behaviour of composite plasma polymer/metal films," Solar Energy Mat. **15,** 135 (1987).

[207] D. Polder and J. H. van Santen, "The effective permeability of mixtures of solids," Physica (Utrecht) **12,** 257 (1946).

[208] P. Clippe, L. Evrard, A. Lucas, and M. Ausloos, "Aggregation effect on the infrared absorption spectrum of small ionic crystals," Phys. Rev. B **14,** 1715 (1976).

[209] R. H. Doremus, "Optical properties of small gold particles." J. Chem. Phys. **40,** 2389 (1964).

[210] D. Dalacu and L. Martinu, "Spectroellipsometric characterization of plasma deposited Au/SiO_2 nanocomposite films," J. Appl. Phys. **87,** 228–235 (2000).

[211] T. Swanson, Natl. Bur. Stand., Circ. 539,1,33 (1953).

[212] G. P. Agrawal, C. Cojan, and C. Flytzanis, "Chain-pairing in one-dimensional conjugated polymers and semiconductors," Phys. Rev. Lett. **38,** 711 (1977).

[213] F. Hache, D. Ricard, and C. Flytzanis, "Optical nonlinearities of small metal particles: surface-mediated resonance and quantum size effects," J. Opt. Soc. Am. B **3,** 1647 (1986).

[214] S. Ohtsuka, K. Tsunetomo, T. Koyama, and S. Tanaka, "Embedment of gold and CdTe particles in glass matrix and their nonlinear optical properties," Nonlinear Optics **13,** 101 (1995).

[215] H. B. Liao, R. F. Xiao, J. S. Fu, P. Yu, G. K. L. Wong, and P. Sheng, "Large third-order optical nonlinearity in Au:SiO_2 composite films near the percolation threshold," Appl. Phys. Lett. **70,** 1 (1997).

[216] M. Mori, T. Kineri, K. Kadono, T. Sakaguchi, M. Miya, H. Wakabayashi, and T. Tsuchiya, "Effect of the atomic ratio of Ba and Ti on optical properties of gold-dispersed $BaTiO_3$ thin films," J. Am. Ceram. Soc. **78,** 2391 (1995).

[217] D. Dalacu and L. Martinu, "Spectroellipsometric characterization of plasma deposited Au/fluoropolymer nanocomposite films," J. Vac. Sci. Technol. A **17,** 877 (1999).

[218] G. K. Wertheim, "Electronic structure of metal clusters." Z. Phys. D **12,** 319 (1989).

[219] S. T. Lee, G. Apai, and M. G. Mason, "Evolution of band structure in gold clusters as studied by photoemission," Phys. Rev. B **23,** 505 (1981).

[220] H. Roulet, G. D. J. M. Mariot, and C. F. Hague, "Size dependence of the valence bands in gold clusters," J. Phys. F **10,** 1025–1030 (1980).

[221] J. E. Klemberg-Sapieha, O. M. Kuttel, L. Martinu, and M. R. Wertheimer, "Dual microwave-RF plasma deposition of functional coatings," Thin Solid Films **93-94,** 965–972 (1990).

[222] L. Martinu, J. E. Klemberg-Sapieha, O. M. Kuttel, A. Raveh, and M. R. Wertheimer, "Critical ion energy and ion flux in the growth of films by plasma-enhanced chemical-vapor deposition," J. Vac. Sci. Technol. A **12,** 1360–1364 (1994).

[223] A. Heilmann and J. Werner, "In situ observation of microstructural changes of embedded silver particles," Thin Solid Films **317,** 21–26 (1998).

[224] D. Dalacu and L. Martinu, "Optical properties of discontinuous gold films: Finite size effects," J. Opt. Soc. Am. B **18,** 85–92 (2001).

[225] R. J. Warmack and S. L. Humphrey, "Observation of two surface-plasmon modes on gold particles," Phys. Rev. B **34,** 2246–2252 (1986).

[226] G. B. Bachelet, F. Bassani, M. Bourg, and A. Julg, "Surface and size effects on the electronic states of small metallic clusters: a model calculation," J. Phys. C **16,** 4305 (1983).

[227] R. Lässer and N. V. Smith, "Interband optical transitions in gold in the photon energy range 2–25 eV," Solid State Commun. **37,** 507–509 (1981).

[228] U. Kreibig, "Anomalous frequency and temperature dependence of the optical aborption of small gold particles," J. Physique C2 **27,** 97–103 (1977).

[229] K. Liang, W. Salaneck, and I. Aksay, "X-ray photoemission studies of thin gold films," Solid State Commun. **19,** 329–334 (1976).

[230] P. Winsemius, M. Guerrisi, and R. Rosei, "Splitting of the interband absorption edge in Au: Temperature dependence," Phys. Rev. B **12,** 4570 (1975).

[231] P. M. Ajayan and L. D. Marks, "Quasimelting and phases of small particles," Phys. Rev. Lett. **60,** 585 (1988).

[232] T. E. Faber, in *The Physics of Metals*, J. M. Ziman, ed., (Cambridge University Press, London, 1969), Chap. 6, p. 282.

[233] J. Urban, "Crystallography of clusters," Cryst. Res. Technol. **33,** 1009 (1998).

[234] J. F. Hamilton and P. C. Logel, "Vapor deposition of silver, gold and palladium on carbon and silicon dioxide in ion-pumped vacuum," Thin Solid Films **23,** 89 (1974).

[235] H. Schmeisser, "Growth and mobility effects of gold clusters on rocksalt (100) surfaces studied with the method of quantitative image analysis part I: cluster size distributions," Thin Solid Films **22,** 83 (1974).

[236] H. Schmeisser, "Growth and mobility effects of gold clusters on rocksalt (100) surfaces studied with the method of quantitative image analysis part II: spatial distribution of clusters," Thin Solid Films **22,** 99 (1974).

[237] H.-J. Freund, M. Bäumer, J. Libuda, H. Kuhlenbeck, T. Risse, K. Al-Shamery, and H. Hamann, "Metal aggregates on oxide surfaces: structure and adsorption," Cryst. Res. Technol. **33,** 977 (1998).

[238] H. Shirakawa and H. Komiyama, "Migration-coalescence of nanoparticles during deposition of Au, Ag, Cu, and GaAs on amorphous SiO_2," J. Nano. Res. **1,** 17 (1999).

[239] M. Hirasawa, H. Shirakawa, Hamamura, Y. Egashira, and H. Komiyama, "Growth mechanism of nanoparticles prepared by radio frequency sputtering," J. Appl. Phys. **82,** 1404 (1997).

[240] L. Zhang, F. Cosandey, R. Persaud, and T. E. Madey, "Initial growth and morphology of thin Au films on TiO_2 (110)," Surf. Sci. **439,** 73 (1999).

[241] C. Xu, W. S. Oh, G. Liu, D. Y. Kim, and W. Goodman, "Characterization of metal clusters (Pd and Au) supported on various metal oxide surfaces (MgO and TiO_2)," J. Vac. Sci. Technol. A **15,** 1261 (1997).

[242] T. Kizuka and N. Tanaka, "Atomic process of epitaxial growth of gold on magnesium oxide studied by cross-sectional time-resolved high-resolution electron microscopy," Phys. Rev. B **56,** R10079 (1997).

[243] S. Regnier and M. Gillet, "Growth mechanism of gold particles on Al_2O_3," Z. Phys. D **19,** 311 (1991).

[244] D. Jarret and L. Ward, "Optical properties of discontinuous gold films," J. Phys. D: Appl. Phys. **9,** 1515–1527 (1976).

[245] V. Truong and G. Scott, "Optical constants of aggregated gold films," J. Opt. Soc. Am. **66,** 124–131 (1976).

[246] S. Norrman, T. Andersson, and C. Granqvist, "Optical properties of discontinuous gold flims," Phys. Rev. B **18,** 674–695 (1978).

[247] D. Bedeaux and J. Vlieger, "A statistical theory for the dielectric properties of thin island films: application and comparison with experimental results," Thin Solid Films **102,** 265–281 (1983).

[248] G. A. Niklasson, "Optical properties of gas-evaporated metal particles: effects of a fractal structure," J. Appl. Phys. **62,** 258–265 (1987).

[249] M. Bloemer, M. Buncick, R. Warmack, and T. Ferrel, "Surface electromagnetic modes in prolate spheroids of gold, aluminum, and copper," J. Opt. Soc. Am. B **5,** 2552–2559 (1988).

[250] G. Bader, P. Ashrit, F. Girouard, and V. Truong, "p-polarized optical properties of aggregrated Au films," J. Appl. Phys. **68,** 1820–1824 (1990).

[251] R. Doremus, "Optical absorption of island films of nobel metals: wavelength of the plasma absorption band," Thin Solid Films **326,** 205–210 (1998).

[252] K. Mümmler and P. Wißmann, "Spectroscopic ellipsometry on gold clusters embedded in a Si(111) surface," Thin Solid Films **313-314,** 522–526 (1998).

[253] C. G. Granqvist, N. Calander, and O. Hunderi, "Optical properties of ultrafine silver particles," Solid State Commun. **31,** 249-252 (1979).

[254] J. Little, T. Callcott, T. Ferrel, and E. Arakawa, "Surface-plasmon radiation from ellipsoidal silver spheroids," Phys. Rev. B **29,** 1606–1615 (1984).

[255] T. Yamaguchi, M. Ogawa, H. Takahashi, and N. Saito, "Optical absorption of submonolayer silver films: size dependence of ϵ_{bound} in small island particles," Surf. Sci. **129,** 232–246 (1983).

[256] L. Serra and A. Rubio, "Optical response of Ag clusters," Z. Phys. D **40,** 262–264 (1997).

[257] T. Yamaguchi, S. Yoshida, and A. Kinbara, "Anomalous optical absorption of aggregated silver films," Thin Solid Films **18,** 63–70 (1973).

[258] T. Yamaguchi, S. Yoshida, and A. Kinbara, "Optical effect of the substrate on the anomalous absorption of aggregated silver films," Thin Solid Films **21,** 173–187 (1974).

[259] T. Yamaguchi, H. Hidetoshi, and A. Sudoh, "Optical behavior of a metal island film," J. Opt. Soc. Am. **68,** 1039–1044 (1978).

[260] T. Gerfin and M. Grätzel, "Optical properties of tin-doped indium oxide determined by spectroscopic ellipsometry," J. Appl. Phys. **79,** 1722 (1996).

[261] B. G. Streetman, *Solid State Electronic Devices* (Prentice Hall, New Jersey, 1990).

[262] L. Oberli, R. Monot, H. J. Mathieu, D. Landolt, and J. Buffet, "Auger and x-ray photoelectron spectroscopy of small Au particles," Surf. Sci. **106,** 301 (1981).

[263] D. M. Cox, B. Kessler, P. Fayet, W. Eberhardt, Z. Fu, D. Sondericher, R. Sherwood, and A. Kaldor, "Chemical and electronic properties of size selected metal clusters: XPS studies of gold clusters," Nanostructured Mat. **1,** 161 (1992).

[264] K. J. Taylor, C. L. Pettiette-Hall, O. Cheshnovsky, and T. E. Smalley, "Ultraviolet photoelectron spectra of coinage metal clusters," J. Chem. Phys. **96,** 3319 (1992).

[265] C. N. R. Rao, V. Vijayakrishnan, H. N. Aiyer, G. U. Kulkarni, and G. N. Subbanna, "An investigation of well-characterized small gold clusters by photoelectron spectroscopy, tunneling spectroscopy, and cognate techniques," J. Phys. Chem. **97,** 11157 (1993).

[266] T. Ogama, "Energy correction by evaporated gold in x-ray photoelectron spectroscopy," J. Vac. Technol. A **14,** 1309 (1996).

[267] G. K. Wertheim and S. B. DiCenzo, "Cluster growth and core-electron binding energies in supported metal clusters," Phys. Rev. B **37,** 844 (1988).

[268] P. Ascarelli, M. Cini, G. Missoni, and Nistico, "X.P.S. line broadening in small metal clusters," J. Physique C2 **38,** 125 (1977).

[269] J. C. Fuggle, M. Campagna, Z. Zolnierek, R. Lässer, and A. Platau, "Observation of a relationship between core-level line shapes in photoelectron spectroscopy and the localization of screening orbitals," Phys. Rev. Lett. **45,** 1597 (1980).

[270] R. C. Baetzold, "Study of evaporated metal nuclei by Auger spectroscopy," J. Appl. Phys. **47,** 3799 (1976).

[271] A. Domingue, L. Dignard-Bailey, E. Sacher, A. Yelon, and T. H. Ellis, in *Metallization of Polymers*, Vol. 440 of *ACS Symposium Series*, E. Sacher, J.-J. Pireaux, and S. P. Kowalczyk, eds., (American Chemical Society, Washington, DC, 1990), Chap. 20, p. 272.

[272] L. Martinu, V. Pische, and R. d'Agostino, in *Metallization of Polymers*, Vol. 440 of *ACS Symposium Series*, E. Sacher, J.-J. Pireaux, and S. P. Kowalczyk, eds., (American Chemical Society, Washington, DC, 1990), Chap. 12, p. 170.

[273] D. Dalacu, A. P. Brown, J. E. Klemberg-Sapieha, L. Martinu, M. R. Wertheimer, S. I. Najafi, and M. A. Andrews, in *Plasma Deposition and Treatment of Polymers*, Vol. 544 of *MRS Symp. Proc.*, W. W. Lee, R. d'Agostino, and M. R. Wertheimer, eds., (Materials Research Society, Pennsylvania, 1999), p. 167.